DAMAGE IDENTIFICATION OF CIVIL STRUCTURES VIA RESPONSE RECONSTRUCTION

ZHANG CHAODONG

Ph.D

The Hong Kong Polytechnic University

2017

The Hong Kong Polytechnic University

Department of Civil and Environmental Engineering

DAMAGE IDENTIFICATION OF CIVIL STRUCTURES VIA RESPONSE RECONSTRUCTION

ZHANG Chaodong

A thesis submitted in partial fulfillment of the requirements for

the Degree of Doctor of Philosophy

August 2016

CERTIFICATE OF ORIGINALITY

I hereby declare that this thesis is my own work and that, to the best of my knowledge and belief, it reproduces no material previously published or written, nor material that has been accepted for the award of any other degree or diploma, except where due acknowledgement has been made in the text.

_____(Signed)

ZHANG Chaodong (Name of student)

To my family

for their love and support

ABSTRACT

To ensure the safety and functionality of civil structures, it is vital to detect and quantify structural deteriorations in a timely manner for remedial work, before these deteriorations propagate and become detrimental to the entire structure. Structural health monitoring has been developing in past two decades, aiming to continually monitor loading conditions and assess structural conditions so that prompt decisions can be made if any damage is detected and quantified.

Vibration-based damage identification, as a significant focus for structural condition assessment and health monitoring, has been the subject of many research efforts in recent years. Despite considerable progress in the structural health assessment of oil rigs, mechanical systems, and aerospace structures, such assessment still encounters some obstacles when it is applied to complex civil structures. These barriers mainly exhibit the following aspects: (1) the limited number of sensors compared to the number of structural components, which makes it difficult to capture enough dynamic responses for structural condition assessment; (2) the significance of model error, which is due to the difficulty of establishing a finite element (FE) model to represent the real dynamic behavior of large and complex structures; (3) the ill-posedness and non-identifiability of the inverse problem, which is due to the significant dimension of damaged areas corresponding to the numerous structural components; (4) the fact that the higher mode vibrations of cumbersome civil structures, which are more sensitive to local

damage, are not easily excited under operating conditions; and (5) the enormous, unaffordable computational demand associated with the large dimensions of discretized FE model matrices and the scope of dynamic FE analysis during iterations.

Taking these obstacles into consideration, this thesis aims to develop novel vibration-based damage identification methods specifically suited for application to civil structures of large-scale and geometric complexity. To accomplish this aim, the following research efforts have been made. First, an optimal multi-type sensor placement method is proposed for the best response reconstruction on the location where no sensors are installed as well as the time evolution of the pre-located deterministic excitations; Second, sparse regularization is proposed to replace the traditional Tikhonov regularization in finite element (FE) model updating based damage identification. The superiority of sparse regularization is highlighted not only in constraining the solution norm but also in promoting solution sparsity. Third, the Kalman filter based response reconstruction and multi-type response fusion are integrated with the sparse regularized FE model updating to supplement the limitation of sensor measurements as well as take the benefits of both global and local response fusion in structural damage identification. Fourth, the proposed response reconstruction-oriented damage identification strategy is extended from circumstances where the time evolution of external excitations is required to the conditions where external excitations acting on the structure are unknown. And finally, multi-level damage identification via response reconstruction is proposed for identification of element-level damages on

large civil structures. This method firstly detects possible damaged regions over the condensed and assembled substructures through dynamic substructuring technique using measured responses; then, the damage at the element level is further localized and quantified over suspicious substructures using the reconstructed responses of the identified substructures. As a result, the damage dimensions are dramatically decreased in the identification of both levels; the computational efforts are dramatically decreased, while the identifiability of the damage is increased.

Besides the theoretical studies, numerical studies and experimental investigations are also conducted to demonstrate the procedures of these proposed methods and verify their effectiveness. Simulation studies and experimental investigations are performed on an overhanging beam of 40 elements on the following issues: optimal sensor placement for joint response and excitation reconstruction, sparse regularization in FE model updating based damage identification, and damage identification via response reconstruction under both known and unknown excitations. Performance evaluation of the proposed optimal sensor placement method for joint response and excitation reconstruction as well as multi-level damage identification via response reconstruction is also conducted through experimental investigation on the long-span Tsing Ma suspension bridge testbed at the Structural Dynamic Laboratory of The Hong Kong Polytechnic University. The research works presented and the results obtained in this thesis contribute to the damage identification of the major civil structures.

PUBLICATIONS ARISING FROM THE THESIS

Journal papers

J. He, Y.L. Xu, **C.D. Zhang** and X.H. Zhang, Optimum control system for earthquake-excited building structures with minimal number of actuators and sensors, *Smart Structures and Systems* 16 (6) (2015): 981-1002.

C.D. Zhang and Y.L. Xu, Optimal multi-type sensor placement for response and excitation reconstruction, *Journal of Sound & Vibration* 360 (2016): 112-128.

C.D. Zhang and Y.L. Xu, Comparative studies on damage identification with Tikhonov regularization and sparse regularization, *Structure Control & Health Monitoring* 23 (2016): 567-579.

C.D. Zhang and Y.L. Xu, Structural damage identification via multi-type sensors and response reconstruction, *Structural Health Monitoring* 15(6) (2016): 715–729).

C.D. Zhang and Y.L. Xu, Structural damage identification via response reconstruction under unknown excitation, *Structural Control & Health Monitoring* (2016), DOI: 10.1002/stc.1953.

C.D. Zhang and Y.L. Xu, Multi-level damage identification with response reconstruction (Under review).

Conference papers and presentations

C.D. Zhang and Y.L. Xu, Multi-sensing damage detection of civil structures via response reconstruction, The 6th International Conference on Structural Health Monitoring of Intelligent Infrastructure, SHMII-6, Hong Kong, China, 09-11 December 2013.

C.D. Zhang and Y.L. Xu, Multi-sensing damage detection of civil structures via response reconstruction: theoretical development. The 6th World Conference on Structural Control and Monitoring, Spain, 15-17 July 2014.

Y.L. Xu and **C.D. Zhang**, Multi-sensing damage detection of civil structures via response reconstruction: experimental investigation. The 6th World Conference on Structural Control and Monitoring, Spain, 15-17 July 2014.

C.D. Zhang and Y.L. Xu, Optimal multi-type sensor placement for response reconstruction under unknown excitation. The Asia-Pacifica Workshop on Structural Health Monitoring, Shenzhen, China, 04-05 December 2014.

C.D. Zhang, Y.L. Xu. Kalman filter based response reconstruction using the fictitious noise model for damage identification of multi-story structures. 4th International Symposium and Workshop on Acoustics and Vibration, Harbin, China, 25-29 July, 2016.

ACKNOWLEDGEMENTS

First of all, I would like to express my sincere gratitude to my chief supervisor, Professor You-lin Xu for offering me the opportunity to pursue my Ph.D. study in The Hong Kong Polytechnic University (PolyU). His valuable advice, insightful guidance, and generous support are indispensable in outlining, conducting and completing the works culminating in this thesis. I have learned and achieved much more than what constitutes this thesis during the past five years.

I would also like to express my profound appreciation to my former chief supervisor Prof. Shi-zhao Shen and co-supervisor Prof. Yue Wu when I pursued my master study at the Harbin Institute of Technology (HIT). Prof. Shen's modesty and rigorous scholarship and lavish and active lifestyles have been consistently impacting on my academic and professional development. Prof. Wu not only provided the insightful and valuable guidance towards my research work but also offered the timely and generous support in my life. All of these have helped me a lot to begin my academic career. Thanks also go to all the teachers and friends in the Space Structure Research Center of HIT.

I gratefully acknowledge the financial support received from the Studentship of The Hong Kong Polytechnic University and the Hong Kong Research Grant Council through my Ph.D. study. PolyU has offered me the excellent working environment and research facilities.

I particularly thank the Board of Examiners members, Dr. Eddie Siu-Shu Lam from

Department of Civil and Environmental Engineering, PolyU, Prof. Satish Nagarajiaiah from Rice University, USA, and Prof. Francis Tat-Kwong Au from the University of Hong Kong for attending my oral examination and providing insightful comments on my thesis.

My heartfelt gratitude also goes to my friends, housemates, and members of the research group at the Hong Kong Polytechnic University. They have contributed in different ways in guiding me through the highs and the lows and giving me the inspiration to keep on going during the past research journey. For the works presented here, particular thanks go to Mr. Sheng Zhan, Dr. Xiao-hua Zhang, Dr. Bin Wang, Dr. Liang Hu, Dr. Jia He, Dr. Qing Huang, Dr. Wen-ai Shen, Dr. Wen-yu He, Dr. Yue Zheng, Dr. Feng-yang Wang, Dr. Jing-hua Lin, Miss. Yi-xin Peng, Mr. Jian-fu Lin, Mr. Rong-pan Hu and Mr. Zhi-lu Wang for their valuable advice and warm assistances during my study. Getting through my Ph.D. study requires more than academic support, and I cannot begin to express my gratitude and appreciation for their friendship and company over the past years.

I am forever indebted to my parents, who indeed cannot be thanked enough, for consistently providing me with the support and encouragement, which enabled me to achieve every goal in my life. I also thank my elder brother and sister, who always support my research and my life. Finally, special thanks go to my wife, Lilian Sun, who shared me with her happiness and affections, and supported me through these years since we met with her love, encouragement, incredible understanding and sacrifices.

CONTENT

LIST OF FIGURES

LIST OF TABLES

LIST OF NOTATIONS

$\mathbf{A}_c, \mathbf{B}_c, \mathbf{C}_c, \mathbf{D}_c$	Continuous state, input, output and transmission matrices
$\mathbf{A}_d$, $\mathbf{B}_d$, $\mathbf{C}_d$, $\mathbf{D}_d$	Discrete state, input , output and transmission matrices
α	Mass proportional damping coefficient
β	Stiffness proportional damping coefficient
$\mathbf{B}$	Transformation matrix between the displacement and strain
$\mathbf{B}^s$	Transforming matrix between displacement and strain of the s-th substructure
$\mathbf{B}_0$, $\mathbf{B}_1$	Intermediate matrix depends on the inter-sample assumption on the input
$\mathbf{d}$	Nodal displacement
$\mathbf{d}_i^s, \mathbf{d}_b^s$	Displacement of interface DOFs and internal DOFs in the *s*-th substructure
$\mathbf{e}$	A standard normal distribution vector with zero mean and unit standard deviation

$\boldsymbol{\delta}$	Response reconstruction error
$\boldsymbol{\Lambda}$	Response reconstruction error covariance
$\overline{\boldsymbol{\Lambda}}$	The stable reconstruction error covariance matrix
Δt	Sampling interval
$\Delta\mathbf{y}$	Weighted response discrepancy
$\Delta\hat{\boldsymbol{\theta}}$	Estimate of the incremental damage vector
E	Expectation operation
$\boldsymbol{\varepsilon}$	Stain response
$\boldsymbol{\varepsilon}^s$	Strain response of the *s*-th substructure
$\boldsymbol{\eta}_k^s$	Truncated set of generalized modal coordinates for $\boldsymbol{\Phi}_k^s$
η	Solution norm
$\hat{\mathbf{g}}^s$	Transformed connecting forces acting on the *s*-th substructure
$\overline{\mathbf{g}}$	Assembled transformed connecting forces of all the substructures
J	Objective function

$\mathbf{K}_k$	Kalman filter gain
$\boldsymbol{\Xi}$	Diagonal modal damping ratio matrix
ξ_i	The *i*-th modal damping ratios
$\mathbf{L}$	Mapping matrix connecting the excitation and its location
$\bar{\mathbf{L}}$	Boolean matrix localizing the interface DOF of the substructures
λ	Regularization parameter
$\mathbf{M}_k$	Gain matrix
$\mathbf{M}, \mathbf{C}, \mathbf{K}$	Mass, Damping, and Stiffness matrices
$\mathbf{M}^s, \mathbf{C}^s$ and $\mathbf{K}^s$	Mass, damping, and stiffness submatrices of the *s*-th substructure
$\hat{\mathbf{M}}^s, \hat{\mathbf{C}}^s$ and $\hat{\mathbf{K}}^s$	Reduced mass, damping and stiffness matrices of the *s*-th substructure
$\bar{\mathbf{M}}, \bar{\mathbf{C}}$ and $\bar{\mathbf{K}}$	Block-diagonally assembled matrices of all the substructures
$\hat{\mathbf{M}}_s, \hat{\mathbf{C}}_s$ and $\hat{\mathbf{K}}_s$	Global mass, damping, and stiffness contributed by the *s*-th substructure
$\tilde{\mathbf{M}}_s, \tilde{\mathbf{C}}_s$ and $\tilde{\mathbf{K}}_s$	Transformed mass, damping, and stiffness contributed by the *s*-th substructure

$\bar{\mathbf{M}}_i^s, \bar{\mathbf{C}}_i^s$ and $\bar{\mathbf{K}}_i^s$	Mass, damping and stiffness matrices provided by the *i*-th element in the *s*-th substructure
$\tilde{\mathbf{M}}, \tilde{\mathbf{C}}$ and $\tilde{\mathbf{K}}$	Assembled global mass, damping and stiffness matrices
N_m	Dimension of observation vector
n	Number of DOF
n_k^s	Number of kept mode in $\mathbf{\Phi}_{ik}^s$
n_s	Dimension of the *s*-th substructure
$\hat{n}_s$	Dimension of the reduced *s*-th substructure
n_{max}	Preset maximum iteration number
N	Number of candidate locations
N_n	Number of the divided substructures
N_e	Number of the elements
N_s	Element number in the *s*-th substructure
$\mathbf{\Omega}$	Diagonal eigenfrequencies matrix
p	Number of excitation

$\boldsymbol{\Phi}$	Mode shapes matrix
$\boldsymbol{\Phi}_k^s$	Fixed-interface normal modes of the *s*-th substructure
$\boldsymbol{\Phi}_c^s$	Interface constraint modes of the *s*-th substructure
$\boldsymbol{\Phi}_{ik}^s$	Kept interior partition of $\boldsymbol{\Phi}_k^s$
$\boldsymbol{\Psi}$	Strain mode shapes matrix
$\boldsymbol{\Psi}_{ib}^s$	Interior partition of $\boldsymbol{\Phi}_c^s$
ω_i	Natural frequencies of i-th mode
$\mathbf{p}$	A unique set of the generalized coordinates
$\mathbf{P}_k^u$	excitation estimate error variance
$\mathbf{P}^{x-}$, $\mathbf{P}^{x+}$	Priori and posterior state estimation error covariance
$\mathbf{P}^{xu}$	the cross-covariance of the estimate errors of state and excitation
$\mathbf{q}^s$	Generalized coordinates of the *s*-th substructure
$\bar{\mathbf{q}}$	Assembled generalized coordinates of all the substructures
$\mathbf{Q}$	Covariance matrices of modeling error

$\mathbf{R}$	Covariance matrices of measurement noise
R_{std}	Ratio of noise stand deviation to real response stand deviation
r	Number of truncated mode shapes
R_{fit}	Coefficient of goodness-of-fit
ρ	Residual norm
$\mathbf{S}_{\tilde{\boldsymbol{\theta}}}$	Response sensitivity on the substructural level damage vector
$\mathbf{S}_{\boldsymbol{\theta}^s}$	Sensitivity on the damage vector of the s-th substructure
$\mathbf{S}$	Weighted sensitivity matrix
S_p	Optimal sensor placement configuration
S_N	The set of all distinct sensor configurations
$\boldsymbol{\theta}$	Damage vector
$\boldsymbol{\theta}^s$	Damage vector of the *s*-th substructure
$\boldsymbol{\Sigma}$	Singular values matrix of $\mathbf{S}$
$\mathbf{T}^s$	Craig-Bampton transformation matrix of the *s*-th substructure

$\mathbf{u}$	External excitation
$\tilde{\mathbf{u}}$	Excitation estimation error
$\hat{\mathbf{u}}$	Estimate of excitation $\mathbf{u}$
$\hat{\mathbf{u}}^s$	Transformed external forces applied to the *s*-th substructure
$\bar{\mathbf{u}}$	Assembled transformed external forces of all the substructures
$\mathbf{U}$	Left singular vectors of $\mathbf{S}$
$\mathbf{V}$	Right singular vectors of $\mathbf{S}$
$\mathbf{w}$, $\mathbf{v}$	Modeling error and measurement noise
$\bar{\mathbf{W}}$	Weighting matrix
$\mathbf{x}$	State vector
$\|\mathbf{x}\|_p$	The *p*-norm of the vector $\mathbf{x}$.
$\hat{\mathbf{x}}^-$	Priori state estimates of state vector $\mathbf{x}$
$\hat{\mathbf{x}}^+$	Posteriori state estimates of state vector $\mathbf{x}$
$\mathbf{y}$	Observation vector

$\mathbf{y}^r$, $\mathbf{y}^e$ and $\mathbf{y}^n$	Real, estimated and noise-polluted response
$\mathbf{y}_a$	Analytical response
y_{amp}	Noise amplitude

LIST OF ABBREVIATIONS

ANN	Artificial neural network
CMS	Component mode synthesis
CoMAC	Coordinate modal assurance criterion
DOF	Degree of freedom
DLV	Damage locating vector
DPR	Driving point residue
EfI	Effective independence
EMA	Experimental modal analysis
EMD	Empirical mode decomposition
FBG	Fiber Bragg grating
FE	Finite element
FEA	Finite element analysis
FIM	Fisher information matrix

FRF	Frequency response function
GCV	Generalized cross-validation
IE	Information entropy
IMF	Instinct Mode Functions
KE	Kinetic energy
KF	Kalman filter
KF-UI	Kalman filter under unknown input
MAC	Modal assurance criteria
MSE	Modal strain energy
PSD	Power spectral density
PDF	Probability density functions
RBF	Radial-basis-function
RHS	Right-hand-side
RPE	Response percentage error
SHM	Structural health monitoring

SPO	Sensor placement optimization
SNR	Signal to noise ratio
STD	Standard deviation
TMB	Tsing Ma Bridge
TSVD	Truncated singular value decomposition

CHAPTER 1

INTRODUCTION

1.1 Research Motivation

The aging and deterioration of large infrastructures, such as long-span bridges under heavy loadings and harsh environment conditions, have become major worldwide concerns. According to the American Infrastructure Report Card issued by the American Society of Civil Engineers (ASCE 2013), one in nine bridges in the United States are either structurally deficient or functionally obsolete, and that clearing the deficient bridges before 2028 would require an annual investment of $20.5 billion USD, which is $8 billion USD greater than the current level. A similar report by the Institution of Civil Engineers (ICE 2014) indicates that one-third of the local transportation systems in the United Kingdom require urgent maintenance. In Canada, more than 40% of the bridges currently in use were built over 50 years ago (Bisby el al, 2004), and a significant number of these structures need strengthening, rehabilitation, or replacement, using limited maintenance budgets. Japan currently has over 140,000 existing bridges, each 15 meters long or longer. The average age of bridges will soon reach 40 or even 50 years, and so the necessity of frequent and detailed inspection and maintenance/repair is also expected to increase significantly in the near future (Fujino et al, 2011). The economic boom in China has prompted the construction of massive large-scale and complex civil structures over the past three decades. Similar to other emerging economies, China is expected to experience infrastructure deterioration in the very near future. This phenomenon emphasizes the

need for the autonomous and economical monitoring and maintenance of these civil structures.

Structural health monitoring (SHM), which aims to monitor the loading conditions continually and assess the structural condition of structures, has been recently proposed as a solution to the issue at hand (Aktan et al., 2000; Ko and Ni, 2005; Xu and Xia, 2011). To identify structural deterioration at an early stage for maintenance and repair works and to maximize the lifespan of the structure at minimum life-cycle costs, it is necessary to perform long-term continuous health monitoring of the structure during its service life. As indicated and demonstrated by Xu and Xia (2011), although SHM systems have found certain practical applications in monitoring loading and environmental effects, verifying the design criteria and guiding the timely inspection and maintenance on large civil structures, such as long-span suspension bridges, to perform robust damage detection and quantification on these structures, as the core task of SHM, is still in their infancy at the present stage.

In the past decades, many studies have attempted to detect structural damage using vibration data. Vibration-based damage identification mainly involves the practice of detecting, localizing and quantifying defects in structures from using the measured vibration responses. The damage identification outcomes made through monitoring may subsequently be used to make informed decisions on remedial work. Vibration-based damage identification posits that structural defects will change the dynamic features of a structure, including its acceleration response, frequency response function, frequency, and mode shapes. As its fundamental process,

vibration-based damage identification maps the relationship between the changes in the dynamic features and local damages of the structure. Given its increasing complexity, the damage assessment problem can be classified into the following hierarchies (Rytter, 1993): (1) detection, or determining the presence of a damage in a structure, (2) localization, or locating the spatial position of the damage, (3) quantification, or quantifying the extent of the damage, and (4) prognosis, or predicting the future structural condition. In this thesis, vibration-based damage identification involves the localization and quantification of the actual damage in a structure.

Many vibration-based damage identification methods have been developed over the past decades (Doebling et al., 1996, Sohn et al., 2003, Farrar et al., 2000). The literature review reveals that there are roughly two kinds of approaches addressing the damage identification problem, namely, the model-based approach and the data-driven (or model-free) approach. Figure 1.1 shows the main comparison between these two kinds of methods.

Data-driven approaches are entirely built upon the availability of an extensive collection of vibration data without recourse to law-driven models. The dynamic responses of the structure are processed using several signal processing technologies, such as empirical mode decomposition, Hilbert–Huang transform, principal component analysis, wavelet analysis and others, to extract the dynamic sensitive features. These features are then used to interpret the condition of the structure through nonparametric techniques, such as statistical pattern recognition, support vector machines, and neural networks and others, to establish classification schemes that can

detect structural defects from vibration data.

Data-driven damage identification, which does not require a priori information upon the physical model of the structure, is particularly advantageous in dealing with complicated structures. However, predicting the dynamic behaviors of these structures requires a parametric model that is nearly impossible to construct. By contrast, given the difficulty in establishing an explicit relationship between the damage and the structure, the results from nonparametric methods cannot be easily interpreted because of their “black-box” nature. Moreover, the limited amount of data on damaged structures in real-world scenarios makes the data-driven damage identification approaches unsuitable for assessing conditions of civil structures; higher-level damage identification methods, such as damage localization and severity quantification, are even more difficult to use.

Model-based damage identifications commonly rely on the availability of an analytical model, such as FE model, state-space model or polynomial model (autoregressive model with exogenous input or autoregressive–moving-average model with exogenous inputs and others), which represents the dynamics of the structure under suspicion. After establishing an initial analytical model based on the laws of physics, the dynamic properties extracted from the experimental data are used to update the analytical model and make this model consistent with the tested structure. Damage detection, localization, and quantification are then conducted through the solution of an inverse problem using the data collected from the damaged structure.

The FE model updating method is the first notable scheme for model-based damage identification (Friswell, 1995; Brownjohn et al., 2011). Given the advancements in FE modeling and analysis, the FE model updating method has drawn a significant amount of research attention over the past decades because of its capability of not only detecting damage and quantifying its extent. The structural defects in the FE model are localized and quantified through model updating by minimizing the discrepancy between the measured features of the damaged structure and the analytical features predicted by the FE model. Although several numerical and laboratory experiments have been successfully conducted on some simple and regular structures, the FE model updating method has rarely been successfully applied to large structures. The robust identification of damages in large civil structures is mainly hindered by the following factors:

1. For the model-based identification of damage to great civil structures, establishing an analytical model has been proven difficult because of the challenges in setting up an elaborate FE model of a vast and complex civil structure. The FE models of actual structures show inevitable discrepancies, and civil structures usually operate in outdoor conditions where measurement noises are omnipresent. Therefore, such discrepancies and measurement noises must be considered when formulating a damage identification method for civil structures.

2. A complex civil structure typically consists tens of thousands of structural components. The corresponding damage vector has a very large dimension. Identifying structural damage over a significant damage space presents a difficult task because of the ill-posedness and non-identifiability of the problem. Therefore, a proper

regularization technology that imposes additional constraints to the solution must be proposed.

3. Given the budget constraints and measurement inaccessibility under operational conditions, the sensor deployments for capturing the structural responses of large civil structures are always limited compared with the substantial structural components. Therefore, a damage identification method that heavily relies on dense sensor installments and measurements cannot be applied to large civil structures.

4. Despite the global and disastrous effects of structural failure, damage generation and propagation are common local phenomena. Therefore, both global and local responses are required to detect the incipient damage before such impairment spreads into and negatively affects the entire structure. The advancements in sensor technology allow for the deployment of a heterogeneous mix of multi-type sensors on a civil structure. Fusing the global (i.e., acceleration and displacement) and local responses (i.e., strain) captured by multiple sensors and taking advantage of the heterogeneity of these responses have significant roles in identifying the damages in civil structures.

5. Unlike mechanical structures, large and cumbersome civil structures rarely experience high-mode vibrations, which are more sensitive to local damage. In this regard, high-mode-vibration-based damage identification approaches are unsuitable for identifying damage in large civil structures. Besides, civil structures are often monitored under operational conditions in which the environmental effects and operational loads can hinder the interpretation of vibration data. Therefore, civil

structures require a damage identification method that mainly depends on several low-order vibrations and is highly robust to environmental effects.

6. The FE modeling and updating of large civil structures are computationally demanding because of the large dimension of the discretized FE model matrices and a large number of dynamic FE analyses involved in the updating procedure. Furthermore, FE model updating may not guarantee the global identifiability of damage despite the unaffordable computational costs of this method.

Given the above problems, a novel damage identification method that integrates multi-type responses reconstruction and fusion with multi-level sparse regularized FE model updating must be proposed for the accurate identification of damages in the major civil structures. Multi-type responses reconstruction is performed to overcome the limitations in sensor measurement and obtain comprehensive information, while multi-level damage identification is conducted to enhance the identifiability of damage and decrease the computation costs.

1.2 Research Objectives

This thesis proposes a novel model-updating-based method for identifying damage in the major civil structures. This method applies multi-type response reconstruction to address the limitations in sensor measurements, sparse regularization to handle the ill-posedness problem, and the substructuring technique to enhance the identifiability of damage. The main aims of this research are specifically described as follows:

1. To propose a multi-type sensor placement method that optimally fuses the

multi-metric measurements of the sensors to reconstruct the unmeasured responses on the key locations and the excitation acting on the structure.

2. To exploit the superiority of sparse regularization over the traditional Tikhonov regularization in dealing with the ill-posedness problem involved in model updating-based damage identification.

3. To propose a response reconstruction oriented damage identification method to overcome the limitations in sensor measurements and to take advantage of the benefits of multi-type response fusion in identifying damages in the major civil structures.

4. To extend the proposed damage identification via response reconstruction method from the situation where the excitation acting on the structure must be fully described to the situation where the knowledge on excitation time history is not required.

5. To propose a multi-level damage identification method via the response reconstruction method to enhance the identifiability of the incipient damage in large structures and to decrease the computation costs in iterative updatings.

6. To demonstrate and verify the effectiveness of the proposed method by conducting simulated and experimental studies on a simple overhanging beam and a relatively large structure as the Tsing Ma Bridge testbed.

1.3 Assumptions and Limitations

The development and application of multi-sensing and multi-level damage identification via the proposed response reconstruction framework are subjected to the

following assumptions and limitations:

1. In the optimal sensor placement for joint response and excitation reconstruction, the system modeling errors and measurement noises are assumed to be normally distributed and independent of one another, thereby indicating a zero covariance between these two. Besides, sufficient measurement instants are assumed to dirive the state error variance converge to a stable value, which is directly related to the response reconstruction error.

2. In damage identification, the structural damage can be modeled as a degradation of the stiffness (or mass) of the damaged region and simulated as saw-cut in a laboratory test. The main reason is that the severity of saw cut damage can be more easily controlled and quantified accurately. The structure is supposed to behave linearly and operate under the same working conditions before and after the occurrence of damage.

3. In multi-level damage identification, the FE model discrepancy induced by the Craig-Bampton reduction is much less than that caused by structural damage. The substructure partition, the location of the master degree of freedom, and the number of kept interior partitions of fixed-interface normal modes are all related to the accuracy of the dynamic substructuring technique.

4. In identifying the damages in the Tsing Ma suspension bridge, the dynamic vibrations of the cable system are adequately small to ignore the non-linear behavior of bridge motion. The damage-induced stress redistribution under gravity can also be neglected.

1.4 Outline and Scope

This thesis covers various topics to achieve the objectives above. This thesis is divided into 10 chapters, and Figure 1.2 presents an overview of the thesis structure. The chapters are organized as follows:

Chapter 1 introduces the problem, motivation, objectives, assumptions, and scope of this work.

Chapter 2 presents an extensive literature review on relevant topics, including the dynamic response reconstruction method, the optimal sensor placement method, the FE model updating based damage identification method in both frequency and time domains, the associated regularization techniques, and the dynamic substructuring technologies.

Chapter 3 introduces a multi-type sensor placement of response reconstruction in the absence of external excitation. The Kalman filter under unknown input is introduced, and the convergence properties of its state and input estimation are used for the optimal sensor placement design.

Chapter 4 addresses the ill-posedness in FE model updating based damage identification methods. Sparse regularization, or specifically ℓ_1 norm regularization, is proposed to constrain the solution norm and promote the sparsity of the solution. The motivation of sparse regularization and its difference from the popular Tikhonov technique are highlighted.

Chapter 5 combines the Kalman filter based response reconstruction method with the sparse regularized FE model updating method to identify the damage in large structures. The advantages of fusing multi-metric responses in damage identification are also investigated.

Chapter 6 extends the framework of the response reconstruction oriented damage identification method established in Chapter 5 from the situation of known excitation to that of unknown excitation.

Chapter 7 presents experimental studies over an overhanging beam to investigate the issues in optimal sensor placement for response and excitation reconstruction, sparse regularization in FE model updating, and damage identification via response under known and unknown excitations.

Chapter 8 proposes a multi-level damage identification method to narrow down the damage dimension in both substructure- and element- level damage identification and to enhance the identifiability of damage in large structures.

Chapter 9 examines the effectiveness of the proposed optimal sensor placement method for response and excitation reconstruction and that of the multi-level damage identification method via response reconstruction in identifying the damage in a relatively large and complex structure, namely, the Tsing Ma suspension bridge testbed.

Chapter 10 summarizes the contributions, findings, and conclusions of this thesis. The limitations of this study are discussed and some recommendations for future study are

provided.

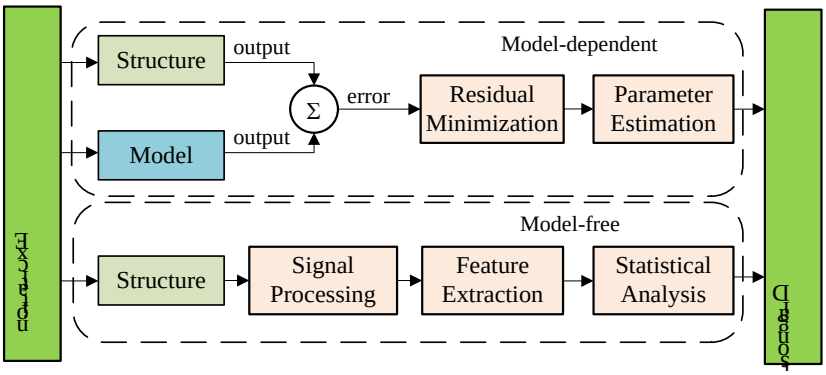

Figure 1.1 The model-dependent and model-free damage diagnosis

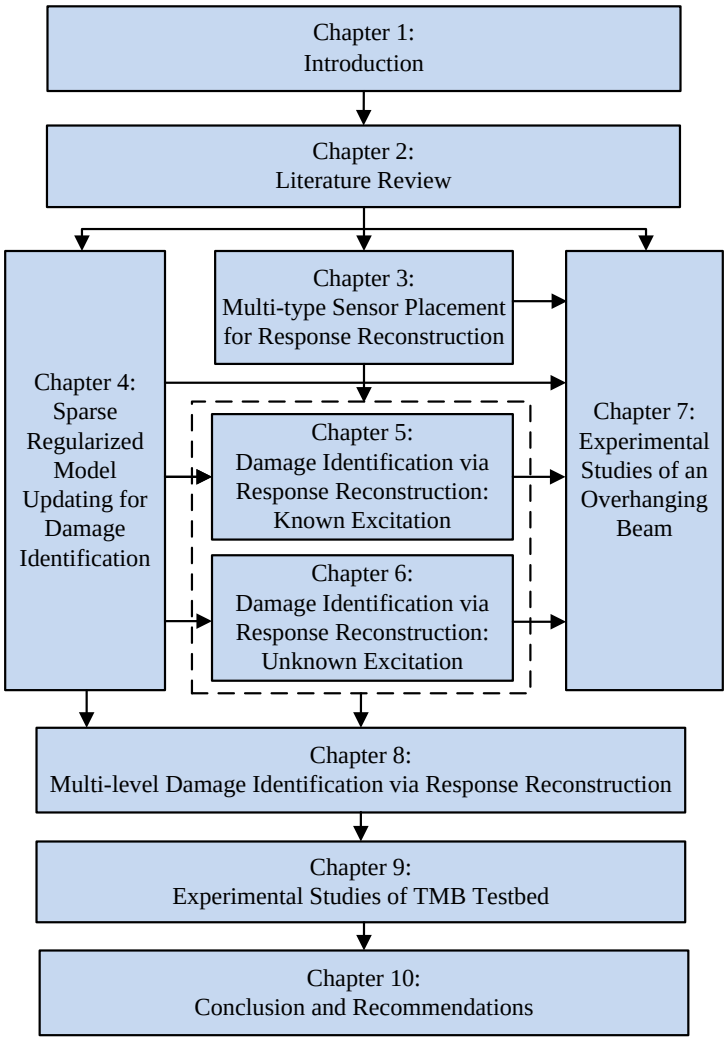

Figure 1.2: Overview of the thesis structure.

CHAPTER 2

LITERATURE REVIEW

Equation Section 2As mentioned in Chapter 1, this thesis aims to develop novel model updating based damage identification methods in consideration of response reconstruction, sparse regularization, and substructuring technique for large civil structures. The current state-of-the-art development of some relevant topics will be reviewed in this chapter, including dynamic response reconstruction, optimal sensor placement, model updating based damage detection and the associated regularization techniques, dynamic substructuring technique, and some advances in damage identification of large structures.

2.1 Dynamic Response Reconstruction

Due to sensor cost and installment accessibility, it is not practical to instrument sensors on every point of a structure and the measured set of dynamic responses is thus usually incomplete. This is the main reason for the implementation of response reconstruction. Dynamic response reconstruction is the process of estimating an unmeasured response of a structure by using the limited measured response on other locations.

The literature review on recent studies reveals several types of approaches for dynamic response reconstruction of a structure. The first type of response reconstruction methods can be classified as the transmissibility based method. The transmissibility is initially defined as the ratio of the response amplitude over the harmonic excitation

amplitude for a single DOF system (Urgueira et al., 2011). Later it has been extended to the *N* DOF systems by Ewins and Liu (1998) and Varoto et al. (1998). Basing on the generalized transmissibility concept in the frequency domain proposed by Ribeiro et al. (2000), Law et al. (2010) performed dynamic response reconstruction in a substructure as:

$$\mathbf{X}_u(\omega) = \mathbf{T}_{aku}(\omega)\mathbf{X}_k(\omega) \tag{2.1}$$

where $\mathbf{X}(\omega)$ is the response in the frequency domain and the time-domain response should be obtained through inverse Fourier transformation; the subscript u and k denote unknown response and known response, respectively and a denotes the excitation acting location. The transmissibility matrix $\mathbf{T}_{aku}(\omega)$ is expressed as:

$$\mathbf{T}_{aku}(\omega) = \mathbf{H}_{ua}(\omega)\left[\mathbf{H}_{ka}(\omega)\right]^{\dagger} \tag{2.2}$$

in which $\mathbf{H}(\omega)$ is the frequency response function (FRF); the symbol † denotes the pseudo-inverse. The sensors number should be larger than the excitation number and the excitation location should be known. Li et al. (2011) extended this method to the wavelet domain using the unit impulse response function. Simulation studies show that discrete wavelet transform yields more accurate response reconstruction than discrete Fourier transformation. Kammer (1997) presented a similar method, in which the responses of a structure at the inaccessible locations during its operation are reconstructed by transforming the response at other locations as:

$$\mathbf{y}_u = \mathbf{H}_u\left[\mathbf{H}_m\right]^{\dagger}\mathbf{y}_m \tag{2.3}$$

where $\mathbf{H}$ is the Markov parameter matrix, which represents the response of the structure to unit force pulses at the excitation locations; the subscript m and u denote the measured and unmeasured response, respectively. Similarly, this approach requires the knowledge of external excitations location and the number of sensors larger than that of excitation. Moreover, it is usually applicable for the single type of structural response only. The associated issue of optimal sensor placement was investigated in the reference (Wang et al., 2014). Zhang et al. (2011) utilized the truncated mode shape matrix $\mathbf{\Gamma}$ in the forming of transmissibility matrix for response reconstruction as:

$$\mathbf{y}_u = \mathbf{\Gamma}_u \left[\mathbf{\Gamma}_m^T \mathbf{\Gamma}_u \right]^{-1} \mathbf{\Gamma}_m^T \mathbf{y}_m = \mathbf{\Gamma} \mathbf{\Gamma}^{\dagger} \mathbf{y}_m \tag{2.4}$$

The shape matrix $\mathbf{\Gamma} = \left\{ \mathbf{\Phi}^T, \mathbf{\Psi}^T \right\}^T$ includes the strain $\mathbf{\Psi}$ and displacement $\mathbf{\Phi}$ mode shape derived from finite element (FE) model and a fusion of strain and displacement was conducted to predict the unobserved strain and displacement response of interest better. A normalization procedure was employed to deal with the ill-posedness due to the different magnitudes of strain and displacement responses.

The second type of response reconstruction methods is based on mode decomposition. Empirical mode decomposition (EMD) (Norden et al., 1998) together with the FE model of a structure is a notable approach of this kind. The measurement data available at limited locations are decoupled into several Intrinsic Mode Functions (IMFs), which is considered to be the approximation of modal response, using the EMD method as:

$$y_m(t) = \sum_{i=1}^{m} \phi_{mi} q_i(t) + r(t) = \sum_{i=1}^{m} x_{mi}(t) + r(t) \tag{2.5}$$

where $x_{mi}(t)$ is the modal response (also an IMF) for the *i*-th mode, which is a mono-component response; ϕ_{mi} is the *i*-th model shape on *m* location and $q_i(t)$ is the generalized modal response. Term $r(t)$ represents the mean trend or constant of the signal. Those IMFs are applied to extrapolate the dynamic response at the critical locations where the direct response measurements are not available as:

$$y_u(t) = \sum_{i=1}^{m} \phi_{ui} q_i(t) + r(t) = \sum_{i=1}^{m} (\phi_{ui} / \phi_{mi}) x_{mi}(t) + r(t) \tag{2.6}$$

He et al. (2012) performed the structural response reconstruction based on the EMD with intermittency criteria and the transformation equations derived from the FE model of the structure. Wan et al. (2014) combined the EMD method with the transmissibility method and made it applicable to the situation where the structure exhibits the vibration of closely-spaced modes. Besides, Ma et al. (2001) reconstructed the transient response using Karhuen-Loeve mode decomposition (also termed as proper orthogonal decomposition). The results of a series of experiments with a three-bay linear truss showed that the Karhuen-Loeve based low-order models can capture satisfactory dynamics of the truss, but less so in the higher-order modes. Through the above reviews, it is noted that the quality of the response reconstruction relies heavily on the mode decomposition technique.

Another kind of dynamic response reconstruction is the state estimation based method. State estimation is usually fulfilled through a filter or an observer, which uses an

analytical model and measurements of a system to provide estimates of the state of the system. A block diagram of state estimation based response reconstruction is depicted in Figure 2. 1. The basic idea of this approach is that after the state estimate is abstained through an estimator, the measured noise-corrupted response can be estimated with noise filtered out and the unmeasured responses can be reconstructed using the observation matrix of these unmeasured locations. Various estimators can be employed in kind of method. The Kalman filter (Kalman, 1960) is the most renowned estimator with a broad range of applicability. Zhang et al. (2012) and Xu et al. (2016) presented a Kalman filter based dynamic response reconstruction method, in which the state vector of generalized coordinates was obtained using the real-time responses measured by limited sensors; then the response at the locations of interest can then be reconstructed by multiplying their mode shapes with the estimated state vector. Nasseri et al. (2010) presented a similar method for seismic response reconstruction. Kalman filter under unknown input (KF-UI) was also used by Lourens et al. (2012) for response reconstruction under unknown excitation using acceleration measurement. A practical application example was presented in reference (Limongelli, 2016). Liu et al. (2016) derived an extended Kalman filter under unknown (EKF-UI) similar to the procedures of KE-UI and applied the filter to estimate structural displacement and unknown inputs by fusing of displacement and acceleration.

Aside from the aforementioned three kinds of methods, some other types of the response reconstruction methods have also been developed. Hong (2010) utilized two types of finite impulse response filters to reconstruct dynamic displacement responses using measured acceleration responses. Setola (1998) reconstructed the dynamic

response of a flexible beam basing on the interpolation of available measurements by spline shape functions. A very similar method was presented by Liongelli (2003). The unknown responses of a multi-story frame were reconstructed based on the interpolation of available response through a spline shape function. The accuracy of reconstructed responses increases with the number of recorded sensors, and it is strongly influenced by the number and layout of sensors.

2.2 Sensor Placement Optimization

The success of damage detection largely depends on the quality of measurement data. Thus, an important question is the placement of sensors regarding types, numbers, and locations on the structure. These areas should be given attention to ensure that predefined sensors capture informative dynamic signature regarding the structural condition. The goal in sensor placement is to determine the spatial location for a collection of sensors in a spatial domain that maximizes the information achievable for structural condition assessment. Generally, sensor placement addresses the questions that could be stated as "given a set of n possible locations, find the subset of a locations, where $a << n$, which provides the best possible performance" (Padula et al., 1991; Doebling et al., 1996). Given that sensors should be deployed at discrete locations corresponding to the notes of the discretized FE model, the sensor placement optimization (SPO) issue could be mathematically formatted as a discrete optimization problem. Thus, the topic of SPO mainly involves two subproblems, namely, what evaluation criterion is used and how the optimization problem is solved. This section presents the theoretical basis underlying several approaches and the optimization solving methods for SPO. The descriptions have been kept intentionally

mathematically light for easy understanding.

2.2.1 Theoretical Basis

The position of sensors can be determined according to various evaluation criteria for different purposes, which results in the development of many SPO methods. The main theoretical basis of the existing SPO methods is introduced in the subsequent section, followed by the reviews on the optimization methods for SPO.

Effective independence based method

On the basis of the principles of sensitivity analysis, Kammer et al. (1991) and Kammer and Tinker (2004) proposed the effective independence (EfI) method, which is closely related to the Fisher information matrix (FIM), as expressed in Eq.(2.7).

$$\mathbf{H} = \left[\frac{\sigma^2}{\mathbf{\Phi}^T \mathbf{\Phi}} \right]^{-1} \tag{2.7}$$

where $\mathbf{\Phi} \in \Re^{m \times n}$ is a matrix of *n* target modes with *m* measurement locations and σ^2 is the noise variance level on each sensor. The EfI method tends to select sensor positions that make the mode shapes of interest as linearly independent as possible while reserving sufficient responses of the target modes in the measurements. Two assumptions are implicitly assumed in the EfI method. First, the target mode shape matrix $\mathbf{\Phi}$ should be a rectangle, which indicates that the number of sensors must be no less than the number of the target modes, and second, measurement noise is assumed uncorrelated among sensors and of equal variance σ^2. From different optimization criteria, several methods were proposed based on the FIM matrix. Kammer (1991) first defined the EfI distribution vector, as expressed in Eq.(2.8), to distinguish critical

DOFs from redundant DOFs:

$$\mathbf{E}_D = diag\left(\boldsymbol{\Phi}\left[\boldsymbol{\Phi}^T\boldsymbol{\Phi}\right]^{-1}\boldsymbol{\Phi}^T\right) \tag{2.8}$$

The contribution of each DOF to the rank of the matrix $\left(\boldsymbol{\Phi}^T\boldsymbol{\Phi}\right)$ is determined by sorting the elements in the vector $\mathbf{E}_D$. The DOF with the smallest contribution should be removed, and the number of DOFs could be reduced until the required number is achieved by repeating the process. EfI leads to making the mode shapes of interest as linearly independent as possible for the selected sensor locations. The determinant of the FIM indicates the linear independence of the target modes on the reduced set of sensor locations. This idea was exploited in several references (Kammer et al., 1992; Yao et al., 1993) through the maximization of the determinant of the FIM. Several derivative methods based on EfI are proposed (Kirkegaard et al., 1994; Meo et al., 2005). In other studies (Zavoni et al., 1998; Zavoni et al., 1999), optimal sensor configuration has been chosen as the method to minimize the expected Bayesian loss function involving the trace of the inverse of the FIM.

However, in the EfI method, sensor locations with low energy content could be selected, which makes the measurement vulnerable to noise. The EfI-DPR method proposed by Imamovic (1998) eliminates the locations with low energy by multiplying the EfI of the candidate sensor contribution with the driving point residue (DPR) coefficient:

$$\mathbf{E}_{D_j} = \mathbf{E}_D DPR_j \tag{2.9}$$

in which the DPR is expressed with the form:

$$DPR_j = \sum_{i=1}^{N} \frac{\varphi_{ji}^2}{\omega_i} \tag{2.10}$$

where φ_{ji} is the *j*-th element of the *i*-th mode shape, and ω_i is the *i*-th modal frequency. The DPR provides a measure of the contribution of any point to the overall modal response. This adaptation leads to a greater likelihood of sensors being placed in locations of high vibration strength.

Kinetic energy based method

The kinetic energy (KE) of a flexible structure is usually unevenly distributed over every location. Positions with high KE are heuristically selected to increase the signal-to-noise ratio. This idea later evolved into the KE method, which selects sensor locations based on the ranking of their dynamic contribution to the target mode shapes (Heo et al., 1997; Papadopoulos et al., 1998; Worden et al., 2001). This method follows a similar procedure used in the EfI method, but the key difference is that a KE measure, as expressed in Eq.(2.11), is maximized.

$$KE = \mathbf{\Phi}^T \mathbf{M} \mathbf{\Phi} \tag{2.11}$$

The KE can be regarded as the FIM weighted by the corresponding component of the mass matrix $\mathbf{M}$. The sensor locations that provide the highest KE are selected as the measurement locations. The connection between the EfI and the modal KE methods was addressed by Li et al. (2007). In the cited study, the KE method is an iterated version of the EfI method and the reduced mode shapes are repeatedly

orthonormalized during iterations of the KE method.

Another SPO method that bears the similar idea is the model reduction based method. Model reduction is commonly used to condense the original model to reduce the DOFs while giving much faster computation. In model reduction, the DOFs of the initial model are divided into two parts as $\mathbf{x} = \{\mathbf{x}_m, \mathbf{x}_s\}^T$, in which $\mathbf{x}_m$ and $\mathbf{x}_s$ denote the master DOF and the slave DOF, respectively. Guyan reduction method (Guyan, 1965) assumes that the inertial items on the slave DOFs can be ignored and it can be obtained that:

$$\mathbf{K}_{sm}\mathbf{x}_m + \mathbf{K}_{ss}\mathbf{x}_s = \mathbf{0} \tag{2.12}$$

$$\mathbf{x} = \begin{Bmatrix} \mathbf{x}_m \\ \mathbf{x}_s \end{Bmatrix} = \begin{bmatrix} \mathbf{I} \\ -\mathbf{K}_{ss}^{-1}\mathbf{K}_{sm} \end{bmatrix} \{\mathbf{x}_m\} = \mathbf{T}\{\mathbf{x}_m\} \tag{2.13}$$

where subscript *m* and *s* denote the master and the slave DOFs, respectively. The reduced mass matrix $\mathbf{M}_m$ and stiffness matrix $\mathbf{K}_m$ can be calculated as:

$$\mathbf{M}_m = \mathbf{T}^T\mathbf{M}\mathbf{T}; \mathbf{K}_m = \mathbf{K}^T\mathbf{M}\mathbf{K}; \tag{2.14}$$

Some researcher (Jarvis, 1991; Penny et al., 1994) exploited the idea of model reduction for SPO by assuming that the master DOF selected by the model reduction method are the appropriate measurement locations for the model test. SPO is conducted through a process of sequential deletion of slave DOFs from the original FE model until the retained master DOFs of the reduced model matches the number of sensors required.

Information entropy based method

Information entropy (IE), which measures uncertainty in structural parameters, has been adopted as the performance measure of a sensor configuration by several researchers (Papadimitriou et al., 2004; Papadimitriou et al., 2000; Yuen et al., 2001; Papadimitriou, 2004; Papadimitriou, 2005). In particular, the optimal sensor placement is selected by minimizing the IE, which is defined as follows:

$$H(D) = E_\theta\left[-\ln p(\boldsymbol{\theta}|D)\right] = -\int p(\boldsymbol{\theta}|D)\ln p(\boldsymbol{\theta}|D)\,d\boldsymbol{\theta} \tag{2.15}$$

where $\boldsymbol{\theta}$ is the uncertain parameter set to be estimated; D is the dynamic test data; and E_θ denotes the mathematical expectation on $\boldsymbol{\theta}$. Papadimitriou (2004) showed that the IE depends on the determinant of the FIM asymptotically for large data.

Controllability and observability based method

In structural control engineering, many sensor placement schemes have long been developed (Kubrusly et al., 1985; Abdullah et al., 2001) based on the concept of controllability and observability (Skelton, 1988; Gawronski, 2004). If the so-called observability matrix as Eq. (2.16) has rank *n*, i.e., $rank(\mathrm{O}) = n$, the linear discrete-time system is observable; if the controllability matrix, defined by Eq. (2.17) has full rank, i.e., $rank(C) = n$, the linear discrete-time system is controllable, where $\mathbf{A}_d \in \Re^{n\times n}$, $\mathbf{B}_d \in \Re^{n\times r}$ and $\mathbf{C}_d \in \Re^{m\times n}$ are the system matrices.

$$\mathrm{O}(\mathbf{A}_d, \mathbf{C}_d) = \begin{bmatrix} \mathbf{C}_d \\ \mathbf{C}_d\mathbf{A}_d \\ \cdots \\ \mathbf{C}_d\mathbf{A}_d^{(n-1)} \end{bmatrix} \in \Re^{(n\cdot m)\times n} \tag{2.16}$$

$$C(\mathbf{A}_d, \mathbf{B}_d) = \left[\mathbf{B}_d, \mathbf{A}_d\mathbf{B}_d, \cdots, \mathbf{A}_d^{n-1}\mathbf{B}_d \right] \in \Re^{n\times(r\cdot n)} \tag{2.17}$$

It is well known from control theory that the observability of a system depends critically on the location of the sensors. Lim (1990) employed the generalized Hankel matrix to develop an approach to determine sensor locations based on a given rank for the system observability matrix while satisfying modal test constraints. Park et al. (2003) presented an optimal placement method for sensors and actuators by using new measures of modal controllability and observability defined in a balanced coordinate system to assure that the most controllable and observable locations could be selected as the optimal sensor locations. Sassano et al. (2014) introduced the notion of dynamic generalized controllability and observability functions for sensor deployment and model reduction problems.

Sensitivity based method

In damage identification applications, Cobb and Liebst (1997) initially proposed a sensitivity-based method that prioritizes the DOFs to instrument sensors by examining the sensitivity of the first-order partial eigenstructure with respect to changes in the structural stiffness of each element. Shi et al. (2000) proposed the eigenvector sensitivity method for the optimal placement of sensors with attention to damage detection. Zhou et al. (2013) presented a similar method for structural damage detection considering measurement uncertainties. Danai (2013) demonstrated an optimal sensor location selection for structures via response sensitivities analysis in the timescale domain. The sensitivities of sensor outputs to structural properties could be assessed by transforming output sensitivities via continuous wavelet transforms into a time-scale domain. Azarbayejani et al. (2004) demonstrated a probabilistic

approach to optimal sensor location for SHM by utilizing a priori knowledge of probable damage locations and severities in the structure.

Besides, there also are some SPO methods for several specific objectives. Wang et al. (2013) presented a sensor placement method for improving the force identification in state space based on the correlation analysis of the Markov matrix. Moreover, a two-step SPO method is also presented (Wang et al., 2014) for dynamic response reconstruction. The response reconstruction is based on the transmissibility matrix between two sets of sensor locations. Firstly, the initial combination of the sensor is determined based on the ill-posedness of the response reconstruction equation and then in the second step, the number and locations of the final sensor placement were obtained basing on the minimization of the defined measurement noise index. Zhang et al. (2012) proposed an optimal multi-type sensor placement for response reconstruction based on the classical Kalman filter theory, in which the modeling errors and measurement noise were taken into consideration. He et al. (2015) proposed a methodology to determine the minimal number and optimal location of actuators and sensors for vibration control of building structures in a combination of response reconstruction under earthquake excitation.

2.2.2 Optimization Strategy

The problem of deriving the optimal sensor configuration could be formulated as a discrete minimization problem. Considering that *m* sensors of the same type are intended to be deployed among a set of *n* candidate locations, the criterion would have to be evaluated among the $C_n^m = n!/\left[m!(n-m)!\right]$ different candidate sensor suites, let

alone in the situation of multi-type sensors. A number of traditional deterministic optimization methods (e.g., Newton iteration and the recursive quadratic programming) can be used for simple and regular structures. However, for a civil structure that usually comprises tens of thousands of components, an exhaustive search of the optimal sensor configuration is probably computationally prohibitive.

Kammer and Yao (1994) proposed an efficient iterative algorithm for sensor placement, in which sensors resulting in the lowest reduction in the determinant of the FIM are sequentially removed from the candidate locations until the desired number of sensors is reached. Udwadia (1994) demonstrated that using the trace feature of the FIM is computationally attractive because the solution of the underlined discrete optimization problem is straightforward. Lopes et al. (2004) formulated the optimal sensor placement as a binary mixed integer nonlinear programming problem, where each possible sensor location is represented by a binary variable. Two computationally efficient heuristic algorithms, namely, the forward and backward sequential sensor placements (SSP), were presented in several references (Papadimitriou et al., 2004; Papadimitriou et al., 2005) based on the theoretical asymptotic results on IE and FIM. In the forward SSP algorithm, the N-th optimal sensor is determined in such a way that, in addition to the fixed (N -1) selected sensors, placing one sensor at a position will result in the highest reduction in the objective function. The backward SSP algorithm is the inverse of the forward SSP algorithm. Although the SSP algorithm could not be guaranteed as the optimal algorithm, this algorithm is well-known because of its computational efficiency in obtaining a proper sensor configuration (Liu et al., 2000). The numerical results indicate that this systemic and heuristic SSP algorithm provides

suboptimal sensor configurations that could generate good approximations of the optimal sensor configuration (Papadimitriou, 2004; Papadimitriou, 2005). Zhang (2012) employed a similar strategy, such as backward SSP, when deriving the optimal multi-type sensors for best response reconstruction. These heuristic algorithms are simple to implement in software and are computationally efficient.

Genetic algorithms (GA), which are well suited for approximately solving the resulting discrete optimization problem, have been proposed as an effective alternative (Papadimitriou et al., 2000; Yuen et al., 2001; Papadimitriou, 2004; Yao et al., 1993) to the previous heuristic algorithm. Intelligent techniques, such as neural networks and swarm algorithms (Yao et al., 1993; Abdullah et al., 2001; Worden and Burrows, 2001), which yield optimal solutions, are used to improve the optimality of the selected sensor configuration.

2.2.3 Comments on the Existing Methods

Although extensive research effort has been devoted to the problem of SPO over the past decades, there are still some issues that should be addressed when designing optimal sensor placement for large civil structure. Firstly, basing on the above reviews, it is noted that the optimal sensor placement configuration indeed varies along with the optimization objective to achieve and sensor type to deploy. Most of the existing SPO methods were proposed for the purpose of modal test, parameter identification or damage detection. For the dynamic response reconstruction which is very promising and fulfilling in condition assessment of large civil structure, the transmissibility based method presented in reference by Wang et al. (2014) did not take model error into

account; while Kalman filter based method proposed by Zhang et al. (2012), the external excitations are needed. All the features limit their applications in civil structures. Secondly, due to advance in sensor development, many types of sensor are available for civil structure. Some are localized, and some are distributed, with their own advantages and disadvantage. Different sensors provide more comprehensive information and various features. However, their distinct properties considerably complicate the design procedure of optimal multi-type sensor deployment. This problem has not been explicitly addressed in the existing SPO methods except the method proposed by Zhang et al. (2012). Another obstacle is that most of the existing SPO methods are model based, in which the well-established FE model or the mode shape matrix is needed. The error in model building or extracting mode shapes from field measurement should be taken into consideration for robust sensor placement. Lastly, the large size of large civil structure usually results in large numbers of initial candidates of sensor location. An exhaustive searching over the candidate location is forbidden due to great computational expense. Therefore, a feasible multi-type sensor optimal placement procedure for jointly reconstructing response and excitation should be developed.

2.3 FE Model Updating Based Damage Identification

2.3.1 Problem Formulation

The model updating method involves deriving the parameters of a structural model to minimize the residual between the measured data and the corresponding quantities calculated from the model (Mottershead et al., 1993). This method was initially

developed in the model validation process with the motivation of improving the accuracy of an initial FE model, such that the predicted dynamic behavior matches the observed features during an experiment. Recently, abundant applications have been determined in structural damage identification. The main reason is that the method could locate and quantify the damage after establishing the explicit relationship between damage and dynamic behavior. Comprehensive literature reviews on the model updating techniques (Natke et al., 1993; Mottershead et al., 1993) and their applications to damage detection and structural health monitoring (SHM) (Doebling et al., 1998) could be found.

FE model updating based damage identification is commonly based on the availability of a well-established FE model that represents the dynamics of the structure under suspicion. After an initial analytical model has been established, dynamic properties extracted from experimental data are employed to update the analytical model for consistency with the tested structure. Damage detection, location, and quantification are possibly obtained by solving the inverse problem formed using the analytical model and the collected data in test. The problem is usually formulated in a least-squares sense as the minimization of the following objective function:

$$J(\boldsymbol{\theta}) = \left\| \mathbf{W}^{1/2} \left(\mathbf{z}_m - \mathbf{z}(\boldsymbol{\theta}) \right) \right\|_2^2 = \boldsymbol{\varepsilon}_z^T \mathbf{W} \boldsymbol{\varepsilon}_z \tag{2.18}$$

where $\mathbf{z}(\boldsymbol{\theta})$ is the prediction of the FE model, which is dependent on the structural parameters vector $\boldsymbol{\theta}$; $\mathbf{z}_m$ represents the corresponding measurements from the physical structure and $\boldsymbol{\varepsilon}_t$ is the residual vector between the two. $\mathbf{W}$ is a weight matrix that eases the ill-conditioning of the problem. All the dynamic features in the modal

domain, such as natural frequencies (Salawu, 1997), mode shapes and their derivatives (Pandey et al., 1991), and flexibility (Pandey et al., 1994; Jaishi et al., 2006), and in the time domain, such as response sequences (Lu et al., 1994) and statistical moments of responses (Xu et al., 2009; Zhang et al., 2007), are possibly selected to assess the integrity of the structures.

After the formation of the objective function $J(\boldsymbol{\theta})$, its minima may be sought through some optimization methods and thus the optimal estimate of the unknown parameters. The two broad categories concerning model updating techniques are the direct and the iterative updating methods.

2.2.3 Direct Updating Methods

Most direct methods for FE model updating directly update the global mass and stiffness matrices or the perturbation matrices of the damaged structure by contemplating single matrix equations (Natke et al., 1993; Natke et al., 1994; Friswell et al., 1998; Kim et al., 1993). The Lagrange multiplier (Baruch et al., 1978; Berman et al., 1983; Shih et al., 1988), error matrix (He et al., 1986; Sidhu et al., 1984), matrix mixing (Ross, 1971; Thoren, 1972; Caesar, 1987), and eigenstructure assignment methods (Ziaei-Rad et al., 1996; Cawley et al., 1979) are all well-known direct updating methods. The basic idea of the Lagrange multiplier method is that, among three sets of parameters, including the measured modes as well as the analytical mass and stiffness matrices, one set is considered correct and the other two sets will be updated by minimizing a penalty function constrained by Lagrange multipliers. Error matrix methods comprise a group of methods that directly estimate the error in the

mass and stiffness matrices. The matrix mixing methods assume that all vibration modes are measured at all DOFs, and the mass and stiffness matrices could be constructed directly. The eigenstructure assignment method is developed from the view of system control. In the method, a feedback matrix is found, such that a looped system has the desired eigenvalues and eigenvectors. Then, the feedback matrix perturbs the stiffness and damping matrices to obtain an updated model.

The updated model generated from each of these direct updating methods could reproduce the reference data exactly, and no iteration is required in the updating procedure. Nonetheless, test data needed in these direct updating methods should be measured on all DOFs of the analytical FE model. However, in most cases, the number of DOFs measured in the test is smaller than that in the FE model. An alternative scheme is to reduce the number of discretized elements on the initial FE model or to expand the test data, although reduction and expansion might bring erroneous information into the process. The methods are usually unable to keep the connectivity and physical meaning of the structure. Thus, fully populated matrices are usually generated after updating and the sparseness of the matrices of the initial FE model is destroyed. Moreover, the positive definiteness of the updated mass and stiffness matrices cannot be guaranteed.

Given that the parametric FE model of the structure is not required in the direct model updating, the connection between updated matrices and damage is implicit. Moreover, the physical meanings of the updated matrices are difficult to retain. For these reasons, the iterative updating methods are more well-known in damage identification.

2.2.3 Iterative Updating Methods

In contrast to direct updating methods, which focus on global system matrices, iterative sensitivity-based model updating employs a parametric FE model, which is defined regarding physical parameters, such as its geometrical or physical properties. Structural damage could be determined by seeking the physical parameters of the damaged state through the minimization problem expressed in Eq.(2.18). In the sensitivity-based model updating method, the solution to the nonlinear minimization problem is usually sought by linearizing the residual using as a truncated Taylor series and solving iteratively as

$$\mathbf{S}_k \Delta\boldsymbol{\theta}_k = \Delta\mathbf{z}_k \tag{2.19}$$

in which $\Delta\boldsymbol{\theta}_k = \boldsymbol{\theta} - \boldsymbol{\theta}_k$ and $\Delta\mathbf{z}_k = \mathbf{W}^{1/2} \cdot \left[\mathbf{z}_m - \mathbf{z}\left(\boldsymbol{\theta}_k\right)\right]$. $\mathbf{S}_k$ is the sensitivity matrix obtained from the first derivatives of the predictions with respect to the parameters as:

$$\mathbf{S}_k = \mathbf{W}^{1/2} \cdot \frac{\partial \mathbf{y}}{\partial \boldsymbol{\theta}}\Big|_{\boldsymbol{\theta}=\boldsymbol{\theta}_k} \tag{2.20}$$

An ideal dynamic feature (usually called the damage indicator) that is sensitive to structural damage while robust to environment effects should be selected as $\mathbf{z}$ in Eq.(2.18). From the dynamic feature used in the formulation of the penalty function, two categories of methods, namely, modal domain and time domain, could be classified.

2.2.3.1 Minimization of Modal Domain Residuals

The frequencies and possibly mode shapes of a structure are the first notable pioneering indicator for model updating based damage identification (Natke et al., 1993, Salawu, 1997). Frequencies are analytically direct indicators that reflect variation in the stiffness and/or mass of a structure, and model shapes have advantages in indicating the spatial location of damage. The first-order derivatives of frequencies and mode shapes were derived by Fox and Kapoor (1968). The result for the derivative of the *r*-th eigenvalue λ_r with respect to the *k*-th parameter θ_k is:

$$\frac{\partial \lambda_r}{\partial \theta_k} = \boldsymbol{\varphi}_r^T \left[-\lambda_r \frac{\partial \mathbf{M}}{\partial \theta_k} + \frac{\partial \mathbf{K}}{\partial \theta_k} \right] \boldsymbol{\varphi}_r \tag{2.21}$$

where **M**, **K** are the FE mass and stiffness matrices, respectively. $\boldsymbol{\varphi}_r$ is the *r*-th mode shape and its sensitivity can be empirically expressed as (2.22) basing on expanding the gradients into a weighted sum of the eigenvectors.

$$\frac{\partial \boldsymbol{\varphi}_r}{\partial \theta_k} = \sum_{h=1}^{H} a_{rkh} \boldsymbol{\varphi}_h \tag{2.22}$$

in which the factor a_{rkh} is in the form

$$a_{rkh} = \begin{cases} \dfrac{\boldsymbol{\varphi}_h^T \left(-\lambda_r \dfrac{\partial \mathbf{M}}{\partial \theta_k} + \dfrac{\partial \mathbf{K}}{\partial \theta_k} \right) \boldsymbol{\varphi}_r}{\left(\lambda_r - \lambda_h \right)}; h \neq r \\ -\dfrac{1}{2} \boldsymbol{\varphi}_h^T \left(\dfrac{\partial \mathbf{M}}{\partial \theta_k} \right) \boldsymbol{\varphi}_h; h = r \end{cases} \tag{2.23}$$

Other methods for calculating mode shape derivatives have been proposed by Ojalve (1987), Tan et al. (1989), and Nelson (1976). As a preliminary step, a number of

corresponding modes must be identified from the measured responses. The pairing of predicted and measured modes is needed and often performed by a quantitative measure, such as the modal assurance criteria (MAC) coefficient, which measures the spatial correlation and similarity between two tested and analytical mode shapes. In MAC, a value of 0 indicates complete dissimilarity and a value of 1 indicates complete similarity between the two compared mode shapes. From this principle, several forms of penalty functions are defined and used for model updating applying the model parameters (Cobb et al., 1996; Link et al., 1992; Farhat et al., 1993; Fritzen et al 1998; Friswell et al., 1995).

However, frequency, as the global indicator of a structure, is insensitive to local and incipient damage. One of the notable facts on using natural frequency information for damage detection is that the shift of natural frequencies could be induced by the effects of the ambient environment. Experimentally, fundamental frequencies can show 5% to 10% change because of natural ambient environment variations (Cobb et al., 1996). Therefore, if damage occurs to an important part of the structure that brings approximately less than 10% change in the natural frequency, then such damage would stand unrecognized (Chen et al., 1995). Experimental proofs are obtained by conducting tests on the I-40 Bridge (Farrar et al., 1994).

Another damage indicator adopted in model updating based damage identification is the modal strain energy (MSE). The MSE confined to the specific *i*-th mode $\boldsymbol{\varphi}_i$ is expressed by Eq.(2.24)

$$U_i = \frac{1}{2}\int_0^l EI\left(\frac{\partial^2 \boldsymbol{\varphi}_i}{\partial x^2}\right)^2 dx \tag{2.24}$$

where EI denotes the flexural stiffness. It has been used for damage identification in several references (Cornwell et al., 1999; Shi et al., 1998; Shi et al., 2000; Wang, 2013).

Besides, the modal flexibility matrix is also adopted in defining the penalty function due to its higher sensitivity to damage. It can be constructed directly basing on available eigenvalues λ and eigenvectors $\boldsymbol{\varphi}$ as:

$$\mathbf{F} = \sum_{r=1}^{N_r} \frac{1}{\lambda_r} \boldsymbol{\varphi}_r \boldsymbol{\varphi}_r^T \tag{2.25}$$

Several researchers have employed the modal flexibility matrix in model updating for damage identification (Wu et al., 2004a; Wu et al., 2004b; Jaishi et al., 2006; Yan et al. 2014). The sensitivity of truncated modal flexibility can be derived basing the sensitivity of natural frequencies and mode shapes. A direct algebraic derivation of modal flexibility sensitivity was also provided by Yan et al. (2014).

The frequency response functions (FRF) of a structure could provide comprehensive information to identify and locate damage (Pereira et al., 1994; Richardson et al., 1990; Huang et al., 2012). FRF has the basic formula as:

$$\mathbf{H}(\omega) = \frac{\mathbf{X}(\omega)}{\mathbf{F}(\omega)} = \sum_{r=1}^{n} \frac{\boldsymbol{\varphi}_r \boldsymbol{\varphi}_r^T}{\Omega_r - \omega^2 + 2j\zeta_r \Omega_r \omega} \tag{2.26}$$

in which Ω_r and ζ_r are the *r*-th natural frequency and modal damping coefficient, respectively. One remarkable advantage of using FRFs in sensitivity-based model updating is that FRF model updating exempts the necessity of extracting modal parameters from the measurement and mode pairing exercises. Thus, the propagation of errors in the process of parameter estimation is avoided. Another distinct difference is that, in contrast to the updating of eigenvalues and eigenvectors, the updating penalty function computations, as indicated in Eq.(2.19), could be easily performed into an overdetermined set of equations at many frequency points. Thus, a massive collection of references is devoted to this topic (Park et al., 2003; Asma et al., 2005; Esfandiari et al., 2010; Sanayei et al., 2012; Esfandiari et al., 2010; Wang et al., 2012; Garcia et al., 2013; Gang et al., 2014; Yuan et al., 2015). The penalty function could be defined in terms of nodal forces (input data) or structural responses (output data).

Moreover, other modal domain properties are used in model updating for damage identification. Steenackers et al. (2007) presented a new technique to update the FE model from output-only transmissibility measurement, which refers to the ratio of the response spectra $\mathbf{X}_i(\omega)$ and $\mathbf{X}_j(\omega)$ as Eq. (2.27)

$$\mathbf{T}_{ij}(\omega)=\frac{\mathbf{X}_i(\omega)}{\mathbf{X}_j(\omega)}=\frac{\mathbf{H}_{ik}(\omega)}{\mathbf{H}_{jk}(\omega)} \tag{2.27}$$

in which $\mathbf{H}_{ik}(\omega)$ and $\mathbf{H}_{jk}(\omega)$ are the measured FRFs between output DOF *i* and *j*, respectively, when input acts at the DOF *k*. It is assumed that the location of the excitation force is known. Zheng et al. (2015) investigated the utilization of response power spectral density (PSD) expressed as Eq.(2.28) for damage identification.

$$\mathbf{S}_{xx}(\omega) = \left|\mathbf{H}(\omega)\right|^2 \mathbf{S}_{ff}(\omega) \tag{2.28}$$

where $\mathbf{H}(\omega)$ is the FRF and $\mathbf{S}_{ff}(\omega)$ is the auto-power spectrum of stationary random excitation. The dynamic response of structures and sensitivity of PSD are obtained using stationary, random excitation with the pseudo-excitation method to obtain the damage parameters through model updating.

From the previously presented reviews, we find that the limitations of the frequency domain damage detection methods lay in the following aspects:

(1) Modal identification, which extracts the modal properties from the measurement of response and mode pairing exercises, is always needed in frequencies and mode shapes based on damage identification. These procedures inevitably introduce subsequent errors in frequencies and mode shapes, and the right pairing of modes is not necessarily guaranteed.

(2) Natural frequencies of a structure are insensitive to local damages and have only minimal capacity in indicating damage locations. Moreover, the mode shapes of higher modes cannot be easily measured and their accuracy is usually low because of limited measurement points and unavoidable measurement noises.

(3) For the FRF or response transmissibility-based damage identification, the amplitude varies largely because of resonance and antiresonance, which make the ill-posedness problem prominent.

We can see that although these methods appear intuitive and straightforward, the

modal parameters based damage identification methods pose significant technical challenges and limitations in application. Given these limitations, research has been focusing on model updating algorithms using the time domain response directly.

2.2.3.2 Minimization of Time Domain Residuals

Another group of techniques is employed to detect identification using the raw measurement in time domain directly to overcome the limitations of modal parameters based on damage identification. Compared with the frequency domain approach, the time domain FE model updating takes advantage of the time dimension with a large amount of measured data to formulate an overdetermined set of equations in the penalty function. Another remarkable advantage is that the process of extracting modal parameters from the measurements and mode pairing exercises are exempted; thus, the propagation of errors involved in these procedures is avoided.

Majumder and Manohar (2003) developed a time domain approach within the framework of FE model updating to detect the damages in bridge structures using the vibration data induced by a moving vehicle. The time domain approach developed in this study leads to solving a set of overdetermined linear algebraic equations for damage indicator variables. Lu et al. (2003) proposed a structural damage identification approach based on response sensitivity analysis in the time domain. The relationship between the responses and fractional damage in elements was explicitly derived and used for identifying elemental level damages. Ding et al. (2008) proposed a time domain damage identification method based on energy variations of responses decomposed using wavelet packet transform. The method takes advantage of

sufficient measure data and yields satisfactory results. Cacciola et al. (2011) presented a time domain least square identification method based on the minimization of a penalty function using the time domain deterministic and stochastic responses. One of the main advantages of the proposed procedure operating in the time domain is the avoidance of rank deficiency, which reduces biasing. Various numerical tests have been conducted, such as the ASCE benchmark that manifested perfect matching between the targets and estimated structural parameters. Zhang et al. (2011) investigated a novel structural damage detection method with the statistical moments of dynamic responses of the shear building as a new damage index. Various damage scenarios of the frame structure showed that the moments of dynamic responses are sensitive to structural damage and insensitive to measurement noise, even with a high-level measurement noise of 15%. A stochastic damage detection method was proposed by Xu et al. (2011) for damage detection of structures with uncertainties. The damage locations and severities are identified based on a special probability function that is calculated by using the probability density functions of the structural stiffness parameters before and after damage occurrence. One of the advantages of the proposed method is that it can deal with uncertainty parameters of non-normal distributions.

2.2.4 Regularization Techniques in FE Model Updating

Due to the limitation of sensors compared with the uncertain parameter number, Eq. (2.19) involved in model updating based damage identification probably formed as an ill-posed problem. Then, the sensitivity matrix $\mathbf{S}$ is close to being rank deficient and a small disturbance in $\Delta\mathbf{z}$ may lead to a significant deviation in $\Delta\boldsymbol{\theta}$ from its exact value. Two regularization techniques, namely, truncated singular value decomposition

(TSVD) (Golub et al., 1996; Hansen, 1998) and Tikhonov regularization technique (Tikhonov et al., 1977; Groetsch, 1984; Bui, 1994; Hansen et al., 1998) are widely employed to address the ill-posedness problem, and these techniques will be introduced in the subsequent section.

Truncated Singular Value Decomposition

A straightforward approach to obtaining a rational solution is to truncate the least square solution to Eq.(2.19), yielding

$$\Delta\boldsymbol{\theta} = \sum_{i=1}^{n_t} \frac{\mathbf{u}_i^T \Delta\mathbf{z}}{\sigma_i} \mathbf{v}_i \tag{2.29}$$

where n_t is truncation level. Since the contribution of $i > n_t$-th singular value to the solution is omitted to decrease the solution error, the choice of the truncation level in the TSVD method should be chosen delicately. σ_i, $\mathbf{u}_i$ and $\mathbf{v}_i$ are the singular values, the portion of left and right singular vectors obtained by performing a singular value decomposition on the sensitivity matrix $\mathbf{S} \in \Re^{m \times n}$ as

$$\mathbf{S} = [\mathbf{u}_1, \mathbf{u}_2, \cdots, \mathbf{u}_m] \cdot diag\left([\sigma_1, \sigma_2, \cdots, \sigma_r]\right) \cdot [\mathbf{v}_1, \mathbf{v}_2, \cdots, \mathbf{v}_n]^T = \sum_{i=1}^{r} \sigma_i u_i v_i^T \tag{2.30}$$

Tikhonov Regularization

Tikhonov regularization (Tikhonov et al., 1977) approximates the solution of Eq. (2.19) by transferring it into the following well-posed problem:

$$\Delta\boldsymbol{\theta} = \left(\mathbf{S}^T\mathbf{S} + \lambda^2\mathbf{I}\right)^{-1} \mathbf{S}^T \Delta\mathbf{z} = \sum_{i=1}^{n} \frac{\sigma_i^2}{\sigma_i^2 + \lambda^2} \frac{\mathbf{u}_i^T \Delta\mathbf{z}}{\sigma_i} \mathbf{v}_i = \sum_{i=1}^{n} f_i \frac{\mathbf{u}_i^T \Delta\mathbf{z}}{\sigma_i} \mathbf{v}_i \tag{2.31}$$

where λ is a positive number and f_i can be viewed as a kind of filter factor: if σ_i approaches to 0, f_i approaches to 0 at the same time; otherwise, f_i approaches to 1. Thus the contribution of these near-zeros singular values to the solution is filtered out. It can be noted that Eq. (2.31) reverts back to the least square solution for $\lambda = 0$. An optimal regularization factor is needed and usually determined by the several well-defined methods such as the L-curve method (Hansen, 1992), generalized cross-validation (GCV) method, geometric mean scheme (Park, 2002), and the variable regularization factor (Lee *et al*., 1999).

In the realm of damage identification, D'Ambrogio et al. (1998) applied the TSVD method as a regularization technique to reduce ill-conditioning in model updating, in which the truncation parameter n_t was chosen by simultaneous minimization of the natural frequency error and response residual error.

Ahmadian et al. (1998) presented the adoption of L-curve and GCV methods for determining the regularization parameter in FE model updating. Ziaei-Rad and Imregun (1999) investigated a number of regularization methods and concluded that the L-curve method was straightforward in determining the regularization parameter. Mares et al. (2002) explored the robust estimation and the Tikhonov regularization methods for the output-error-based FE model updating by using only modal frequencies and applied an uncertainty bound model and L-curve method to determine the regularization parameters. Titurus and Friswell (2007) investigated the output-error-based model updating method with an additional regularization criterion by using experimental modal frequencies and mode shapes and explored the regularization technique from a geometric perspective. Weber et al. (2009) applied

Tikhonov regularization and TSVD consistently to a nonlinear updating problem. The optimal regularization parameter is determined by the GCV method. Hua et al. (2009) proposed a minimum product criterion to select the optimal regularization parameter during every iteration in output-error-based FE model updating for damage identification. Compared with the commonly used L-curve method and the GCV through numerical studies of a truss bridge using noise-free and noise-corrupted modal data, the minimum product criterion was effective and robust in determining the regularization parameter. An adaptive regularization approach for solving the model updating problem was presented by Li et al. (2010). A reference value is selected to ensure that the accumulated damage vector is less than 0. The study revealed that the adaptive Tikhonov regularization was superior to the traditional Tikhonov regularization.

2.4 Dynamic Substructuring Technique

2.4.1 General Framework

Dynamic substructuring technique refers to dividing a large and complex structure into several smaller substructures, modeling and reducing them separately and reassembling the reduced models together in order to investigate the dynamic of structures which are too big to be analyzed as one piece. After the division of the structure into substructures, more insight can be gained over the local dynamic of the substructures and local reanalysis is feasible. More specifically, the procedure of dynamic substructuring technique can be described as follows: (1) separate the whole structure into different substructures or components; (2) reduce the substructure

model and describe the linear substructures in their dominant dynamics; (3) reassemble the substructure models to form a reduced-order model with respect to the boundary connections between the interfaces of different components; (4) perform the time-domain or frequency domain analysis of the whole condensed model; (5) obtain the analysis of concerned components in the initial physical coordinate by coordinate transform.

The substructuring techniques can be classified as the fixed-interface method, the free-interface method or the hybrid interface method that combines the two, depending upon whether the generalized coordinates are obtained with boundary DOFs fixed or free. The first ideas for dynamic substructuring were published by Hurty (1965) and Gladwell (1964). Gladwell proposed to use so-called branch modes for the reduction. Hurty (1965) proposed to use a combination of vibration modes, rigid body modes and static modes. Both of them are the fixed-interface methods. Later, Craig and Bampton simplified this approach and the classical component mode synthesis (CMS) methods (Craig et al., 1968) were introduced. Nowadays the Craig-Bampton method and its refinements (Rixen, 2004) are widely used because the procedure is straightforward and typically produces accurate models with few component modes. Other popular methods were developed by Mac Neal (1971) and Rubin (1975). These methods have found a broad range of applications in the field of structural dynamics for evaluating the dynamic behavior of large structures. From the 1980’s onward, substructuring coupling techniques caught the attention of the experimental society. Due to much improved measurement hardware and experimental techniques, measurements could now be used in substructuring analyses (Jetmundsen et al., 1998). Crowley et al.

(1984) presented a method for the direct assembly of FRFs for structural modification using experimental FRFs. An alternative method was proposed by Jetmundsen et al. (1988), and it is often referred to as the classical frequency based substructuring method. Recently, De Klerk et al. (2006) proposed a frequency based substructuring approach using the dual assembly formalism, which became known as Lagrange multiplier frequency based substructuring. For a more extensive historical overview of substructuring methods, the interested reader is referred to the reference (De Klerk, 2008).

Following the general introduction given above, a brief introduction of dynamic substructuring will be given. The application of dynamic substructuring techniques in the community of SHM and damage identification will be reviewed in Section 2.5.

2.4.2 Model Portioning and Reduction

A large structure is assumed to be divided into N_n non-overlapping substructures. The *s*-th physical substructure is described by its mass, stiffness and damping distributions given by the $\mathbf{M}^s$, $\mathbf{K}^s$ and $\mathbf{C}^s$ matrices respectively and the associated displacements $\mathbf{x}^s(t)$. The equations of motion for the s-th substructure are given as:

$$\mathbf{M}^s\ddot{\mathbf{x}}^s(t)+\mathbf{C}^s\dot{\mathbf{x}}^s(t)+\mathbf{K}^s\mathbf{x}^s(t)=\mathbf{f}^s(t)+\mathbf{g}^s(t) \tag{2.32}$$

where $\mathbf{f}^s$ (t) and $\mathbf{g}^s$ (t) are the applied external forces and the connecting forces from the adjacent substructures, respectively. Model reduction is performed by approximating the full set of DOFs $\{\mathbf{x}^s\}$ using a set of possible generalized DOFs $\{\mathbf{q}^s\}$ as:

$$\left\{\mathbf{x}^s\right\} = \mathbf{T}_c^s \left\{\mathbf{q}^s\right\} \tag{2.33}$$

Then, Eq.(2.32) can be reduced by substitution of Eq.(2.33):

$$\hat{\mathbf{M}}^s \ddot{\mathbf{x}}^s(t) + \hat{\mathbf{C}}^s \dot{\mathbf{x}}^s(t) + \hat{\mathbf{K}}^s \mathbf{x}^s(t) = \hat{\mathbf{f}}^s(t) + \hat{\mathbf{g}}^s(t) \tag{2.34}$$

where

$$\hat{\mathbf{K}}^s = \mathbf{T}_c^{sT} \mathbf{K}^s \mathbf{T}_c^s, \hat{\mathbf{M}}^s = \mathbf{T}_c^{sT} \mathbf{M}^s \mathbf{T}_c^s, \hat{\mathbf{C}}^s = \mathbf{T}_c^{sT} \mathbf{C}^s \mathbf{T}_c^s; \hat{\mathbf{f}}^s(t) = \mathbf{T}_c^{sT} \mathbf{f}^s; \hat{\mathbf{g}}^s(t) = \mathbf{T}_c^{sT} \mathbf{g}^s \tag{2.35}$$

In theory, all the model reduction methods such as Guyan reduction (Guyan, 1965), Craig-Bampton reduction (Craig, 1968), Rubin reduction (Rubin, 1975) and others can be used in Eq.(2.33). These reductions use different modes (in fact Ritz vectors) as the reduction basis, such as exact eigenmodes, free interface vibration modes, the interface constraint modes, fixed-interface normal modes, etc. Craig-Bampton reduction (Craig and Bampton, 1987) is preferred among them due to its straightforward implement and considerably high accuracy. Detailed introduction of this method can be found in Chapter 8.

2.4.3 Substructures Assembling

In general, we can identify two domains in which dynamic substructuring coupling can be performed: the time domain and frequency domain. In the time domain, the structure is assembled in terms of generalized (modal) DOF and their associated reduced matrices; while in the later former substructures are assembled whose dynamics are described in terms of FRF. Regardless of whether the substructures are

modeled in the time or frequency domain, compatibility condition and equilibrium condition must be satisfied when assembling the substructures. The former states that interface displacements of the substructures must be compatible while the latter ensures the forces connecting the substructures' interface DOFs in equilibrium. Two common assembly methods in FE modeling which satisfy both conditions are:

(1) Primal assembly: by choosing a unique set of degrees of freedom (DOF), one set of interface DOF is eliminated. Both substructures thus share the same set of interface DOF, and compatibility and equilibrium are both a priori satisfied.

(2) Dual assembly: by choosing a unique set of interface forces, which will a priori satisfy the equilibrium condition, to enforce the connection forces on both sides of the interface in equilibrium. The compatibility condition is then explicitly added to the set of equations.

We can see that the difference between primal and dual assembly is that in the primal assembly a unique set of DOFs is found and thereby merges both interfaces to one unique interface. Dual assembly, on the other hand, retains all the substructure DOFs and uses an additional set of coupling DOFs to connect the substructures.

2.4.3.1 Substructures Assembly in Time Domain

The reduced substructures should be assembled so that the dynamics of the entire structure can be analyzed. The equations of motion of the N_n substructures that are to be coupled can be block-diagonally assembled as:

$$\mathbf{M}\ddot{\mathbf{q}}(t) + \mathbf{C}\dot{\mathbf{q}}(t) + \mathbf{K}\mathbf{q}(t) = \mathbf{f}(t) + \mathbf{g}(t) \tag{2.36}$$

with

$$\mathbf{M} = diag\left(\hat{\mathbf{M}}^1,\cdots,\hat{\mathbf{M}}^s,\cdots,\hat{\mathbf{M}}^{N_n}\right);\mathbf{K} = diag\left(\hat{\mathbf{K}}^1,\cdots,\hat{\mathbf{K}}^s,\cdots,\hat{\mathbf{K}}^{N_n}\right);\mathbf{C} = diag\left(\hat{\mathbf{C}}^1,\cdots,\hat{\mathbf{C}}^s,\cdots,\hat{\mathbf{C}}^{N_n}\right)$$

$$\mathbf{q}^T = \left[\mathbf{q}^{1T},\cdots,\mathbf{q}^{sT},\cdots,\mathbf{q}^{N_nT}\right];\mathbf{f}^T = \left[\hat{\mathbf{f}}^{1T},\cdots,\hat{\mathbf{f}}^{sT},\cdots,\hat{\mathbf{f}}^{N_nT}\right];\mathbf{g}^T = \left[\hat{\mathbf{g}}^{1T},\cdots,\hat{\mathbf{g}}^{sT},\cdots,\hat{\mathbf{g}}^{N_nT}\right]$$

where $\mathbf{q} \in \Re^{n_q}$ ($n_q = \sum_{s=1}^{n} \hat{n}_s$) is the vector of generalized coordinates for all the *n* substructures. The compatibility condition can also be written in a matrix form as:

$$\mathbf{Bq} = \mathbf{0} \tag{2.37}$$

where the $\mathbf{B}$ matrix operates on the interface degrees of freedom and is a signed Boolean matrix which contains only 1, -1, and 0. The compatibility condition states that any pair of matching interface degrees of freedom must have the same displacement. The equilibrium condition writes in the matrix form as：

$$\mathbf{L}^T\mathbf{g} = \mathbf{0} \tag{2.38}$$

where the matrix ***L*** is the Boolean matrix localizing the interface DOF of the substructures in the global set of DOFs, making that sum of connection forces acting on each boundary DOFs equals to zero. Since multiple substructures may share some common boundary DOFs, there are multiple entries for these boundary DOFs in the assembled vector $\mathbf{q}$. It can be proved that ***B*** and ***L*** are in each other's null space as $\mathbf{BL} = \mathbf{0}$.

Substructures assembly can be performed in the time domain using the interface displacements, using interface forces or using mixed interface. The former is

introduced as follows.

Primal assembly using the interface displacements

In a primal assembly, a unique set of interface DOFs $\tilde{\mathbf{q}}$ is defined that automatically satisfies the compatibility condition:

$$\mathbf{q}(t) = \mathbf{L}\tilde{\mathbf{q}}(t) \tag{2.39}$$

By substituting Eq.(2.39) into Eq. (2.36) and pre-multiplying with $\mathbf{L}^T$, the primal assembled structure is obtained as:

$$\tilde{\mathbf{M}}\ddot{\tilde{\mathbf{q}}}(t) + \tilde{\mathbf{C}}\dot{\tilde{\mathbf{q}}}(t) + \tilde{\mathbf{K}}\tilde{\mathbf{q}}(t) = \mathbf{L}^T\mathbf{f}(t) \tag{2.40}$$

with the primal assembled structure matrices defined as:

$$\tilde{\mathbf{M}} = \mathbf{L}^T\bar{\mathbf{M}}\mathbf{L}; \tilde{\mathbf{C}} = \mathbf{L}^T\bar{\mathbf{C}}\mathbf{L}; \tilde{\mathbf{K}} = \mathbf{L}^T\bar{\mathbf{K}}\mathbf{L} \tag{2.41}$$

Please be noted that the equilibrium condition allows removing the interface forces $\mathbf{g}$ from the equations, since $\mathbf{L}^T\mathbf{g} = \mathbf{0}$.

Dual assembly using the interface displacements

In dual assembly, the full set of degrees of freedom $\mathbf{q}$ is retained while the interface forces are chosen in the form of

$$\mathbf{g} = -\mathbf{B}^T\boldsymbol{\lambda} \tag{2.42}$$

The interface forces are now described by the Lagrange multipliers $\boldsymbol{\lambda}$, which are the

interface force intensities. Due to the construction of B the interface forces on both sides of the connection will always be opposite and equal, so equilibrium on the interface is a priori satisfied since $-\mathbf{L}^T\mathbf{B}^T\boldsymbol{\lambda}=\mathbf{0}$. The system of equations (2.36) now reduces to

$$\begin{bmatrix}\mathbf{M} & \mathbf{0}\\ \mathbf{0} & \mathbf{0}\end{bmatrix}\begin{Bmatrix}\ddot{\tilde{\mathbf{q}}}\\ \boldsymbol{\lambda}\end{Bmatrix}+\begin{bmatrix}\mathbf{C} & \mathbf{0}\\ \mathbf{0} & \mathbf{0}\end{bmatrix}\begin{Bmatrix}\dot{\tilde{\mathbf{q}}}\\ \boldsymbol{\lambda}\end{Bmatrix}+\begin{bmatrix}\mathbf{K} & \mathbf{B}^{\mathrm{T}}\\ \mathbf{B} & \mathbf{0}\end{bmatrix}\begin{Bmatrix}\tilde{\mathbf{q}}\\ \boldsymbol{\lambda}\end{Bmatrix}=\begin{bmatrix}\mathbf{f}\\ \mathbf{0}\end{bmatrix} \tag{2.43}$$

The main difference between the primal and dual assembly of interface displacements is that in primal assembly the compatibility condition is satisfied *a priori*, whereas in dual assembly the equilibrium is satisfied *a priori*. Physically this can be interpreted as an assembly by interface displacements or interface forces, respectively.

2.4.3.2 Substructures Assembly in Frequency Domain

Performing a Fourier transform on Eq.(2.36) , Eq.(2.37) and Eq.(2.38) gives the following set of governing equations in the frequency domain:

$$\begin{cases}\mathbf{Z}(\omega)\mathbf{q}(\omega)=\mathbf{f}(\omega)+\mathbf{g}(\omega)\\ \mathbf{B}\mathbf{q}(\omega)=\mathbf{0};\mathbf{L}^T\mathbf{q}(\omega)=\mathbf{0}\end{cases} \tag{2.44}$$

in which $\mathbf{f}(\omega)$ and $\mathbf{g}(\omega)$ are the acting and connecting forces in Fourier domain; $\mathbf{Z}(\omega)$ is the block-diagonal matrix containing the dynamic stiffness matrices of the substructures, i.e.,

$$\mathbf{Z}(j\omega)=-\omega^2\mathbf{M}+j\omega\mathbf{C}+\mathbf{K} \tag{2.45}$$

The same procedure as before can be followed to obtain either a primal or dually assembled system of equations.

Primal Formulation in the Frequency Domain

The interface compatibility is imposed by choosing a unique set of interface DOF as

$$\tilde{\mathbf{Z}}\mathbf{q} = \tilde{\mathbf{f}} \tag{2.46}$$

where $\tilde{\mathbf{Z}} = \mathbf{L}^T\mathbf{Z}\mathbf{L}$ and $\tilde{\mathbf{f}} = \mathbf{L}^T\mathbf{f}$ are the primal assembled frequency response function matrices and forcing amplitudes.

Dual assembly in the Frequency Domain

For a dual assembly of Eq.(2.44), the equilibrium condition is imposed by choosing the interface forces a $\mathbf{g}(\omega) = -\mathbf{B}^T\boldsymbol{\lambda}(\omega)$. Analog to dual assembly in the time domain, the set of equations given in (2.47) is assembled.

$$\begin{bmatrix} \mathbf{Z} & \mathbf{B}^{\mathbf{T}} \\ \mathbf{B} & \mathbf{0} \end{bmatrix} \begin{Bmatrix} \mathbf{q} \\ \boldsymbol{\lambda} \end{Bmatrix} = \begin{bmatrix} \mathbf{f} \\ \mathbf{0} \end{bmatrix} \tag{2.47}$$

The above equation can be rewritten from a dynamic equation in terms of stiffness to one in terms of flexibility.

$$\begin{cases} \mathbf{q} = \mathbf{Y}\mathbf{f} - \mathbf{Y}\mathbf{B}^{\mathbf{T}}\boldsymbol{\lambda} \\ \mathbf{B}\mathbf{q} = \mathbf{0} \end{cases} \tag{2.48}$$

The first equation can be substituted in the compatibility condition as:

$$\mathbf{B}\mathbf{Y}\mathbf{f} - \mathbf{B}\mathbf{Y}\mathbf{B}^{\mathbf{T}}\boldsymbol{\lambda} = \mathbf{0} \tag{2.49}$$

The first term ($\mathbf{BYf}$) describes the deformation of the (separate) interfaces due to the external forces, thereby resulting in a gap between the substructures. The second term ($\mathbf{BYB^T\lambda}$) describes the deformation of the (separate) interfaces due to the external forces, thereby resulting in a gap between the substructures. The second term is written as:

$$\boldsymbol{\lambda} = \left(\mathbf{BYB^T}\right)^{-1}\mathbf{BYf} \tag{2.50}$$

By substituting this expression into the equations of motion a direct and convenient expression for the dual assembled system is obtained.

$$\mathbf{q} = \mathbf{Yf} - \mathbf{YB^T}\left(\mathbf{BYB^T}\right)^{-1}\mathbf{BYf} \tag{2.51}$$

The obtained set of equations is known as Lagrange multiplier frequency based substructuring (Klerk et al., 2006; Jetmundsen et al., 1988).

Dynamic substructuring technique allows analyzing large structures that would otherwise be too large and/or complex to be analyzed as a whole. Recently, it has been developed with the attention of being applied to model updating and damage identification of large structures, which will be introduced in the next section.

2.5 Damage Identification for Large Civil Structures

As mentioned in Chapter 1, although certain achievements have been obtained in damage identification on small and moderate structures, the application of vibration-based damage identification to large civil structures is still a long way to go.

Currently, research efforts have been dedicating to promoting damage identification methods that are more suitable for large structures in several aspects.

2.5.1 Multi-scale Sensing for Damage Identification

The first method is fusing multiple responses for SHM and damage identification, which is called multi-scale sensing SHM or damage detection in several references (Sim and Spencer, 2007; Sung et al., 2013). In light of rapid advances in sensor technologies, various types of sensors are usually deployed in the SHM system to measure different types of responses of large-scale structure (Balageas et al., 2006; Xu and Xia, 2011; Farrar and Worden, 2012). Heterogeneous responses captured by various types of sensors are capable of providing comprehensive (local and global) information regarding the condition of the structure. For instance, among frequently used responses, acceleration is often preferred because of relatively more KE on higher vibrational modes and easy installment of accelerometers. Displacement, which contains more energy in the modal vibration of low orders, sometimes could directly indicate structural integrity (e.g., inter-story displacement of high-rise buildings). These two types of responses are usually regarded as a global response, which has the advantage of indicating that the existing damage globally. Strain, as a kind of local response, is utilized because of its better capacity of providing quantification on local structural degradation. However, achieving the functionality of strain sensors usually requires that sensors should be located near areas of damage. A fusion of different types of responses, which manifests a broad spectral bandwidth, is expected to take full advantage of these dynamic responses for structural condition assessment.

Data fusion that combines different types of responses was first investigated for better structural response monitoring. For example, a fusion of GPS and acceleration data (Chan et al., 2006; Meng et al., 2007; Smyth et al., 2007) has been explored for better displacement measurement. Park et al. (2003) presented a displacement sensing system based on the fusion of strain and acceleration measurements and further implemented this method into a wireless sensor network for displacement estimation in simply supported bridges (Park et al., 2014). Smyth and Wu (2007) applied the multi-rate Kalman filter to fuse displacement and acceleration with different sampling rates to produce more accurate velocity and displacements. Papadimitriou et al. (2010) adopted the Kalman filter to predict strain response by using output-only strain measurements in the case of stochastic excitations for estimating damage accumulation of a metallic structure. Hernandez et al. (2013) proposed a finite element model-based state estimator that could account for spatial correlation and the colored nature of the excitation to estimate wind-induced stresses and fatigue damage. Various experimental results of stress estimation in a cantilever beam using noise-contaminated acceleration measurements were reported by Erazo et al. (2014). Palanisamy et al. (2015) presented an experimental validation of Kalman filter-based strain estimation of structures subjected to nonzero mean input by fusing different types of data of acceleration, strain, and tilt responses. Zhang (2012) and Xu et al. (2016) developed a Kalman filter-based dynamic response reconstruction method using multi-type real-time measurement and investigated the optimal sensor placement method for best response reconstruction.

Furthermore, studies have explored damage identification with a fusion of multi-type

sensors. Studer and Peters (2004) presented a damage identification method with fusion multi-scale measurements, including strain, integrated strain, and strain gradient strain fields by embedded fiber optic sensors. A neural network data fusion approach was proposed for a realistic fusion of data and their different forms. A simulation study of a two-dimensional isotropic, linear elastic, and homogeneous plane with cracks shows the feasibility and significant improvement in damage identification provided by the combined use of multi-scale sensing data and neural network data fusion. Sim and Spencer (2011) proposed a multi-metric damage detection approach based on the stochastic damage-locating vector (DLV) method using a combined flexibility matrix, including displacement and strain flexibility matrices, to detect structural damage. Numerical simulations were performed on a 53-DOF planar truss model excited by a band-limited white noise input force. Damage was simulated by using 40% stiffness reduction in one element. The results indicated that the proposed multi-scale data damage detection strategy could yield better results than the stochastic DLV method (Bernal, 2006) that uses only a single type of data in numerical simulation. Sung et al. (2013) proposed a multi-scale sensing and diagnosis system combining accelerometers and gyroscopes for bridge health monitoring in a two-step strategy. The damage diagnosis based on acceleration measurement that is first performed on the entire structure of a simply supported beam by using deflection estimated by modal flexibility. The angular-velocity-based damage diagnosis is additionally conducted to localize the damage near the hinged support, which was missed by acceleration-based approaches. Experimental validations have been carried out to confirm the superiority of the proposed multi-scale sensing system.

The previous studies showed that damage detection methods that use multi-scale measurements outperform methods that use only one type of measurement. Multi-scale sensing may be used for more effective SHM, such as better displacement monitoring. However, potential benefits of utilizing multi-type responses for damage identification have not been fully explored. Moreover, few references are available on the problem of multi-type response reconstruction and multi-scale sensing fusion for damage detection. Damage may occur at locations that are remote from the measured locations. As a result, integrating multi-scale sensing and response reconstruction is more desirable for identifying damage on large-scale civil structures.

2.5.2 Substructuring Methods for Damage Identification

Some research efforts have been devoted to deal with the large-scale computation demand and the non-global identifiability of damage identification for large civil structures.

The first notable strategy is the dynamic substructuring technique, or specifically, the CMS-based methods. Detailed introduction to the dynamic substructuring techniques can be found in Section 4.4. For damage detection in terms of model updating, Weng et al. (2010) proposed a substructure-based FE model updating method performed in the frequency domain for damage identification. Computational demand was dramatically reduced given that only concerned substructures and the eigenequation of the condensed structure were reanalyzed in updating procedures. Liu et al. (2014) combined the CMS technique with Kriging predictor in the model updating of a complex structure using eigenvalues of the structure. Updating the FE model of an

arch bridge was investigated to demonstrate the effectiveness of the proposed method. Chen et al. (2014) applied the free-interface modal synthesis method to substructure sensitivity-based damage detection. Simulation study of an 11-story frame structure indicated that the substructure-based method could detect damage with better speed and stability in multi-damage cases. Papadimitriou et al. (2013) integrated the CMS technique as an efficient model reduction technique into Bayesian FE updating by using modal characteristics to alleviate the computation burden involved in damage identification of a highway bridge. A similar strategy was reported (Jensen et al., 2014) in Bayesian FE updating using dynamic response data. Shan (2015) introduced a novel FE model updating method for bridge structures by combining the substructure FE model updating method with the response surface method using natural frequency and static displacement. Yu et al. (2016) applied the free-interface CMS method to the element-by-element model updating of large-scale structures. The global model is updated using the assembled eigensensitivity of the global structure using the eigensensitivities of each substructure with respect to the element parameters. Thus, computational time was shorter compared with that consumed by the conventional global-based approach.

Another similar but different strategy has been reported in substructural damage identification. In substructural identification, the entire structure is divided into substructures with a certain substructure selected as the target substructure for analysis. Usually, the focus is on structural degradations inside the investigated substructure and treating interaction effects at the interface DOFs as external forces to the substructure. A diverse set of methods of the topic has been reported by many

researchers. Koh et al. (1991) proposed a first-noted application of substructural identification and adopted the extended Kalman filter to solve the state and observation equation with and without overlapping members for the identification of structural parameters in the time domain. With a limited set of measured acceleration response, substructural identification significantly outperformed the identification using the complete structural model. Yun and Lee (1997) proposed a substructural identification method for the estimation of local damage in the compound structure using sequential prediction error and an autoregressive and moving average with stochastic input model. A new technique, that is, the progressive substructure identification, was proposed and investigated by Koh et al. (2003) and Trinh and Koh (2011) to identify the stiffness parameters of a chain structure with GA. The proposed strategy works by gradually expanding the substructure under survey while including new unknown parameters for identification. The numerical results of Koh et al. (2003) showed that progressive substructure identification performs best compared with substructure identification with overlap and without overlap. Tee et al. (2005) provided two methods for system identification at the substructural level in first-order and second-order models, which used the eigensystem realization algorithm and the Kalman filter.

The superiority of substructural level identification over global structural identification was illustrated by numerical simulation studies of a 12-story shear building and a 50-story shear building in terms of improvement in accuracy and computational efficiency. Yuen and Katafygiotis (2006) presented a substructure identification procedure in a Bayesian context in the frequency domain. A numerical

simulation of a 100-DOF structure was conducted with successful detection of damages as small as 5% stiffness loss in one floor. Hou et al. (2011) developed a substructure isolation method by adding a virtual fixed support to the substructure. Then, system identification could be performed on the isolated substructure. Xing and Mita (2012) applied a time domain substructural identification to shear buildings with discrete masses by utilizing an autoregressive and moving average with exogenous terms model of one-DOF substructures. The simulation study results of a five-story shear building showed that damage was detected with statistical significance for all the damage cases with stiffness loss greater than 20%. Li et al. (2012) proposed a substructural damage identification approach in which the responses and forces at the interface DOFs were reconstructed using the unit impulse response function in the wavelet domain. The substructural FE model updating was performed on the FE model of the target substructure by using acceleration data on the damaged substructure. The simulated damage on a three-dimensional box section girder can be identified effectively even with 10% measurement noises. Weng et al. (2012) proposed a new substructural model updating method in which the modal data measured from the global structure was disassembled to obtain the dynamic flexibility matrices of independent substructures. The extracted substructural flexibility matrices are then used as references for updating the corresponding substructural models, in which only the sub-models were reanalyzed in the updating process, resulting in a rapid convergence of optimization.

2.5.3 Multi-scale Modeling for Damage Identification

Essentially, the damage is a complex process and affects structures at many different

scales. At the incipient stage, the damage is initiated by cracks or intrinsic material imperfection in structural components. As damage progresses, the properties of the component are degraded, which ultimately causes component-level changes and even comes to a structure-level failure without timely remedial works. A multi-scale modeling that characterizes the complicated process in multifarious scale is needed for elaborate and accurate damage simulation and detection. Another motivation for developing multi-scale model is related to computation accuracy and efficiency. In civil infrastructures, such as long-span bridges in kilometers, incipient damage occurs typically on hotspot connections or components of the order of millimeters due to localized stress concentration. Thus, to model numerically and analyze the global and local behavior of response and damage is impossible in a unified spatial scale. To capture accurately minor or localized damage generation and growth in hotspot locations, elaborate FE models at small scale are needed to obtain high-resolution dynamic properties of these substructures. Also, other substructures can be modeled in coarse elements with large scale for computation ease.

The concept of using multi-scale FE model for SHM or damage identification has been embraced by several researchers. Li et al. (2007) developed an approach for the multi-scale analysis of structural dynamic response and local damage in a multi-scale model of the Tsing Ma Bridge. The global dynamic response of the bridge and local damage accumulation of two typical weld details in the longitudinal truss of TMB under traffic loading are numerically analyzed by using the developed model and computational procedures. A concurrent multi-scale FE modeling for civil infrastructures, where a large-scale model is adopted for the global responses of

structures with a linear behavior, and a small-scale model is used for nonlinear damage analysis of the local welding was investigated by Li et al. (2009) and applied to the cable-stayed Runyang Bridge (Chan et al., 2009). Ding et al. (2010) developed a multi-scale FE model that combines a global scale model for modal analysis of the entire bridge and local-scale models for local stress analysis of the concerned components for a long-span cable-stayed bridge. The results of the multi-scale FE model agreed well with the measured ones in terms of modal properties and stress distributions. Zhu et al. (2014) established a multi-scale FE model of Stonecutters Bridge, in which the twin-box deck of the bridge was modeled by using elaborate shell elements and other components using simple beam or truss elements. Each segment of the girder was condensed into a super-element by using the substructuring method. This model could achieve a balance between the modeling of precise geometry and computation time.

Furthermore, Xiao et al. (2014) updated the multi-scale model by minimizing an objective function that involves dynamic response (modal frequencies) and static response (displacement and stress influence lines). The response surface method was adopted in the updating process to enhance computation efficiency. He and Zhu (2013) proposed an adaptive scale damage detection strategy, in which dynamic equations and modal properties of beam structures are modeled by spatially varying the beam-type wavelet FE model. Thus, damage could be detected progressively. The suspected region is first identified using a low-scale structural model and the more accurate location and severity of the damage could then be estimated by using a multi-scale model with local refinement in the suspected region. Experimental

validation of a one-bay steel portal frame was also presented (Zhu et al., 2014). Sun et al. (2016) developed a new multi-scale model for fatigue damage accumulation evaluation, which could describe continuous average damage evolution for easier engineering application and internal collective behavior of short and long cracks for a better understanding of metal fatigue failure mechanisms. The multi-scale fatigue model was further used in the image-based simulation of the collective process of the short crack nucleation and growth in micro-scale, as well as continuous fatigue damage evolution in macro-scale (Sun et al., 2016).

From the previously presented references, research efforts in several aspects are required for the realization of damage identification on large civil structures. First, a model-dependent damage identification method requires a multi-scale model that could characterize the damage on hotspot locations in high-resolution while balancing computation demand. Second, multi-type sensors that capture the global and local responses should be deployed at optimized locations and a fusion of the mixed response should provide more comprehensive information regarding structural condition. Finally, the local damage on the structure should be sought in the appropriate manner to overcome the computation burden constraints and guarantee the global identifiability of locally exciting damages. A framework that incorporates all the aspects is desperately desired for damage identification in larger civil structures.

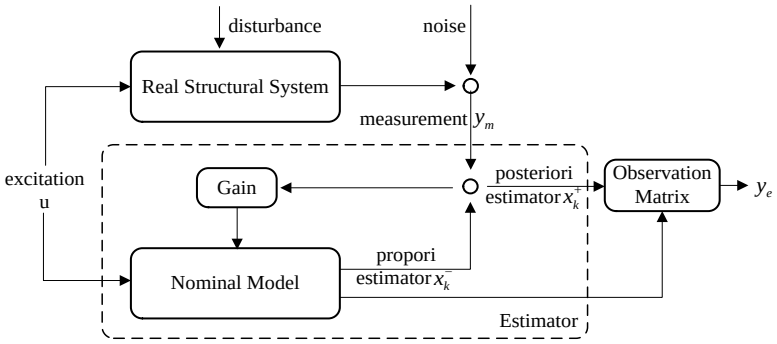

Figure 2. 1 Block diagram of estimator based response reconstruction

CHAPTER 3

OPTIMAL MULTI-TYPE SENSOR PLACEMENT FOR JOINT RESPONSE AND EXCITATION RECONSTRUCTION

3.1 Introduction

Equation Chapter (Next) Section 3Accurate knowledge of structural response is vital to vibration-based structural performance monitoring of a civil structure. The need to perform dynamic response reconstruction always arises as the sensor deployment is often limited to a few predefined locations due to measurement accessibility and budget constraint, especially for a large civil structure. Besides, advances in sensor technologies enable installing multiple types of sensors on the monitored structure to measure not only global response (*e.g.* acceleration and displacement) but also local response (*e.g.* stress and strain). As a result, how to design an optimal sensor configuration of multi-type sensors for the best reconstruction of the responses of key components where there are no sensors installed becomes a meaningful question that should be answered to ensure the functionality of the SHM system. Zhang et al. (2012) and Xu et al. (2016) presented a multi-type sensor placement method for dynamic response reconstruction, in which the classical Kalman filter was used to reconstruct the responses at the key locations by taking advantages of the structural model information and the real-time responses measured by limited sensors. Their method accounts for the effect of measurement noise and modeling errors. However, the full

description of external excitation (in terms of time history and excitation location) is required in the procedure. The necessity of knowledge on external excitation has constrained the application of their method in the circumstances where the acting excitations on the structure are difficult to be measured. This chapter thus presents an algorithm for optimal placement of multi-type sensors, including strain gauges, displacement meters, and accelerometers, for the best reconstruction of desired structural responses of key locations as well as the best estimation of external excitations acting on the structure simultaneously. The algorithm is developed in the framework of Kalman filter under unknown input (KF-UI), in which minimum-variance unbiased estimates of the generalized state of the structure and the external excitations are obtained by virtue of limited sensor measurements. The structural responses of key locations without sensors can then be reconstructed with the estimated generalized state and excitation. The asymptotic stability feature of the filter is utilized for optimal sensor placement. The number and spatial location of the multi-type sensors are determined by a forward sequential sensor placement method: adding the *n*-th optimal sensor which gains the maximal reduction of the estimation error of reconstructed responses when the first (*n*-1) optimal sensors are fixed. A simply-supported overhanging steel beam under multiple types of excitation is numerically studied to demonstrate the feasibility and superiority of the proposed method, and the corresponding experimental works on the overhanging beam will be presented in Chapter 7.

3.2 State Space Representation

3.2.1 Continuous State Space Model

The dynamics of a structure modeled by n degrees of freedom (DOFs) can be expressed by

$$\mathbf{M}\ddot{\mathbf{d}}(t) + \mathbf{C}\dot{\mathbf{d}}(t) + \mathbf{K}\mathbf{d}(t) = \mathbf{L}\mathbf{u}(t) \tag{3.1}$$

where $\mathbf{M}$, $\mathbf{C}$ and $\mathbf{K} \in \Re^{n\times n}$ denote the mass, damping and stiffness matrices of the structure, respectively; the matrix $\mathbf{L} \in \Re^{n\times p}$ is the mapping matrix relating the excitations with the corresponding DOFs of the structure; the vector $\mathbf{u}(t) \in \Re^{p}$ contains p inputs; and $\mathbf{d}(t) \in \Re^{n}$ is the vector of nodal displacement, and a dot over the vector denotes differentiation with respect to time. Using the coordinate transformation $\mathbf{d}(t) = \mathbf{\Phi}\mathbf{q}(t)$ and premultiplying by $\mathbf{\Phi}^{\mathbf{T}}$, Eq. (3.1)can be transformed to

$$\mathbf{\Phi}^{\mathbf{T}}\mathbf{M}\mathbf{\Phi}\ddot{\mathbf{q}}(t) + \mathbf{\Phi}^{\mathbf{T}}\mathbf{C}\mathbf{\Phi}\dot{\mathbf{q}}(t) + \mathbf{\Phi}^{\mathbf{T}}\mathbf{K}\mathbf{\Phi}\mathbf{q}(t) = \mathbf{\Phi}^{\mathbf{T}}\mathbf{L}\mathbf{u}(t) \tag{3.2}$$

in which $\mathbf{\Phi} \in \Re^{n\times n}$ is the matrix of mode shapes, which can be obtained by undamped eigenvalue analysis from $\mathbf{K\Phi} = \mathbf{M\Phi\Omega^2}$. If mass-normalized eigenvectors are chosen, $\mathbf{\Phi}^{\mathbf{T}}\mathbf{M\Phi} = \mathbf{I}$ and $\mathbf{\Phi}^{\mathbf{T}}\mathbf{K\Phi} = \mathbf{\Omega^2}$. If the proportional damping is further assumed, $\mathbf{\Phi}^{\mathbf{T}}\mathbf{C\Phi} = \mathbf{2\Xi\Omega}$ holds. Eq. (3.2) can be further decoupled as

$$\ddot{\mathbf{q}}(t) + \mathbf{2\Xi\Omega}\dot{\mathbf{q}}(t) + \mathbf{\Omega^2}\mathbf{q}(t) = \mathbf{\Phi}^{\mathbf{T}}\mathbf{L}\mathbf{u}(t) \tag{3.3}$$

Where $\mathbf{\Omega} \in \Re^{n \times n}$ and $\mathbf{\Xi} \in \Re^{n \times n}$ are the diagonal matrices containing the eigenfrequencies ω_i in rad/s and the modal damping ratio ξ_i, respectively. Eq. (3.3) can be further written in state-space form as:

$$\begin{aligned} \dot{\mathbf{x}}(t) &= \mathbf{A}_c \mathbf{x}(t) + \mathbf{B}_c \mathbf{u}(t) \\ \mathbf{y}(t) &= \mathbf{C}_c \mathbf{x}(t) + \mathbf{D}_c \mathbf{u}(t) \end{aligned} \tag{3.4}$$

with

$$\mathbf{x}(t) = \begin{Bmatrix} \mathbf{q}(t) \\ \dot{\mathbf{q}}(t) \end{Bmatrix}, \mathbf{A}_c = \begin{bmatrix} \mathbf{0} & \mathbf{I} \\ -\mathbf{\Omega}^2 & -2\mathbf{\Xi\Omega} \end{bmatrix}, \mathbf{B}_c = \begin{bmatrix} \mathbf{0} \\ \mathbf{\Phi}^{\mathrm{T}}\mathbf{L} \end{bmatrix} \tag{3.5}$$

where $\mathbf{x}(t) \in \Re^{N_n}$ and $\mathbf{y}(t) \in \Re^{N_m}$ denote the state vector and the observation vector, respectively, of the structure, where $N_n = 2n$ is the system mode number; $\mathbf{A}_c \in \Re^{N_n \times N_n}$, $\mathbf{B}_c \in \Re^{N_n \times N_n}$, $\mathbf{C}_c \in \Re^{N_m \times N_n}$ and $\mathbf{D}_c \in \Re^{N_m \times p}$ represent the continuous state matrix, input matrix, output matrix and transmission matrix, respectively; and $\mathbf{I} \in \Re^{N_n \times N_n}$ is the identity matrix. If strain, displacement and acceleration are output responses, the observation vector should be as follows:

$$\mathbf{y}(t) = \begin{Bmatrix} \boldsymbol{\varepsilon}(t) \\ \dot{\mathbf{d}}(t) \\ \ddot{\mathbf{d}}(t) \end{Bmatrix} = \begin{bmatrix} \mathbf{\Psi} & \mathbf{0} \\ \mathbf{\Phi} & \mathbf{0} \\ -\mathbf{\Phi\Omega}^2 & -2\mathbf{\Phi\Xi\Omega} \end{bmatrix} \begin{Bmatrix} \mathbf{q}(t) \\ \dot{\mathbf{q}}(t) \end{Bmatrix} + \begin{bmatrix} \mathbf{0} \\ \mathbf{0} \\ \mathbf{\Phi}^{\mathrm{T}}\mathbf{\Phi}\mathbf{L} \end{bmatrix} \cdot \mathbf{u}(t) \tag{3.6}$$

where $\mathbf{\Psi}$ is the strain mode shapes. The output matrix and transmission matrix corresponding to Eq. (3.6) should be

$$\mathbf{C}_c = \begin{bmatrix} \boldsymbol{\Psi} & \mathbf{0} \\ \boldsymbol{\Phi} & \mathbf{0} \\ -\boldsymbol{\Phi}\boldsymbol{\Omega}^2 & -2\boldsymbol{\Phi}\boldsymbol{\Xi}\boldsymbol{\Omega} \end{bmatrix}, \mathbf{D}_c = \begin{bmatrix} \mathbf{0} \\ \mathbf{0} \\ \boldsymbol{\Phi}^{\mathrm{T}}\boldsymbol{\Phi}\mathbf{L} \end{bmatrix} \tag{3.7}$$

3.2.2 Discrete State Space Model

As measurement data of structural responses are always recorded at the discrete time by sampling, the continuous-time state space model in Eq. (3.4) shall be transferred into a discrete-time state space model as:

$$\begin{aligned} \mathbf{x}_{k+1} &= \mathbf{A}_d \mathbf{x}_k + \mathbf{B}_d \mathbf{u}_k \\ \mathbf{y}_k &= \mathbf{C}_d \mathbf{x}_k + \mathbf{D}_d \mathbf{u}_k \end{aligned} \tag{3.8}$$

where $\mathbf{x}_k = \mathbf{x}(k\Delta t)$ is the discrete-time state vector with $k = 0,1,2,...$; and Δt is the sampling interval. The relationships of system matrices between the discrete model and the continuous model are established as

$$\begin{cases} \mathbf{A}_d = e^{\mathbf{A}_c \Delta t}; \mathbf{B}_d = \mathbf{B}_0 + \mathbf{A}_d \mathbf{B}_1 \\ \mathbf{C}_d = \mathbf{C}_c; \mathbf{D}_d = \mathbf{C}_c \mathbf{B}_1 + \mathbf{D}_c \end{cases} \tag{3.9}$$

in which the matrix $\mathbf{B}_0$ and $\mathbf{B}_1$ depends on the inter-sample assumption on the input $\mathbf{u}$. The most common assumptions about the inter-sample behavior are zero order hold (ZOH) and first order hold (FOH). For the ZOH assumption, it states that $\mathbf{u}(\tau) = \mathbf{u}_k$ ($k\Delta t \le \tau < (k+1)\Delta t$); while for the FOH assumption, $\mathbf{u}(\tau) = (1-\tau/\Delta t)\mathbf{u}_k + (\tau/\Delta t)\mathbf{u}_k$ ($k\Delta t \le \tau < (k+1)\Delta t$).The closed form solutions of $\mathbf{B}_0$ and $\mathbf{B}_1$ for ZOH and FOH assumptions are presented in Table 3.1. The detailed derivation of the relationships between Eq.(3.4) and Eq.(3.8) is given in Appendix A. The FOH assumption is

adopted in this study due to its higher accuracy.

Under in-service conditions, high modes of vibration of the structure usually have minimal and negligible contributions to total structural responses. As a result, structural responses can be expressed as the superposition of the first several mode responses $\mathbf{d}(t) = \mathbf{\Phi}^r \mathbf{q}^r(t)$, where $\mathbf{\Phi}^r \in \Re^{n \times r}$ is the collection of the selected first $r < n$ mode shapes. The matrices $\mathbf{A}_d, \mathbf{B}_d, \mathbf{C}_d, \mathbf{D}_d$ should then be formatted with proper dimensions accordingly. Considering the modeling error and sensor noise corruption in practice, Eq. (3.8) shall be written as

$$\begin{aligned} \mathbf{x}_{k+1} &= \mathbf{A}_d \mathbf{x}_k + \mathbf{B}_d \mathbf{u}_k + \mathbf{w}_k \\ \mathbf{y}_k^{\mathbf{m}} &= \mathbf{C}_d^m \mathbf{x}_k + \mathbf{D}_d^m \mathbf{u}_k + \mathbf{v}_k \end{aligned} \tag{3.10}$$

where $\mathbf{y}^m$ denotes the sensor measurements; $\mathbf{C}_d^m$ and $\mathbf{D}_d^m$ are composed of the mode shapes with measured DOFs; $\mathbf{w}_k \in \Re^{2r} \sim N(0, \mathbf{Q})$ and $\mathbf{v}_k \in \Re^{N_m} \sim N(0, \mathbf{R})$ represent the independent, white, and normally distributed modeling error and measurement noise vectors with covariance matrices $E\left[\mathbf{w}_p \mathbf{w}_q^T\right] = \mathbf{Q}\delta_{pq}$ and $E\left[v_p v_q^T\right] = \mathbf{R}\delta_{pq}$, respectively, where δ_{pq} denotes the Kronecker delta. If $\mathbf{w}_k$ and $\mathbf{v}_k$ are correlated, it is easy to transform Eq. (3.10) into an equivalent system where modeling error and measurement noise are uncorrelated (Anderson, 1979). The deterministic excitation vector $\mathbf{u}_k$ is assumed to be unknown in this study.

3.3 Response and Excitation Reconstruction

3.3.1. Joint State and Input Estimation

The development of filters for state estimation in the presence of unknown excitations has attracted considerable attention in recent years. A recursive three-step filter was proposed by Gillijns et al. (2007) for unbiased minimum-variance state and excitation estimation, and it was also derived by Pan et al. (2007) in the perspective of weighted least-square estimation. The necessary and sufficient conditions for the existence of unbiased minimum variance estimate of state and input were also given. Recently, Lourens et al. (2012) extended the filter for joint input-response reconstruction using limited acceleration measurement. However, the sensor placement issue was not investigated. The invertibility condition of a linear system for instantaneous input estimation or joint input-state estimation was derived in the reference (Maes et al., 2015), which provides a fundamental guideline for sensor network design. This filter is briefly introduced in the following section, and the detailed derivation can be found in the Appedix B. The framework of this filter and its asymptotically stable convergence properties are the major premise of the optimal multi-type sensor placement for response reconstruction as proposed in this study.

Denote $\hat{\mathbf{x}}_k^-$ and $\hat{\mathbf{x}}_k^+$ as the priori and posteriori state estimates of the structure at time instant k and assume the filter with the initial unbiased estimate $\mathbf{x}_0^-$ and the error variance $\mathbf{P}_0^{x-}$. The excitation and state estimates can be computed recursively by the three steps in the following form

$$\hat{\mathbf{x}}_{k+1}^{-} = \mathbf{A}_d \hat{\mathbf{x}}_k^{+} + \mathbf{B}_d \hat{\mathbf{u}}_k \tag{3.11}$$

$$\hat{\mathbf{u}}_k = \mathbf{M}_k \left(\mathbf{y}_k^m - \mathbf{C}_d^m \hat{\mathbf{x}}_k^{-} \right) \tag{3.12}$$

$$\hat{\mathbf{x}}_k^{+} = \hat{\mathbf{x}}_k^{-} + \mathbf{K}_k \left(\mathbf{y}_k - \mathbf{C}_d^m \hat{\mathbf{x}}_k^{-} - \mathbf{D}_d^m \hat{\mathbf{u}}_k \right) \tag{3.13}$$

The minimum-variance unbiased estimate of excitation $\hat{\mathbf{u}}_k$ is obtained by Eq.(3.12) with the gain matrix $\mathbf{M}_k$ given by

$$\mathbf{M}_k = \left(\mathbf{D}_d^{mT} \tilde{\mathbf{R}}_k^{-1} \mathbf{D}_d^m \right)^{-1} \mathbf{D}_d^{mT} \tilde{\mathbf{R}}_k^{-1} \tag{3.14}$$

in which $\tilde{\mathbf{R}}_k$ is expressed as.

$$\tilde{\mathbf{R}}_k = \mathbf{C}_d^m \mathbf{P}_k^{x-} \mathbf{C}_d^{mT} + \mathbf{R} \tag{3.15}$$

where $(\cdot)^T$ denotes the transposition of the matrix. The variance of the excitation estimate error, defined as $\mathbf{P}_k^u = E\left[\left(\mathbf{u}_k - \hat{\mathbf{u}}_k \right) \left(\mathbf{u}_k - \hat{\mathbf{u}}_k \right)^T \right]$ is then given by

$$\mathbf{P}_k^u = \left(\mathbf{D}_d^{mT} \tilde{\mathbf{R}}_k^{-1} \mathbf{D}_d^m \right)^{-1} \tag{3.16}$$

The minimum-variance unbiased estimate of the state vector $\hat{\mathbf{x}}_k^{+}$ is obtained by Eq. (3.13)with the Kalman filter gain $\mathbf{K}_k$ given by

$$\mathbf{K}_k = \mathbf{P}_k^{x-} \mathbf{C}_k^{mT} \tilde{\mathbf{R}}_k \tag{3.17}$$

The corresponding state estimation error covariance is now updated to the posterior

state estimation error covariance as

$$\mathbf{P}_k^{x+} = \mathbf{P}_k^{x-} - \mathbf{K}_k \left(\tilde{\mathbf{R}}_k - \mathbf{D}_d^m \mathbf{P}_k^u \mathbf{D}_d^{mT} \right) \mathbf{K}_k^T \tag{3.18}$$

Then the optimal state estimate $\hat{\mathbf{x}}_k^+$ at time instant k is propagated to the next time instant priori estimate $\hat{\mathbf{x}}_{k+1}^-$ using Eq. (3.11), and its error covariance matrix is

$$\mathbf{P}_{k+1}^{x-} = \begin{bmatrix} \mathbf{A}_d & \mathbf{B}_d \end{bmatrix} \begin{bmatrix} \mathbf{P}_k^{x+} & \mathbf{P}_k^{xu} \\ \mathbf{P}_k^{ux} & \mathbf{P}_k^{u} \end{bmatrix} \begin{bmatrix} \mathbf{A}_d^T \\ \mathbf{B}_d^T \end{bmatrix} + \mathbf{Q} \tag{3.19}$$

in which $\mathbf{P}_k^{xu} = \mathbf{P}_k^{uxT} = E\left[\left(\mathbf{x}_k - \hat{\mathbf{x}}_k^+ \right) \left(\mathbf{u}_k - \hat{\mathbf{u}}_k \right)^T \right] = -\mathbf{K}_k \mathbf{D}_d^m \mathbf{P}_k^u$ denotes the cross-covariance of the estimate errors of both state and excitation. Consequently, unbiased minimum variance estimates of state and excitation are simultaneously derived using the above three-step recursive filter.

3.3.2. Response and Excitation Reconstruction

It is noted from the above implementation of the filter that no prior information on the type and statistics of excitations is required except for their locations on the structure. It is also noted that the filter works on condition that the matrix $\left(\mathbf{D}_d^{mT} \tilde{\mathbf{R}}^{-1} \mathbf{D}_d^m \right)$ in Eq. (3.12) is non-singular or in other words that the rank of excitation matrix $\mathbf{D}_d^m$ is equal to the number of external excitations, i.e., $\text{rank}\left(\mathbf{D}_d^m \right) = p$. This condition implies that the number of sensors should not be less than the number of excitations, i.e. $m \geq p$. Furthermore, when response reconstruction is performed using mode superposition method in which the transmission matrix is constructed as $\mathbf{D}_d^m = \begin{bmatrix} \mathbf{0} & \mathbf{0} & \boldsymbol{\Phi}^{rT} \boldsymbol{\Phi}^r \mathbf{L} \end{bmatrix}^T$, it is

readily shown that $\text{rank}\left(\mathbf{D}_d^m\right) = \min\left(m, p, r\right)$, where r refers to the number of modes required for response reconstruction, and that the number of modes used shall be larger than the number of excitations, $r \geq p$. The global optimality of the above filter is proven in reference (Hsieh, 2010).

After the minimum-variance unbiased estimates $\hat{\mathbf{x}}_k^+$ and $\hat{\mathbf{u}}_k$ are obtained, the reconstructed responses $\mathbf{y}_k^e$ at the interested locations and their real values $\mathbf{y}_k^r$ are respectively

$$\mathbf{y}_k^e = \mathbf{C}_d^e \hat{\mathbf{x}}_k^+ + \mathbf{D}_d^e \hat{\mathbf{u}}_k \tag{3.20}$$

$$\mathbf{y}_k^r = \mathbf{C}_d^e \mathbf{x}_k + \mathbf{D}_d^e \mathbf{u}_k \tag{3.21}$$

where $\mathbf{C}_d^e$ and $\mathbf{D}_d^e$ are composed of strain and displacement mode shapes with the DOFs of the concerned response reconstruction locations where no sensors are installed.

The accuracy of the reconstructed responses can then be measured by the reconstruction error $\boldsymbol{\delta}_k$ defined as follows:

$$\boldsymbol{\delta}_k = \mathbf{y}_k^r - \mathbf{y}_k^e = \left(\mathbf{C}_d^e \mathbf{x}_k + \mathbf{D}_d^e \mathbf{u}_k\right) - \left(\mathbf{C}_d^e \hat{\mathbf{x}}_k^+ + \mathbf{D}_d^e \hat{\mathbf{u}}_k\right) = \mathbf{C}_d^e \tilde{\mathbf{x}}_k^+ + \mathbf{D}_d^e \tilde{\mathbf{u}}_k \tag{3.22}$$

The covariance matrix of reconstruction error is expressed as:

$$\boldsymbol{\Lambda}_k = E\left[\boldsymbol{\delta}_k \boldsymbol{\delta}_k^T\right] = \begin{bmatrix} \mathbf{C}_d^e & \mathbf{D}_d^e \end{bmatrix} \begin{bmatrix} \mathbf{P}_k^{x+} & \mathbf{P}_k^{xu} \\ \left(\mathbf{P}_k^{xu}\right)^T & P_k^u \end{bmatrix} \begin{bmatrix} \mathbf{C}_d^{eT} \\ \mathbf{D}_d^{eT} \end{bmatrix} = \overline{\mathbf{C}}_d^e \overline{\mathbf{P}}_k \overline{\mathbf{C}}_d^{eT} \tag{3.23}$$

3.4 Sensor Placement for Response and Excitation Reconstruction

3.4.1. Asymptotic Stability of the Reconstruction Error

The prior error covariance of state vector at time step $k+1$ is

$$\mathbf{P}_{k+1}^{x-}=\begin{bmatrix}\mathbf{A}_d & \mathbf{B}_d\end{bmatrix}\begin{bmatrix}\mathbf{P}_k^{x+} & \mathbf{P}_k^{xu}\\ \mathbf{P}_k^{ux} & \mathbf{P}_k^{u}\end{bmatrix}\begin{bmatrix}\mathbf{A}_d^T\\ \mathbf{B}_d^T\end{bmatrix}+\mathbf{Q}=\begin{bmatrix}\mathbf{A}_d & \mathbf{B}_d\end{bmatrix}\bar{\mathbf{P}}_k\begin{bmatrix}\mathbf{A}_d & \mathbf{B}_d\end{bmatrix}^T+\mathbf{Q} \tag{3.24}$$

It can be further expressed as:

$$\mathbf{P}_{k+1}^{x-}=\left(\mathbf{A}_d-\mathbf{H}_k\mathbf{C}_d^m\right)\mathbf{P}_k^{x-}\left(\mathbf{A}_d-\mathbf{H}_k\mathbf{C}_d^m\right)^T+\mathbf{H}_k\mathbf{R}\mathbf{H}_k^T+\mathbf{Q} \tag{3.25}$$

where

$$\mathbf{H}_k=\mathbf{A}_d\mathbf{K}_k\left(\mathbf{I}-\mathbf{D}_d^m\mathbf{M}_k\right)+\mathbf{B}_d\mathbf{M}_k \tag{3.26}$$

If the external excitations are known and the classical Kalman filter is used, the priori state error covariance of state vector at time step $k+1$ is given as (Anderson, 1979):

$$\mathbf{P}_{k+1}^{-}=\left(\mathbf{A}_d-\mathbf{A}_d\mathbf{K}_k\mathbf{C}_d^m\right)\mathbf{P}_k^{-}\left(\mathbf{A}_d-\mathbf{A}_d\mathbf{K}_k\mathbf{C}_d^m\right)^T+\mathbf{A}_d\mathbf{K}_k\mathbf{R}\left(\mathbf{A}_d\mathbf{K}_k\right)^T+\mathbf{Q} \tag{3.27}$$

It is noticed that similarities exist between Eq.(3.25) and Eq.(3.27). Therefore, the stability condition of the classical Kalman filter can be extended to the present case (Fang et al., 2012). As a result, if the matrix $\left(\mathbf{A}_d-\mathbf{H}_k\mathbf{C}_d^m\right)$ in Eq. (3.27) has all the eigenvalues inside the unit circle and $\left(\mathbf{A}_d,\mathbf{Q}^{1/2}\right)$ is stabilizable, the prior error covariance matrix $\mathbf{P}_k^{x-}$ exponentially converges to a unique positive $\bar{\mathbf{P}}^{x-}$ for any

nonnegative initial condition $\mathbf{P}_0^{x-}$ (Fang *et al.*, 2013).

$$\lim_{k\to\infty}\mathbf{P}_k^{x-}=\bar{\mathbf{P}}^{x-} \tag{3.28}$$

Eq. (3.28) indicates that if the measurement data are long enough and the recursive steps are large enough, the prior error covariance matrix $\mathbf{P}^{x-}$ is bounded and asymptotically stable and the steady state error covariance $\bar{\mathbf{P}}^{x-}$ is the solution of the following equation.

$$\bar{\mathbf{P}}^{x-}=\left(\mathbf{A}_d-\bar{\mathbf{H}}\mathbf{C}_d^m\right)\bar{\mathbf{P}}^{x-}\left(\mathbf{A}_d-\bar{\mathbf{H}}\mathbf{C}_d^m\right)^T+\bar{\mathbf{H}}\mathbf{R}\bar{\mathbf{H}}^T+\mathbf{Q} \tag{3.29}$$

with

$$\begin{aligned}\bar{\mathbf{H}}&=\mathbf{A}_d\bar{\mathbf{P}}^{x-}\mathbf{C}_d^{mT}\left(\mathbf{C}_d^m\bar{\mathbf{P}}^{x-}\mathbf{C}_d^{mT}+\mathbf{R}\right)^{-1}\left(\mathbf{I}-\mathbf{D}_d^m\bar{\mathbf{M}}\right)+\mathbf{B}_d\bar{\mathbf{M}}\\ \bar{\mathbf{M}}&=\left[\mathbf{D}_d^{mT}\left(\mathbf{C}_d^m\bar{\mathbf{P}}^{x-}\mathbf{C}_d^{mT}+\mathbf{R}\right)^{-1}\mathbf{D}_d^m\right]^{-1}\mathbf{D}_d^{mT}\left(\mathbf{C}_d^m\bar{\mathbf{P}}^{x-}\mathbf{C}_d^{mT}+\mathbf{R}\right)^{-1}\end{aligned} \tag{3.30}$$

Using Eq. (3.24) and Eq.(3.23), one can further conclude that the reconstruction error covariance matrix is also asymptotically stable, converging to a fixed value $\bar{\mathbf{\Lambda}}$ for any initial condition if a considerable large number of measurement instants are available.

$$\lim_{k\to\infty}\mathbf{\Lambda}_k=\bar{\mathbf{\Lambda}} \tag{3.31}$$

In the case of the standard Kalman filter, the steady state error covariance can be obtained by solving the associated Riccati equation (Anderson, 1979). However, it is not straightforward to solve Eq. (3.29) for the steady state error covariance. To obtain the steady state error covariance $\bar{\mathbf{P}}^{x-}$ and then the constant state reconstruction error

covariance $\bar{\mathbf{\Lambda}}$, one can assign the initial value $\mathbf{P}_0^{x-}$ any nonnegative value and use Eq. (3.15) ~(3.19) recursively until a stable value is reached. In consideration that the reconstruction error covariance $\bar{\mathbf{\Lambda}}$ is stable and independent of the external excitation $\mathbf{u}_k$, it is desirable to develop the optimal sensor placement method based on the constant state reconstruction error covariance for the best response reconstruction.

3.4.2. Optimal Multi-type Sensor Placement Design

To determine the optimal multi-type sensor placement based on the steady state reconstruction error covariance for the best response reconstruction, the response reconstruction location set and the measurable location fixed for the structure shall be determined first. The response reconstruction location set is the collection of those locations whose responses are critical to the condition assessment of the structure. The size of response construction location set is often much smaller than the number of DOFs of the structure because the responses of some DOFs are so small that they can be ignored in the condition assessment and excluded from the response reconstruction. The measurable location set is the collection of those locations where the sensors can be installed, and the responses can be measured. The measurable location set is often the subset of the response reconstruction location set. For instance, it is tough, if not impossible, to measure rotational responses and thus these sites shall not be included in the measurable location set. Furthermore, some sites are even inaccessible for measurement under the in-service condition and they shall be excluded from the measurable location set as well. As a result, the optimal multi-type sensor placement in this study becomes a fundamental optimization problem that the type, number, and

location of sensors shall be selected from the measurable location set to achieve the minimum response reconstruction error from the response reconstruction location set. The objective function can then be expressed as

$$S_P = \arg\min_{S \in S_N} \left[trace\left(\bar{\boldsymbol{\Lambda}}\right) \right] \tag{3.32}$$

in which $\bar{\boldsymbol{\Lambda}}$, parameterized by the output matrix $\mathbf{C}_d^e$ and transmission matrix $\mathbf{D}_d^e$, is the steady response reconstruction error covariance of the response reconstruction location set; N_n is the number of locations in the response reconstruction location set; S_P implies the optimal sensor placement configuration and S_N denotes the set of all distinct sensor configurations.

In the references (Zhang et al., 2012; Zhu et al., 2013; and Xu et al., 2016), the optimization procedure was implemented by deleting the sensor location from the measurable location set one by one, producing the least response reconstruction error. This procedure is easily implemented for simple structures, but when the measurable location set is large, especially when the optimal sensor number is small compared with the size of the measurable location set, the entire procedure is computationally intensive and time-consuming. In this study, the optimization procedure is implemented by adding the sensor location one by one within the measurable location set. The similar strategy was utilized in reference (Papadimitriou, 2004) named sequential sensor placement algorithm when performing optimal sensor placement for parametric identification. It should be pointed out that the global optimal sensor placement configuration should be obtained through an exhaustive search over all

sensor configurations, which is extremely time-consuming and computation unaffordable for most cases of practical interest. The proposed algorithm cannot guarantee the global optimality since when adding the *n*-th sensor that contributes most in minimization of the objective function, the first (*n*-1) selected sensor configuration is fixed. However, this algorithm is much more computationally efficient and practical, often giving quite accurate results.

To this end, the first step in the proposed procedure is to decide the least number of sensors and their locations. The least number of sensors shall be larger than the number of excitations to meet the non-singular condition as discussed before. Also, the least number of sensors shall be selected so that the matrix $\left[\mathbf{A}_d - \bar{\mathbf{H}}\mathbf{C}_d^m\right]$ has all the eigenvalues inside the unit circle in the complex plane. After the least sensor number n_0 is determined, the initial optimal sensor in term of type and locations can be so determined that the minimum value of $\left[trace\left(\bar{\mathbf{\Lambda}}\right)\right]$ can be achieved by an exhaustive search among the $C_N^{n_0} = N_n!/\left[n_0!\left(N_n - n_0\right)!\right]$ possible location configurations and its layout be termed as S_0.

The next step of the optimal multi-type sensor placement is to add one more sensor to the initial optimal sensor. There are $\left(N_n - n_0\right)$ alternative configurations, namely $S_0 + s_k$, where s_k denotes the additional one selected from the left $\left(N_n - n_0\right)$ locations. The sensor that introduces the minimum response reconstruction error among the $\left(N_n - n_0\right)$ possible location is chosen as the $\left(n_0 + 1\right)$-th optimal one. Consequently, the steady reconstruction error is further reduced due to the additional sensor. In a similar

fashion, the same procedure could be repeated for the left $\left(N_n - n_0 - 1\right)$ possible sensor location. In this way, the type, number, and location of sensors can be finally determined.

It shall be mentioned that multi-type sensors are used in this study and the signal and noise levels for each type of sensors are different, which make the matrix $\left(\mathbf{C}_d^m \mathbf{P}_k^{x-} \mathbf{C}_d^{mT} + \mathbf{R}\right)$ ill-conditioned. Zhang *et al.* (2012) proposed a normalization procedure to make the Kalman filter numerically stable. The similar treatment is adopted here using the weighting matrix $\bar{\mathbf{W}}$ to scale the reconstructed multi-type responses. The normalized output matrix and transmission matrix are calculated by

$$\bar{\mathbf{C}}_d^m = \bar{\mathbf{W}}^{1/2} \mathbf{C}_d^m, \bar{\mathbf{D}}_d^m = \bar{\mathbf{W}}^{1/2} \mathbf{C}_d^m \tag{3.33}$$

The measured responses $\mathbf{y}^m$ are also normalized as

$$\bar{\mathbf{y}}^m = \bar{\mathbf{W}}^{1/2} \mathbf{y}^m \tag{3.34}$$

As a straightforward and shared case, the weighting matrix $\bar{\mathbf{W}}$ could be set as the inversion of covariance of the noise, namely $\bar{\mathbf{W}} = \mathbf{R}^{-1}$, and then the reconstructed response is an unbiased estimate for response at each location. It can be seen from above discussions that the entire procedure for the optimal multi-type sensor placement can be conducted in the absence of external excitations. Thus, the optimal multi-type sensor placement achieved can be used for any external excitation, provided that the number of mode shapes, loading locations, and environmental noise remains the same.

3.5 Numerical Investigation

3.5.1 Descriptions of a Beam and Its FE Model

This section describes a numerical investigation to demonstrate the optimization procedure of multi-type sensor placement and the superiority of the optimal sensor placement over alternative placements. A simply-supported overhanging steel beam, which was tested in a laboratory and will be introduced in Chapter 7, is employed for numerical investigation in this section.

The geometric configuration of the simply-supported overhanging beam is shown in

Figure 3.1. It is $4\,\mathrm{m}$ in length and has a cross-sectional area $b(\text{width}) \times \mathrm{h}(\text{height}) = 50 \times 15.6\,\mathrm{mm}$. The beam is constrained by a hinge support at $1\,\mathrm{m}$ from the left-side end and a roller support at $1\,\mathrm{m}$ from the right-side end, respectively. The elastic modulus of the beam is $2.6\,\mathrm{GPa}$ and the density is $7780\,\mathrm{Kg/m^3}$. It is discretized into 40 Euler beam elements with 41 nodes and 120 DOFs (exclude two supports).

A stochastic force with a frequency bandwidth ranging from 2 Hz to 102 Hz is applied on node 18 vertically. The excitation frequency bandwidth covers the first seven modes of vibration (as shown in Table 3). Classical Rayleigh damping model is adopted here and defined as $\mathbf{C} = \alpha\mathbf{M} + \beta\mathbf{K}$, in which α and β are the mass and stiffness proportional damping coefficient, respectively. The first two modal damping ratios are set as $\xi_1 = 0.010$ and $\xi_2 = 0.008$ based on the modal test results. The mass and stiffness damping coefficients can thus be obtained with

$\alpha = 2\omega_1\omega_2\left(\xi_1\omega_2 - \xi_2\omega_1\right)/\left(\omega_2^2 - \omega_1^2\right)$ and $\beta = 2\left(\xi_2\omega_2 - \xi_1\omega_1\right)/\left(\omega_2^2 - \omega_1^2\right)$. The sampling frequency is 500 Hz, and the sample duration is 16 s. The dynamic response is numerically simulated with FOH state space formulation. To include noise corruption, the normally distributed random noise is added to the response as

$$\mathbf{y}^n = \mathbf{y}^r + y_{\text{amp}} \times \mathbf{e} \tag{3.35}$$

where $\mathbf{y}^n$ and $\mathbf{y}^r$ are the noise-polluted response and pollution-free response respectively; $\mathbf{e}$ denotes a standard normal distribution vector with zero mean and unit standard deviation; y_{amp} is the noise amplitude, and it is assigned $0.201\,\mu\varepsilon$, $0.01\,\text{mm}$ and $0.04\ \text{m}/\text{s}^2$ for strain gauge, displacement transducer and accelerometer, respectively, in this simulation study based on the laboratory measurement data.

3.5.2. Optimal Multi-type Sensor Placement

For this simple overhanging beam, the axial response can be omitted as the excitation acts vertically. A total of 200 multi-type responses, including 40 element strain responses, 39 vertical displacements and acceleration responses and 41 rotational displacement and acceleration responses, are considered to form the response reconstruction location set. In considering that it is not easy to measure the rotational responses, the rotational responses are eliminated when deciding the measurable location set. As a result, totally 118 multi-type responses, including 40 element strain, 39 vertical displacement and acceleration responses, are selected to form the measurable location set.

The rational process noise covariance $\mathbf{Q}$ and the measurement noise covariance $\mathbf{R}$ are indispensable for the good estimation and even the convergence of the Kalman filter. From the theoretical basis above, we can see that these two statistics also influence the optical sensor placement layout. In this study, they are assigned by the auto-covariance least-squares method proposed by Odelson (2006) for its easy computation and implementation. The multi-type sensor placement optimization is then performed with the initial state error covariance $\mathbf{P}_0^{x-}$ as $1.0\times10^{-12}\times\mathbf{I}^{14\times14}$. The first 7 modes of vibration are used in the optimization. The least sensor number is 2 to make the filter stable. In this circumstance, the stable reconstruction error is independent of the initial state error covariance $\mathbf{P}_0^{x-}$ theoretically. The optimal locations of the two sensors are decided as one strain gauge on element 14 and one accelerometer on node 21 by an exhaustive search over the C_{118}^2 sensor configurations. Then, the optimal sensor is added one by one to gain the maximum reduction of response reconstruction error until it is less than the threshold value.

Figure 3.2 illustrates a variation of the average trace of reconstruction error covariance with the number of sensors increasing from 2 to 118. Clearly, the average trace of reconstruction error covariance decreases as the growth of optimal sensor number, but when the number of sensors increases to above 10, the reduction of reconstruction error becomes very small. This tendency can be used to determine the number of selected sensors as the optimal sensor configuration. In this study, the first 11 sensors, which include 4 strain gauges, 1 displacement transducer, and 6 accelerometers, are finally used as the optimal sensor placement for the beam. This configuration is denoted as the reference sensor placement configuration (SP0). To assess the

superiority of the proposed optimal placement method, another three sensor placement configurations are considered. The first one (SP1) is that the number of each type sensor is identical to that in SP0, but the locations are chosen differently from SP0. In the second configuration (SP2), 6 accelerometers and 5 strain gauges are arranged alternately on the beam without displacement transducer. In the last configuration (SP3), only 11 accelerometers are arranged on the beam with equal space. The four sensor placement configurations are all shown in Figure 3.3.

To facilitate comparison, a relative response percentage error (RPE) is defined as a metric of response reconstruction accuracy:

$$RPE\left(\mathbf{y}^r, \mathbf{y}^e\right) = \frac{\left\|\mathbf{y}^r - \mathbf{y}^e\right\|_2}{\left\|\mathbf{y}^r\right\|_2} \times 100\% \tag{3.36}$$

where $\mathbf{y}^r$ and $\mathbf{y}^e$ are the real and reconstructed response vectors, respectively. $\|\cdot\|$ denotes the Frobenius norm.

3.5.3. Superiority of Optimal Sensor Placement

The superiority of the optimal multi-type sensor placement is first confirmed by considering a broadband white noise excitation as shown in Figure 3.4. Its bandwidth is $2 \sim 102$ Hz, covering the first seven mode shapes of the beam (see Figure 3.5), and its standard deviation is 6.4 N.

Figure 3.6 presents a close view of the original and reconstructed vertical displacement of node 23 with the optimal sensors placement configuration SP0. The

noise-corrupted response termed as “measured” response, is also plotted in Fig. 6. It is found that the reconstructed response matches well with the real one. Figure 3.7 shows a close view of the real and estimated excitations with the same optimal sensors placement configuration. A good correspondence is also found between the estimated excitation and real excitation. These results demonstrate that the aforementioned three-step filter works well for reconstructing response as well as excitation.

The average RPEs of response and excitation of the first three placement configurations are listed in Table 3.2, where symbols *S*, *A*, *D* and *U* represents the strain, acceleration, displacement and excitation, respectively, and the subscripts denote the coordinate direction. Figure 3.8 gives the comparison of reconstruction results between SP0 and SP1 configurations. It can be found that in general, the reconstructed strain and displacement response match well with their real values with average RPEs less than 5%. The other observation is that acceleration, especially rotational acceleration, has the greatest reconstruction error among the three types of responses. This is related to the fact that acceleration responses contain more high-frequency components and that there are no rotational responses used for response reconstruction. By comparing the results of SP0 with those of SP1 and SP2, one may conclude that the optimal multi-type sensor placement is superior to the SP1 and SP2 configurations, for the mean RPEs of responses as well as the excitation in SP0 are all less than those in SP1 and SP2.

For the sensor placement configuration SP3, it is showed that using 11 equally spaced accelerometers leads the estimated excitation error to diverge, giving unacceptable response reconstruction error. Actually, the numerical results indicate that the

maximum radius of eigenvalues of the matrix $\left(\mathbf{A}_d - \bar{\mathbf{H}}\mathbf{C}_d^m\right)$ is 0.986, 0.966 and 0.987, respectively, for SP0, SP1 and SP2 configuration but this value is 1.0 for SP3 configuration, indicating that the filter is not stable in this sensor placement configuration. As a result, the mean RPEs of reconstructed responses for SP3 configuration are meaningless and not presented here. This scenario, however, further demonstrates the necessity and superiority of the proposed multi-type sensor placement method for collective response and excitation reconstruction. Table 1 also shows that the trace of prediction state error covariance is 1.67e-6, 5.12e-6 and 5.15e-6, respectively, for the sensor placement configuration SP0, SP1 and SP2 with the smallest value for the configuration SP0.

3.5.4 Independence of Optimal Sensor Placement on Excitation

As pointed out in the previous section, the optimal sensor placement can be conducted in the absence of external excitation. To examine the independence of optimal sensor placement on excitation type, the overhanging beam is further investigated in consideration of two more different excitations, namely triangular pulsing excitation and harmonic excitation in addition to the white noise excitation discussed previously.

The amplitude of the triangular pulsing excitation is 50 N and its duration is from $0.008 \sim 0.032$ s (see Figure 3.9). The single-sided spectrum of the pulsing excitation is shown in Figure 3.10. For the optimal multi-type sensor placement SP0, the reconstructed, real and virtually “measured” vertical acceleration responses of node 23 are plotted in Figure 3.11. It is observed that the signal-to-noise ratio (SNR) of the response decreases as vibration amplitude decays. The filter yields a satisfying

response reconstruction compared with the measured one, especially when the SNR is low. The triangular pulsing excitation is also well estimated by using the optimal sensor placement configuration SP0, as shown in Figure 3.9.

The harmonic excitation, expressed as $u(t) = 12 \times \sin(2\pi \times 30t)$ N, acting on node 18 of the overhanging beam is adopted as another loading condition. By using the optimal multi-type sensor placement configuration SP0, the reconstructed strain response of element 23 and the estimated excitation are given in Figure 3.12 and Figure 3.13 respectively. It can be seen that the response and excitation both are well reconstructed as the real and estimated response and excitation display a high degree of agreement.

Table 3.3 presents the mean standard deviations (STDs) of response and excitation reconstruction errors of the beam with the optimal sensor placement configuration SPO under the three different types of excitations. It can be seen that with the optimal sensor placement configuration SPO, the trace of steady priori state error stays the same. Accordingly, the STD of response reconstruction error also stays the same although the excitation type varies. This implicates that the response reconstruction error is directly related to the sensor placement configuration and independent of the type of external excitation. Thus, it is readily inferred that the optimal sensor placement can be applied to any other type of external loading, provided that the external loading location, the modes used in response reconstruction and environmental noise characteristics stay the same.

3.6 Concluding Remarks

An optimal multi-type sensor placement method for a structure under unknown excitation has been proposed in this chapter for the best excitation and response reconstruction at the key locations where no sensors are installed. The joint response and excitation reconstruction using the noise-corrupted measurement data from the limited sensors is performed by extending the simultaneous input and state estimation theory of a linear stochastic system. Basing on that, an optimal multi-type sensor placement has been proposed by selecting a proper subset from the measurable location set to minimize the stable reconstruction error covariance trace. The effectiveness of the proposed method has been demonstrated by virtue of numerical studies of an overhanging beam. Basing on the study, the following remarks should be highlighted:

(1) When the number of measurement instants is large enough, the state error or the error covariance matrix exponentially converges to a unique positive value for any nonnegative initial condition. This asymptotic stability property is the theoretical basis of the proposed SPO method for joint response and excitation reconstruction.

(2) There is no assumption set on the excitation type when deriving the recursive filter. The designed optimal sensor works well for any excitation, provided that the selected subset of modes is fixed, the excitation location is determined, and the environmental noise characteristics remain the same. Selecting the proper subset of mode shapes for response reconstruction can be performed basing on the expert knowledge about the operation conditions or analysis on the loading histories.

(3) Different types of sensor have their own properties. Fusion of the sensors of multiple types is advantageous to increase the accuracy of response and excitation reconstruction. Although only 3 frequently-used sensors, including strain gauges, displacement meters, and accelerometers, are used in this study, other types of sensors, for example, clinometer, velocity-instrument and others could also be incorporated in the proposed framework for some specific objectives. Different types of sensor are equally weighted in this study by setting the weighting matrix as the inversion of noise covariance. Other weighting strategies, for instance taking the cost of each type sensor into consideration, could also be employed in practical applications.

(4) When solving the optimization, an exhaustive searching is computationally unaffordable, especially for a large civil structure. Thus the sequential sensor placement algorithm which produces a sub-optimal solution with a great decrease in computation effort may be a wise choice.

The proposed SPO method can handle the multi-type sensor placement issue in the absence of knowledge of exerted excitations. It can make up the limitation number of measurement sensors, thus benefiting greatly to the vibration based damage identification problem that will be investigated in Chapter 6. The experimental validation of the proposed SPO method will be represented in Chapter 7. Before that, the ill-posedness problem involved in damage identification shall be paid special attention to and it will be discussed in the forthcoming chapter.

Table 3.1 Closed discrete form input to state matrices

Inter-sample assumption	$\mathbf{B}_0$	$\mathbf{B}_1$
Zero order hold	$\left(\mathbf{A}_d-\mathbf{I}\right)\mathbf{A}_c^{-1}\mathbf{B}_c$	0
First order hold	$\left(\mathbf{A}_d-\mathbf{I}\right)\mathbf{A}_c^{-1}\mathbf{B}_c-\mathbf{B}_1$	$\left(\mathbf{A}_d-\mathbf{A}_c\Delta t-\mathbf{I}\right)\mathbf{A}_c^{-2}\mathbf{B}_c/\Delta t$

Table 3.2 RPE of responses and excitation under random excitation

Mean RPE	S	D_{y}	D_{z}	A_{y}	A_{z}	U	$\mathrm{Trace}(\bar{P}^{x\text{-}})$
SP0	1.96	1.29	1.35	5.63	12.30	27.16	1.67e-4
SP1	2.40	1.83	1.89	6.03	12.52	47.23	5.12e-4
SP2	2.29	1.96	1.97	5.86	12.32	30.55	5.15e-4

Table 3.3 Mean STDs of response and excitation reconstruction errors under various types of excitation

Mean STD	S	D_{y}	D_{z}	A_{y}	A_{z}	U	$\mathrm{Trace}\left(\bar{P}^{x\text{-}}\right)$
	uε	mm	mm	ms-2	ms-2	N	—
Random	0.215	0.010	0.011	0.203	0.375	0.821	1.67e-6
Pulsive	0.215	0.010	0.011	0.203	0.375	0.821	1.67e-6
Harmonic	0.215	0.010	0.011	0.203	0.375	0.821	1.67e-6

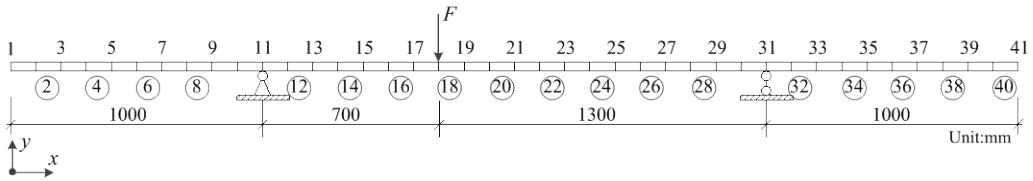

Figure 3.1 Geometric configuration of an overhanging steel beam

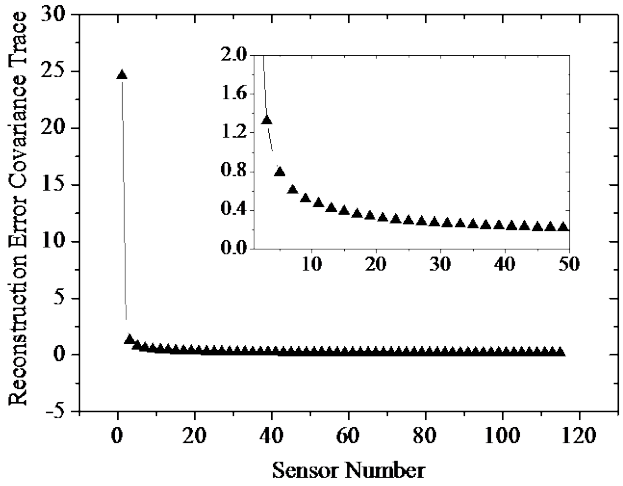

Figure 3.2 Variation of the average trace of reconstruction error covariance with the number of sensors (Right top: a close-view)

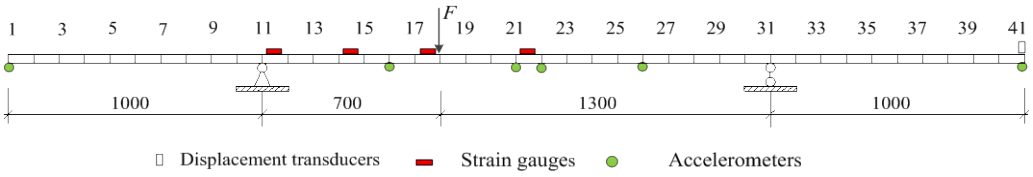

(a)

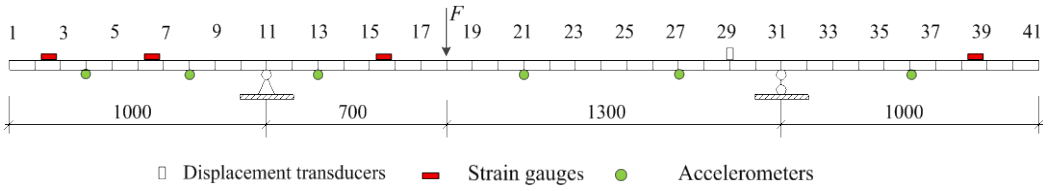

(b)

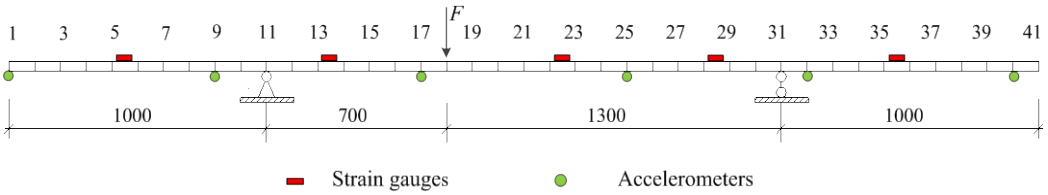

(c)

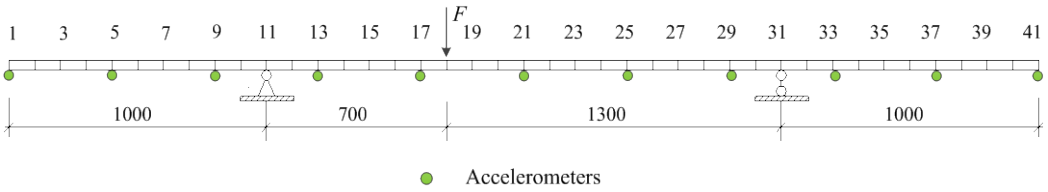

(d)

Figure 3.3 Four sensor placement configuration on a simply supported overhanging steel beam: (a) SP0, (b) SP1, (c) SP2 and (d) SP3

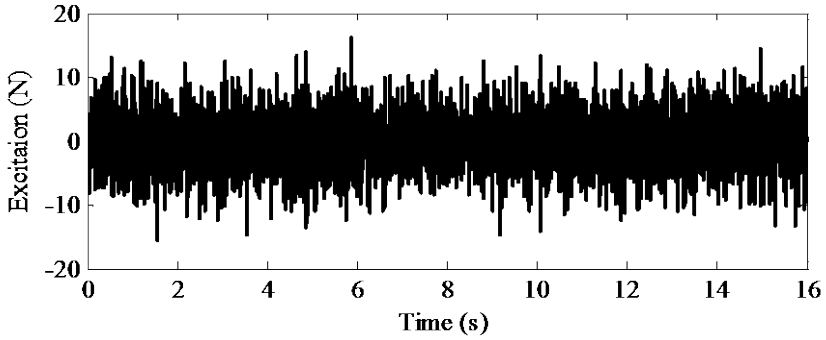

Figure 3.4 Time history of random excitation

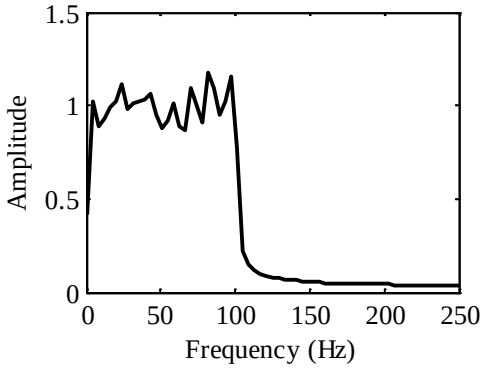

Figure 3.5 Single-sided amplitude spectrum of random excitation

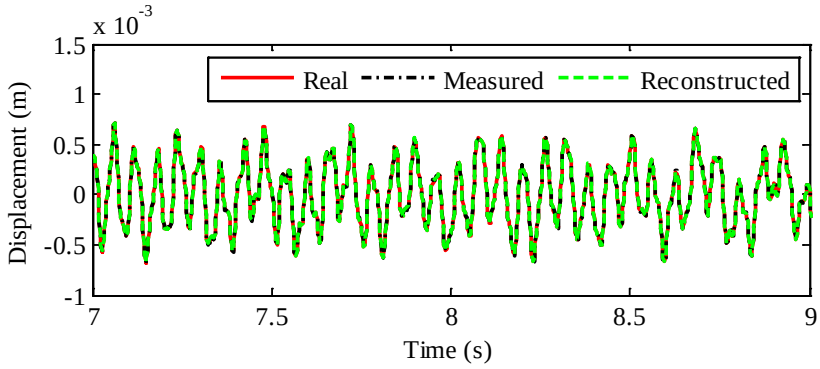

Figure 3.6 Close view of the real, measured and reconstructed displacement on N23

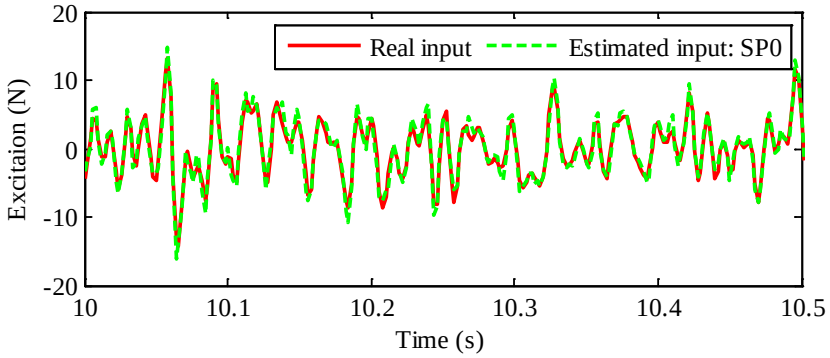

Figure 3.7 A close review of real and estimated random excitation

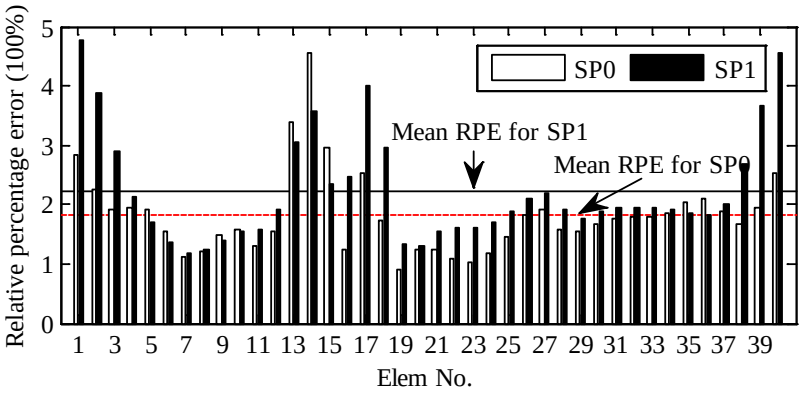
Relative percentage error (100%)
SP0
SP1
Mean RPE for SP1
Mean RPE for SP0
Elem No.

(a)

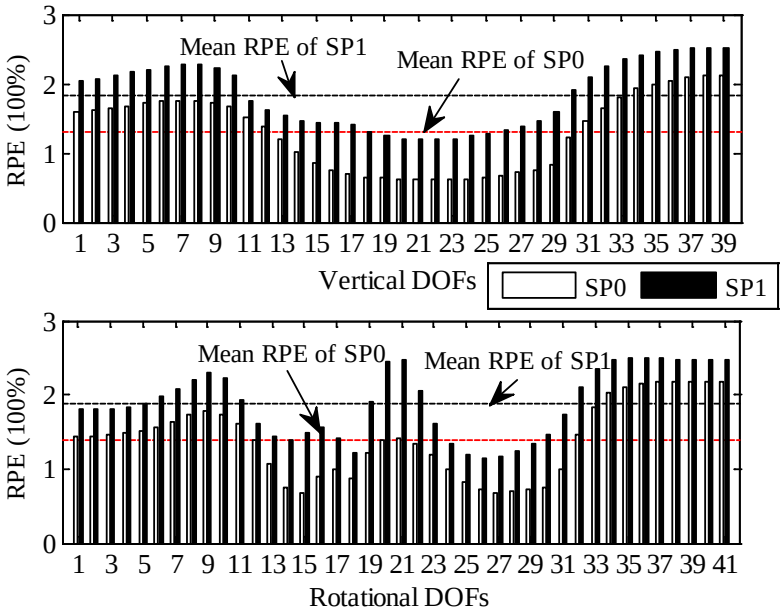
RPE (100%)
Mean RPE of SP1
Mean RPE of SP0
Vertical DOFs
SP0
SP1
Mean RPE of SP0
Mean RPE of SP1
Rotational DOFs

(b)

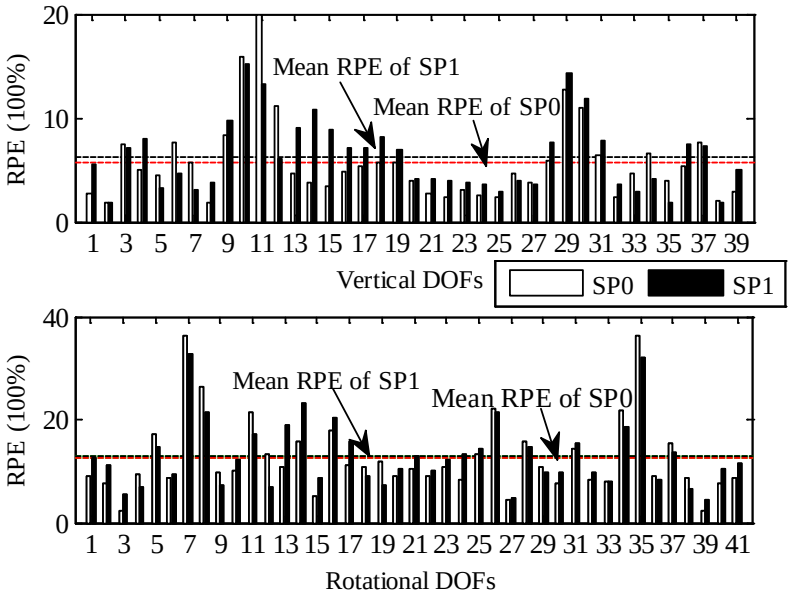

(c)

Figure 3.8 Comparison of response reconstruction result between SP0 and SP1for (a) strain, (b) displacement and (c) acceleration

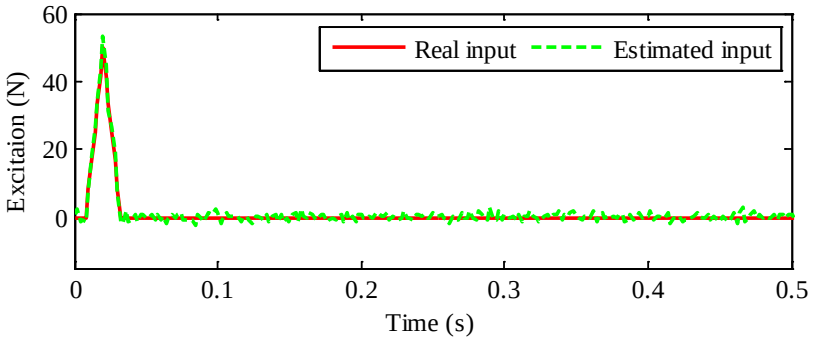

Figure 3.9 Close view of the real and estimated impulsive excitation

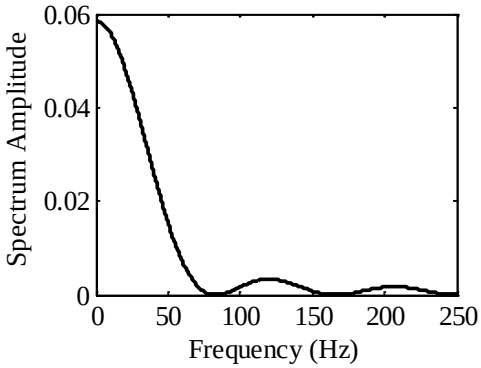

Figure 3.10 Single-sided amplitude spectrum of the impulsive excitation

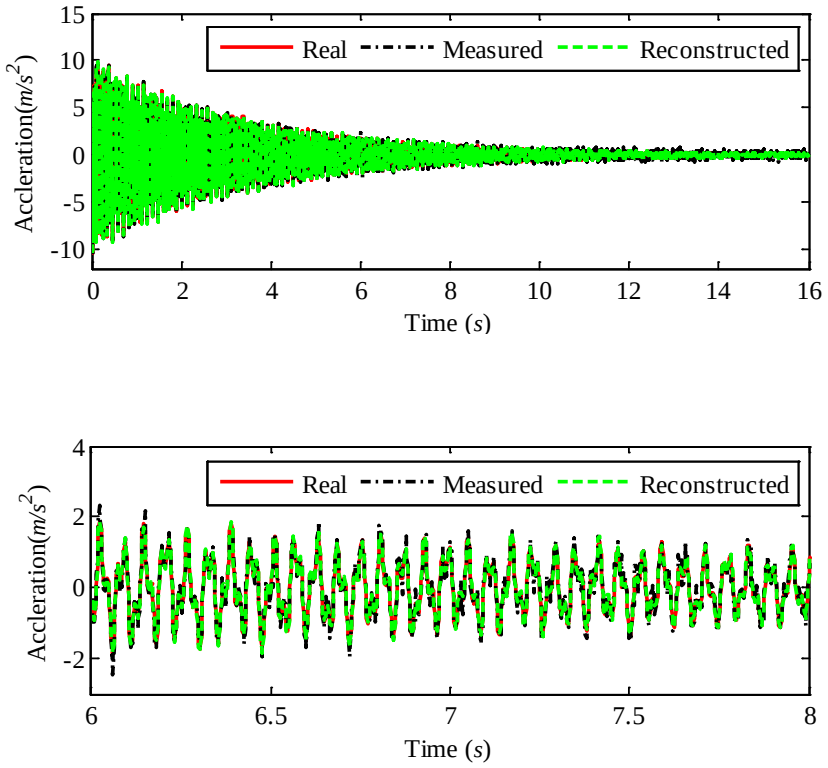

Figure 3.11 The reconstructed acceleration of Node 23 under the impulsive excitation: the whole evolution (top) and a close-view (bottom)

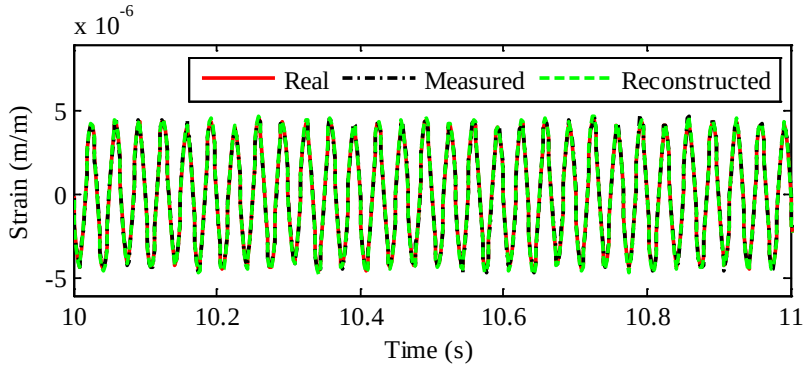

Figure 3.12 A close the real, measured and reconstructed strain of E 23

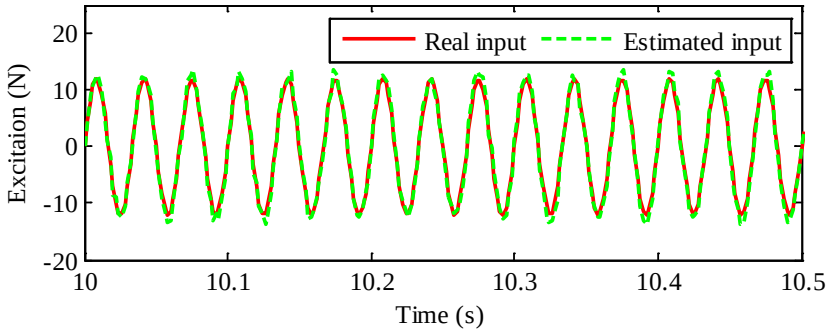

Figure 3.13 A close of real and estimated harmonic excitation

CHAPTER 4

SPARSE REGULARIZATION FOR FE MODEL UPDATING BASED DAMAGE IDENTIFICATION

4.1 Introduction

Sensitivity-based finite element (FE) model updating for structural damage identification is essentially an inverse problem, in which the structural defect is sought and quantified using vibration measurement. The inverse problem is prone to ill-posed, especially when the dimension of damage vector is large and the effective measurements are limited. The ill-posedness features can injury the existence and uniqueness of the solution, inducing much difficulty in seeking the physically meaningful damage vector. Tikhonov regularization, also termed as ℓ_2 norm regularization, is a common approach to handling the ill-posedness problem and yields an acceptable and smooth solution. It enjoys more popular applications due to its explicit solution, computational efficiency, and convenience for implementation. However, as the ℓ_2 norm term promotes smoothness, the solution is sometimes over-smoothed, especially in the case that the sensor number is limited compared with the entire structural components. Due to the fact that typically only a small number of components of the structure are damaged in comparison with the whole structure, the solution to the inverse problem usually bears sparse properties. In this regard, this chapter proposes an alternative way, sparse regularization, or specifically ℓ_1 norm regularization, to handle the ill-posedness problem involved in response

sensitivity based damage identification. The motivation and implementation of sparse regularization are firstly introduced, and its differences with Tikhonov regularization are highlighted. Re-weighting sparse regularization is adopted to enhance the sparsity in the solution as well as to alleviate the difficulty in choosing regularization parameter. Simulation studies on a planar frame, and a simply supported overhanging beam are finally presented, and the results show that the sparse regularization exhibits certain superiority over Tikhonov regularization as less false-positive errors (indicating damage when it is not present) exist in damage identification results.

4.2 Inverse Problem in Damage Identification

Structural damage identification is essentially an inverse problem, in which the structural defects (usually modeled as damage vector) are sought to account for the discrepancy between the damaged and intact states of the structure. Sensitivity-based FE model updating method is a common approach to detecting as well as quantifying the damage of civil structures (Friswell, 1995). It seeks the damage vector by minimizing the residue of FE model-predicted dynamic features of modal domain or time and the measured one in the damaged state. Traditionally, modal features, such as natural frequencies and/or mode shapes, are the preferred quantities for defining the penalty function in model updating (Doebling *et al.*, 1996). Alternative strategies are proposed recently in the time-domain FE model updating (Majumder et al., 2003; Lu et al., 2007; Cacciolaa et al., 2011; Zhang et al., 2011) since transient or closed-loop responses are available more readily during operation and appear to be more suitable for online damage detection than approaches based on frequency

changes. Besides, immediate utilization of time-domain dynamic response can avoid information-losing in data manipulations such as Fourier transform. The response sensitivity based damage identification usually formulates the damage identification in a least-squares sense as a minimization problem:

$$J(\boldsymbol{\theta}) = \left\| \mathbf{W}^{1/2} \left(\mathbf{y}_d - \mathbf{y}_a(\boldsymbol{\theta}) \right) \right\|_2^2 = \boldsymbol{\varepsilon}^T \mathbf{W} \boldsymbol{\varepsilon} \tag{4.1}$$

where $\mathbf{y}_d \in \Re^{n_m}$ are the measured response in damage state and $\mathbf{y}_a(\boldsymbol{\theta})$ is the predicted response from the FE model; $\boldsymbol{\varepsilon} = \mathbf{y}_d - \mathbf{y}_a(\boldsymbol{\theta})$ is the residual vector between the two responses. $\mathbf{W}$ is the diagonal weighting matrix which eases the ill-posedness of the problem; its entries could be set as the reciprocals of the variance of the response of the structure without damage. The subscript T denotes vector transpose. $\boldsymbol{\theta} \in \Re^{n_e}$ is the vector of structural physical parameters, such as stiffness or elasticity modulus. $n_m = N_m \times N_t$, in which N_m and N_t are the number of sensors and time instants recorded by each sensor. It should be pointed out that the dynamic response of a structure is dependent to the external excitations. To make sure that the response discrepancy is only induced by the damage, the excitation should stay the same before and after damage occurrence. The residual in Eq. (4.1) is a non-linear function of the parameters and the minimization is usually solved through a gradient-based optimization like Gaussian-Newton iteration as:

$$\mathbf{S}^k \Delta\boldsymbol{\theta}^{k+1} = \Delta\mathbf{y}^k \tag{4.2}$$

where $\mathbf{S}^k = \mathbf{W}^{1/2} \left[\partial \mathbf{y}\left(\boldsymbol{\theta}^k\right) / \partial \boldsymbol{\theta} \right]$ is the weighted sensitivity matrix of the measured DOFs

with respect to damage parameter $\boldsymbol{\theta}$ in the *k*-th iteration; it could be calculated by theoretical formulation (Greene et al., 1991; Li et al., 2010) when damage takes certain formulations or using numerical central difference method as:

$$\mathbf{S}_{ij}^{k}=\frac{\partial \mathbf{y}_i}{\partial \theta_j}=\frac{\mathbf{y}_i\left(\boldsymbol{\theta}_k+d\theta_j\right)-\mathbf{y}_i\left(\boldsymbol{\theta}_k-d\theta_j\right)}{2d\theta_j} \tag{4.3}$$

Where $d\theta_j$ is a small disturbance on *j*-th component of damage parameter $\boldsymbol{\theta}$. The right-hand side $\Delta\mathbf{y}^k=\mathbf{W}^{1/2}\left[\mathbf{y}_d-\mathbf{y}_a\left(\boldsymbol{\theta}^k\right)\right]=\mathbf{W}^{1/2}\left[\mathbf{y}_d-\mathbf{y}_a^k\right]$ is the weighted response discrepancy on the measured DOFs of the damaged structure with the analyzed ones and $\boldsymbol{\theta}^k=\sum_{l=1}^{k}\Delta\boldsymbol{\theta}^l$ is the cumulative damage parameter in all *k*-th iterations. $\mathbf{S}^k$ and $\Delta\mathbf{y}^k$ are assembled by stacking the columns of sensitivity sequences and response discrepancy sequences, respectively, namely

$$\begin{aligned}\mathbf{S}^{kT}&=\begin{bmatrix}\mathbf{S}_1^{kT} & \cdots & \mathbf{S}_i^{kT} & \cdots & \mathbf{S}_{n_m}^{kT}\end{bmatrix}\\ \Delta\mathbf{y}^{kT}&=\begin{bmatrix}\Delta\mathbf{y}_1^{kT} & \cdots & \Delta\mathbf{y}_i^{kT} & \cdots & \Delta\mathbf{y}_{n_m}^{kT}\end{bmatrix}\end{aligned} \tag{4.4}$$

$$\mathbf{S}_i^k=\begin{bmatrix}\frac{\partial\mathbf{y}_i^k(t_1)}{\partial\theta_1} & \frac{\partial\mathbf{y}_i^k(t_1)}{\partial\theta_2} & \cdots & \frac{\partial\mathbf{y}_i^k(t_1)}{\partial\theta_{n_e}}\\ \vdots & \vdots & & \vdots\\ \frac{\partial\mathbf{y}_i^k(t_j)}{\partial\theta_1} & \frac{\partial\mathbf{y}_i^k(t_j)}{\partial\theta_2} & \cdots & \frac{\partial\mathbf{y}_i^k(t_j)}{\partial\theta_{n_e}}\\ \vdots & \vdots & & \vdots\\ \frac{\partial\mathbf{y}_i^k(t_{n_s})}{\partial\theta_1} & \frac{\partial\mathbf{y}_i^k(t_{n_s})}{\partial\theta_2} & \cdots & \frac{\partial\mathbf{y}_i^k(t_{n_s})}{\partial\theta_{n_e}}\end{bmatrix},\Delta\mathbf{y}_i^k=\begin{bmatrix}\mathbf{y}_{d,i}(t_1)-\mathbf{y}_{a,i}^k(t_1)\\ \vdots\\ \mathbf{y}_{d,i}(t_i)-\mathbf{y}_{a,i}^k(t_i)\\ \vdots\\ \mathbf{y}_{d,i}(t_{n_s})-\mathbf{y}_{a,i}^k(t_{n_s})\end{bmatrix} \tag{4.5}$$

in which the entries are expressed as Eq.(4.5).

The flowchart of the damage identification procedure is shown in Figure 4.1. If the

following convergence criterion is met, iteration could be finished.

$$\left\|\Delta\boldsymbol{\theta}^k\right\| \Big/ \left\|\boldsymbol{\theta}^k\right\| \le Tol \tag{4.6}$$

4.3 Regularization Techniques

In practical applications, some modeling uncertainties, environmental influences, and measurement noise can make Eq. (4.2) difficult to solve directly. Another difficulty exists that due to budgetary constraints, the number of available sensors that can be utilized is relatively small, may even less than the number of damage parameter. All of these issues make Eq. (4.2) an ill-posed equation, in which some singular values of the inverse of sensitivity matrix $\mathbf{S}^k$ are close to zeros and an arbitrary slight perturbation in the right-hand-side (RHS) of Eq. (4.2) can lead to unrealistic and enormous deviation in the solution. The least square solution of Eq. (4.2) is expressed as:

$$\Delta\boldsymbol{\theta} = \left(\mathbf{S}^T\mathbf{S}\right)^{-1}\mathbf{S}^T\Delta\mathbf{y} \tag{4.7}$$

It is noted that the subscript j is omitted here for simplicity. Perform singular value decomposition on the sensitivity matrix $\mathbf{S} \in \Re^{n_m \times n_e}$ as:

$$\mathbf{S} = \mathbf{U}\boldsymbol{\Sigma}\mathbf{V}^T = \sum_{k=1}^{r}\mathbf{u}_k^T\sigma_k\mathbf{v}_k \tag{4.8}$$

where $\mathbf{U} = \left[\mathbf{u}_1, \mathbf{u}_2, \cdots, \mathbf{u}_{n_m}\right]$ and $\mathbf{V}^T = \left[\mathbf{v}_1, \mathbf{v}_2, \cdots, \mathbf{v}_{n_e}\right]^T$ are the left and right singular vectors. $\boldsymbol{\Sigma} = diag\left(\left[\sigma_1, \sigma_2, \cdots, \sigma_r\right]\right)$ is the singular value vector in which the elements are arranged in non-increasing order, i.e., $\sigma_1 \ge \sigma_2 \ge \cdots \ge \sigma_r$. Then the least square

solution is expressed as

$$\Delta\hat{\boldsymbol{\theta}} = \sum_{k=1}^{r} \frac{\mathbf{u}_i^T \Delta\mathbf{y}}{\sigma_k} \mathbf{v}_k \tag{4.9}$$

Common for all discrete ill-posed problems is that the matrix $\mathbf{S}$ has a cluster of singular values at zero. Then any certain noise in the right-hand-side of Eq. (4.7) will probably introduce tremendous error in the solution since the noise could be greatly amplified by the near-zero singular value. Regularization, which refers a process of introducing additional constraints, is often needed to obtain a stable and meaningful solution of such problems. A well-established regularization method, which has been extensively used in damage detection, is the so-called Tikhonov regularization (Tikhonov, 1977). For the sake of comparison, Tikhonov regularization is briefly introduced in next section, followed by the adaptation motivation and detailed introduction of sparse regularization.

4.3.1 Tikhonov Regularization

After introduced independently by Tikhonov (Tikhonov, 1977) almost half a century ago, Tikhonov regularization has been extensively analyzed and used for the solution of discrete ill-posed problems. Tikhonov regularization in its simplest form replaces the linear problem Eq. (4.2) by the following optimization problem:

$$\Delta\hat{\boldsymbol{\theta}} = \underset{\Delta\boldsymbol{\theta}\in\Re}{\operatorname{argmin}} \left(\left\| \mathbf{S}\Delta\boldsymbol{\theta} - \Delta\mathbf{y} \right\|_2^2 + \lambda^2 \left\| \Delta\boldsymbol{\theta} \right\|_2^2 \right) \tag{4.10}$$

where $\lambda^2 \geq 0$ is a regularization parameter to be chosen. It balances the trade-off

between the norm of residual and the norm of the solution. An explicit solution, denoted by $\Delta\hat{\boldsymbol{\theta}}$, is given by

$$\Delta\hat{\boldsymbol{\theta}} = \left(\mathbf{S}\mathbf{S}^T + \lambda^2\mathbf{I}\right)^{-1}\mathbf{S}^T\Delta\mathbf{y} \tag{4.11}$$

It can be observed that the estimated vector $\Delta\hat{\boldsymbol{\theta}}$ converges to the solution obtained from the least-squares method as the parameter λ^2 approaches zero. Using Eq.(4.8), the regularized solution is thus given by

$$\Delta\hat{\boldsymbol{\theta}} = \mathbf{V}\left(\boldsymbol{\Sigma}^2 + \lambda^2\mathbf{I}\right)^{-1}\boldsymbol{\Sigma}\mathbf{U}^T\Delta\mathbf{y} = \sum_{k=1}^{r}\frac{\sigma_k^2}{\sigma_k^2+\lambda^2}\frac{\mathbf{u}_k^T\boldsymbol{\Delta}\mathbf{y}}{\sigma_k}\mathbf{v}_k \tag{4.12}$$

We can see that $\sigma_k^2/\left(\sigma_k^2+\lambda^2\right)$ can be viewed as a filtering factor, which suppresses the solution terms corresponding to the small singular values and makes the solution insensitive to disturbances. By letting $\lambda^2 = 0$, Eq. (4.12) reduces to the unregularized least-squares solution as Eq.(4.9) in which the filter factors are the unit for all singular values. Using the orthogonality condition of singular vectors, the solution norm is

$$\eta(\lambda) = \left\|\Delta\hat{\boldsymbol{\theta}}\right\|_2^2 = \sum_{k=1}^{r}\left(\frac{\sigma_k^2}{\sigma_k^2+\lambda^2}\frac{\mathbf{u}_k^T\boldsymbol{\Delta}\mathbf{y}}{\sigma_k}\right)^2 \tag{4.13}$$

This quantity represents the smoothness of the solution. The residual norm can be expressed as

$$\rho(\lambda) = \left\|\mathbf{S}\Delta\hat{\boldsymbol{\theta}} - \Delta\mathbf{y}\right\|_2^2 = \sum_{k=1}^{r}\left(\frac{\lambda^2}{\sigma_k^2+\lambda^2}\frac{\mathbf{u}_k^T\boldsymbol{\Delta}\mathbf{y}}{\sigma_k}\right)^2 \tag{4.14}$$

The regularization parameter which balances the trade-off between the solution norm $\eta(\lambda)$ and the residual norm $\rho(\lambda)$ should be chosen properly. The optimal regularization parameter λ is usually unknown and often determined by an *ad hoc* method in practical problems. The L-curve criterion (Hansen, 1998), the discrepancy principle (Morozov, 1984) and the general cross-validation (GCV) (Golub et al., 1979) are popular techniques for the selection of the regularization parameter. In the following studies, the L-curve criterion will be employed due to its easy implementation. The L-curve is a plot in log–log scale of the corresponding values of the residual norm $\rho(\lambda)$ and solution norm $\eta(\lambda)$ as a function of the regularization parameter λ. The corner of the L-curve, where the curvature has a maximum value, approximately indicates an optimal regularization parameter.

4.3.2 Sparse Regularization

Sparsity refers to that only very few entries in a vector are non-zero. Recently, sparsity constraints are increasingly applied to regularize inverse problems in the field of applied mathematics (Bruckstein et al., 2009; Ghosh et al., 2009). In the context of detecting the incipient and isolated damage to the structures, damage solution bears the sparse properties since usually only part of elements or substructures of the whole structure are damaged. A more accurate solution is probably provided in such an inverse problem if this sparse property of the solution is properly exploited (Bao et al., 2012; Hernandez et al., 2014). If the sparsity restriction is imposed to the solution, the regularization term in Eq. (4.10) should be changed as

$$\Delta\hat{\boldsymbol{\theta}} = \underset{\Delta\boldsymbol{\theta}\in\Re}{\operatorname{argmin}}\left(\left\|\mathbf{S}\Delta\boldsymbol{\theta} - \Delta\mathbf{y}\right\|_2^2 + \lambda\left\|\Delta\boldsymbol{\theta}\right\|_p^p\right) \tag{4.15}$$

where $\|\mathbf{x}\|_p = \sqrt[p]{\sum |x|^p}$ is the *p*-norm of the vector $\mathbf{x}$. Mathematically, the regularization norms $\|\Delta\boldsymbol{\theta}\|_p^p$ with $0 \le p \le 1$ all can enforce sparsity in solution $\Delta\hat{\boldsymbol{\theta}}$ (Candes et al., 2008). From Figure 4.2, we can see that as *p* approaches zero, $\|x_k\|_p^p$ approaches the indicator function which is 1 for nonzero x_k and 0 for zero x_k, so that $\lim_{p\to 0}\|\mathbf{x}\|_p = \|\mathbf{x}\|_0$ counts the number of nonzero entries in $\mathbf{x}$. It also gives some motivation for why the choice $0 \le p \le 1$ in the penalty $\|\Delta\boldsymbol{\theta}\|_p^p$ leads to sparser solutions. When *p*=0, ℓ_0-norm regularization is an NP-hard problem. Solving the ℓ_0-norm problem is more difficult due to its strong no-convexity. It can be theoretically proved that ℓ_1-norm minimization is equivalent to ℓ_0-norm minimization on signal recovery if the restricted isometric property (Candes and Tao, 2006; Donoho, 2006) is satisfied.

Due to the non-smoothness of the regularization norms $\|\Delta\boldsymbol{\theta}\|_p^p$ ($0 \le p \le 1$), methods capable of handling the non-smoothness are necessary for computing minimizers involving these norms. Here we specify the sparse regularization as ℓ_1-norm regularization, i.e., $p = 1$ in Eq.(4.15). The main reason is that although the ℓ_1-norm is weaker than the $p < 1$ norm in ensuring sparsity (as shown in Figure 4.1). ℓ_1-norm regularized optimization is a convex problem and admits efficient solution via linear programming techniques (Malioutov, 2003; Boyd et al., 2004). Then Eq. (4.15) is solved in a sparse regularization strategy as Eq. (4.16) as:

$$\Delta\hat{\boldsymbol{\theta}} = \underset{\Delta\boldsymbol{\theta}\in\Re}{\operatorname{argmin}}\left(\left\|\mathbf{S}\Delta\boldsymbol{\theta} - \Delta\mathbf{y}\right\|_2^2 + \mu\left\|\Delta\boldsymbol{\theta}\right\|_1\right) \tag{4.16}$$

in which the term $\left\|\mathbf{S}\Delta\boldsymbol{\theta} - \Delta\mathbf{y}\right\|_2^2$ forces the residual to be small, whereas the term $\left\|\Delta\boldsymbol{\theta}\right\|_1$ enforces sparsity of the solution. The parameter $\mu > 0$ controls the tradeoff between the sparsity of the solution and the residual norm. Physically, the damage parameter should be constrained as $-1 \le \theta_j \le 0$ ($j = 1, 2, \cdots, N_e$). If the constraint is imposed to Eq.(4.15), the problem is formed as sparse regularization with constraint.

Care must be taken to choose the right proper regularization parameter to come up with an acceptable solution. Sometimes we must do multiple runs to determine the right penalty parameter. However, this difficulty can be relieved by using a re-weighting strategy as explained in next section. It can be proved that ℓ_1 norm minimization is sparseness promoting (Santosa *et al.*, 1986). For an intuitive explanation of why the ℓ_1 norm is sparseness promoting, a two-dimensional example that compares the ℓ_1 norm and ℓ_2 norm solution is presented in Figure 4.3. In Figure 4.3, we notice that the ℓ_1 norm solution has a zero entry in the intersection point while the ℓ_1 norm solution has two nonzero entries. There are much more opportunities for the components of the solution to be zero subject to the ℓ_1 constraint, or in other words, the ℓ_1 norm regularization induces sparsity by having a discontinuous gradient at zero. Actually, the regularization term in ℓ_2 norm and ℓ_1 norm regularization is the following respectively.

$$\left\|\Delta\boldsymbol{\theta}\right\|_2^2 = \sum_{k=1}^{N_e} \Delta\theta_k^2 \tag{4.17}$$

$$\left\|\Delta\boldsymbol{\theta}\right\|_1^1 = \sum_{k=1}^{N_e}\left|\Delta\theta_k\right| = \sum_{k=1}^{N_e} w_k \Delta\theta_k^2 \tag{4.18}$$

$$w_k = \begin{cases} \dfrac{1}{\left|\Delta\theta_k\right|}, \left|\Delta\theta_k\right| \neq 0 \\ \infty, \left|\Delta\theta_k\right| = 0 \end{cases} \tag{4.19}$$

where N_e is the dimension of $\Delta\boldsymbol{\theta}$. Comparing Eq. (4.17) and (4.19), it is found that in ℓ_2 norm regularization every entry of $\Delta\boldsymbol{\theta}$ weights equally while in ℓ_1 norm regularization every entry of $\Delta\boldsymbol{\theta}$ weights inversely proportion to the solution amplitude. In other words, small entries in the solution weight heavily, which is the reason why ℓ_1 norm regularization promotes sparsity. This observation suggests more generally that large weights could be used to encourage zero entries in the solution, while small weights could be used to promote nonzero entries. Basing on this, reweighted ℓ_1 norm minimization was proposed to enhance the sparsity in reference recently (Candes *et al.*, 2008; Friedlande *et al.*, 2012). It is modified and adopted in this study as follows:

1. For the initial reweighting iteration, the iteration count and initial weighting factors are set as $n = 0$ and $w_i^0 = 1,\ i = 1,\cdots,N_e$.

2. The formed weighted ℓ_1 norm regularization problem $\Delta\hat{\boldsymbol{\theta}}^n =$

   $\underset{\Delta\boldsymbol{\theta}\in\Re}{\operatorname{argmin}}\left(\left\|\mathbf{S}\Delta\boldsymbol{\theta} - \Delta\mathbf{y}\right\|_2^2 + \sum_{k=1}^{N_e} w_k^n\left|\Delta\theta_k\right|\right)$ is solved.

3. Update the weights as Eq. (4.20) and solve

   $\Delta\hat{\boldsymbol{\theta}}^{n+1} = \underset{\Delta\boldsymbol{\theta}\in\Re}{\operatorname{argmin}}\left(\left\|\mathbf{S}\Delta\boldsymbol{\theta} - \Delta\mathbf{y}\right\|_2^2 + \sum_{k=1}^{N_e} w_k^{n+1}\left|\Delta\theta_k\right|\right)$

$$w_k^{n+1} = \frac{1}{\left|\Delta\theta_k^n\right| + \varepsilon} \tag{4.20}$$

4. The reweight iteration terminates on the convergence $\left\|\Delta\hat{\boldsymbol{\theta}}^{n+1} - \Delta\hat{\boldsymbol{\theta}}^{n}\right\| \le Tor$ or when n reaches a preset maximum iteration number n_{max}. Otherwise, set $n = n+1$ and go to step 2.

In Eq. (4.20) $\varepsilon > 0$ is introduced to provide stability and to ensure that zero-valued entries in $\Delta\boldsymbol{\theta}^n$ do not strictly prohibit a nonzero estimate at the next step. Simulation results show that the solution $\Delta\hat{\boldsymbol{\theta}}$ is reasonably robust to the choice of ε. It is set as $\varepsilon = 0.001$ and $n_{max} = 3$ in this study. The iterative strategy to determine the weights $\mathbf{W}$ tends to permit better estimation of the nonzero entry locations successively. Even if the inaccurate solution is obtained in the early iterations, the largest entries in the solution are most likely to be identified as nonzero. These locations are then down-weighted to pass weights to the remaining small but nonzero entries once they are identified in the early iterations. In this regard, the difficulty to choose the proper regularization parameter λ is alleviated as nonzero entries of the solution can still successively identified in re-weighting sparse regularization even when the regularization parameter λ is roughly selected.

In contrast to Tikhonov regularization problem in Eq. (4.10) , which has an explicit solution and can be readily solved in the orthonormal basis associated with the singular value decomposition (Hansen,1998), the sparse regularization in Eq. (4.16) has no closed form solution and its solving procedure should be paid special attention to. There are a number of solvers with strong theoretical guarantees that are available

to solve the problem (Tibshirani, 1996; Beck *et al.*, 2009; Yun *et al.*, 2011). The primal-dual interior point algorithm proposed by Boyd (2004) is employed in this study.

4.4 Numerical Studies

Most common types of damage on civil structures are stiffness reduction due to steel corrosion or extensive concrete cracking, thus stiffness damage can be modeled as Eq.(4.21), while inertial properties are assumed unchanged before and after damage occurrence.

$$\mathbf{K}_d(\boldsymbol{\theta}) = \mathbf{K}_u + \sum_{i=1}^{N_e} \theta_i \mathbf{K}_i, (-1 \le \theta_i \le 0) \tag{4.21}$$

in which $\mathbf{K}_u$ is the global stiffness matrix of the structure under the intact state; $\mathbf{K}_i$ is i-th element stiffness in the global coordinates and θ_i is the fractional stiffness damage parameter of $\mathbf{K}_i$. The *i*-th element is undamaged when $\theta_i = 0$ and the stiffness of the *i*-th element is completely lost when $\theta_i = -1$. N_e is the number of the elements. It should be pointed out that damage identification solution bears sparsity property when damage is modeled in such a way that damage-free corresponds the zero while damage-existence corresponds to nonzero in damage parameter. For example, if the damage in Eq. (4.21)is modeled as $\mathbf{K}_d = \sum_{i=1}^{N_e} \theta_i \mathbf{K}_i$, where θ_i should be $0 \le \theta_i \le 1$ for physical meaning, the solution of damage is then not sparse. However, it is very easy to transfer damage vector to be sparse if the baseline (damage-free) is set as zero.

We will exam two types of structures in this section; the first one is a 25 degree of freedom (DOFs) planar truss and the second one is an overhanging beam composed of 40 elements. The convergence criteria are set as $Tol = 2\times10^{-7}$, and the maximal iteration number is 40 in the following simulation section.

4.4.1 A Planer Truss

A planar truss composed of 31 bar elements as shown in Figure 4.4 serves as the first numerical case study. The section dimension is $b\times h = 0.05\,\mathrm{m}\times 0.05\,\mathrm{m}$ with the elastic modulus of $E = 70\,\mathrm{GPa}$ and the density of $\rho = 2770\ \mathrm{Kg/m^3}$. The length is $1.52\,\mathrm{m}$ for vertical and horizontal components and $2.15\,\mathrm{m}$ for diagonal bars. It is simply supported on the two ends (node 1 and node 7), forming 25 effective DOFs. The first 24 mode frequencies are shown in Table 4.1.

A stochastic force sequence is applied on node 12 vertically and node 14 horizontally simultaneously. Rayleigh damping model is adopted here and defined as $\mathbf{C} = \alpha\mathbf{M} + \beta\mathbf{K}$, in which α and β are the mass and the stiffness proportional Rayleigh damping coefficient, respectively. The first two modal damping ratios are set as $\xi_1 = \xi_2 = 0.01$ in this study. The sampling frequency is 2000 Hz with a duration length of 5s. The dynamic response is numerically simulated with First-Order-Hold state space formulation. To include noise corruption, normally distributed random noise is added to the response as

$$\mathbf{y}^n = \mathbf{y}^r + R_{std}\cdot std\left(\mathbf{y}^r\right)\cdot\mathbf{e} \tag{4.22}$$

where $\mathbf{y}^n$ and $\mathbf{y}^r$ are the noise polluted response and pollution-free response , respectively; R_{std} is the standard deviation ratio of noise and response and it is set as $R_{std} = 0.05$ in this study; $\mathbf{e}$ is a standard normal distribution vector with zero mean and unit standard deviation. The vertical acceleration of node 8 and horizontal acceleration of node 12 are utilized in the following damage identification.

4.4.1.1 Single-damage scenario

Single damage is simulated as 10% reduction of elastic modulus on element 3. Figure 4.5-a illustrates the result of response sensitivity based damage identification using Tikhonov regularization. It is found that although the damage on the element is roughly identified, there are considerable false-positive errors on some elements, such as element 5, 11, 25 and element 26. When using sparse regularization, the single-damage is identified remarkably accurate (as shown in Figure 4.5-b), only approximately 3% errors occur on element 5 and element 11. If the constraint $\left(-1 \le \theta_i \le 0\right)$ is set in the iteration process, the damage identification result is shown in Figure 4.5c. We can see that the false-positive error on element 11 is suppressed.

4.4.1.2 Multi-damage scenario

The case that there are 12%, 15% and 10% reduction of elastic modulus on element 3, 8 and 24 respectively is designed to serve as a multi-damage scenario of the truss. The result of Tikhonov regularized damage identification is given in Figure 4.6-a. It is noticed that there are significant false-positive errors on some elements, and damage on element 24 even cannot be localized exactly. A remarkable improvement is

observed when using sparse regularization (shown in Figure 4.6-b), as all the three damages are identified almost exactly, although about 2% errors exist on quantifying the damage severity/ extent of element 8 and 24. If the additional constraint $\left(-1 \le \theta_i \le 0\right)$ is imposed to the updating, the sparsity of the solution increases (shown in Figure 4.6-c). However, a slight decade in damage quantification is also noticed. The possible reason is that the fractional damage parameter is constrained as $-1 \le \Delta\boldsymbol{\theta} \le 0$ in each updating rather than constraining $\boldsymbol{\theta}$. Besides, the iteration number may be different for with and without constraint cases even with the same convergence criterion. So although the sparse regularization with constraint can remove the positive errors, it may distort damage quantification to some extent.

4.4.2 An Overhanging Beam

A simply supported overhanging steel beam (shown in Figure 4.7) corresponding to the testbed in the laboratory is adopted as the second numerical case study. The length of the beam is $L = 4\,\text{m}$ and its cross-sectional area is $b \times h = 50 \times 15.65\,\text{mm}$. It is modeled by 40 Euler beam elements with 41 nodes and a total of 123 DOFs. The beam is constrained by a hinge support on the node 11 and a roller support on the node 31. The physical parameters of the FE model can be found in Chapter 3.

A broadband stochastic excitation with a standard deviation of 6.4 N is applied on node 18 vertically. Its frequency bandwidth ranges from 2 Hz to 302 Hz. The mass and the stiffness proportional Rayleigh damping coefficient are determined with the first two modal damping ratios as $\xi_1 = 0.010$ and $\xi_2 = 0.008$ according to the laboratory modal test result. Sample frequency is 1250Hz, and the sample duration is 8s. The

dynamic response is numerically simulated with FOH state space formulation. Noise corruption is simulated as normally distributed random noise adding to the noise-free response; the noise amplitude is set as $0.04\ \mathrm{m/s^2}$ for acceleration, yielding an approximate 6% standard deviation ratio of response and noise. The vertical accelerations of 6 nodes as shown in Figure 4.7 are captured and utilized for damage identification in next section.

4.4.2.1 Single-damage scenario

Single-damage of the beam is simulated as 20% reduction of elastic modulus on element 23. Figure 4.8a gives the result of response sensitivity based damage identification using Tikhonov regularization. It is found that although the damage on the element is roughly identified, there are considerable false-positive errors on a large number of elements. If sparsity constraint is set in solution, the single-damage is identified remarkably accurate (as shown in Figure 4.8b), as the damage extent on element 23 is identified as -19.65% while the pre-set damage is -20%. Comparing the two, we can conclude that Tikhonov regularization yields non-sparse solutions, while sparse regularization has the advantage of promoting a sparse solution.

4.4.2.2 Multi-damage scenario

Multi-damage of the beam is simulated as 10% and 20% reduction of elastic modulus on element 7 and element 23 respectively. To show the variations of damage parameter in whole updating procedure, the evolutions of damage parameter along with iterations are illustrated in Figure 4.9. It is seen that that for the case of Tikhonov regularization,

the damage parameter begins from zero values corresponding to damage free condition and converge to a fixed value after 16 iterations; the updating procedure stops as the preset convergence criteria are met. However, there are remarkable errors as many near zero entries in the final identification. Contrarily, the damage parameters obtained from sparse regularization almost converge to the true value after only 5 iterations. As already pointed out, the existence of closed form solution of Tikhonov regularization allows its solutions to be calculated computationally efficiently. However, much less iterations can drive sparse regularization convergence, thus generally sparse regularized model updating is more computationally efficient than Tikhonov regularization. This result evidences the superiority of the sparse regularization over the Tikhonov in terms of not only identification accuracy but also computational consumption. The final results of the two cases are presented in Figure 4.10. As shown in Figure 4.10-a, Tikhonov regularized damage identification generates an incorrect non-sparse solution. Besides many false-positive errors in many elements, there is even a false-negative error (no indication of damage when it is present) that the existence of damage on element 7 is not detected. A noteworthy improvement is observed when using sparse regularization (shown in Figure 4.10-b), as the damages on elements 7 and 23 are both identified almost exactly, although less than 2% errors exist on quantifying the damage extent. The simulation case of overhanging beam further exhibits that sparse regularization can prevent the solution from spreading out and provide a more accurate solution.

4.5 Concluding Remarks

To handle the ill-posedness problem in structural damage identification, sparse

regularization is adopted in the context of response sensitivity based model updating for damage identification. This idea corresponds to minimizing discrepancy between the analytical and tested response as well as keeping the number of non-zero entries in solution as small as possible in order to describe the solution accurately. The sparsity promoting property of ℓ_1 norm regularization, contrary to the Tikhonov regularization is emphasized, and the re-weighted sparse regularization is employed to enhance the sparsity of solution as well as alleviate the difficulty in choosing regularization parameter. Comparative simulation studies of a planar truss and an overhanging beam show that the proposed sparse regularization is superior to the traditional Tikhonov regularization in terms of identification accuracy as well as computational efficiency when using the noise-corrupted response from a small number of sensors. Basing on the studies, some concluding remarks are given as follows:

(1) The traditional Tikhonov regularization constrains the norm of the solution to be small while the sparse regularization not only constrains the solution norm but also promotes the sparseness of the solution, i.e. keeping the number of nonzero entries in the solution as small as possible. This motivation is consistent with the fact of incipient damage. Thus a better damage identification result is obtained using the sparse regularization under the same conditions.

(2) An explicit solution exists for Tikhonov regularization; thus it is easier to be implemented for computation. Although several methods have been proposed for solving the sparse regularization, solving the problem is still not a

straightforward task. However, according to the studies, sparse regularization is found to exhibit a quicker convergence in the FE model updating iterations for damage identification.

(3) Although the *p*-norm ($0 \le p < 1$) constraint promotes more sparsity, ℓ_1 norm regularization ($p = 1$) is adopted in this study. The main reason is that ℓ_1 norm regularized optimization is a convex problem and admits efficient solution via linear programming techniques.

(4) The regularizing parameter which balances the trade-off between the residual norm and the solution norm should be chosen properly. For Tikhonov regularization, several well-known methods like L-curve method or GCV are available in determining the regularization parameter. For the sparse regularization, although GCV can be also used, to select a reliable regularization parameter is not a straightforward task. Fortunately, the solution to the ℓ_1 norm regularization is not so sensitive to the regularization parameter. Additionally, the re-weighted strategy could also be adopted to alleviate the difficulty in choosing regularization parameter.

Thus, this sparse regularization, which provides more accurate results for solving the inverse problem of damage identification, will be employed in the forthcoming damage identification via response reconstruction in Chapter 5-6 and multi-level damage identification in Chapter 8, based on the works presented in Chapter3. The

corresponding experimental studies on the overhanging beam to assess the performance of the sparse regularization will be presented in Chapter 7.

Table 4.1 First 24 mode frequencies of the truss

Mode	Freq (Hz)	Mode	Freq (Hz)
1	36.43	13	570.52
2	76.10	14	576.94
3	133.82	15	604.16
4	223.39	16	654.32
5	250.19	17	700.81
6	359.37	18	724.81
7	372.88	19	727.25
8	443.57	20	742.43
9	478.43	21	753.25
10	508.03	22	757.09
11	538.52	23	802.06
12	547.43	24	936.42

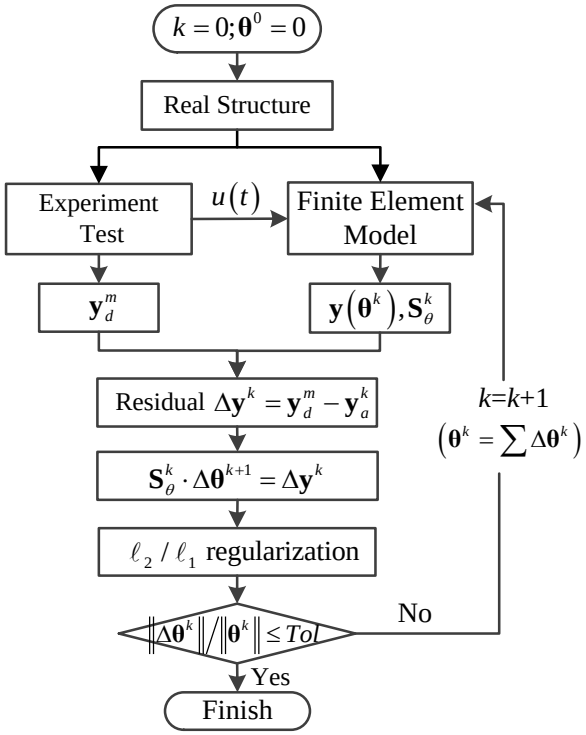

Figure 4.1 Flowchart of the damage identification procedure

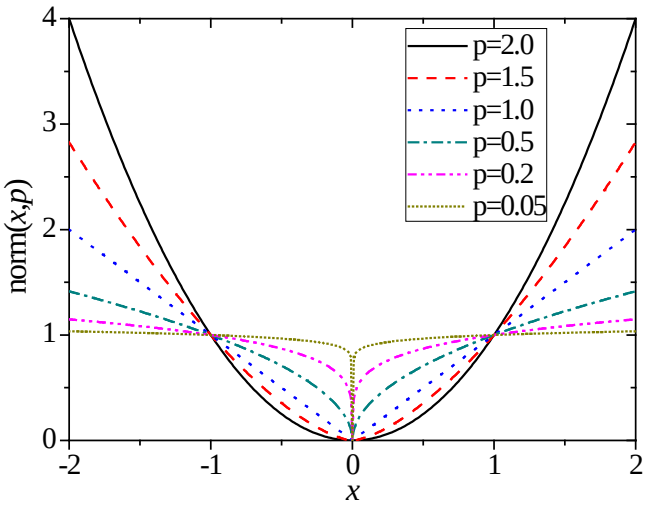

Figure 4.2 $\|x\|_p^p$ plotted for different p values.

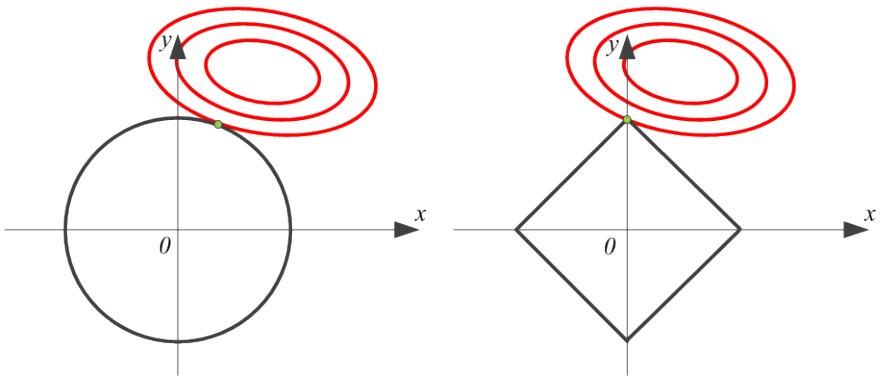

Figure 4.3 Illustration of ℓ_2 (left) and ℓ_1 minimization (right) in $\Re^2$

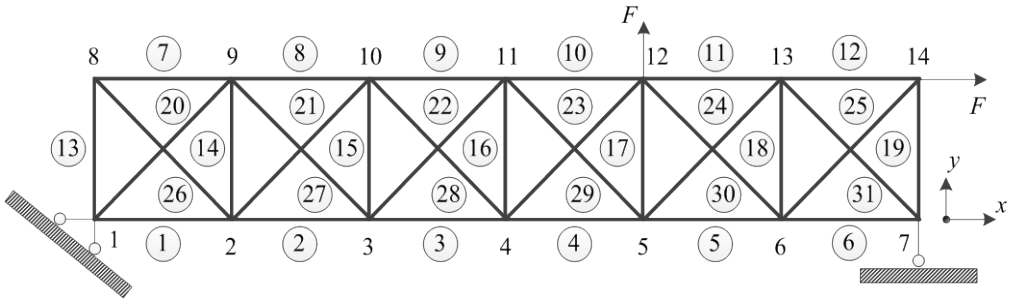

Figure 4.4 Geometric configuration of a planar truss

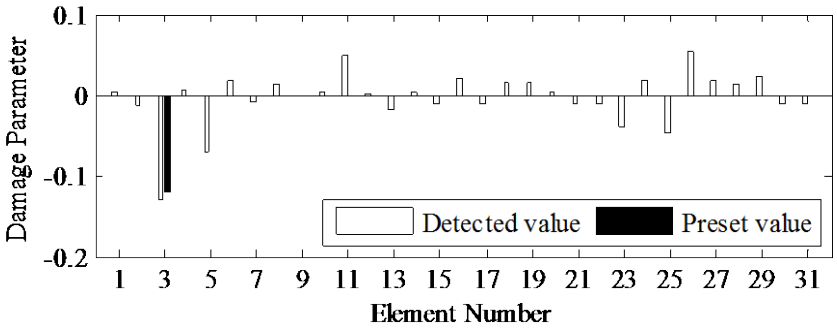

(a)

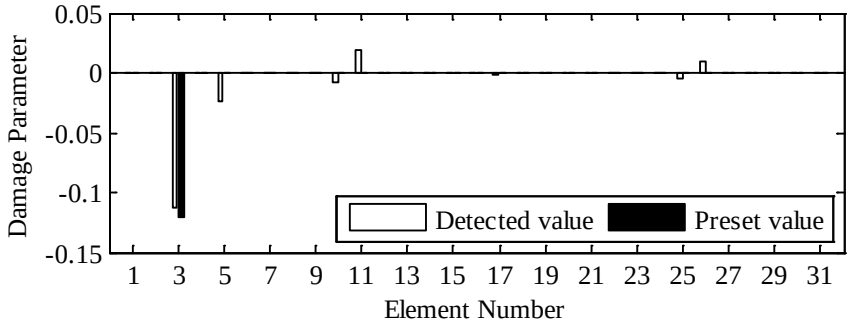

(b)

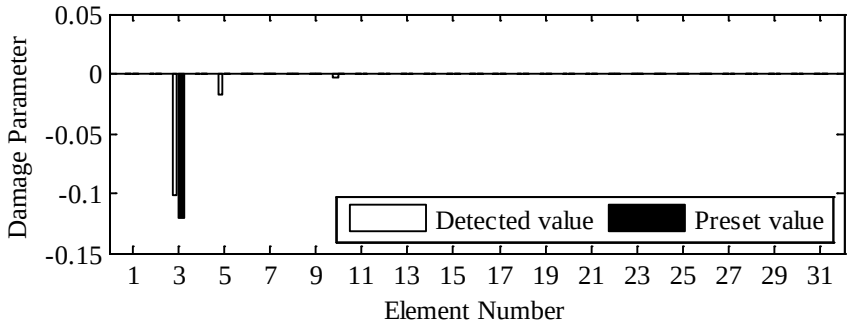

(c)

Figure 4.5 Single-damage identification of a truss using (a) Tikhonov regularization, (b) sparse regularization and (c) using sparse regularization with constraint.

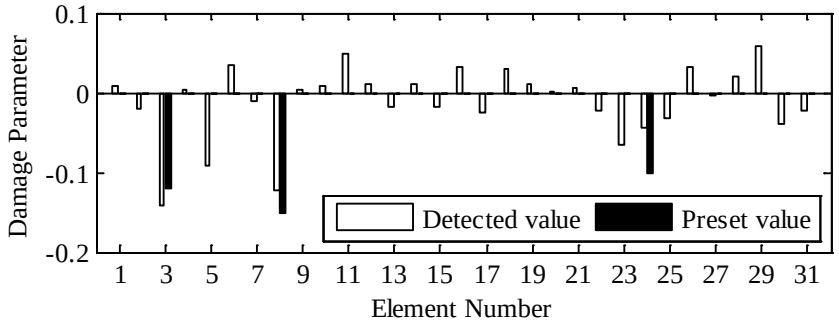

(a)

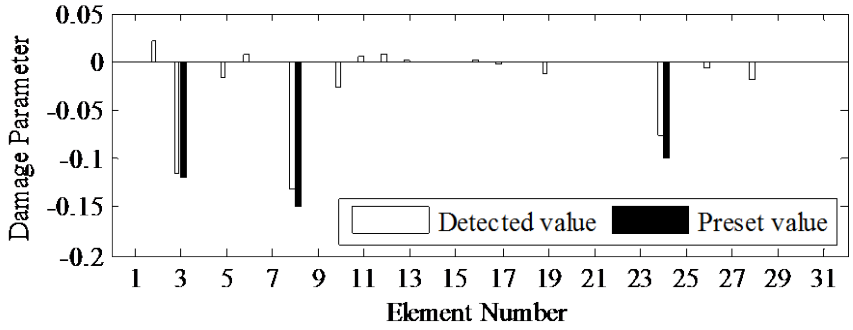

(b)

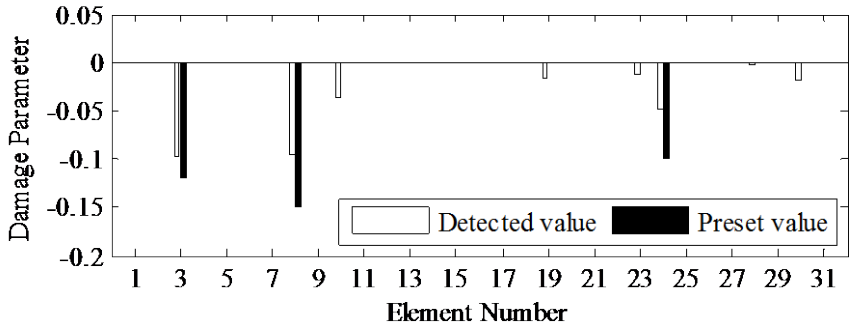

(c)

Figure 4.6 Multi-damage identification of a truss using (a) Tikhonov regularization, (b) sparse regularization and (c) using sparse regularization with constraint.

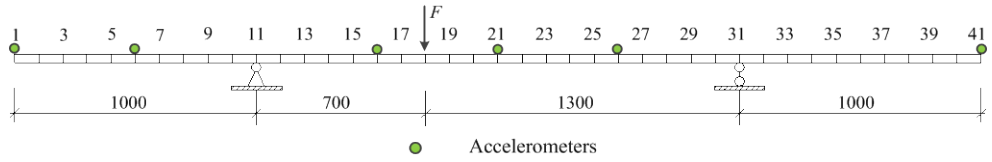

Figure 4.7 Geometric configuration of an overhang beam and the spatial deployment of the accelerometers

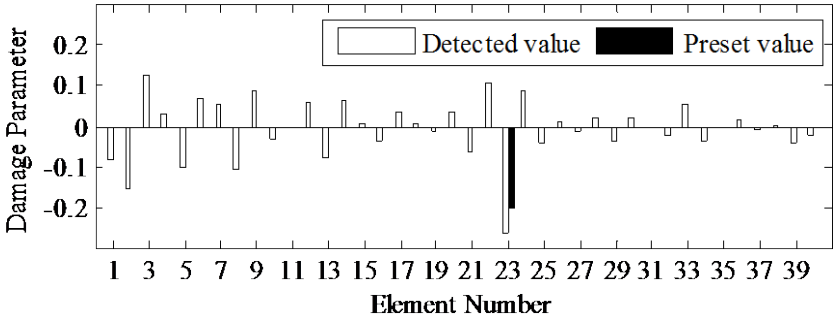

(a)

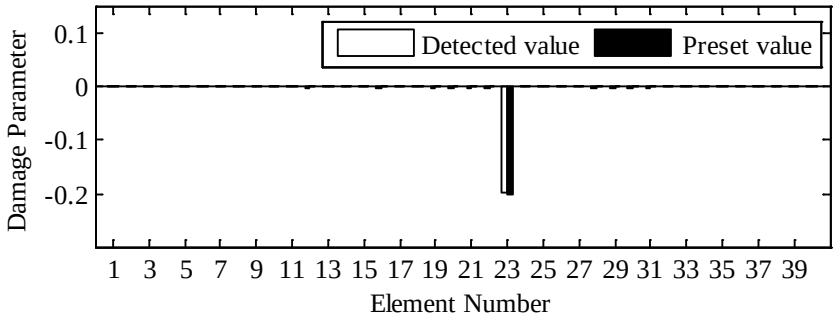

(b)

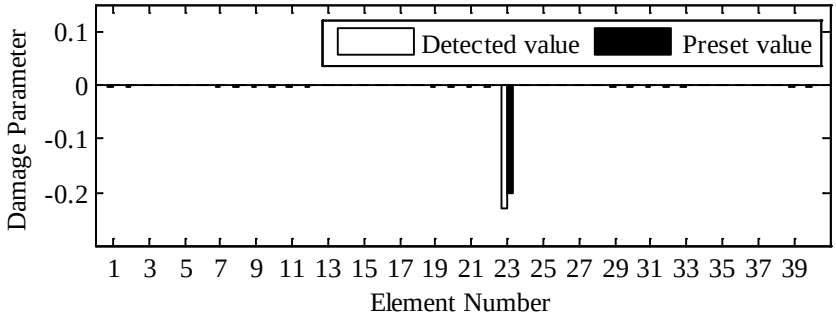

(c)

Figure 4.8 Single damage identification of an overhanging beam using (a) Tikhonov regularization, (b) sparse regularization and (c) sparse regularization with constraint.

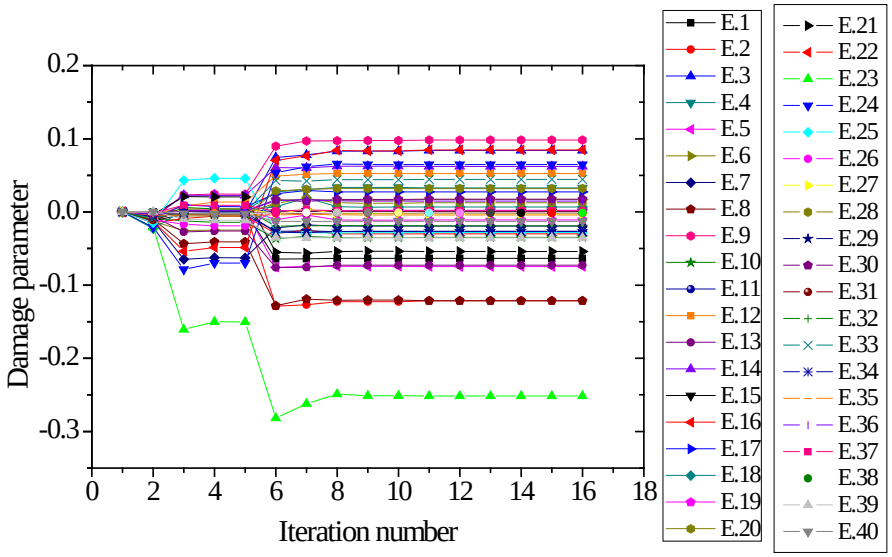

(a)

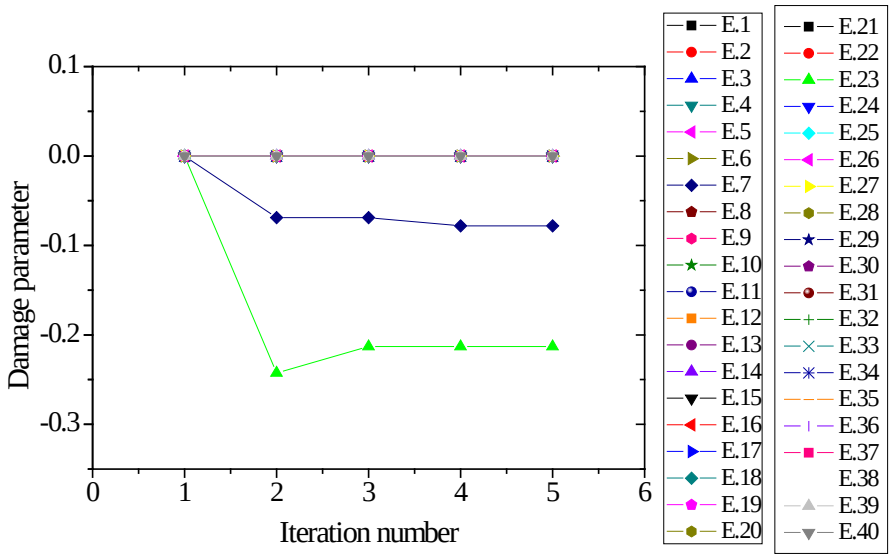

(b)

Figure 4.9 Damage parameter evolutions in iteration using (a) Tikhonov regularization and (b) sparse regularization

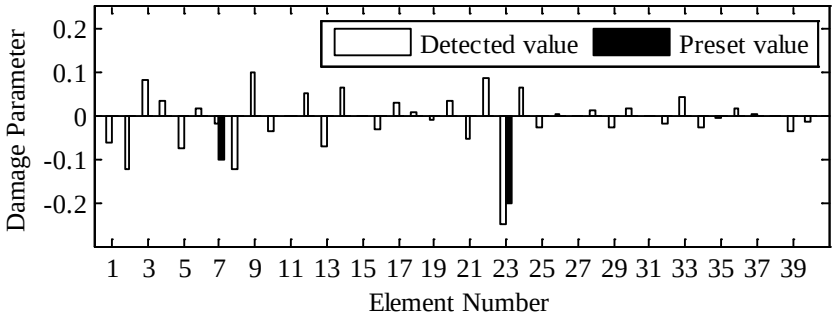

(a)

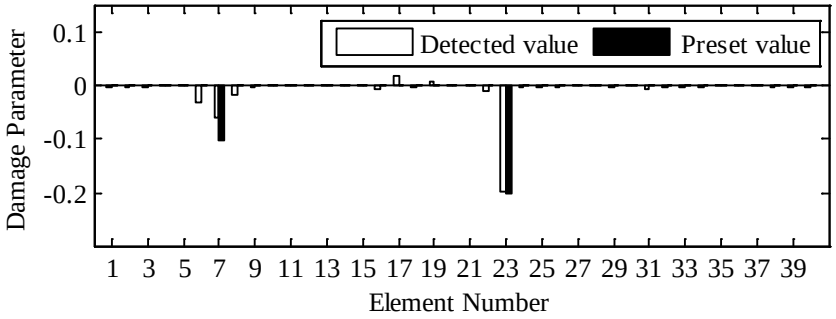

(b)

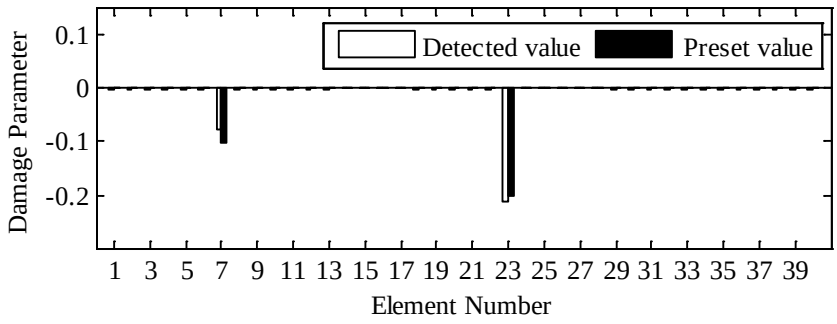

(c)

Figure 4.10 Multi-damage identification of an overhanging beam using (a) Tikhonov regularization, (b) sparse regularization and (c) sparse regularization with constraint.

CHAPTER 5

DAMAGE IDENTIFICATION VIA RESPONSE RECONSTRUCTION UNDER KNOWN EXCITATION

5.1 Introduction

One outstanding obstacle that hinders robust application of FE model updating based damage identification to civil structures is that the point measurements captured by the predefined sensors cannot cover adequately all possible damage location, which is not known *a priori* on a complex civil structure. Kalman filter based response reconstruction and the associated optimal sensor placement method proposed by Zhang (2012) and Xu et al. (2016) are promising in supplementing the limitation of sensor measurements and beneficial to vibration based damage identification of civil structures. Besides, the responses of multi-type sensors are fused together for the best response reconstruction in this method, which is also potentially advantageous to damage identification. Every type of response has its own merits and drawbacks. For instance, acceleration is frequently preferred due to its easy measurement and relatively more kinetic energy on higher vibrational modes. Strain response, regarding as a kind of local response, is also utilized because of its better capacity of indicating local degradation on condition that they are in the vicinity of damage. Displacement, containing more energy in the vibration of low order modes, sometimes can directly indicate the structural integrity (e.g. inter-story displacement

of a high-rise building). These multiple responses, which manifest a large spectral bandwidth, could capture both local and global response features and provide comprehensive information about the structure's condition. But to date, these kinds of dynamic responses are usually utilized individually and little effort has been devoted to exploring the potential benefits of utilizing multi-type response for damage identification.

To explore the potential benefits of response reconstruction and fusion of heterogenous response for damage identification, this chapter presents a novelty damage identification method by combining the response reconstruction technique, which is partially discussed in Chapter 3, with the sparse regularized finite element (FE) model updating, which is fully presented in Chapter 4. The number and location of various sensors, such as accelerometers, displacement transducers, and strain gauges are optimally determined to obtain the best reconstruction of multi-type responses of a structure before damage. After damage occurrence, radial basis function (RBF) network is employed to predict the mode shapes using the modal properties extracted from the measurement data by experimental modal analysis (EMA), and these modal properties are further used to reconstruct responses of the damaged structure. The reconstructed responses are finally used to identify the damage in terms of sensitivity-based FE model updating. In every updating, the sparse regularization is employed to increase the identification accuracy. The same simply supported overhanging steel beam composed of 40 elements and used in the previous two chapters serves as a numerical study to demonstrate the procedure and feasibility of the proposed method.

5.2 Kalman Filter Based Response Reconstruction

One possible solution to alleviating the necessity of deploying dense sensors for local damage identification is to reconstruct the responses of key locations where no sensors are installed using FE model information and limited measurement data. Zhang (2012) and Xu et al. (2016) presented a multi-type sensors optimal placement method that aimed to reconstruct multi-type responses best using Kalman filter. As a foundation of the proposed method, it is briefly introduced in this section.

Including model errors and observation noise, the dynamics of a structure can be represented in a discrete-time state space formulation in modal coordinate system as Eq.(5.1), which has been fully introduced in Section 3.2.

$$\mathbf{x}_{k+1} = \mathbf{A}_d \mathbf{x}_k + \mathbf{B}_d \mathbf{u}_k + \mathbf{w}_k \tag{5.1}$$

where $\mathbf{x}_k = \mathbf{x}(k\Delta t) = \left\{ \mathbf{q}_k^r \quad \dot{\mathbf{q}}_k^r \right\}^T \in \Re^{2r}$ is the discrete-time state vector with $k = 0,1,2,\ldots$; Δt is the sampling interval; $\mathbf{w}_k \in \Re^{2r} \sim N(0, \mathbf{Q})$ the normally distributed modeling error with covariance matrices $E\left[\mathbf{w}_p \mathbf{w}_q^T\right] = \mathbf{Q}\delta_{pq}$. Usually, only a part of outputs are measured with limited deployed sensors, and accordingly, the measurement equation can be expressed as

$$\mathbf{y}_k^m = \mathbf{C}_d^m \mathbf{x}_k + \mathbf{D}_d^m \mathbf{u}_k + \mathbf{v}_k^m \tag{5.2}$$

where $\mathbf{y}_k^m$ denotes the measurements at k-th instants and $\mathbf{v}_k \in \Re^{N_m} \sim N(0, \mathbf{R})$ represent the normally distributed measurement noise; $\mathbf{C}_d^m$ and $\mathbf{D}_d^m$ are the associated

measurement matrix and the feedthrough matrix, composed of the strain and displacement mode shapes of the measurement location.

Kalman filter is a recursive data processing algorithm which can obtain an unbiased minimal-variance estimate of the state vector by taking advantages of the system model and measurement information (Kalman, 1960; Zhang, 2012). By setting the initial conditions as $\hat{\mathbf{x}}_1 = \mathbf{x}_0; \mathbf{P}_k^- = \mathbf{P}_0$ Kalman filter is capable of providing an optimal estimate of state vector as:

$$\hat{\mathbf{x}}_k = \left(\mathbf{I} - \mathbf{K}_k \mathbf{C}_d^m\right)\left(\mathbf{A}_d \hat{\mathbf{x}}_k + \mathbf{B}_d \mathbf{u}_{k-1}\right) + \mathbf{K}_k \left(\mathbf{y}_k^m - \mathbf{D}_d^m \mathbf{u}_k\right) \tag{5.3}$$

in which $\mathbf{K}_k$ is the Kalman gain, which is optimally determined as

$$\mathbf{K}_k = \mathbf{P}_k^- \mathbf{C}_d^{mT} \left(\mathbf{C}_d^m \mathbf{P}_k^- \mathbf{C}_d^{mT} + \mathbf{R}_m\right)^{-1} \tag{5.4}$$

where $\mathbf{P}_k^-$ is the priori state error covariance. Then the desired responses of key locations can be reconstructed as:

$$\mathbf{y}_k^e = \mathbf{C}_d^e \hat{\mathbf{x}}_k + \mathbf{D}_d^e \mathbf{u}_k \tag{5.5}$$

in which $\mathbf{C}_d^e$ and $\mathbf{D}_d^e$ are composed of modal shapes corresponding to DOFs of the key location, whose responses are to be reconstructed. The reconstruction error $\boldsymbol{\delta}_k$ and associated covariance matrix are expressed as

$$\boldsymbol{\delta}_k = \left(\mathbf{C}_d^e \hat{\mathbf{x}}_k + \mathbf{D}_d^e \mathbf{u}_k\right) - \left(\mathbf{C}_d^e \mathbf{x}_k + \mathbf{D}_d^e \mathbf{u}_k\right) = \mathbf{C}_d^e \left(\hat{\mathbf{x}}_k - \mathbf{x}_k\right) \tag{5.6}$$

$$\mathbf{\Lambda}_k = E\left[\boldsymbol{\delta}_k \boldsymbol{\delta}_k^T\right] = \mathbf{C}_d^e \mathbf{P}_k^x \mathbf{C}_d^{eT} \tag{5.7}$$

where $\mathbf{P}_k^x$ is the posteriori state error covariance of the state vector at time step k and E denotes the expectation operator. It can be proved that reconstruction error covariance matrix converges to a stable value $\overline{\mathbf{\Lambda}}$, independent of external excitation $\mathbf{u}_k$ when the measurement instants $\mathbf{y}_k^m$ are enough, and the Kalman filter is well-structured. The number and location of sensors are optically designed by selecting the proper measurement output matrix $\mathbf{C}_d^m$ and transmission matrix $\mathbf{D}_d^m$ to obtain the well estimated $\hat{\mathbf{x}}_k$ and then minimize the trace of stable reconstruction error covariance matrix $\overline{\mathbf{\Lambda}}$. The optimal configuration and the number of sensors could be determined when the average reconstruction error approaches a stable value in an optimization procedure.

The limited measured dynamic responses of the structure at intact state are collected through the optimized sensors that are installed on the structure. The FE model of the structure is updated using the measured dynamic response if needed. The precise FE model corresponding to the structure of the intact state is established; it is further used for later damage identification as a reference model.

5.3 RBF Network for Mode Shape Prediction

As mentioned before, the responses from limited sensors installed on a real-world structure may not contain enough information for identifying local damages. An intuitive idea is to reconstruct the responses at the locations that are in the vicinity of

damage. However, it is not straightforward to reconstruct the responses of the structure in the damaged state based on Kalman filter as introduced in the above section. From Eq.(5.1)~Eq.(5.5), we note that the estimation system matrices $\mathbf{A}_d$, $\mathbf{B}_d$, $\mathbf{C}_d^m$ and $\mathbf{D}_d^m$ are composed of modal properties, including frequencies, damping ratios and modal shapes corresponding to the measurement points, which are all possibly extracted from the limited measured data by the EMA. EMA is a procedure whereby the natural frequencies, damping ratios and mode shapes of a linear, time-invariant structural system are derived from experimentally measured response data. Several well-established techniques are reported in the literature to extract modal parameters from measured noise-corrupted response. Subspace identification methods have drawn tremendous research interest and have been widely recognized for its computational efficiency and strong capacity in modal identification. For reconstructing the response of unmeasured positions, the modal shapes of these locations $\mathbf{\Psi}_d^e$ and $\mathbf{\Phi}_d^e$ are needed in the formulation of $\mathbf{C}_d^e$ and $\mathbf{D}_d^e$. Here artificial neural network (ANN) is adopted to estimate the strain and displacement modal shapes of unmeasured places in the damaged state.

5.3.1 RBF Network

ANNs are computational tools inspired by the human biological brain and nervous system functioning, whereby they imitate the parallel and distributed processing nature of the biological neurons to approach a specific problem by using certain rules to achieve favorable results. Usually, a typical ANN structure consists of an input layer, an output layer and at least one hidden layer. The processing elements, namely

neurons, are interconnected with the next layer through their connectivity. Radial-basis-function (RBF) network is a kind of the multi-hidden-layer feedforward network with sigmoid and linear functions as activation (transfer) functions for the neurons in the hidden layers and the output layer, respectively. Park and Sandberg (1991) proved that radial-basis-function (RBF) networks are capable of providing an arbitrarily good approximation to any prescribed function using only a finite number of parameters. A typical RBF network with *i* input and *j* output is shown in Figure 5.1. The output of the network is a function of the input vector and is given by:

$$y_i = f(\mathbf{x}) = \sum_{p=1}^{N_l} \omega_p \psi\left(\left\|\mathbf{x} - \mathbf{c}_p\right\|\right) \tag{5.8}$$

where N_l is the number of neurons in the hidden layer, $\mathbf{c}_p$ is the center vector for neuron *p*, and ω_p is the weight of neuron *p* in the linear output neuron. ψ, termed as RBF, is the function that depends only on the distance from a center vector and radially symmetric about that vector. The output $\mathbf{y}$ is then taken to be a linear combination of the basis functions, which is a function of the input $\mathbf{x}$ and the center vector $\mathbf{c}_p$. Network training is a process to find the weights ω_p and the center vector $\mathbf{c}_p$ such that the function goes through the data points in the training set $\left\{\mathbf{x}^i, \mathbf{y}^i\right\}$.

5.3.2 Mode Shape Prediction with RBF Network

ANNs have found extensive applications, including function approximation, data processing, classification, and system control. Application of ANN for mode shape prediction has been investigated in by Goh *et al.* (2013). The basic idea of ANN

applications in mode shapes prediction is to build a model to establish relationships between modal parameters and mode shapes through a training process. The RBF network is employed in this study to predict displacement and strain mode shapes of the structure in the damaged state due to its easier implementation and fast training. The input of the network is frequencies and mode shapes of the structure in the damaged state, which can be extracted by EMA. To avoid the mass normalization (a scaling procedure to ensure the modal shape matrix mass-normalized as $\mathbf{\Phi}^T\mathbf{M}\mathbf{\Phi}=\mathbf{I}$) in EMA, the coordinate modal assurance criterion (CoMAC) defined below is utilized:

$$CoMAC\left(\mathbf{\Phi}_u^m,\mathbf{\Phi}_d^m\right)=\frac{\left(\mathbf{\Phi}_u^{mT}\cdot\mathbf{\Phi}_d^m\right)^2}{\left(\mathbf{\Phi}_u^{mT}\mathbf{\Phi}_u^m\right)\left(\mathbf{\Phi}_d^{mT}\mathbf{\Phi}_d^m\right)} \tag{5.9}$$

where $\mathbf{\Phi}_u^m$ and $\mathbf{\Phi}_m^d$ are the displacement mode shapes of the structure in damage-free and damaged state at a relatively small number of discrete measurement points, respectively. $CoMAC\left(\mathbf{\Phi}_u^m,\mathbf{\Phi}_d^m\right)$ is a symmetric matrix indicating the spatial comparison of mode shapes before and after damage, and only its lower triangular parts are utilized; when the strain mode shape before damage $\mathbf{\Psi}_u^m$ and after damage $\mathbf{\Psi}_d^m$ are used in Eq. (5.9), it forms the strain CoMAC. In a word, the frequencies, displacement CoMAC and strain CoMAC are imported to the trained RBF network to predict mass-normalized displacement mode shapes $\mathbf{\Phi}_d^e$. Then the strain mode shapes could be predicted as $\mathbf{\Psi}_d^e=\mathbf{B}\mathbf{\Phi}_d^e$.

Although ANNs mimic the mechanism of the brain, they do not have analytical function form, and ANNs should be trained using modal data of sets of damage

scenarios. The appropriate training sets (damage scenarios) are obtained by numerical analysis. For *k*-th damage scenario, the input data and output data for ANN is $\left\{\mathbf{f}_k, Tri\left[CoMAC\left(\boldsymbol{\Psi}_u^m, \boldsymbol{\Psi}_k^m\right)\right], Tri\left[CoMAC\left(\boldsymbol{\Phi}_u^m, \boldsymbol{\Phi}_k^m\right)\right]\right\}$ and $\boldsymbol{\Phi}_k\left(k=1,2,\cdots N\right)$, respectively, where $\mathbf{f}_k$ is frequencies; $\boldsymbol{\Psi}_k^m$ and $\boldsymbol{\Phi}_k^m$ are the strain and displacement mode shapes of the measurement points in the *k*-th damage scenario and N is the number of training sets; Tri converts a symmetric matrix $n \times n$ A into a vector of $Tri(A) = [\, A_{11}, A_{21}, A_{22}, A_{31}, ..., A_{n1}, A_{n2}, ..., A_{nn}\,]$.

The RBF networks are trained using the virtually generated damage scenarios to make the sum-squared error to approach the preset value. The mode shapes and damping ratios extracted from EMA and the mass-normalized mode shapes predicted by EMA are used to format the system matrices of the damaged state. Then in the damaged state, the response of the structure can be reconstructed using the Kalman filter-based method introduced in Section 5.2.

5.4 Damage Identification via Response Reconstruction

5.4.1 Sparse Regularized FE Model Updating

FE model updating as introduced in Section 4.2 is employed to identify damage. The main difference is that the reconstructed responses $\mathbf{y}_d^e \in \Re^{n_s \cdot (n_e + 2n)}$ instead of the limited measured responses $\mathbf{y}_d^m \in \Re^{n_s \cdot n_e}$ are used in RHS of Eq.4.2, and the response sensitivity matrix corresponding to the reconstructed response locations is used in left-hand-side (LHS) of Eq.4.2. Thus the problem is formatted as

$$\mathbf{S}^{e,k}\Delta\boldsymbol{\theta}^{k+1}=\Delta\mathbf{y}^{e,k} \tag{5.10}$$

where $\Delta\mathbf{y}^{e,k}=\mathbf{y}_d^e-\mathbf{y}_a^e\left(\boldsymbol{\theta}^k\right)$ is the response discrepancy between the reconstructed responses of damaged state and the analytical responses of the corresponding locations. $\boldsymbol{\theta}^k=\sum_{l=1}^{k}\Delta\boldsymbol{\theta}^l$ is the cumulative damage parameter in all *k*-th iterations. $\mathbf{S}^{e,k}$ and $\Delta\mathbf{y}^{e,k}$ are formatted by stacking the columns of sensitivity sequences and response discrepancy sequences respectively as

$$\begin{aligned}\mathbf{S}^{e,kT}&=\left[\mathbf{S}_1^{e,kT}\quad\cdots\quad\mathbf{S}_i^{e,kT}\quad\cdots\quad\mathbf{S}_{n_m}^{e,kT}\right]\\ \mathbf{y}^{e,kT}&=\left[\Delta\mathbf{y}_1^{e,kT}\quad\cdots\quad\Delta\mathbf{y}_i^{e,kT}\quad\cdots\quad\Delta\mathbf{y}_{n_m}^{e,kT}\right]\end{aligned} \tag{5.11}$$

Similarly, the sparsity regularization or specifically ℓ_1 norm regularization (Zhang *et al*. 2016) is employed to constrain the solution. Then, Eq. (5.10) is formatted as

$$\Delta\hat{\boldsymbol{\theta}}^{k+1}=\underset{\Delta\boldsymbol{\theta}^{k+1}\in\Re^p}{\operatorname{argmin}}\left(\left\|\mathbf{S}^{e,k}\Delta\boldsymbol{\theta}^{k+1}-\Delta\mathbf{y}^{e,k}\right\|_2^2+\mu\left\|\Delta\boldsymbol{\theta}^{k+1}\right\|_1^1\right) \tag{5.12}$$

where $\left\|\Delta\boldsymbol{\theta}^{k+1}\right\|_1^1$ is the ℓ_1 -norm of the vector $\Delta\boldsymbol{\theta}^{k+1}$; the term $\left\|\mathbf{S}^{e,k}\Delta\boldsymbol{\theta}^{k+1}-\Delta\mathbf{y}^{e,k}\right\|_2^2$ constrains the residual, whereas the term $\left\|\Delta\boldsymbol{\theta}^{k+1}\right\|_1^1$ enforces sparsity of the solution. The tradeoff between the two terms is balanced by the penalty parameter $\mu>0$, of which the proper value should be chosen carefully for an acceptable solution. A re-weighting strategy as explained in Section 4.3 could be employed to relieve this difficulty. The primal-dual interior point algorithm proposed by Boyd (Boyd, 2004) is adopted to solve Eq. (5.12) in this study.

5.4.2 Flowchart and Computation Procedure

The flowchart of the proposed damage detection via response reconstruction is shown in Figure 5.2, and Figure 5.3 shows the schematic illustration of response reconstruction process based on mode shape prediction using ANN. The whole procedure is introduced in detail as follows.

Step 1: The numbers and locations of accelerometers, displacement transducers, and strain gauges are optimized using a sensor placement optimization proposed in (Zhang *et al.*, 2012; Zhu *et al.*, 2013) to obtain the best reconstruction of multi-type responses of a structure in its intact state. The optimized sensors are installed at the selected locations.

Step 2: On the damage-free state, the multi-sensing responses $\mathbf{y}_u^m$ are collected by the optimally selected sensors. The finite element model corresponding to the intact state of the structure is updated using these measured responses to establish a precise reference model for the subsequent damage identification.

Step 3: After damage occurs, the multi-sensing responses $\mathbf{y}_d^m$ are also collected and utilized for response reconstruction, and they are combined with model updating for damage identification. In this process, the modal parameters extracted from EMA are imported into the trained RBF neural network to predict the mass-normalized mode shapes in the damaged state. Then the response on interested locations can be reconstructed by virtue of Kalman filter.

Step 4: Response sensitivity-based updating is performed to identify the existing

damage. For $k=0$, the damage parameter is set as $\boldsymbol{\theta}^0=\mathbf{0}$ for the intact state. Response sensitivity matrix $\mathbf{S}^0$ on the instate state is calculated with FEA and assembled in the form of Eq.(5.11). Damage perturbation vector $\Delta\boldsymbol{\theta}^1$ is calculated by Eq. (5.10)with $\Delta\mathbf{y}^0$ being the normalized difference between reconstructed responses $\mathbf{y}_d^e$ and the analytical responses $\mathbf{y}_a^0(\mathbf{0})$. The FE of the structure is updated with the damage vector $\boldsymbol{\theta}^1=\sum_{i=1}^{1}\Delta\boldsymbol{\theta}^i$.

Step 5: For the next iteration $k=k+1$, the analytical responses $\mathbf{y}_a^k$ are derived by FEA with the updated damage parameter $\boldsymbol{\theta}$. Response sensitivity matrix $\mathbf{S}^k$ for *k*-th iteration is calculated and assembled as Eq. (5.11)and then normalized accordingly. Damage perturbation vector $\Delta\boldsymbol{\theta}^{k+1}$ is obtained by $\mathbf{S}^{e,k}\cdot\Delta\boldsymbol{\theta}^{k+1}=\Delta\mathbf{y}^{e,k}$ with $\Delta\mathbf{y}^{e,k}=\mathbf{y}_d^e-\mathbf{y}_a^k$. The sparse regularization is employed to give a meaningful solution. Then the FE of the structure is further updated with new damage vector $\boldsymbol{\theta}^{k+1}=\sum_{i=1}^{k+1}\Delta\boldsymbol{\theta}^i$.

Step 6: The stiffness damage vector is updated iteratively. Repeat Step 3 until the convergence criterion is satisfied.

5.5 Numerical Studies

5.5.1 An Overhanging Beam

A simply-supported overhanging steel beam corresponding to the testbed in a laboratory serves as the numerical study. The geometric dimension and physical parameters have been introduced in Section 3.5.1. In this study, the damage is

simulated as a corresponding reduction of element stiffness and mass matrix as Eq. (5.13) because cutting the sectional width of the beam on the corresponding element causes the element stiffness and mass reduction to the same extent simultaneously.

$$\mathbf{K}_d = \mathbf{K}_u + \sum_{i=1}^{N_e} \theta_i \mathbf{K}_i, \mathbf{M}_d = \mathbf{M}_u + \sum_{i=1}^{N_e} \theta_i \mathbf{M}_i, (-1 \le \theta_i \le 0) \tag{5.13}$$

in which $\mathbf{K}_u$ and $\mathbf{M}_u$ are the global stiffness and mass matrix of the structure before damage occurrence, respectively; $\mathbf{K}_i$ and $\mathbf{M}_i$ are the stiffness and mass matrix contributions of the *i*-th element and θ_i is the fractional damage parameter. The damping matrix is formed using the Rayleigh damping model as $\mathbf{C} = \alpha\mathbf{M} + \beta\mathbf{K}$ where α and β are determined with the first two damping coefficients set as $\xi_1 = \xi_2 = 0.01$.

The external excitation vertically applied on node 18 is a broadband stochastic force sequence with a standard deviation of 6.4 N (same as that of laboratory test). Integration time step is 1/500 s, and the sample duration is 40s. Based on the studies in Chapter 3, it is noted that the 7-th mode of the beam (with a frequency around 99.7 Hz) has a negligible contribution to the overall response, thus the excitation sequences are deliberately designed as in a frequency bandwidth of 2 Hz to 82 Hz, only covering the first 6 modes. The dynamic response is numerically simulated with FOH state space formulation. Noise corruption is simulated by adding normally distributed random noise to the noise-free response as Eq.3.35; the noise amplitude is set as $0.201\,\mu\varepsilon$, $0.01\,\text{mm}$ and $0.04\ \text{m/s}^2$ for strain, displacement and acceleration, respectively according to the laboratory measurement data; and the standard deviation of noise over the standard deviation of noise corrupted response, is approximately 1%~2% in

the simulation.

5.5.2 Optimal Sensor Placement

Firstly, the optimized sensor placement is obtained with aforementioned multi-type sensors placement optimization method. The strain gauges are attached to the upper face at the middle of the elements to measure the flexural deformation of the beam. Rotational DOFs are excluded in the candidate location considering that it was difficult to measure the rotations at nodes directly. As a result, 40 element strains, and 39 vertical nodal displacements and 39 vertical nodal accelerations are selected as the candidate locations for three types of sensors. The first 6 modes are used for response reconstruction, i.e. $N_m = 6$, since the excitation bandwidth only covers the first 6 orders mode (as shown in Table 7.3). For a detailed introduction on this subtopic, please refer to the references (Zhang *et al*. 2012; Zhu *et al*., 2013). Here the final optimization results are listed: if 11 optimal sensors are selected, there are 5 strain gauges and 2 displacement transducers and 4 accelerometers; the corresponding placement configuration is shown in Figure 5.4.

5.5.3 RBF Network Training

Damage scenarios are virtually generated by introducing given damage to the intact FE model. Then analytical dynamic responses are added by the normally distributed noise sequences at laboratory test level. Modal identification is further performed to derive the modal parameters. Due to the computer's limited memory, the virtually simulated damage scenarios only cover the case that damages are on single or two elements and damage extent is from 0 to -0.2 at an increment of -0.1 and the number of

training sets N=3200. The accuracy of modal identification is crucial to the realization of this proposed method, since if the level of uncertainty is higher than or close to the level of actual changes of modal properties due to structural damage, the real information of structural damage will be masked and the structural damage cannot be accurately identified. In order to increase the robustness of the trained ANN over the uncertainty induced by the procedure of modal identification, zero-mean Gaussian white noise processes are added to the simulated responses and modal parameters extracted from the noise-corrupted response of these scenarios are then dedicated to training the BBF networks. In each damage scenario, the input data for ANN training are the vector $\left\{\mathbf{f}_k, Tri\left[CoMAC\left(\mathbf{\Phi}_u^m, \mathbf{\Phi}_k^m\right)\right], Tri\left[CoMAC\left(\mathbf{\Psi}_u^m, \mathbf{\Psi}_k^m\right)\right]\right\}^T$ which is derived from the model properties extracted through EMA; and the output data $\mathbf{\Phi}_k$ is obtained through model analysis. It should be pointed out that each mode shape of $\mathbf{\Phi}_k = \left\{\phi_{1,k}, \phi_{2,k}, \cdots, \phi_{N_m,k}\right\}$ in different damage scenario may be in the same or opposite direction. A preprocessing procedure is performed to make mode shapes in all damage scenarios are in the same direction: if $\left(\phi_{i,u} \cdot \phi_{i,k}^T\right) < 0$, then $\phi_{i,k} = -\phi_{i,k}$ where $i = 1, 2, \cdots, N_m$ and $\phi_{i,u}$ is the i-th mode shape of the structure in the undamaged state. The RBF network is trained using the virtually generated damage scenarios, and the sum-squared error goal in RBF Network training is set as 5e-8 for displacement mode shapes prediction. Then the strain mode shapes could be predicted as $\mathbf{\Psi}_d^e = \mathbf{B}\mathbf{\Phi}_d^e$.

5.5.4 Damage Identification

The damage is simulated by cutting notches with different sectional width reduction

on the corresponding element area, generating an equal reduction of element stiffness matrix and element mass matrix. Two typical damage scenarios have been considered in this simulation study: single damage scenario and multi-damage scenario. Please note that in this section, damages are virtually introduced in the area where no sensors are installed. This is purposely designed to demonstrate the superiority of the proposed response reconstruction in damage identification. The convergence criteria are set as $Tol = 1\times10^{-5}$, with a maximal iteration of 20 in the following study, which is enough for convergence of iteration.

5.5.4.1 Single-damage scenario

The single-damage scenario is designed as reducing 20% of width on element 23. Firstly, the noise-corrupted responses virtually recorded by the 11 optimized sensors are utilized for identifying the frequencies, displacement mode shapes, and strain mode shapes. These modal parameters are extracted through subspace algorithms for the identification of combined deterministic-stochastic systems (N4SID) (Overschee, 1994), and the identified modal parameters are listed in Table 5.1. Then the frequencies $\mathbf{f}_d$ as well as the displacement CoMAC and strain CoMAC are imported to the trained RBF network to predict mass-normalized strain and displacement mode shapes. The predicted mode shapes are further used in response reconstruction. The reconstructed and real strain responses are plotted in Figure 5.5. These two curves of responses are almost overlapping, which demonstrates that more damaged state information is contained in the reconstructed response.

Finally, the reconstructed responses are used for damage identification in iteratively

updating as introduced in section 5.4. Reweighting sparse regularization is also utilized for solving Eq.(5.12); all the results shown here are achieved through sparse regularized FE model updating. The identification result (shown in Figure 5.6b) indicates that the accuracy of damage detection via response reconstruction is pretty satisfactory, as the damage extent on element 23 is identified as -17.6% and errors on other elements are acceptable. For the sake of comparison, the result of damage identification without response reconstruction, namely directly using the noised responses on the 11 sensors for damage identification, is also presented in Figure 5.6a. It can be found that as the sparse is imposed on the solution, there are much less false-positive (indicating damage when it is not present) errors in the identification result, but the damage on element 23 is mistakenly located at element 21. Accelerometers are widely employed in vibration test due to its easy installment and relatively high sign-to-noise ratio. To show the superiority of using multi-type responses for damage detection, the result using acceleration on the equivalent locations, i.e. the response virtually collected from 9 accelerometers installed on node 1, 7, 12, 16, 22, 26, 32, 36 and 41, is also shown in Figure 5.6c. It is noted that with only acceleration, the 20% damage on element 23 is identified as around 6% in element 21: both damage location and severity are mistakenly identified. These results demonstrate that the proposed method has certain superiority.

5.5.4.2 Multi-damage scenario

A case of 20% reduction of sectional width on element 23 and 10% reduction on element 7 with respect to the original value is employed here representing a multi-damage scenario to investigate the effectiveness of multi-sensing damage

detection with response reconstruction. It is noted that this damage scenario is not used in ANN training. The frequencies, strain mode shapes and displacement mode shapes obtained using the sensors' data are listed in Table 5.2. Then the frequencies, as well as the displacement CoMAC and strain CoMAC, are imported to the trained RBF network to predict mass-normalized strain and displacement mode shapes. Then the reconstructed responses are used in sparse regularized updating as introduced in the above section. To save the computation effort, the reconstructed response of 2s' duration is used for damage identification. The identification results without and with response reconstruction are both illustrated in Figure 5.7, respectively. By comparing the two, it is observed that without response reconstruction, the damage on element 7 and element 23 cannot be identified. Besides, there are false-positive errors in the same elements. While with response reconstruction, both the damage location and the damage extent are identified with satisfactory accuracy. Figure 5.7c depicts the identification result of first 2 iterations merely using accelerations on the equivalent locations. The updating stopped after 2 iterations because the accumulated damage on elements 21 and 25 are less than -1, making the beam singular (inadequately constrained) and iteration divergent.

Comparing the results, it is observed that the proposed method has certain superiority over both the immediate utilization of multi-type responses at limited locations and homogeneous acceleration response on the equivalent locations. The results of the numerical studies indicate that more damaged state information is contained in the reconstructed response, which is beneficial to identify the local damages.

5.6 Concluding Remarks

This chapter presents a damage detection method via response reconstruction in a strategy of combining response reconstruction and sensitivity-based FE model updating to identify local damage in a structure. The fractional damage parameter is updated iteratively by minimizing the discrepancy between the reconstructed and their simulated counterparts obtained from an analytical model of the structure. The mass normalized mode shapes are predicted by the RBF network for reconstructing the structural response in the damaged state. Numerical studies of a simply supported overhanging beam are conducted to demonstrate the procedure and effectiveness of the proposed method. Basing on these studies, the following remarks should be highlighted:

(1) Strain is usually regarded as a local response while displacement and acceleration reflect more global behavior of a structure. Fusion of multi-type response, including global and local response, is advantageous to not only the response reconstruction but also the consequent damage identification.

(2) The response reconstruction is implemented in the Kalman filter, which has a remarkable superiority in handling the modeling error and measurement noise. To make the filter operate optimally, the modeling error covariance $\mathbf{Q}$ and the measurement noise covariance $\mathbf{R}^m$ should be properly selected. It is assumed that the structure works in the same conditions, i.e., the measurement noise covariance $\mathbf{R}^m$ stays the same before and after damage.

(3) RBF network is employed to predict the mass normalized mode shapes of damaged state, which is used for response reconstruction in the damaged state. The frequencies, strain and displacement CoMAC value are imported to the trained RBF network. Theoretically, other dynamic features can be used in RBF network; even other mode shapes prediction method could be used in the proposed method.

(4) Comparison of the damage identification results by using the reconstructed responses with those by immediate using of measured response shows the former has certain superiority. The results indicate that the proposed response reconstruction method is capable of capturing the kinetic information of the damaged structure.

Numerical studies show that the Kalman filter based multi-type response reconstruction and fusion do benefit to damage identification in supplementing the limitation of sensor measurements. The corresponding laboratory test work will be provided in Chapter 7 for validation. However, the full description of excitation is required in the Kalman filter based response reconstruction in this chapter. In the next chapter, the response reconstruction-oriented strategy will be extended to alleviate the necessity of knowing excitations.

Table 5.1 Identified dynamic properties for single damage

		Mode 1	Mode 2	Mode 3	Mode 4	Mode 5	Mode 6
$\mathbf{f}^d$		4.9837	8.2870	17.0609	42.0704	63.8434	71.5694
$\boldsymbol{\Xi}$		0.0064	0.0039	0.0019	0.0012	0.0011	0.0011
$\boldsymbol{\Phi}_d^m$	S_1	1.60E+02	1.47E+02	-1.12E+02	1.98E+02	1.31E+02	-3.04E+02
	S_2	4.58E+02	3.60E+02	-2.15E+02	8.84E+01	-7.21E+01	2.42E+02
	S_3	6.49E+02	-1.62E+01	1.90E+02	5.97E+01	5.85E+01	3.69E+01
	S_4	5.73E+02	-2.25E+02	2.60E+01	3.24E+02	-4.56E+01	7.34E+01
	S_5	3.80E+02	-3.50E+02	-2.32E+02	-2.20E+02	-1.89E+01	-1.76E+02
$\boldsymbol{\Psi}_d^m$	D_1	9.28E+01	8.59E+01	-7.15E+01	2.14E+02	2.22E+02	-5.96E+02
	D_2	-3.09E+01	-9.05E+00	-4.97E+01	2.94E+02	3.44E+01	1.83E+02
	D_3	-3.06E+01	9.32E+00	-4.85E+01	-3.18E+02	3.16E+01	-1.95E+02
	D_4	9.19E+01	-8.71E+01	-6.91E+01	-2.27E+02	2.12E+02	6.16E+02

Table 5.2 Identified modal parameters for multi-damage

		Mode 1	Mode 2	Mode 3	Mode 4	Mode 5	Mode 6
$\mathbf{f}^d$		4.9850	8.2827	17.0356	42.0282	63.8426	71.6200
$\boldsymbol{\Xi}$		0.0063	0.0039	0.0019	0.0012	0.0011	0.0011
$\boldsymbol{\Phi}_d^m$	S_1	-1.58E+02	-1.43E+02	9.62E+01	2.27E+02	-1.31E+02	-3.00E+02
	S_2	-4.48E+02	-3.48E+02	1.84E+02	9.98E+01	7.34E+01	2.44E+02
	S_3	-5.63E+02	2.18E+02	-2.21E+01	3.76E+02	4.68E+01	7.43E+01
	S_4	-3.73E+02	3.39E+02	2.00E+02	-2.56E+02	1.93E+01	-1.76E+02
	S_5	-1.56E+02	1.44E+02	9.30E+01	-2.43E+02	-1.28E+02	3.13E+02
$\boldsymbol{\Psi}_d^m$	D_1	-9.14E+01	-8.35E+01	6.13E+01	2.48E+02	-2.24E+02	-5.97E+02
	D_2	3.03E+01	8.68E+00	4.27E+01	3.40E+02	-3.51E+01	1.82E+02
	D_3	3.00E+01	-8.97E+00	4.14E+01	-3.68E+02	-3.23E+01	-1.97E+02
	D_4	-9.02E+01	8.42E+01	5.93E+01	-2.63E+02	-2.16E+02	6.15E+02

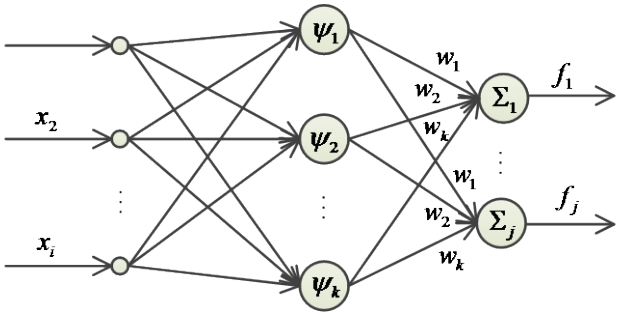

Figure 5.1 The architecture of a typical RBF neural network with *i* input and *j* output

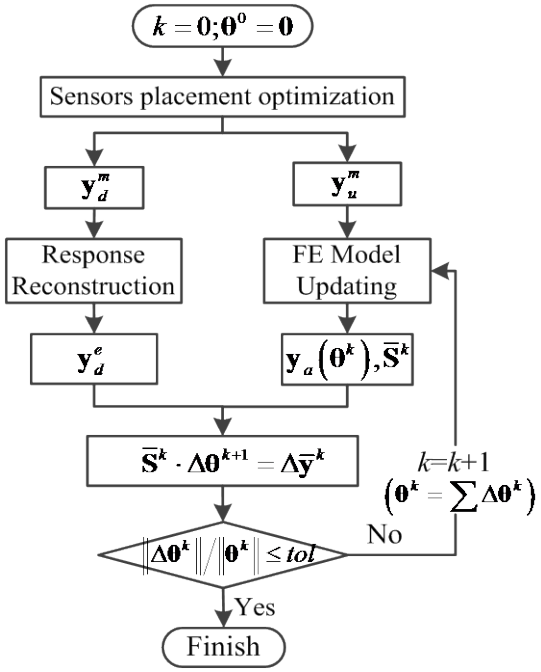

Figure 5.2 Flowchart of damage identification via response reconstruction

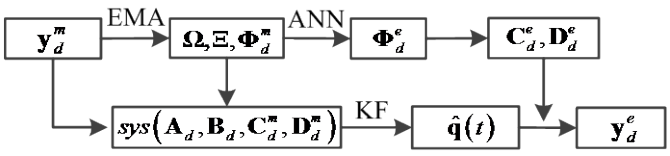

Figure 5.3 Response reconstruction strategy of damaged state

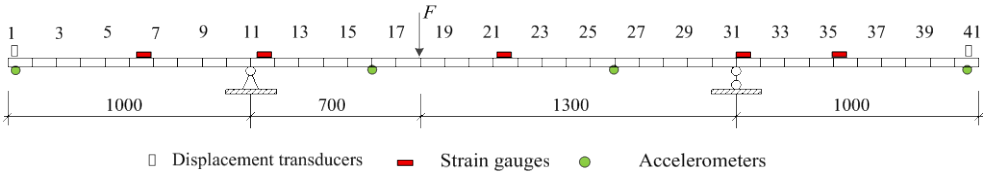

Figure 5.4 Geometric configuration of a simply supported overhanging steel beam and the optimal sensor placement for known excitation

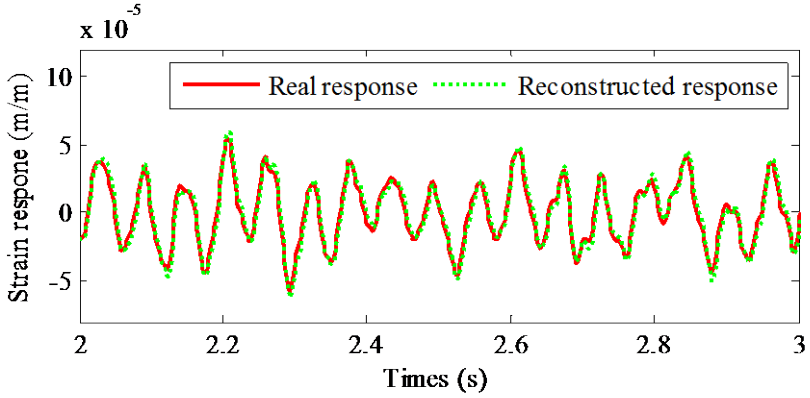

Figure 5.5 Close-view of strain response on Element 33

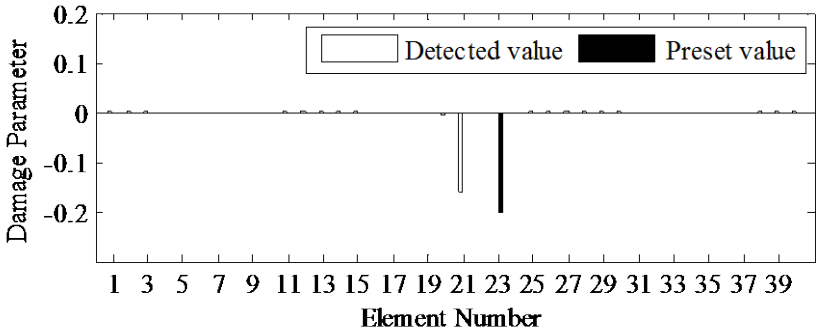

(a)

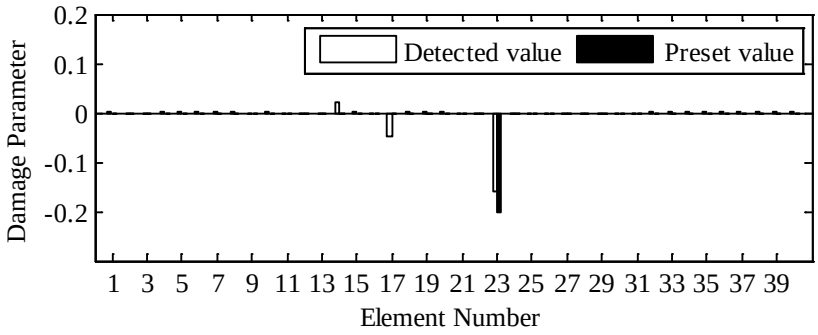

(b)

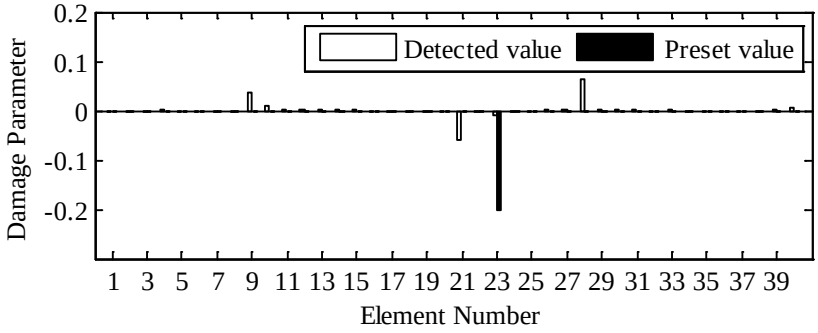

(c)

Figure 5.6 Damage identification result for single damage scenario: (a) without response reconstruction; (b) with response reconstruction; and (c) with equivalent acceleration response.

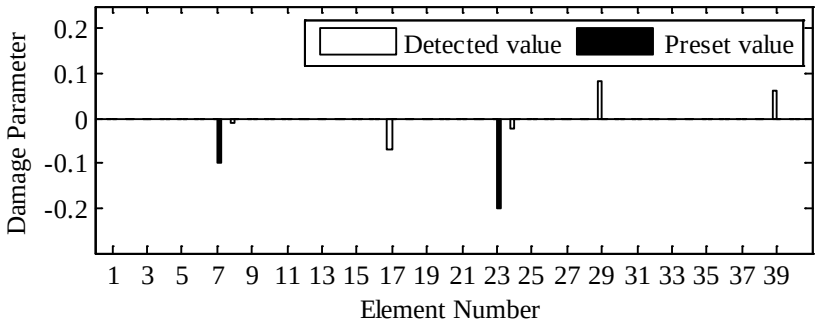

(a)

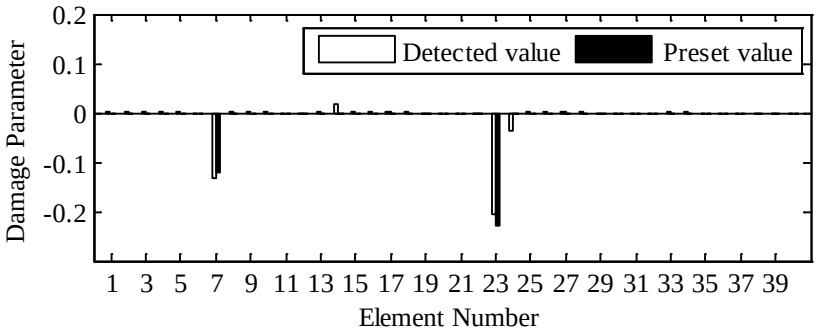

(b)

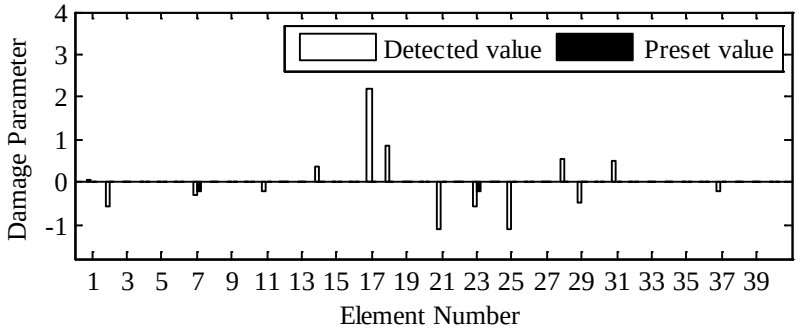

(c)

Figure 5.7 Damage identification for multi-damage: (a) without response reconstruction; (b) with response reconstruction; and (c) with equivalent acceleration response.

CHAPTER 6

DAMAGE IDENTIFICATION VIA RESPONSE RECONSTRUCTION UNDER UNKNOWN EXCITATION

6.1 Introduction

Equation Section 6To overcome the shortages of response measurements acquired by limited sensors for structural condition assessment, Chapter 5 has established a response reconstruction combined FE model updating strategy for damage identification of the major civil structures. The dynamic response reconstruction is performed using multi-type responses through the classical Kalman filter. However, the time series evolution of excitation acting on the structure is required in the classical Kalman filter based response reconstruction. To alleviate the necessity of measuring excitations in response reconstruction, Chapter 3 presents a Kalman filter under unknown input (KF-UI) based response reconstruction method, in which the response reconstruction and the excitation can be reconstructed simultaneously and the optimal multi-type sensors design is also investigated. In view of these, this chapter intends to extend the damage identification via response reconstruction strategy established in Chapter 5 from the situation that excitations are needed to the situation that excitations are absent. Response and excitation are reconstructed simultaneously through the implementation of KF-UI. Radial-basis-function (RBF) network is employed to predict the mode shapes using modal properties extracted by experimental modal

analysis (EMA) after damage occurrence. The reconstructed response and excitation are finally integrated into to sensitivity-based FE model updating for localizing and quantifying the damage. The sparse regularization, which is introduced in Chapter 4, is also employed to produce more accurate damage identification. A numerical simulation study is conducted on an overhanging steel beam under unknown excitation. The feasibility and effectiveness of the proposed method are further ascertained by laboratory tests of the beam, which will be presented in Chapter 7.

6.2 Response Reconstruction under Unknown Excitation

6.2.1 Discrete State Space Model of a Structure

By assuming that the structure behaves linearly in operational conditions, the dynamic vibrations can be expressed as the superposition of the first several model responses as $\mathbf{d}(t) = \boldsymbol{\Phi}^r \mathbf{q}^r(t)$, where $\boldsymbol{\Phi}^r \in \Re^{n \times r}$ is the collection of the selected several mass-normalized mode shapes and $\mathbf{q}^r(t)$ is the vector of modal displacement and a dot over it denotes differentiation with respect to time. The dynamics of a structure can be further represented in a discrete-time state space model as:

$$\mathbf{x}_{k+1} = \mathbf{A}_d \mathbf{x}_k + \mathbf{B}_d \mathbf{u}_k + \mathbf{w}_k \tag{6.1}$$

$$\mathbf{y}_k^m = \mathbf{C}_d^m \mathbf{x}_k + \mathbf{D}_d^m \mathbf{u}_k + \mathbf{v}_k^m \tag{6.2}$$

where $\mathbf{x}_k = \mathbf{x}(k\Delta t) = \left\{ \mathbf{q}_k^r \quad \dot{\mathbf{q}}_k^r \right\}^T \in \Re^{2r}$ is the discrete-time state vector with $k = 0,1,2,\ldots$; Δt stands for the sampling interval. The system matrices $\mathbf{A}_d$, $\mathbf{B}_d$, $\mathbf{C}_d^m$ and $\mathbf{D}_d^m$ are

composed of modal properties of the structure, including the collected strain mode shapes $\boldsymbol{\Psi}^m$ and displacement mode shapes $\boldsymbol{\Phi}^m$, diagonal matrices $\boldsymbol{\Omega}^s$ containing the eigenfrequencies ω_i in rad/s and $\boldsymbol{\Xi}^s$ containing the modal damping ratio ξ_i as introduced in section 4.2 in detail. The vector $\mathbf{u}_k \in \Re^r$ denotes the r external excitation acting on the structure. $\mathbf{w}_k \in \Re^{2r}$ and $\mathbf{v}_k^m \in \Re^{N_m}$ represent the independent white Gaussian modeling error and measurement noise vectors with covariance matrices $\mathbf{Q}$ and $\mathbf{R}^m$, respectively.

6.2.2 Joint Response and Excitation Reconstruction in Damaged State

Kalman filter as a well-known state estimator has found certain applications in response reconstruction (Zhang *et al*.2012; Papadimitriou *et al*. 2010; Hernandez *et al*. 2013; Palanisamy *et al*. 2015) and consequent applications (for example, cumulative fatigue prediction (Papadimitriou *et al*. 2010) and structural control (He *et al.*, 2015)) recently. However, in the response reconstructions, the time evolution of the deterministic excitation as the input to the structural system is usually assumed to be available. The recent development of filters for minimum-variance state estimation in the presence of unknown excitations has made response reconstruction without knowing excitation possible, which has introduced and demonstrated in Chapter 3. A recursive three-step filter (Gillijns *et al*., 2007; Pan *et al*., 2011) named KF-UI is adopted for joint response and excitation reconstruction. In what follows, it will be briefly introduced for completeness.

Assuming the filter with the initial unbiased estimate $\bar{\mathbf{x}}_0$ and the error variance $\mathbf{P}_0^{x-}$,

the excitation and state estimates can be estimated recursively by the three steps in the following form:

$$\hat{\mathbf{x}}_{k+1}^{-} = \mathbf{A}_d \hat{\mathbf{x}}_k^{+} + \mathbf{B}_d \hat{\mathbf{u}}_k \tag{6.3}$$

$$\hat{\mathbf{u}}_k = \mathbf{M}_k \left(\mathbf{y}_k^m - \mathbf{C}_d^m \hat{\mathbf{x}}_k^{-} \right) \tag{6.4}$$

$$\hat{\mathbf{x}}_k^{+} = \hat{\mathbf{x}}_k^{-} + \mathbf{K}_k \left(\mathbf{y}_k - \mathbf{C}_d^m \hat{\mathbf{x}}_k^{-} - \mathbf{D}_d^m \hat{\mathbf{u}}_k \right) \tag{6.5}$$

where $\hat{\mathbf{x}}_k^{-}$ and $\hat{\mathbf{x}}_k^{+}$ denote the priori and posteriori state estimates at time instant *k*, respectively. The minimum-variance unbiased estimate of excitation $\hat{\mathbf{u}}_k$ is obtained by Eq.(6.4) with the gain matrix $\mathbf{M}_k$ given by

$$\mathbf{M}_k = \left(\mathbf{D}_d^{mT} \tilde{\mathbf{R}}_k^{-1} \mathbf{D}_d^m \right)^{-1} \mathbf{D}_d^{mT} \tilde{\mathbf{R}}_k^{-1} \tag{6.6}$$

where $\tilde{\mathbf{R}}_k = \mathbf{C}_d^m \mathbf{P}_k^{x-} \mathbf{C}_d^{mT} + \mathbf{R}^m$. The minimum-variance unbiased estimate of the state vector $\hat{\mathbf{x}}_k^{+}$ is obtained by Eq.(6.5) with the filter gain expressed as:

$$\mathbf{K}_k = \mathbf{P}_k^{x-} \mathbf{C}_k^{mT} \tilde{\mathbf{R}}_k \tag{6.7}$$

The corresponding state estimation error covariance is now updated to the posterior state estimation error covariance as

$$\mathbf{P}_k^{x+} = \mathbf{P}_k^{x-} - \mathbf{K}_k \left(\tilde{\mathbf{R}}_k - \mathbf{D}_d^m \mathbf{P}_k^u \mathbf{D}_d^{mT} \right) \mathbf{K}_k^T \tag{6.8}$$

in which $\mathbf{P}_k^u = \left(\mathbf{D}_d^{mT} \tilde{\mathbf{R}}_k^{-1} \mathbf{D}_d^m \right)^{-1}$ denotes the excitation estimate error covariance. Then the

optimal state estimate $\hat{\mathbf{x}}_k^+$ at time instant k is propagated to the next time instant priori estimate $\hat{\mathbf{x}}_{k+1}^-$ using Eq. (6.3) and its error covariance matrix is:

$$\mathbf{P}_{k+1}^{x-} = \begin{bmatrix} \mathbf{A}_d & \mathbf{B}_d \end{bmatrix} \begin{bmatrix} \mathbf{P}_k^{x+} & \mathbf{P}_k^{xu} \\ \mathbf{P}_k^{ux} & \mathbf{P}_k^{u} \end{bmatrix} \begin{bmatrix} \mathbf{A}_d^T \\ \mathbf{B}_d^T \end{bmatrix} + \mathbf{Q} \tag{6.9}$$

in which $\mathbf{P}_k^{xu} = \left(\mathbf{P}_k^{ux}\right)^T = E\left[\left(\mathbf{x}_k - \hat{\mathbf{x}}_k^+\right)\left(\mathbf{u}_k - \hat{\mathbf{u}}_k\right)^T\right] = -\mathbf{K}_k \mathbf{D}_d^m \mathbf{P}_k^u$ is the cross-covariance of the estimate errors of both state and excitation. Consequently, unbiased minimum variance estimates of state and excitation are simultaneously derived using the above three-step recursive filter. After the minimum-variance unbiased estimates $\hat{\mathbf{x}}_k^+$ and $\hat{\mathbf{u}}_k$ are obtained, the reconstructed responses $\mathbf{y}_k^e$ is expressed as

$$\mathbf{y}_k^e = \mathbf{C}_d^e \hat{\mathbf{x}}_k^+ + \mathbf{D}_d^e \hat{\mathbf{u}}_k \tag{6.10}$$

where $\mathbf{C}_d^e$ and $\mathbf{D}_d^e$ are composed of strain mode shape $\mathbf{\Psi}^e$ and displacement mode shape $\mathbf{\Phi}^e$ corresponding the DOFs of the reconstructed locations. We can see that the excitation sequences can be recursively estimated provided that three-step filter is well structured by choosing the proper measurement locations and the number and location of the acting excitation should be known when forming the system matrices $\mathbf{B}_d$ and $\mathbf{D}_d^m$. It is worth highlighting that the sensor configuration should be optimally designed since improper sensor placement could degrade the response reconstruction accuracy and even causes divergence in state and input estimation, thus prejudicing the final damage identification.

6.3 Damage Identification via Response Reconstruction

6.3.1 Mode Shape Prediction with RBF Network

Referring to Eq. (6.1) and (6.10), we note that the estimation system matrix $\mathbf{A}_d$, $\mathbf{B}_d$, $\mathbf{C}_d^e$ and $\mathbf{D}_d^e$ are composed of modal parameters, including frequencies, damping ratios and mode shapes of the structure in the damaged state, of which the former two could be possibly extracted by the experimental modal analysis (EMA). For the later, Radial-basis-function (RBF) network is employed to estimate the displacement mode shapes of the damaged structure due to its easier implementation and fast training. Radial-basis-function (RBF) network is a kind of the multi-hidden-layer feed-forward artificial neural network (ANN) with sigmoid and linear functions as activation (transfer) functions for the neurons in the hidden layers and the output layer, respectively. Application of ANN for mode shape prediction has been investigated by Goh *et al*. (2013). The basic idea of ANN applications in mode shape prediction is to build a model to establish relationships between modal parameters and mode shapes through a training process. The input of the network is frequencies and the displacement coordinate modal assurance criterion (CoMAC) defined as $CoMAC\left(\boldsymbol{\Phi}_m^u, \boldsymbol{\Phi}_m^d\right) = \left|\boldsymbol{\Phi}_m^{uT} \cdot \boldsymbol{\Phi}_m^d\right|^2 \Big/ \left[\left(\boldsymbol{\Phi}_m^{uT} \cdot \boldsymbol{\Phi}_m^u\right)\left(\boldsymbol{\Phi}_m^{dT} \cdot \boldsymbol{\Phi}_m^d\right)\right]$ of damaged state, where $\boldsymbol{\Phi}_m^u$ and $\boldsymbol{\Phi}_m^d$ are the displacement mode shape of damage-free and damaged state at a relatively small number of discrete measurement points, respectively; when the strain mode shape before damage $\boldsymbol{\Psi}_m^u$ and after damage $\boldsymbol{\Psi}_m^d$ are used, it forms the strain CoMAC. The appropriate training sets (damage scenarios) are obtained by numerical

analysis. For *k*-th damage scenarios, the input data and output data for ANN is $\left\{\mathbf{f}^k, Tri\left[CoMAC\left(\boldsymbol{\Phi}_m^u, \boldsymbol{\Phi}_m^k\right)\right], Tri\left[CoMAC\left(\boldsymbol{\Psi}_m^u, \boldsymbol{\Psi}_m^k\right)\right]\right\}$ and $\boldsymbol{\Phi}^k \left(k = 1, 2, \cdots N\right)$, respectively, where $\boldsymbol{\Phi}_m^k \in \Re^{m \times s}$ and $\boldsymbol{\Phi}^k \in \Re^{n \times s}$ are the mode shapes corresponding to the measurement points and the mass-normalized mode shapes in *k*-th damage scenarios and N is the number of training sets. $Tri(\cdot)$ is denoted as the lower triangular parts of a matrix, which means only the lower triangular parts of the symmetric matrix are utilized.

The RBF networks are trained using the virtually generated damage scenarios over the preset damage domain to make the sum-squared error approach the preset value. The mode shapes and damping ratios extracted from EMA and the mass-normalized mode shapes predicted by EMA are used to form the system matrices of the damaged state. Then the responses of the damaged structure can be reconstructed using the recursive three-step filter introduced above.

6.3.2 Sparse Regularized FE model Updating

After the responses of the structure in the damaged state have been reconstructed, damage identification can be performed through response sensitivity-based model updating, which seeks the damage parameter that minimizes the difference between the reconstructed response of the damage state and analytical counterparts obtained from the FE model of the structure. As introduced in Section 4.2, this problem is usually solved using a gradient-based optimization like Gaussian-Newton iteration as:

$$\mathbf{S}^k \Delta\boldsymbol{\theta}^{k+1} = \Delta\mathbf{y}^k \tag{6.11}$$

with

$$\mathbf{S}^k = \mathbf{W}^{1/2}\,\partial \mathbf{y}_a\left(\boldsymbol{\theta}^k\right)\big/\partial \boldsymbol{\theta} \tag{6.12}$$

$$\Delta \mathbf{y}^k = \mathbf{W}^{1/2}\left[\mathbf{y}_d^e\left(\boldsymbol{\theta}_d, \hat{\mathbf{u}}\right) - \mathbf{y}_a\left(\boldsymbol{\theta}^k, \hat{\mathbf{u}}\right)\right] \tag{6.13}$$

where $\mathbf{S}^k$ is the weighted sensitivity matrix for the *k*-th iteration; and $\mathbf{W}$ is a diagonal weighting matrix whose entries could be set as the reciprocals of the variance of the response on the intact state. $\Delta \mathbf{y}^k$ is the weighted response residual vector; $\mathbf{y}_d^e\left(\boldsymbol{\theta}\right)$ and $\mathbf{y}_a\left(\boldsymbol{\theta}\right) \in \Re^{N_m \cdot N_t \times 1}$ are the reconstructed and computed dynamic response vectors; N_m and N_t are the number of sensors and time instants recorded by each sensor. It is noticed that the main difference of Eq. (6.11) with Eq. 5.10 is that the analytical response calculated by the estimated excitation $\hat{\mathbf{u}}$. $\boldsymbol{\theta} \in \Re^{N_e}$ is the damage vector and $\boldsymbol{\theta}^k = \sum_{l=1}^{k} \Delta \boldsymbol{\theta}^l$ is the cumulative damage parameter in all *k*-th iterations. $\mathbf{S}^k$ and $\Delta \mathbf{y}^k$ are assembled by stacking the columns of sensitivity sequences and response discrepancy sequences, respectively, namely:

$$\mathbf{S}^{kT} = \left[\mathbf{S}_1^{kT} \quad \cdots \quad \mathbf{S}_i^{kT} \quad \cdots \quad \mathbf{S}_{N_m}^{kT}\right], \Delta \mathbf{y}^{kT} = \left[\Delta \mathbf{y}_1^{kT} \quad \cdots \quad \Delta \mathbf{y}_i^{kT} \quad \cdots \quad \Delta \mathbf{y}_{N_m}^{kT}\right] \tag{6.14}$$

Similarly, the ℓ_1 norm regularization, which has been introduced in Section 4.3, is imposed to promote the sparsity in the solution, and Eq. (6.11) can be solved equivalently as:

$$\Delta \hat{\boldsymbol{\theta}}^{k+1} = \underset{\Delta \boldsymbol{\theta}^{k+1} \in \Re}{\operatorname{argmin}}\left(\left\|\mathbf{S}^k \Delta \boldsymbol{\theta}^{k+1} - \Delta \mathbf{y}^k\right\|_2^2 + \mu \left\|\Delta \boldsymbol{\theta}^{k+1}\right\|_1^1\right) \tag{6.15}$$

in which $\|\cdot\|_1$ denotes the ℓ_1 norm. The parameter $\mu > 0$ should be optimally determined to control the tradeoff between the residual $\left\|\mathbf{S}^k \Delta\boldsymbol{\theta}^{k+1} - \Delta\mathbf{y}^k\right\|_2^2$ and the sparsity of the solution. The primal-dual interior point algorithm presented by Boyd (2004) is employed to solve the problem. Updating iterations are performed until the convergence criterion $\left\|\Delta\boldsymbol{\theta}^k\right\| / \left\|\boldsymbol{\theta}^k\right\| \le Tol$ is met.

6.3.3 Flowchart and Computation Procedure

The flowchart of the proposed damage detection via response reconstruction under unknown excitation is shown in Figure 6.1, and the strategy of response reconstruction in the damaged state is shown in Figure 6.2. The whole procedure is introduced in detail as follows.

Step 1: The optimized multi-type sensors designed by the sensor placement optimization proposed in Chapter 3 are installed at the selected location.

Step 2: On the damage-free state, the finite element model corresponding to the intact condition of the structure is updated using these measured responses $\mathbf{y}_u^m$ collected by the optimal limited sensors to establish a precise reference model for the following damage identification.

Step 3: After damage occurs, the multi-sensing responses $\mathbf{y}_d^m$ are also collected and utilized for response reconstruction combined with model updating for damage identification. In this process, the modal parameters extracted from EMA are imported into the trained RBF neural network to predict the mass-normalized mode shapes in

the damaged state. Then the responses on interested locations as well as the external excitation can be reconstructed through KF-UI as introduced in Section 6.2.

Step 4: Response sensitivity-based updating as introduced in section 6.3 is performed to identify the existing damage. For $k=0$, the damage parameter is set as $\boldsymbol{\theta}^0=\mathbf{0}$ for the intact state. Response sensitivity matrix $\mathbf{S}^0$ on the intact state is calculated with FEA using the reconstructed excitation $\hat{\mathbf{u}}(t)$ and assembled in the form of Eq.(6.14). Damage perturbation vector $\Delta\boldsymbol{\theta}^1$ is calculated by Eq. (6.15) with $\Delta\mathbf{y}^0$ being the difference between the reconstructed responses $\mathbf{y}_d^e(t)$ and the analytical responses $\mathbf{y}_a^0(t)$ when $\boldsymbol{\theta}^0=\mathbf{0}$. The FE of the structure is updated with the damage vector $\boldsymbol{\theta}^1=\sum_{s=1}^{1}\Delta\boldsymbol{\theta}^s$.

Step 5: For the next iteration $k=k+1$, the analytical responses $\mathbf{y}_a^k$ are derived by FEA with the updated damage parameter $\boldsymbol{\theta}^k$ and reconstructed external excitation $\hat{\mathbf{u}}(t)$. Response sensitivity matrix $\mathbf{S}^k$ for *k*-th iteration is calculated and the damage perturbation vector $\Delta\boldsymbol{\theta}^{k+1}$ is also obtained by Eq. (6.15). Then the FE of the structure is further updated with new damage vector $\boldsymbol{\theta}^{k+1}=\sum_{i=1}^{k+1}\Delta\boldsymbol{\theta}^i$.

Step 6: The stiffness damage vector is updated iteratively. Repeat Step 3 until following convergence criterion $\left\|\Delta\boldsymbol{\theta}^k\right\|/\left\|\boldsymbol{\theta}^k\right\|\le Tol$ is satisfied.

We can see that the whole procedure of the damage detection via response reconstruction under unknown excitation is similar to that of the situation where

excitations are known. The differences between these two cases include: (1) in response reconstruction part, the state vecto $\hat{\mathbf{x}}(t)$ composed of generalized coordinates and external input $\hat{\mathbf{u}}(t)$ are both optimally estimated by adopting the KF-UI for the response reconstruction at the key locations; thus the response reconstruction error stem not only from the estimated state vector but also from the estimated excitation; (2) in model updating part, the analytical responses $\mathbf{y}_a^k$ and sensitivity matrix $\mathbf{S}^k$ are calculated by FEA using the estimated excitation $\hat{\mathbf{u}}(t)$.

6.4 Numerical study

6.4.1 An Overhanging Beam

To illustrate the procedure of the proposed method, the overhanging beam as adopted in Section 5.5 is revisited. The same beam serves as a numerical study with two aspects of differences: (1) the optimal sensor placement configuration is different and (2) the time histories of the excitation acting on the beam are assumed to be unknown in this simulation study.

The simulated responses on the DOFs and the elements corresponding to the sensor placement configuration optimized in Chapter 3 for joint response and excitation reconstruction are used as virtually “measured” response in the numerical study. There are 11 sensors selected, including 4 strain gauges and 1 displacement transducers and 6 accelerometers; the corresponding placement configuration is shown in Figure 6.3. We may notice that the layout of designed optimal sensor placement is a bit different from the result of situations where excitation is known. The main reason is that under

unknown excitations, the error of response reconstruction stems from not only the estimated state variables but also the estimated excitations.

6.4.2 RBF Network Training

In this study, the damage is simulated as an equivalent reduction of element stiffness and mass matrix as Eq. 5.13 because cutting the sectional width of the beam on the corresponding element causes the element stiffness and mass reduction at the same extent simultaneously.

The RBF Network used for mode shape prediction is trained using modal data of sets of damage scenarios. Damage scenarios are virtually generated by introducing given damage to the intact FE model. Due to the computer's limited memory, the virtually simulated damage scenarios only cover the case that damages are on single or two elements and damage extent is from 0 to -0.2 at an increment of -0.1 and the number of training sets N=3200. The accuracy of modal identification is crucial to the realization of this proposed method, since if the level of uncertainty is higher than or close to the level of actual changes of modal properties due to structural damage, the real information of structural damage will be masked and the structural damage cannot be accurately identified. In order to increase the robustness of the trained ANN over the uncertainty induced in the procedure of modal identification, zero-mean Gaussian white noise processes are added to the simulated responses and modal parameters extracted from the noise-corrupted response of these scenarios are then dedicated to training the RBF networks. The RBF network is trained and the sum-squared error goals are set as 1.0e-7 for displacement mode shapes prediction.

To check the accuracy of mode shape prediction using the trained RBF Network, the mode assurance criterion MAC between the predicted displacement mode shapes and the analytical ones calculated by eigenvalue analysis on the damaged state is depicted in Figure 6.4, from which we can see that a good correlation exists between these two parts, indicating the ability of RBF Network in mode shape prediction. Then the strain mode shapes could be predicted as $\mathbf{\Psi}^e = \mathbf{B}\mathbf{\Phi}^e$.

6.4.3 Damage Identification

The damage is simulated as a reduction of sectional width on corresponding element area, generating an equivalent reduction of element stiffness matrix and mass matrix. Two typical damage scenarios as listed in Table 6.1 have been considered in this simulation study and the subsequent experimental study. The convergence criteria are set as $Tol = 1\times10^{-5}$, and the maximal iteration number is 15 in the subsequent updating.

Firstly, the noise-corrupted responses on the 11 optimized sensors are utilized for identifying the frequencies, displacement mode shapes, and strain mode shapes. These modal parameters are extracted through subspace algorithms for the identification of combined deterministic-stochastic systems (N4SID) (Overschee 1994). Then the identified frequencies $\mathbf{f}^d$, as well as the displacement CoMAC and strain CoMAC, are imported to the trained RBF network to predict the mass-normalized displacement mode shapes. Then the response and excitation can be reconstructed by the implement of KF-UI as introduced in Section 2. The reconstructed excitation and the preset real excitation are depicted in Figure 6.5. A good overlapping between the real excitation and the estimated one is observed.

Then the reconstructed excitation is used to calculate the analytical responses and the discrepancies between the analytical responses and reconstructed responses are minimized in sparse regularized updating to localize as well as quantify the preset damage. The identification results for these two damage scenarios are illustrated in Figure 6.6, respectively. For the single damage scenario, the 20% damage on element 23 is identified almost correctly. The false-positive error (indicating damage when it is not present) in the adjacent element 22 is also acceptable. For the multi-damage scenario, the two damages are both localized correctly. A bit error in quantifying the damage severity on element 7 is also noticed. These errors probably stem from the deviation in mode shape prediction using RBF Network. However, considering the fact that external excitation is unknown and reconstructed in this proposed method, the results are still satisfactory.

6.5 Concluding Remarks

This study extends the proposed response reconstruction-based damage identification method from situations of known excitation to the situations where the external excitations are unknown. The response reconstruction is performed in this case by using Kalman filter under unknown input. The same overhanging beam serves as the numerical model to demonstrate the procedure and feasibility of the proposed method. Compared with the results obtained in Chapter 5, the following remarks should be highlighted:

(1) The main difference from the method presented in Chapter 5 is that the response reconstruction approach is different. From Eq.(6.3) to Eq.(6.5), it can be observed

that the excitation can be estimated recursively after the priori state estimate is obtained. This is the rationale of making the joint response and excitation reconstruction feasible.

(2) In the situation of unknown excitation, the unbiased minimum variance estimate of external excitation is obtained and further used in response reconstruction and analytical response calculation. Response reconstruction can be conducted without imposing any assumptions on the unobserved excitation. Thus, damage identification can be performed under any type of excitation.

(3) When the excitation is absent, the optimal sensor placement is a bit different from that under known excitation. Besides, instantaneous estimation of the external excitation induces a bit of degradation in response reconstruction accuracy and thus influences the final damage identification quality. However, it should be noted that absence of excitation does not introduce noteworthy degradation in final damage identification. One possible reason is that the reconstructed excitation is used in both calculating the reconstructed and analytical response, and the errors induced by reconstructed excitation into the residual between the reconstructed and analytical response are mutually compensated.

Provided that the sensor locations are predefined, all types of excitations, such as impulsive, harmonic and random excitation, can be reconstructed, making the proposed response reconstruction-oriented damage identification enjoy a wider range of applicability. However, if the time histories of the excitation are available, the response can be reconstructed with higher accuracy. Experimental studies on these

issues will be presented in the next chapter.

Table 6.1 Damage scenarios

Damage scenario	Damage description
Single damage	20% [a] at Elem 23
Multi-damage	20% at Elem 23;10% at Elem 7

a. The percentage of reduction of the beam width

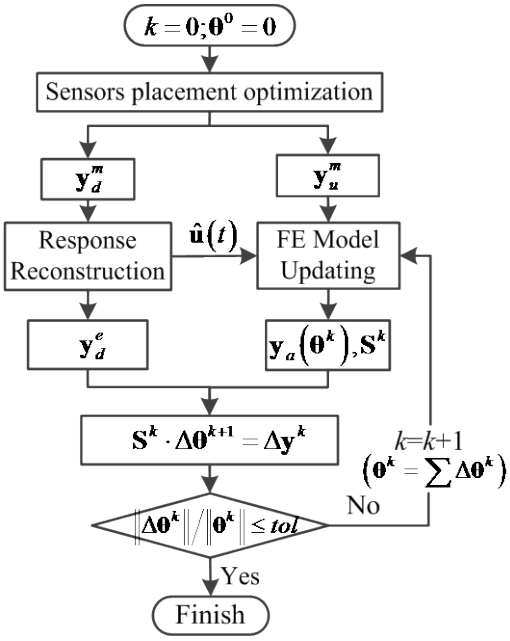

Figure 6.1 Flowchart of damage identification via response reconstruction under unknown excitation

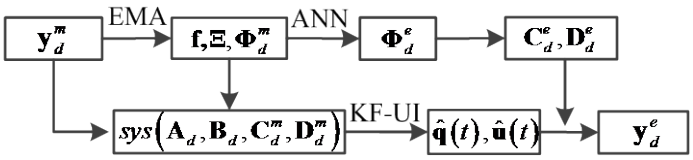

Figure 6.2 Response reconstruction of damaged state under unknown excitation

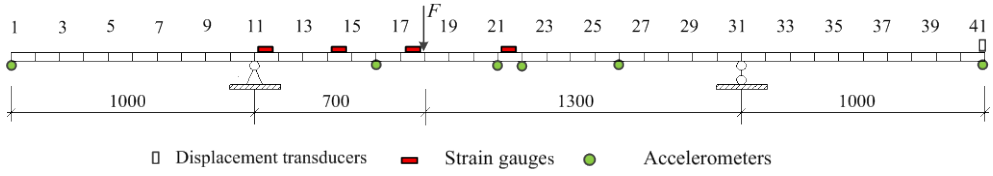

Figure 6.3 Optimal sensor placement under unknown excitation

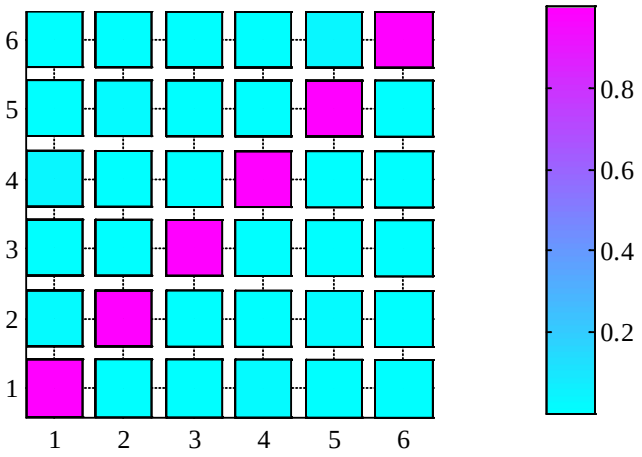

Figure 6.4 MAC between the predicted and real displacement mode shape

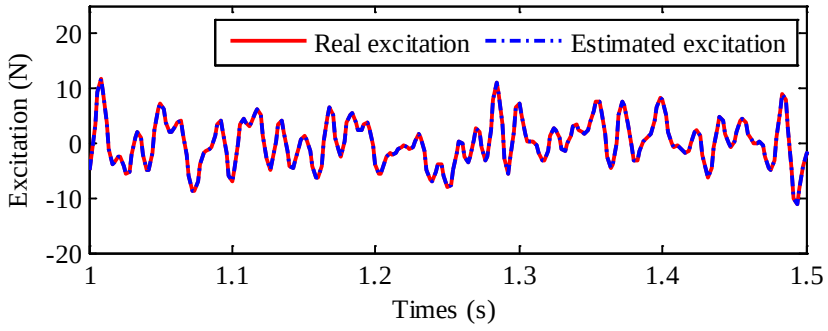

Figure 6.5 Comparison between the reconstructed and the actual excitation

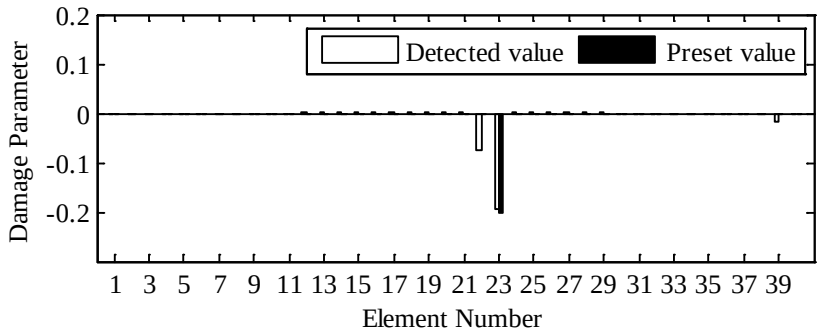

(a)

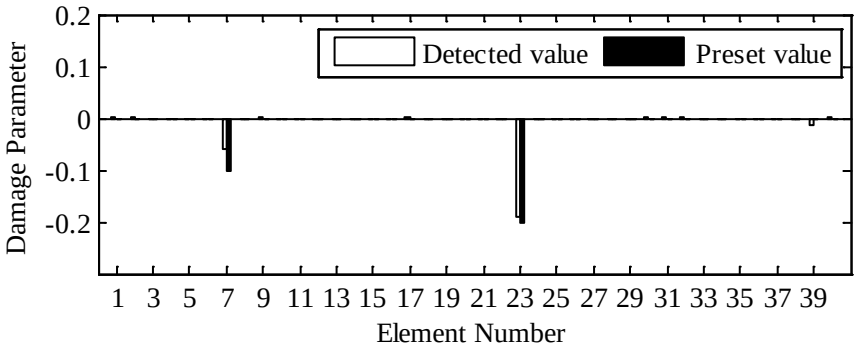

(b)

Figure 6.6 Damage identification with joint response and excitation reconstruction: (a) for single damage and (b) for multi-damage

CHAPTER 7

EXPERIMENTAL INVESTIGATION ON RESPONSE RECONSTRUCTION AND DAMAGE DETECTION OF AN OVERHANGING BEAM

7.1 Introduction

Equation Section 7In Chapter 3, the optimal sensor placement for joint response and excitation is investigated. Simulation on an overhanging beam has been conducted to demonstrate the effectiveness of the proposed response reconstruction method. To handle the ill-posedness in damage identification of large civil structure, the sparse regularization is proposed to constrain the norm as well as promote the sparseness of the solution in Chapter 4. Chapter 5 and Chapter 6 present the response reconstruction combined FE model updating for damage identification in the circumstances of known and unknown excitation, respectively. The procedure and feasibility of these two approaches have been demonstrated in numerical studies of the same overhanging beam. To validate the effectiveness of these proposed methods, relevant experimental studies will be conducted in this chapter. A steel overhanging beam with the same geometric dimension, physical parameters and boundary conditions will be employed in a laboratory test to validate the performance of these approaches. Specifically, the following studies will be carried out on the beam in laboratory: (1) joint response and excitation reconstruction using the optically deployed multi-type sensors; (2) comparative studies on the performance of the Tikhonov regularization and sparse

regularization in FE model updating; (3) damage identification via response reconstruction under known excitation; and (4) damage identification via response reconstruction under unknown excitation. In this chapter, the experimental setup of the overhanging beam will be firstly introduced in detail, followed by the time domain FE model updating to provide a refined FE model for the following studies. Then the listed four problems will be investigated in sequence.

7.2 Experiment Setup

7.2.1 Sensor Installation

Experimental studies of the simply-supported overhanging steel beam were conducted in a laboratory as shown in Figure 7.1. The geometrical and physical properties of the beam are the same as those described in the numerical investigation and shown in Table 7.2. An LDS V451 electromagnetic vibrator (see Figure 7.3a) together with a B&K signal generator and an LDS PA500 power amplifier were mounted on the beam at 1.8 m from the left end of the beam, generating a white noise excitation vertically acting on the beam. The vibrator was connected to the beam by a load cell to record the applied excitation and a spring with a small stiffness (Figure 7.3-b) to shield the side effect of the vibrator on the steel beam. The beam was constrained by a hinge support on the node 11 and a roller support on the node 31. The strain gauges are stuck on the upper surface of the beam at the middle of the element to measure the flexural deformation of the beam. Non-contacting laser displacement transducers are installed to measure the vertical displacements. Accelerometers of 6.5g weight for each are stuck on the top surface of the beam to acquire the acceleration data. The total

multi-type sensors, including 8 BX120-55AA strain gauges, 2 LK-503 laser displacement transducers and 9 KD1008 accelerometers, are installed on the beam in the test and they are shown in Figure 7.2. This configuration covers the optimal sensor placement under both known excitation (as shown in Figure 5.3) and unknown excitation (as shown in Figure 6.3). When the responses captured by the selected optimal sensors are utilized for response reconstruction, the responses on the other sensors could be used to verify the effectiveness of response reconstruction. The general information on sensor placement in the test is listed in Table 7.1.

7.2.2 Data Acquisitions

The vibration data of the beam under low-frequency excitation and high-frequency excitation are recorded respectively for the different purposes. In the former case, the bandwidth of the excitation is from 2 Hz to 102 Hz, which covers the first 7 modes as shown in Table 7.3. The sampling frequency is 500 Hz the sample duration is 24 seconds with zero initial condition. In the high-frequency excitation case, the excitation bandwidth is 2 ~ 802 Hz, which covers the first 11 modes. The test data are recorded at a frequency of 5000 Hz, and with a sampling duration of 8 seconds including the zero initial condition. The data of low-frequency excitation are used in response reconstruction and the consequent damage identification while the low-frequency excitation set is used for comparative studies on Tikhonov regularization and sparse regularization in damage identification. The acceleration signal was amplified by KD5008C charge amplifier (Figure 7.3-e). All three types of responses were collected by the Kyowa EDX-100A data recorder (see Figure 7.3-d) and stored into the personal computer. Data conditioning programs, such as band-pass

filtering and detrending, were employed to perform preliminary data processing before analysis.

7.2.3 Damage Generation

Damage was induced by cutting notches of different widths on the element region (Figure 7.6-a), generating an equal reduction of element stiffness matrix and mass matrix. The steel beam was fixed by installed clamps (Figure 7.6-b) when cutting to make the boundary condition stay the same before and after damage. It should be noticed that there were no sensors installed at the damaged locations. This was arranged to demonstrate the superiority of damage identification method. According to the actual test condition, the element stiffness and mass were damaged to the same extent simultaneously. Thus, the damage hereby should be modeled as Eq. 5.13.

Two typical damage scenarios as listed in Table 6.1including single damage and multi-damage with different damage severities were designed and accomplished in the laboratory test to verify the effectiveness of the proposed method.

7.3 FE Model Updating

A finite element model of the beam was established as presented in the numerical investigation. Uncertainties in geometric dimension, physical property, and boundary conditions will induce deviations in the FE model built using the nominal values. Thus a model updating is needed to produce an FE model that represents the actual dynamic behavior of the structure. To date, most reported model updating case studies make use of modal-based formulations and these are often restricted to updating eigenvalues

only. Since the dynamic responses are mainly investigated in response reconstruction and directly used in damage identification, a two-stage model updating of the FE model is now conducted to provide an elaborate FE model for the following studies. The first-step model updating is performed in the frequency domain to find out initial values of the updated parameters while the second-step model updating is conducted in the time domain to determine the final values of the updated parameters. The data of high-frequency excitation are used for updating the initial FE model. The raw data is resampled to 1250 Hz and band-pass filtered between 2 Hz and 302 Hz using 8-order Butterworth filter before utilization. In the first-step model updating, 7 parameters are selected to be updated. They are the elastic modulus and density of the steel, the width and height of the beam section, the positions of two supports, and the additional mass of fixture connecting the vibrator to the beam. The objective is to minimize the discrepancies in the natural frequencies between the analytical and experimental results by adjusting 7 parameters. The modal parameters are extracted through data-driven stochastic subspace identification algorithm (SSI-data). The objective function in the first step updating is defined as

$$ObjFun1 = \sum_{i=1}^{N} a_i \left(\frac{f_i^a - f_i^m}{f_i^m} \right)^2 + \sum_{i=1}^{N} b_i \frac{(1-\sqrt{MAC_i})^2}{MAC_i} \tag{7.1}$$

where f_i^a and f_i^m are the analytical and experimental frequencies of the $i-th$ mode; a_i and b_i are the weighting factors, whose values depend on the accuracy of identified natural frequencies and mode shapes. They are set as 1.0 and 0.1, respectively, in this study. MAC_i is the modal assurance criteria (MAC) value for the $i-th$ analytical and experimental mode.

Based on the updated results from the first step model updating, the second-step model updating is performed in the time domain to further refine the FE model by minimizing the discrepancies between the dynamic responses from the analytical FE model and the experimental measurement. The objective of this round of model updating is to make the simulated dynamic responses from the FE model match the measured ones as close as possible by adjusting structural damping. The classical Rayleigh damping $\mathbf{C} = \alpha\mathbf{M} + \beta\mathbf{K}$ is adopted to model the structural damping of the beam. The mass and stiffness proportional damping coefficient α and β are determined by two measured mode damping ratios only without considering other measured mode damping ratios. Moreover, it is well known that it is very difficult to identify the damping ratio accurately. In this regard, the damping coefficients α and β are also chosen as updated parameters in the second-step model updating. The measured responses from 11 sensors are used in this round model updating. The objective function in the second step updating is expressed as

$$ObjFun2 = \sum_{i=1}^{N_m} \frac{\left\| \mathbf{y}_i^a - \mathbf{y}_i^m \right\|_2}{\left\| \mathbf{y}_i^m \right\|_2} \tag{7.2}$$

where $\mathbf{y_i^a}$ and $\mathbf{y_i^m}$ are the analytical and experimental dynamic responses from the $i-th$ sensor; N_m is the number of sensor measurements. The results of the two-step FE model updating are presented in Table 7.2. It is found that remarkable changes occur in the two Rayleigh damping coefficients from the second-step model updating. This is probably because the initial Rayleigh damping coefficients are approximately calculated using the identified two modal damping ratios only.

Table 7.3 presents a comparison between the calculated modal frequencies of the updated FE model and those identified experimentally. The fit goodness of responses between calculated and tested ones from the 6 accelerometers as shown in Figure 4.7 is examined by $R_{fit} = \left(1 - \left\|\mathbf{y}_i^a - \mathbf{y}_i^m\right\| / \left\|\mathbf{y}_i^m\right\|\right) \times 100$, and they are listed in Table 7.5. It is found that after the two-step updating, the analytical frequencies computed by the FE model match well with the measured frequencies. The maximum discrepancy, which occurs in the seventh mode, is 1.1%. The response fit goodness is dramatically improved to around 70%, exhibiting the high accuracy of the updated FE model presents the acceleration simulated by the updated computational model and recorded in the test on node 26. As seen in Figure 7.7, there is an excellent match between the simulated response and recorded response. The time-domain FE model updating takes into consideration different contribution weights of different mode responses while the frequency-domain FE model updating usually counts each mode equally. Therefore the time-domain FE model updating presents a more elaborate FE model than the frequency-domain FE model updating in terms of dynamic response representation.

7.4 Joint Response and Excitation Reconstruction

The test data of the low-frequency excitation with of bandwidth of 2~102 Hz are used in the joint response and excitation reconstruction. The dynamic responses recorded by the 11 sensors in their optimal locations as shown in Figure 3.3-a are imported into the KF-UI as introduced in Chapter 3 to reconstruct the responses of the beam within the response reconstruction set where no sensors are equipped. The first 7 modes are utilized in response reconstruction. The initial state estimate is set $\hat{\mathbf{x}}_0^- = 0$ as the zero

initial condition is used in the measurement. The initial state estimate error covariance $\mathbf{P}_0^{x-}$ is assigned the value as 1.0×10^{-12} on its diagonal. The small values indicate a low level of uncertainty regarding the initial state estimate. However, it should be mentioned that the results are relatively insensitive to these initial values.

External excitation was also collected by load cell installed between the beam and the vibration to check the accuracy of excitation estimation. Figure 7.4 illustrates the estimated and measured excitations. The two excitation time histories are almost overlapping, indicating very high excitation reconstruction accuracy.

Table 7.4 shows the mean RPEs of the excitation and the responses at 8 sensors (except the 11 optimally designed sensors) installed for verification. All the RPEs of response are less than 15%, indicating that a good reconstruction of response and excitation is obtained. Figure 7.5 also presents the reconstructed responses of each kind with the maximum discrepancy with the measured ones. It is observed that a good correspondence is found in both the time and frequency domains, demonstrating the effectiveness of the proposed optimal multi-type sensor placement method.

7.5 Sparse Regularization for Damage Identification

The test data of the high-frequency excitation with of bandwidth of 2~302 Hz are used to examine the effectiveness of sparse regularization for damage identification. The dynamic responses recorded by the 6 accelerometers (as shown in Figure 4.7) as well as the excitation record by load cell are utilized for damage identification. Tikhonov regularization and sparse regularization are employed in response sensitivity-based

model updating, respectively. The constraint $(-1 \le \theta_i \le 0)$ is also imposed in the sparse regularized updating. The convergence criteria are set as $Toler = 1 \times 10^{-3}$, and maximal iteration number is 20 in the experimental study. For computation ease, only 4~5s measurement of 1250 time instants data is used for damage identification. The final results are shown in Figure 7.8 for the single damage and in Figure 7.9 for multi-damage scenarios, respectively. It is observed that when using the Tikhonov regularization, besides the remarkable false-positive errors, there are plenty of tiny errors, exhibiting the possible over-fitting of Tikhonov regularization. While using the sparse regularization, the false-positive errors are dramatically reduced, as shown in Figure 7.8-b and Figure 7.9-b. The damage extents are identified as -0.191 on element 23 for the single damage scenarios and -0.078 on element 7 and -0.182 on element 23 for the multi-damage scenarios. The result demonstrates the superiority of sparse regularization in sensitivity-based model updating for damage identification.

7.6 Damage Identification via Response Reconstruction

The data set of low-frequency excitation is adopted in this section to demonstrate the superiority of response reconstruction in damage identification. Since the 7^{th} modal vibration contains low kinetic energy, the first 6 modes are used for response reconstruction. The raw data passed through a band-pass filter of 2 ~ 82 Hz before utilization.

7.6.1 Damage Identification under Known Excitation

The dynamic responses recorded by 11 sensors (shown in Figure 5.4) and excitation by

load cell are imported into the Kaman filter to reconstruct the responses of the beam where no sensors were equipped. To check the accuracy of the FE model and the result of response reconstruction, Figure 7.10 also presents the analytical response by FEA and the corresponding reconstructed responses using Kalman filter. It can be seen that the reconstructed responses match even better than the simulated ones compared with the tested responses. The Kaman filter could obtain the optimal estimated state, thus giving more accurate responses when the model error and noise effect are taken into consideration.

The reconstructed responses of the beam in each damaged state are used for sensitivity-based updating with sparsity regulation separately. Considering the asymptotical convergence property of Kalman filter, the reconstructed responses of first 1000 time instants are eliminated in model updating and only the reconstructed responses, as well as the directly measured responses of 2s' duration, are utilized for damage identification. The results of identification are depicted in Figure 7.11 for single damage and Figure 7.12 for multi-damage, respectively. In the single damage scenario, it is noted that the identified damage extent is quite accurate, while the damage location, which should be element 23, not rather element 17, is totally wrong. This result indicates the response on the limited sensors cannot provide enough information for damage location. However, using multi-sensing damage detection via response reconstruction, the damage locations and severity extents are identified to a certain accuracy. In the multi-damage scenario, we found that there is an obvious false-positive error on element 34 and false-negative error on element 7, damage extent on element 23 are not correctly predicted when directly using the measured

responses. While using multi-sensing damage detection via response reconstruction, there are small false-positive errors on the element adjacent to the damage location, but they are acceptable compared with the rough damage of 10% at element 7 and 20% at the element 23. These small false-positive errors, as well as slight inaccuracy of damage quantification, are mainly attributed to the mode prediction error using RBF network. More accurate mode shapes prediction using more well-trained networks or other mode shapes prediction methods will improve the damage identification accuracy.

7.6.2 Damage Identification under Unknown Excitation

After damage occurrence, the dynamic properties are extracted through EMA. Then the frequencies, as well as the displacement CoMAC and strain CoMAC, are imported to the trained RBF network to predict mass-normalized strain and displacement mode shapes in the damaged state. The dynamic responses recorded by 11 sensors (shown in Figure 6.3, different from the set under known excitation) are imported into the KF-UI to reconstruct the responses of the beam where no sensors were equipped and the external excitation exerted to the beam. Figure 7.13 presents the measured strain response of element 31 and the corresponding reconstructed counterpart using KF-UI. The reconstructed excitation is also shown in Figure 7.14, compared with the recorded one by the load cell. It can be seen that the reconstructed response, as well as the excitation, match well with the measured responses and excitation respectively. These results indicate that the response of the structure in the damaged state can be reconstructed, even in the absence of knowing excitation, which will be advantageous to the subsequent damage identification.

The reconstructed responses of the beam in each damaged state are used for sensitivity-based updating with sparse regulation separately. The results of identification are shown in Figure 7.15. It is noted that while using damage detection via response reconstruction, the damage location and severity extent are identified roughly. There are small false-positive errors, in particular on the elements adjacent to the damage location, but they are still acceptable.

7.7 Concluding Remarks

This chapter presents the experimental validations of the 4 approaches which are proposed to promote the vibration-based damage identification applied to large civil structures. A simply-supported overhanging beam equipped with 19 sensors of 3 types is employed in the laboratory test. A two-step FE model updating, i.e., frequency-domain comes first, and time-domain follows, is conducted to establish a delicate FE model for the subsequent studies. According to the experimental results, the following remarks should be noted:

(1) For joint response and excitation reconstruction, all the RPEs of response on the 8 validation sensors are less than 15%, indicating that with the designed optimal sensor deployment a good reconstruction of response as well as excitation can be obtained.

(2) For model updating based damage identification, the sparse regularization has certain superiority over the traditional Tikhonov regularization. When using sparse regularization, the errors between damage identification results using the

measured and simulated data are also acceptable.

(3) Both simulative and experimental study results show that the response reconstruction-oriented damage identification is more capable of locating and quantifying the damage under both known and unknown excitation circumstances.

Up to now, the numerically and experimentally investigated structure (an overhanging beam) is quite simple, and the dimension of the damage vector is not so large. To cope with the high dimensional damage identification that is more frequently encountered for the large civil structure, a multi-level damage identification method will be proposed and investigated in the forthcoming Chapter 8.

Table 7.1 General information of sensor installment

Scenario	Optimal Multi-type Sensor			
	Strain gauge	Disp. meter	Accelerometer	Sum
Known Excitation	4	1	6	11
Unknown Excitation	5	2	4	11
Total	8	2	9	19

Table 7.2 Result of two-steps FE model updating

Updating parameters	E	ρ	h	b	L_a	L_b	kM	α	β
	MPa	kg/m^3	mm	mm	m	m	kg	rad/s	s/rad
Initial value	2.06E+5	7780	15.6	50.0	1.000	3.000	0.32	0.20	1.5E-05
First-step updating	2.09E+5	8110	15.6	52.0	0.999	3.002	0.25	—	—
Second-step updating	2.12E+5	7465	15.0	48.8	1.001	2.996	0.30	0.48	2.2E-06

Table 7.3 Measured and analytical frequencies

Mode	Tested	Before updating		After first step updating		After second step updating	
		Analytical (Hz)	Error (%)	Analytical (Hz)	Error (%)	Analytical (Hz)	Error (%)
1	5.04	5.03	-0.172	4.98	-0.989	4.99	-0.880
2	8.32	8.36	0.547	8.28	-0.990	8.29	-0.314
3	17.01	17.09	0.441	16.94	-0.847	16.98	-0.208
4	42.12	42.33	0.512	41.94	-0.932	42.12	-0.005
5	63.86	64.40	0.833	63.75	-1.006	63.87	0.004
6	71.59	72.24	0.909	71.60	-0.885	71.59	-0.002
7	99.66	101.00	1.346	99.67	-1.316	100.75	1.100
8	154.00	155.42	0.923	154.02	-0.902	154.58	0.379
9	194.44	197.88	1.773	195.95	-0.978	196.17	0.892
10	208.71	212.07	1.608	210.05	-0.952	210.32	0.771
11	252.43	255.93	1.385	253.29	-1.030	254.82	0.948

Table 7.4 RPEs of the excitation and the responses on 8 sensors for verification

Sensor	S_1	S_2	S_3	S_4	D_1	A_1	A_2	A_3	U
Mean RPE	13.97	14.49	6.73	13.48	5.45	6.73	2.90	7.53	26.24

Table 7.5 Response fit goodness (100%)

Sensor Number	Before updating	After first step updating	After second step updating
A1	11.35	35.03	65.74
A2	-1.09	30.16	73.58
A3	17.31	35.34	73.67
A4	64.08	60.15	69.87
A5	15.94	34.73	73.85
A6	11.95	36.28	66.18

Figure 7.1 Laboratory test setup

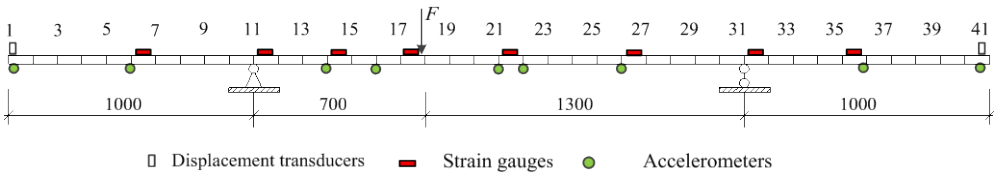

Figure 7.2 Total multi-type sensor placement in laboratory test

(a). (b)

(c). (d).

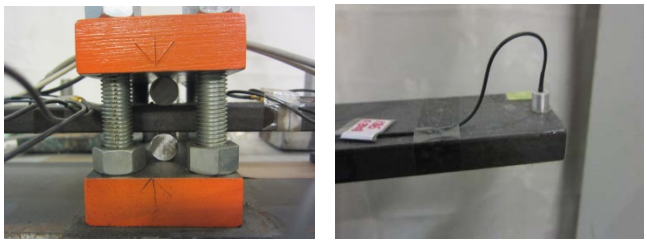

(e) (f)

Figure 7.3 Experiment instruments: (a) electromagnetic vibrator, (b) load cell and spring, (c) charge amplifier, (d) data acquisition board, (e) roller bearing and (f) accelerometer

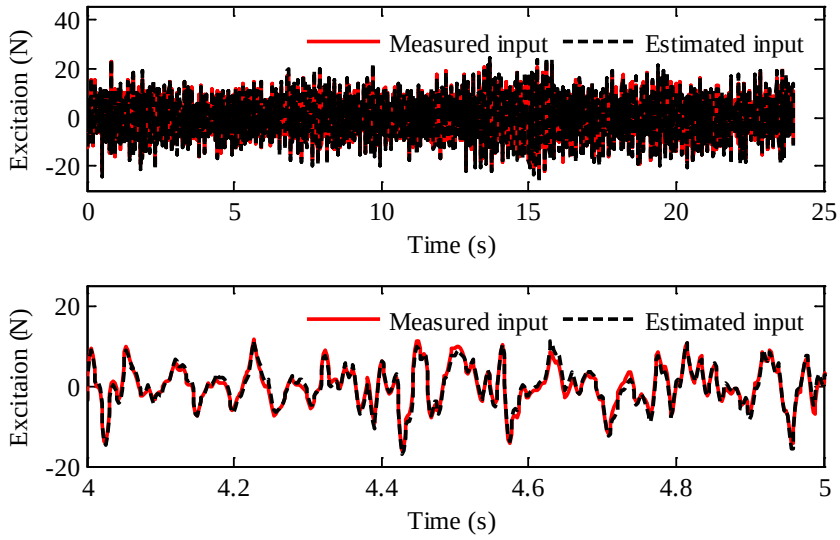

Figure 7.4 Comparison of measured and estimated excitation (Top: the time history; Bottom: a close-up view)

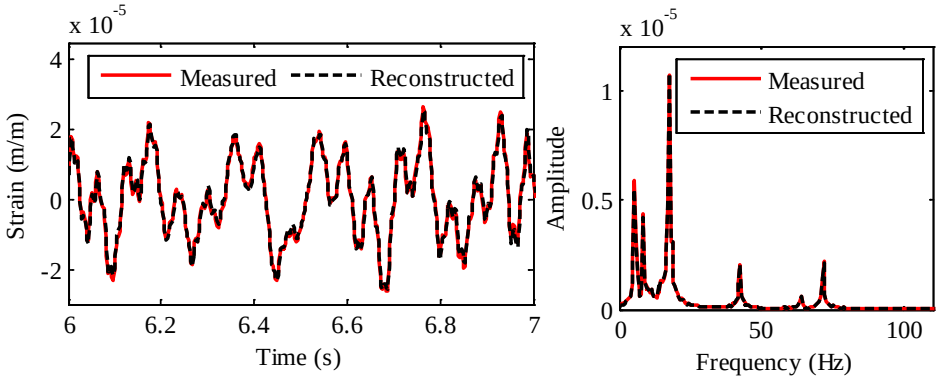

(a)

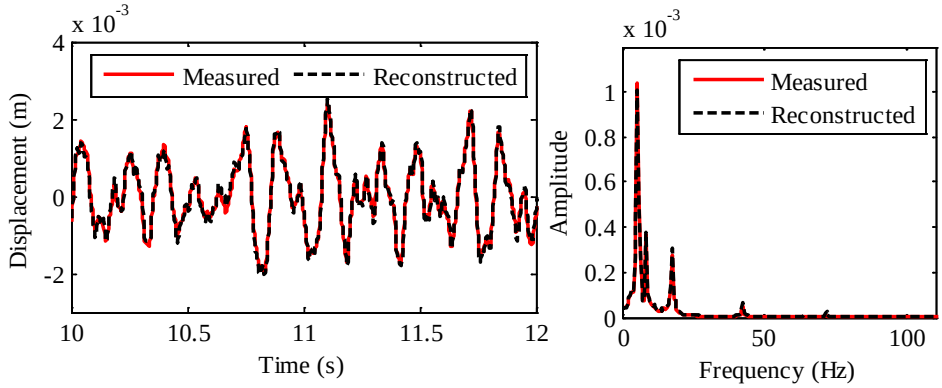

(b)

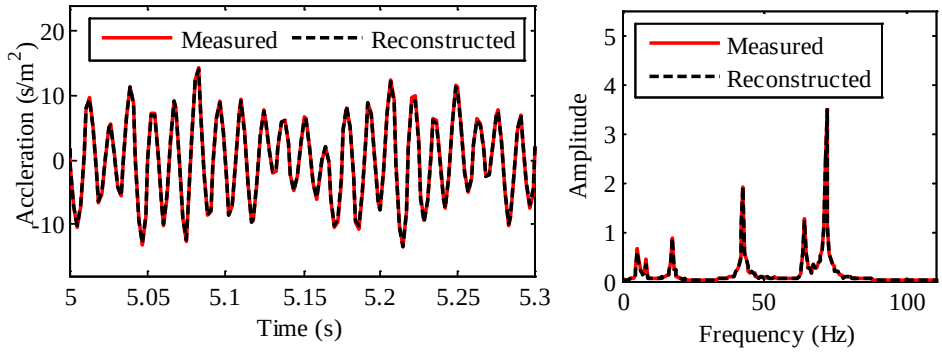

(c)

Figure 7.5 Verification of accuracy of response reconstruction method: (a) strain response at sensor S2, (b) displacement responses at sensor D1 and (c) acceleration responses at sensor A3. (Left: close-up view of time history; Right: single-sided amplitude spectrum)

(a) (b)

Figure 7.6 Damage generation: (a) clamp to fix the beam when cutting; (b) generated rectangular notches

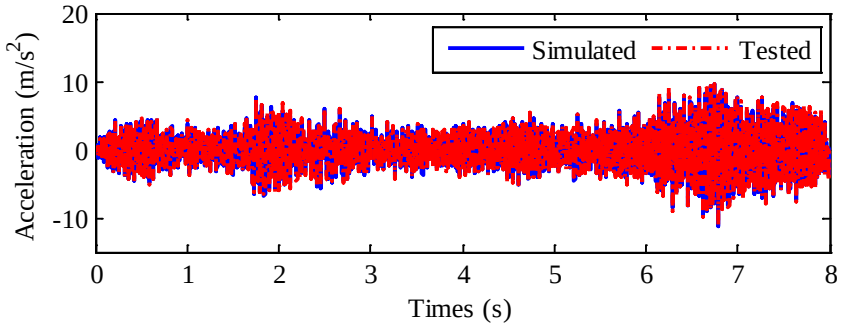

(a)

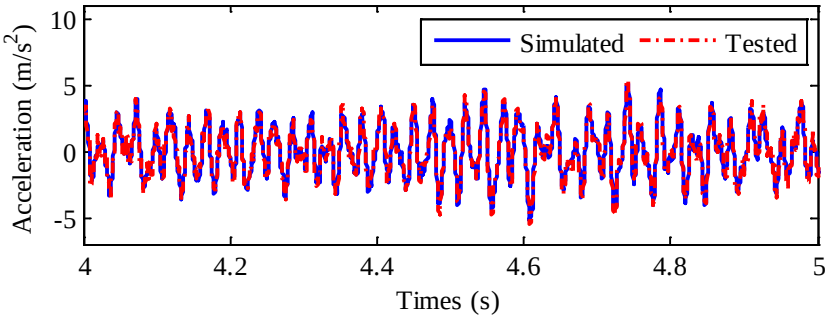

(b)

Figure 7.7 Acceleration on node 26: (a) the whole duration, (b): a close-view

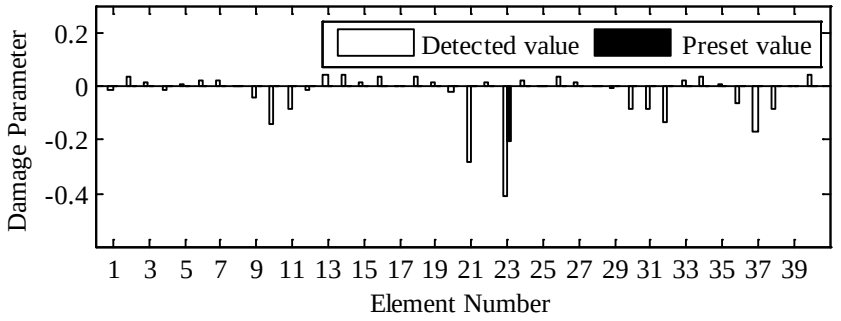

(a)

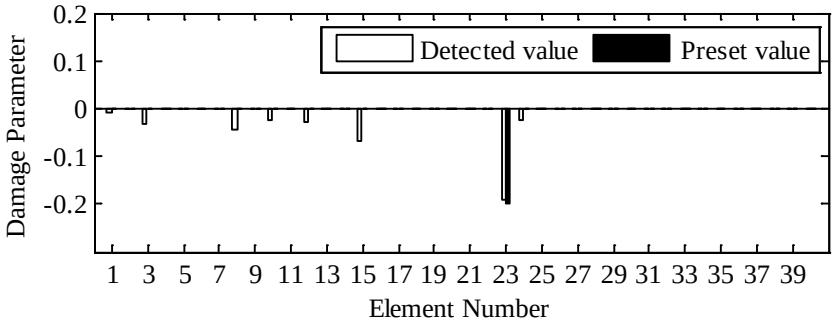

(b)

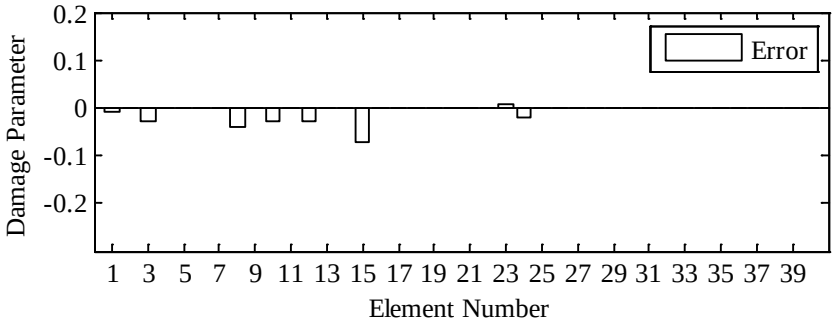

(c)

Figure 7.8 Identification of single-damage in laboratory test using (a) Tikhonov regularization (b) sparse regularization and (c) error between tested and simulated when using sparse regularization.

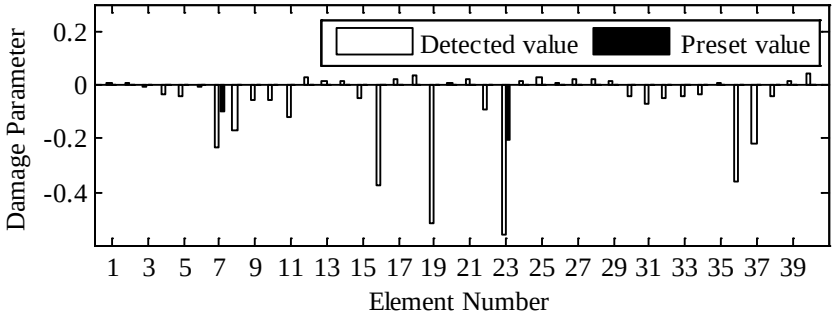

(a)

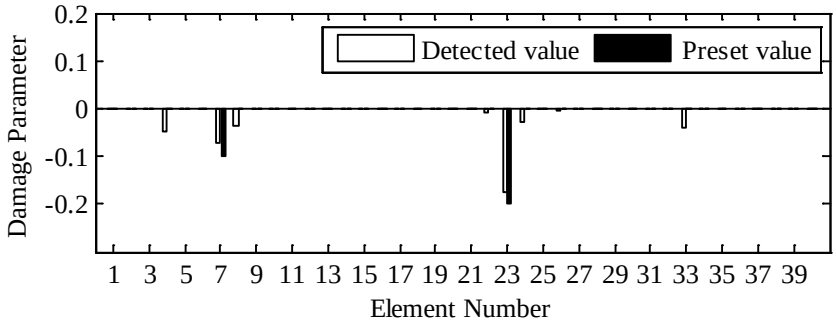

(b)

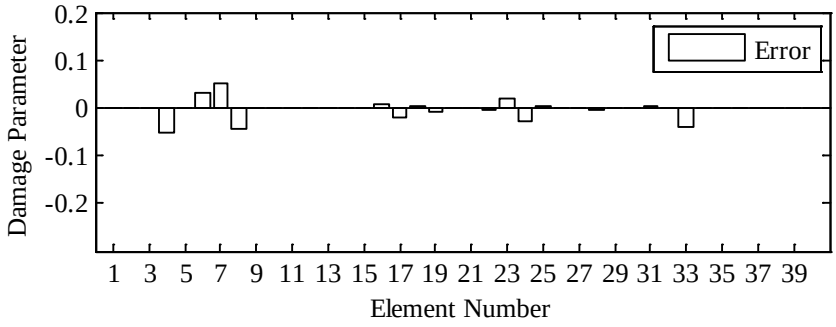

(c)

Figure 7.9 Identification of multi-damage in laboratory test using (a) Tikhonov regularization (b) sparse regularization and (c) error between tested and simulated when using sparse regularization.

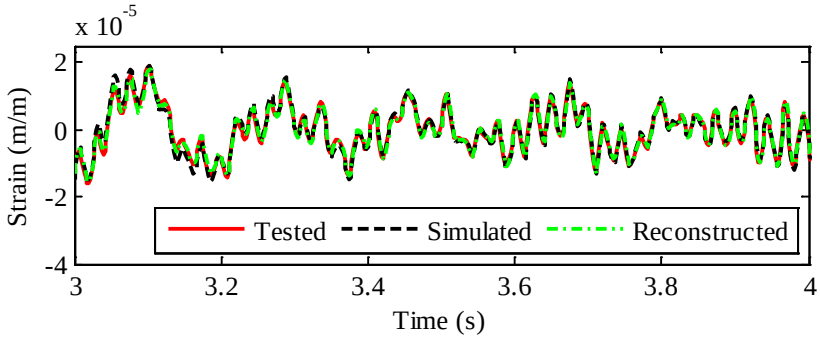

(a)

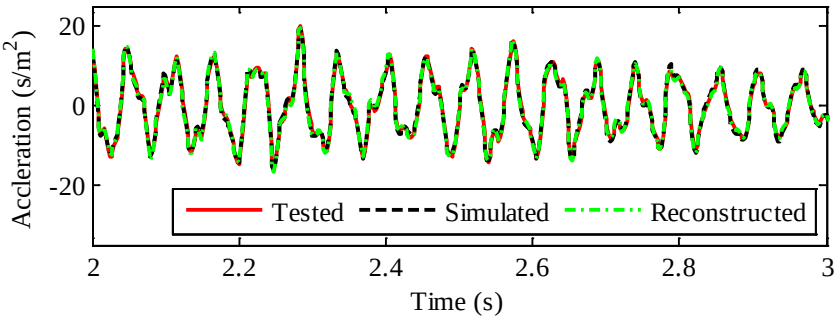

(b)

Figure 7.10 Comparison of analytical and reconstructed response: (a) bending strain at element 26 and (b) vertical displacement at node 22

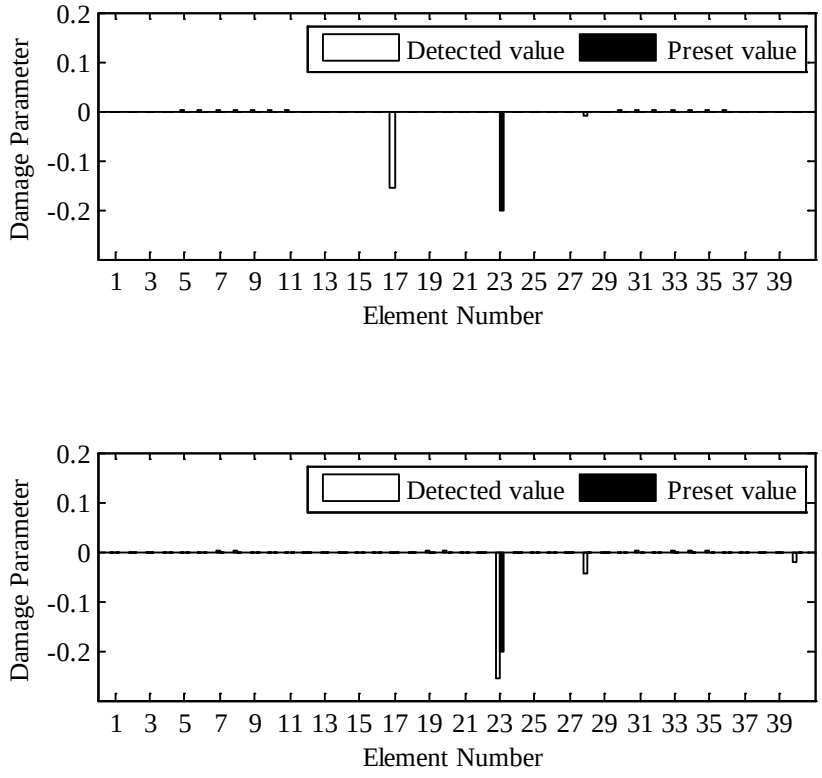

Figure 7.11 Test result of single damage scenario without response reconstruction (top) and with response reconstruction (bottom)

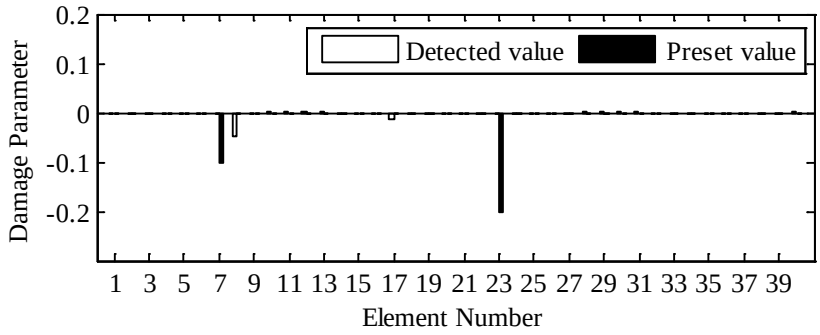

(a)

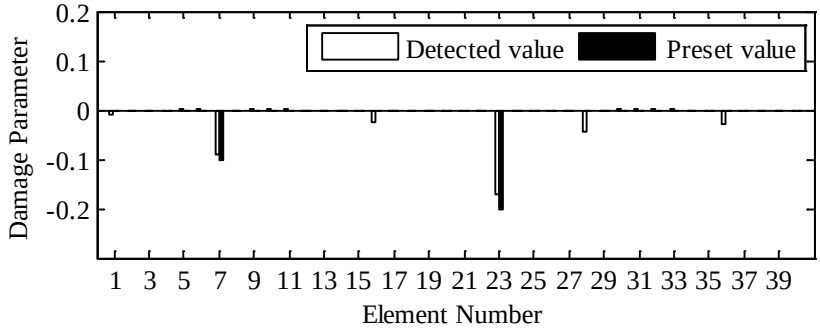

(b)

Figure 7.12 Test result of multi-damage scenario: (a) without response reconstruction and (b) with response reconstruction

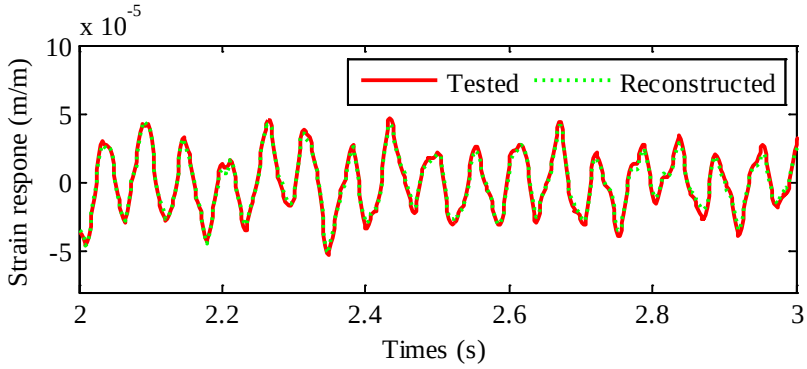

Figure 7.13 Comparison of analytical and reconstructed strain at Element 31

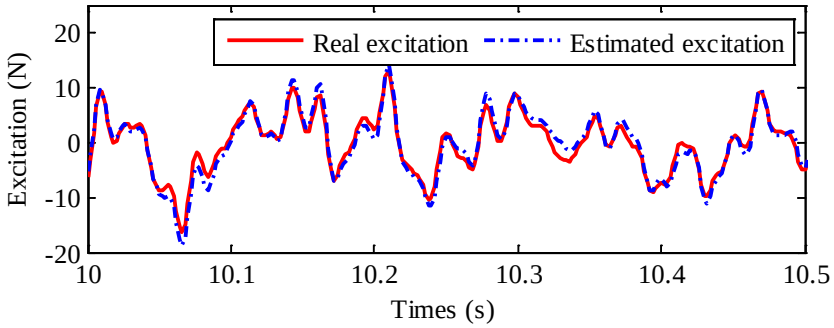

Figure 7.14 Comparison of tested and reconstructed excitation

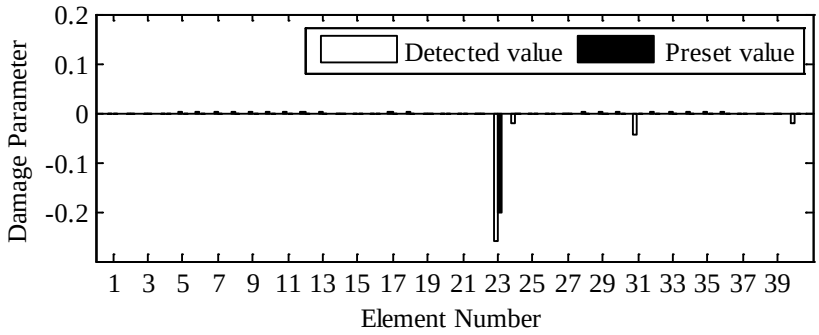

(a)

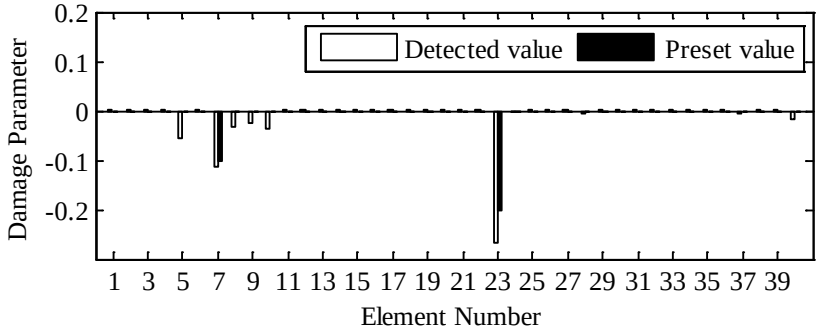

(b)

Figure 7.15 Test result of damage identification under unknown excitation: (a) for single damage and (b) for multi-damage

CHAPTER 8

MULTI-LEVEL DAMAGE IDENTIFICATION VIA RESPONSE RECONSTRUCTION

8.1 Introduction

Equation Section 8Another obstacle existing in the finite element (FE) model updating based damage identification for large civil structures is due to the fact that a complex civil structure typically composes of tens of thousands structural components, and the dimension of the corresponding damage vector is often enormous. Aside from enormous computation efforts needed in iterative updating, the ill-condition and non-global identifiability features of the solution probably make it cumbersome, even impossible, to solve the inverse problem directly. Following a divide-and-conquer strategy, a multi-level damage identification via response reconstruction method is proposed in this chapter. The entire structure is decomposed into several manageable substructures and further condensed as a super element assembly using the component mode synthesis (CMS) technique. The damage identification is performed at two levels: the first is at the substructure level to locate the potential damage region over the partitioned substructures and the second is over the suspicious substructures to further locate as well as quantify the element-level damage location and severity. In each level's identification, the damage searching space over which model updating is performed is notably narrowed down, not only reducing the computation amount but also increasing the damage identifiability. Besides, the Kalman filter based response

reconstruction is performed at the second level to reconstruct the response of the suspicious substructure for exact damage quantification. Numerical studies are conducted on a relatively larger structure, the Tsing Ma Bridge (TMB) testbed to demonstrate the procedure as well as to verify the effectiveness of the proposed multi-level damage identification via response reconstruction.

8.2 Multi-level Damage Identification

A complex real civil structure usually consists of tens of thousands structural components, and the associated potential damage dimension is very large. The response sensitivity-based model updating is in general computationally demanding due to the large dimension of the discretized FE model matrices and the large number of dynamic FE analysis during the updating procedure. Directly solving the inverse problem of damage identification over the large potential damage space is a tough task, especially when the sensor number is limited compared with the number of discrete DOFs of the structure. To address this, a multi-level damage identification strategy is proposed, in which the CMS technique, or more specifically the Craig-Bampton method, as a kind of dynamic substructuring technique, is employed to divide the entire structure into several substructures. The separated substructures are then condensed and assembled to represent the dynamic behavior of the structure for computation ease. Based on that, the damage process is stratified, and a multi-level damage identification method is proposed to narrow the potential damage space for computation convergence: damage identification is firstly performed on the reduced substructure level to locate the suspicious region where the damage may occur and then at the element level to localize the exact damage location as well as to quantify the

damage extent. Figure 8.1 depicts a schematic diagram of the proposed multi-level damage identification with response reconstruction. In this diagram, the entire FE model of a large-scale structure is decomposed into N_{n} substructures, and the scenario that damage exists in the *s*-th substructure is taken as an example for illustration. It is noted that the blocks with colored background indicate the regions over which model updating is performed for damage identification. In what follows, the multi-level damage identification will be introduced in detail.

8.2.1. The Problem Formulation of Damage Identification

The dynamics of a linear and time invariant structure can be represented by the following equation of motion as:

$$\mathbf{M}\ddot{\mathbf{d}}(t)+\mathbf{C}\dot{\mathbf{d}}(t)+\mathbf{K}\mathbf{d}(t)=\mathbf{L}\mathbf{u}(t) \tag{8.1}$$

in which $\mathbf{M}\in\Re^{n\times n}$ and $\mathbf{K}$ are the globally assembled mass and stiffness matrices of the structure. Rayleigh damping is used to characterize the damping effect, that is $\mathbf{C}=\alpha\mathbf{M}+\beta\mathbf{K}$, where the α and β are damping coefficients. $\mathbf{d}(t)\in\Re^{n}$ is the vector of displacements and a dot over it denotes differentiation with respect to time *t*. $\mathbf{L}\in\Re^{n\times p}$ is the mapping matrix, connecting the external force vector $\mathbf{u}(t)\in\Re^{p}$ to the corresponding DOFs.

Here it is assumed that structural defects only cause certain deteriorations in the stiffness matrix and it depends linearly on the damage parameter $\boldsymbol{\theta}=\left[\theta_1,\theta_2,\cdots,\theta_{N_e}\right]^T$, in which N_e is the number of elements and θ_i $(i=1,2,\cdots,N_e)$ denotes the *i*-th damage

coefficient corresponding to the *i*-th element of the structure. In this way, the damage can be modeled as:

$$\mathbf{K}_d(\boldsymbol{\theta}) = \sum_{i=1}^{N_e}\left(1+\theta_i\right)\mathbf{K}_i = \mathbf{K}_u + \sum_{i=1}^{N_e}\theta_i\,\mathbf{K}_i\left(-1 \le \theta_i \le 0\right); \mathbf{M}_d = \mathbf{M}_u \tag{8.2}$$

where $\mathbf{K}_d \in \Re^{n\times n}$ and $\mathbf{K}_u$ are the globally assembled stiffness matrices with and without damage, respectively; $\mathbf{K}_i$ ($i = 1, 2, \cdots, N_e$) is the constant global stiffness matrix partition contributed by the element *i* and $\mathbf{K}_u = \sum_{i=1}^{N_e}\mathbf{K}_i$; It is assumed that the global mass matrix before damage $\mathbf{M}_u$ and after damage $\mathbf{M}_d$ stay the same. The subscript d and u denote the damaged state and undamaged state of the investigated structure.

8.2.2. Substructures Partitioning, Reduction and Assembly

Without losing generality, a large structure is divided into N_n non-overlapping substructures. For the *s*-th substructure, the stiffness submatrix $\mathbf{K}^s$ is in the dimension of $n_s \times n_s$. The substructure number N_n should be properly selected: too small number of substructures will induce considerable accuracy sacrifice of the reduced model, and too large number of substructures will cause too much computation workloads. Accordingly, the damage vector should also be partitioned as:

$$\boldsymbol{\theta}^T = \left[\boldsymbol{\theta}^{1T}, \boldsymbol{\theta}^{2T}, \cdots, \boldsymbol{\theta}^{sT}, \cdots, \boldsymbol{\theta}^{N_nT}\right] \tag{8.3}$$

in which $\boldsymbol{\theta}^s \in \Re^{N_s}$, and $\sum_{s=1}^{N_n} N_s = N_e$. The dynamic behavior of the *s*-th isolated

substructure can be described by the equation of motion as:

$$\mathbf{M}^s\ddot{\mathbf{d}}^s(t)+\mathbf{C}^s\dot{\mathbf{d}}^s(t)+\mathbf{K}^s\mathbf{d}^s(t)=\mathbf{u}^s(t)+\mathbf{g}^s(t) \tag{8.4}$$

where $\mathbf{M}^s \in \Re^{n_s \times n_s}$, $\mathbf{C}^s$ and $\mathbf{K}^s$ are the mass, damping and stiffness matrices of the FE model of the *s*-th substructure, respectively; $\mathbf{u}^s$ (t) is the applied external forces, and $\mathbf{g}^s$ (t) is the connecting forces from the neighboring substructures. Model reduction usually partitions the total DOFs into the set of internal DOFs $\mathbf{d}_i^s \in \Re^{n_i^s}$ and the set of boundary DOFs $\mathbf{d}_b^s \in \Re^{n_b^s}$ and $n_s = n_i^s + n_b^s$. The mass, stiffness and damping matrices of the *s*-th isolated substructure are also partitioned accordingly as:

$$\mathbf{M}^s=\begin{bmatrix}\mathbf{M}_{ii}^s & \mathbf{M}_{ib}^s\\ \mathbf{M}_{bi}^s & \mathbf{M}_{bb}^s\end{bmatrix};\mathbf{K}^s=\begin{bmatrix}\mathbf{K}_{ii}^s & \mathbf{K}_{ib}^s\\ \mathbf{K}_{bi}^s & \mathbf{K}_{bb}^s\end{bmatrix};\mathbf{C}^s=\begin{bmatrix}\mathbf{C}_{ii}^s & \mathbf{C}_{ib}^s\\ \mathbf{C}_{bi}^s & \mathbf{C}_{bb}^s\end{bmatrix} \tag{8.5}$$

where the subscript *b* and *i* denote the boundary and internal DOFs, respectively. Craig-Bampton reduction (Craig and Bampton, 1987) assumes that the internal DOFs can be described in terms of the constraint modes $\mathbf{\Psi}_{ib}^s$ and the fixed-interface vibration modes $\mathbf{\Phi}_{ii}^s$. The displacement transformation from the boundary DOFs to all the DOFs then takes the form as:

$$\left\{\mathbf{d}^s\right\}=\begin{Bmatrix}\mathbf{d}_i^s\\ \mathbf{d}_b^s\end{Bmatrix}=\begin{Bmatrix}\mathbf{\Phi}_{ik}^s\boldsymbol{\eta}_k^s+\mathbf{\Psi}_{ib}^s\mathbf{d}_b^s\\ \mathbf{d}_b^s\end{Bmatrix}=\begin{bmatrix}\mathbf{\Phi}_{ik}^s & \mathbf{\Psi}_{ib}^s\\ \mathbf{0}_{bk}^s & \mathbf{I}_{bb}^s\end{bmatrix}\begin{Bmatrix}\boldsymbol{\eta}_k^s\\ \mathbf{d}_b^s\end{Bmatrix}=\left[\mathbf{\Phi}_k^s,\mathbf{\Phi}_c^s\right]\begin{Bmatrix}\boldsymbol{\eta}_k^s\\ \mathbf{d}_b^s\end{Bmatrix}=\mathbf{T}^s\mathbf{q}^s \tag{8.6}$$

where $\mathbf{\Phi}_{ik}^s \in \Re^{n_i^s \times n_k^s}$ is the n_k^s kept interior partition of fixed-interface normal modes $\mathbf{\Phi}_{ii}^s \in \Re^{n_i^s \times n_i^s}$ ($n_k^s < n_i^s$), which can be obtained by restraining all the boundary DOFs of

the s-th substructure and solving the generalized eigenvalue problem $\left(\mathbf{K}_{ii}^{s}-\mathbf{\Lambda}_{ii}^{s}\mathbf{M}_{ii}^{s}\right)\mathbf{\Phi}_{ii}^{s}=\mathbf{0}^{s}$ with the fixed-interface normal modes normalized as $\mathbf{\Phi}_{ii}^{sT}\mathbf{M}_{ii}^{s}\mathbf{\Phi}_{ii}^{s}=\mathbf{I}_{ii}^{s}$; and $\boldsymbol{\eta}_{k}^{s}\in\Re^{n_k^s}$ is the truncated set of generalized modal coordinates. $\mathbf{\Phi}_{c}^{s}=\left\{\mathbf{\Psi}_{ib}^{s},\mathbf{I}_{bb}^{s}\right\}^{T}$ is the interface constraint mode, which is calculated by setting a unit displacement on the boundary coordinates $\mathbf{d}_{b}^{s}(t)$ and zero forces in the internal DOFs; its interior partition could be obtained as $\mathbf{\Psi}_{ib}^{s}=-\left(\mathbf{K}_{ii}^{s}\right)^{-1}\mathbf{K}_{ib}^{s}$.Substituting Eq. (8.6) into Eq. (8.4) and pre-multiplying with $\mathbf{T}^{sT}$, it yields:

$$\hat{\mathbf{M}}^{s}\ddot{\mathbf{q}}^{s}(t)+\hat{\mathbf{C}}^{s}\dot{\mathbf{q}}^{s}(t)+\hat{\mathbf{K}}^{s}\mathbf{q}^{s}(t)=\hat{\mathbf{u}}^{s}(t)+\hat{\mathbf{g}}^{s}(t) \tag{8.7}$$

where the reduced matrices of the substructures and transformed forces are given by:

$$\hat{\mathbf{K}}^{s}=\mathbf{T}^{sT}\mathbf{K}^{s}\mathbf{T}^{s},\hat{\mathbf{M}}^{s}=\mathbf{T}^{sT}\mathbf{M}^{s}\mathbf{T}^{s},\hat{\mathbf{C}}^{s}=\mathbf{T}^{sT}\mathbf{C}^{s}\mathbf{T}^{s};\hat{\mathbf{u}}^{s}(t)=\mathbf{T}^{sT}\mathbf{u}^{s};\hat{\mathbf{g}}^{s}(t)=\mathbf{T}^{sT}\mathbf{g}^{s} \tag{8.8}$$

Since $n_k^s<n_i^s$, the Craig-Bampton transformation matrix $\mathbf{T}^{s}\in\Re^{n_s\times\hat{n}_s}$ ($\hat{n}_s=n_k^s+n_b^s$) is a rectangular matrix ($\hat{n}_s<n_s$) and the substructure matrix is considerably reduced.

The N_n reduced substructures should be assembled together to represent the dynamics of the entire structure. To this end, the equations of motion of the N_n reduced substructures that are to be coupled can be block-diagonally assembled as:

$$\bar{\mathbf{M}}\ddot{\bar{\mathbf{q}}}(t)+\bar{\mathbf{C}}\dot{\bar{\mathbf{q}}}(t)+\bar{\mathbf{K}}\bar{\mathbf{q}}(t)=\bar{\mathbf{u}}(t)+\bar{\mathbf{g}}(t) \tag{8.9}$$

with

$$\bar{\mathbf{K}} = blockdiag\left(\hat{\mathbf{K}}^1, \cdots, \hat{\mathbf{K}}^s, \cdots, \hat{\mathbf{K}}^{N_n}\right) = \sum_{s=1}^{N_n} \hat{\mathbf{K}}_s \tag{8.10}$$

in which $\hat{\mathbf{K}}_s \left(s = 1, 2, \cdots, N_n\right)$ denotes the global stiffness contribution offered by the s -th substructure and it is formulated as:

$$\hat{\mathbf{K}}_s = diag\left[\mathbf{0}_{\hat{n}_1 \times \hat{n}_1}, \cdots, \mathbf{0}_{\hat{n}_{s-1} \times \hat{n}_{s-1}}, \hat{\mathbf{K}}^s, \mathbf{0}_{\hat{n}_{s+1} \times \hat{n}_{s+1}}, \cdots, \mathbf{0}_{\hat{n}_{N_n} \times \hat{n}_{N_n}}\right] \tag{8.11}$$

The mass $\bar{\mathbf{M}}$ and damping matrices $\bar{\mathbf{C}}$ should be block-diagonally assembled similarly. Additionally,

$$\bar{\mathbf{q}}^T = \left[\mathbf{q}^{1T}, \cdots, \mathbf{q}^{sT}, \cdots, \mathbf{q}^{N_nT}\right]; \bar{\mathbf{u}}^T = \left[\hat{\mathbf{u}}^{1T}, \cdots, \hat{\mathbf{u}}^{sT}, \cdots, \hat{\mathbf{u}}^{N_nT}\right]; \bar{\mathbf{g}}^T = \left[\hat{\mathbf{g}}^{1T}, \cdots, \hat{\mathbf{g}}^{sT}, \cdots, \hat{\mathbf{g}}^{N_nT}\right] \tag{8.12}$$

where $\bar{\mathbf{q}} \in \Re^{n_q}$ ($n_q = \sum_{s=1}^{N_n} \hat{n}_s$) is the vector of generalized coordinates for all the n substructures; $\bar{\mathbf{u}}$ and $\bar{\mathbf{g}}$ are the assembled external forces and the connecting forces, respectively. Since some boundary DOFs are shared by multiple substructures, there are multiple entries for these boundary DOFs in the assembled vector $\bar{\mathbf{q}}$. In a primal assembly, a unique set of the generalized coordinates (including the interface DOFs and the truncated generalized modal coordinates) $\mathbf{p} \in \Re^{n_p}$ is defined that automatically satisfies the compatibility condition:

$$\bar{\mathbf{q}}(t) = \bar{\mathbf{L}}\mathbf{p}(t) \tag{8.13}$$

where the matrix $\bar{\mathbf{L}} \in \Re^{n_q \times n_p}$ is the Boolean matrix localizing the interface DOF of the substructures in the global set of DOF; $n_p = \sum_{s=1}^{N_n} n_k^s + \sum_{s=1}^{N_b} n_b^s$ in which n_b^s is the

number of DOFs at the interface s and N_b is the number of the unique interfaces. By substituting Eq. (8.13) into Eq.(8.9) and pre-multiplying with $\bar{\mathbf{L}}^T$, the primal assembled structure is obtained as:

$$\tilde{\mathbf{M}}\ddot{\mathbf{p}}(t)+\tilde{\mathbf{C}}\dot{\mathbf{p}}(t)+\tilde{\mathbf{K}}\mathbf{p}(t)=\bar{\mathbf{L}}^T\bar{\mathbf{u}}(t) \tag{8.14}$$

with the primal assembled structure matrices defined as:

$$\tilde{\mathbf{M}}=\bar{\mathbf{L}}\bar{\mathbf{M}}\bar{\mathbf{L}};\tilde{\mathbf{C}}=\bar{\mathbf{L}}^T\bar{\mathbf{C}}\bar{\mathbf{L}};\tilde{\mathbf{K}}=\bar{\mathbf{L}}^T\bar{\mathbf{K}}\bar{\mathbf{L}} \tag{8.15}$$

It is noted that the equilibrium condition allows to remove the interface forces $\bar{\mathbf{g}}$ from the equations, since $\bar{\mathbf{L}}^T\bar{\mathbf{g}}=\mathbf{0}$, making that the sum of connection forces acting on each boundary DOF equals to zero. Traditional time integration methods like Newmark method or state space formulation could be used for dynamic response calculation of the boundary DOFs and the truncated generalized modal coordinates in Eq. (8.14). Besides, the local response inside the substructures, for example, the strain on the elements of *s*-th substructure, can also be obtained by the transformation from the boundary displacement as follows:

$$\boldsymbol{\varepsilon}^s=\mathbf{B}^s\mathbf{d}^s=\mathbf{B}^s\mathbf{T}^s\mathbf{q}^s \tag{8.16}$$

where $\mathbf{B}^s\in\Re^{N_s\times n_s}$ characterizes the relationship between displacement and strain of the *s*-th substructure.

8.2.3. Substructure Level Damage Detection

It is assumed that the *s*-th substructure composes of N_s elements and its stiffness

matrix $\mathbf{K}^s \in \Re^{n_s \times n_s}$ takes the form similar to Eq. (8.2) as:

$$\mathbf{K}_d^s\left(\boldsymbol{\theta}^s\right) = \sum_{i=1}^{N_s}\left(1+\theta_i^s\right)\mathbf{K}_i^s = \mathbf{K}_u^s + \sum_{i=1}^{N_s}\theta_i^s\mathbf{K}_i^s\left(-1 \le \theta_i^s \le 0\right) \tag{8.17}$$

where $\mathbf{K}_i^s$ is the constant segmental stiffness matrix contributed by the element *i* to the stiffness matrix of the *s*-th substructure. The stiffness matrix in a damaged state $\mathbf{K}_d^s$ is a function of damage vector $\boldsymbol{\theta}^s = \left[\theta_i^s, \theta_2^s, \cdots \theta_{Ns}^s\right]^T$. To decrease the damage vector dimension, it is assumed at this moment that the stiffness deterioration caused by the certain elements in the *s*-th substructure is expressed as an equivalent deterioration on the substructure as:

$$\mathbf{K}_d^s\left(\boldsymbol{\theta}^s\right) = \sum_{i=1}^{N_s}\left(1+\theta_i^s\right)\mathbf{K}_i^s = \left(1+\tilde{\theta}_s\right)\sum_{i=1}^{N_s}\mathbf{K}_i^s = \left(1+\tilde{\theta}_s\right)\mathbf{K}_u^s \tag{8.18}$$

If any members of the *s*-th substructure are damaged, this parameter $\tilde{\theta}_s$ shows the 'equivalent' damage extent of the substructure. Equation (8.10) and (8.15) show the reduced substructural matrices are block-diagonally assembled and transformed by the Boolean matrix $\overline{\mathbf{L}}$ to constitute the condensed whole structural matrices. By combining Eq.(8.8) with Eq.(8.11), it is noted that $\hat{\mathbf{K}}_s$ is linearly related to $\mathbf{K}^s$ under the assumption (8.18)as:

$$\left(1+\tilde{\theta}_s\right)\hat{\mathbf{K}}_s = diag\left[\mathbf{0}_{\hat{n}_1\times\hat{n}_1}, \cdots, \mathbf{0}_{\hat{n}_{s-1}\times\hat{n}_{s-1}}, \mathbf{T}^{sT}\left(1+\tilde{\theta}_s\right)\mathbf{K}^s\mathbf{T}^s, \mathbf{0}_{\hat{n}_{s+1}\times\hat{n}_{s+1}}, \cdots, \mathbf{0}_{\hat{n}_{N_n}\times\hat{n}_{N_n}}\right] \tag{8.19}$$

Then, submitting Eq.(8.10) and Eq.(8.19) into Eq.(8.15), it can be proved that the reduced substructural matrices linearly depend on the substructure level damage

parameter $\tilde{\boldsymbol{\theta}}=\left[\tilde{\theta}^1,\cdots,\tilde{\theta}^s,\cdots,\tilde{\theta}^{N_n}\right]^T$ as:

$$\tilde{\mathbf{K}}_d\left(\tilde{\boldsymbol{\theta}}\right)=\bar{\mathbf{L}}^T\left(\sum_{s=1}^{N_n}\left(1+\tilde{\theta}_s\right)\hat{\mathbf{K}}_s\right)\bar{\mathbf{L}}=\sum_{s=1}^{N_n}\left(1+\tilde{\theta}_s\right)\bar{\mathbf{L}}^T\hat{\mathbf{K}}_s\bar{\mathbf{L}}=\sum_{s=1}^{N_n}\left(1+\tilde{\theta}_s\right)\tilde{\mathbf{K}}_s=\tilde{\mathbf{K}}_u+\sum_{s=1}^{N_n}\tilde{\theta}_s\tilde{\mathbf{K}}_s \quad (8.20)$$

in which the dimension of damage vector is remarkably reduced from N_e to N_n. By performing the partial differential on both sides of Eq.(8.14) with respect to the *s*-th entry $\tilde{\theta}_s$ of the equivalent damage parameter $\tilde{\boldsymbol{\theta}}$, it yields:

$$\tilde{\mathbf{M}}\frac{\partial\ddot{\mathbf{p}}(t)}{\partial\tilde{\theta}_s}+\tilde{\mathbf{C}}\frac{\partial\dot{\mathbf{p}}(t)}{\partial\tilde{\theta}_s}+\tilde{\mathbf{K}}\frac{\partial\mathbf{p}(t)}{\partial\tilde{\theta}_s}=-\tilde{\mathbf{K}}_s\left[\beta\dot{\mathbf{p}}(t)+\mathbf{p}(t)\right] \quad (8.21)$$

It can be seen that if the measurement locations are all in the boundary DOFs, the response sensitivity can be obtained by calculating $\partial\mathbf{p}(t)/\partial\tilde{\theta}_s$ in Eq.(8.21) using the well-known time integration method like Newmark method or stat-space formulation with the excitation as $\mathbf{u}_s=-\tilde{\mathbf{K}}_s\left[\beta\dot{\mathbf{p}}(t)+\mathbf{p}(t)\right]$. When the measurement matrix is the collection of the multiple responses, such as strain $\boldsymbol{\varepsilon}(t)$, displacement $\mathbf{d}(t)$, and acceleration $\ddot{\mathbf{d}}(t)$, that is $\mathbf{y}(t)=\left\{\boldsymbol{\varepsilon}(t);\mathbf{d}(t);\ddot{\mathbf{d}}(t)\right\}\in\Re^{N_t\cdot N_m}$, its sensitivity matrix $\mathbf{S}_{\tilde{\theta}_S}=\partial\mathbf{y}(t)/\partial\tilde{\theta}_s$ can be transformed as follows:

$$\frac{\partial\mathbf{d}^s(t)}{\partial\tilde{\theta}_s}=\bar{\mathbf{T}}^s\bar{\mathbf{L}}\frac{\partial\mathbf{p}(t)}{\partial\tilde{\theta}_s};\frac{\partial\ddot{\mathbf{d}}^s(t)}{\partial\tilde{\theta}_s}=\bar{\mathbf{T}}^s\bar{\mathbf{L}}\frac{\partial\ddot{\mathbf{p}}(t)}{\partial\tilde{\theta}_s};\frac{\partial\boldsymbol{\varepsilon}^s(t)}{\partial\tilde{\theta}_s}=\frac{\partial\left[\mathbf{B}^s\mathbf{d}^s(t)\right]}{\partial\tilde{\theta}_s}=\mathbf{B}^s\bar{\mathbf{T}}^s\bar{\mathbf{L}}\frac{\partial\mathbf{p}(t)}{\partial\tilde{\theta}_s} \quad (8.22)$$

in which $\bar{\mathbf{T}}^s=diag\left[\mathbf{0}_{\hat{n}_1},\cdots,\mathbf{0}_{\hat{n}_{s-1}},\mathbf{T}^s,0_{\hat{n}_{s+1}},\cdots,\mathbf{0}_{\hat{n}_{N_n}}\right]$, $s=1,2,\cdots,N_n$; N_m denotes the number of measurement sensors and N_t is the number of measurement instants. In the

substructure level damage detection, the equivalent damage parameter $\tilde{\boldsymbol{\theta}}$ can be sought using the discrepancy between the measured responses and the analytical responses of the reduced model of the structure through model updating as:

$$\mathbf{S}_{\tilde{\boldsymbol{\theta}}}^{k}\Delta\tilde{\boldsymbol{\theta}}^{k+1}=\Delta\mathbf{y}_{d}^{m,k} \tag{8.23}$$

where $\Delta\mathbf{y}_{d}^{m,k}=\mathbf{y}_{d}^{m}-\mathbf{y}_{a}^{m,k}=\left[\mathbf{y}_{d}^{m}-\mathbf{y}_{a}^{m}\left(\tilde{\boldsymbol{\theta}}^{k}\right)\right]\in\Re^{N_m\cdot N_t}$ are the discrepancy of measured response in a damaged state $\mathbf{y}_{d}^{m}$ and the analytical response on the measurement location $\mathbf{y}_{a}^{m}$ produced by the FE model with $\tilde{\boldsymbol{\theta}}^{k}$; $\mathbf{S}_{\tilde{\boldsymbol{\theta}}}^{k}=\left[\mathbf{S}_{\tilde{\theta}_1}^{k},\cdots,\mathbf{S}_{\tilde{\theta}_s}^{k},\cdots,\mathbf{S}_{\tilde{\theta}_{Nn}}^{k}\right]\in\Re^{N_m\cdot N_t\times N_n}$ is the sensitivity matrix of the analytical response $\mathbf{y}_{a}^{m}$ with respect the equivalent damage vector. Substructure level damage detection is performed over the N_n condensed substructures through the sparse regularized FE model updating as:

$$\Delta\tilde{\boldsymbol{\theta}}^{k+1}=\min_{\Delta\tilde{\boldsymbol{\theta}}^{k+1}\in\Re^{N_n}}\left(\left\|\mathbf{S}_{\tilde{\boldsymbol{\theta}}}^{k}\Delta\tilde{\boldsymbol{\theta}}^{k+1}-\Delta\mathbf{y}_{d}^{m,k}\right\|_2^2+\mu\left\|\Delta\tilde{\boldsymbol{\theta}}^{k+1}\right\|_1^1\right) \tag{8.24}$$

Generally, the number of substructures is much less than that of the total elements, i.e. $N_n<<N_e$, making the inverse problem easier to be solved and computationally efficient. If the *s*-th entry is identified to be a certain negative value, some damages probably exist in the region corresponding to the *s*-th substructure. Then the second (element) level damage identification is further performed: more precisely damage localization and quantification over the suspiciously damaged region identified in the substructure level damage detection.

8.2.4. Element Level Damage Identification

8.2.4.1 Damage Identification over the Suspicious Substructure

Without losing generality, the scenario that the *s*-th substructure is identified as the suspiciously damaged one in substructure level damage detection is taken as an example for illustration. By substituting the stiffness matrix of the *s*-th substructure, Eq.(8.17), into Eq.(8.2), the global stiffness matrix of the structure is expressed as:

$$\mathbf{K}_d\left(\boldsymbol{\theta}\right)=\mathbf{K}_d\left(\boldsymbol{\theta}^s\right)=\mathbf{K}_u+\sum_{i=1}^{N_s}\theta_i^s\bar{\mathbf{K}}_i^s \tag{8.25}$$

where $\bar{\mathbf{K}}_i^s=\mathbf{L}^s\mathbf{K}^s\mathbf{L}^{sT}$ is the contribution offered by the *i*-th element in the *s*-th substructure to the global stiffness of the structure and $\mathbf{L}^s\in\Re^{n\times n_s}$ is a Boolean matrix mapping the DOFs of the *s*-th substructure to the global stiffness matrix of the structure. Please be noted that the damage dimension in Eq.(8.25) is N_s, which is different from that of N_e in Eq.(8.2). By submitting the damaged stiffness matrix as Eq.(8.25) into Eq. (8.2) and then performing the partial differential on both sides of Eq. (8.2) with respect to the *i*-th entry θ_i^s of the damage parameter $\boldsymbol{\theta}^s$, it yields:

$$\mathbf{M}\frac{\partial\ddot{\mathbf{d}}(t)}{\partial\theta_i^s}+\mathbf{C}\frac{\partial\dot{\mathbf{d}}(t)}{\partial\theta_i^s}+\tilde{\mathbf{K}}\frac{\partial\mathbf{d}(t)}{\partial\theta_i^s}=-\bar{\mathbf{K}}_i^s\left[\beta\dot{\mathbf{d}}(t)+\mathbf{d}(t)\right] \tag{8.26}$$

Similar to Eq.(8.21), the sensitivity matrix $\mathbf{S}_{\theta_i^s}=\partial\mathbf{y}(t)/\partial\theta_i^s$ can be obtained basing on the time integration of Eq.(8.26)as:

$$\mathbf{S}_{\theta_i^s} = \frac{\partial \mathbf{y}(t)}{\partial \theta_i^s} = \frac{\partial}{\partial \theta_i^s}\left[\boldsymbol{\varepsilon}(t); \mathbf{d}(t); \ddot{\mathbf{d}}(t)\right] = \left[\mathbf{B}\frac{\partial \mathbf{d}(t)}{\partial \theta_i^s}; \frac{\partial \mathbf{d}(t)}{\partial \theta_i^s}; \frac{\partial \ddot{\mathbf{d}}(t)}{\partial \theta_i^s}\right] \tag{8.27}$$

Then, the element level damage identification could be performed through model updating over the subset damage parameter $\boldsymbol{\theta}^s \in \Re^{N_s}$. It is reasonable that the local response inside the substructure is mostly advantageous for the element level damage identification. However, in practical situations, there probably exists the scenario that the installed sensors are far from the potentially damaged region. A preferable strategy is to reconstruct the local responses at the locations inside the suspicious substructure. Kalman filter based response reconstruction for damage identification is briefly introduced in the following section.

8.2.4.2 Response Reconstruction on the Suspicious Substructure

The responses inside the suspicious substructure identified in substructure level damage detection are focused on and reconstructed for the element-level damage identification. A state-space formulation of the structural system is needed in Kalman filter based state estimation and response reconstruction. Theoretically, the full model, global model or hybrid model (condensed model on the non-suspicious substructure and full model on the suspicious substructure) are all possible alternatives in formulating the state-space model. To avoid the tedious transformation from boundary DOFs to internal DOFs, the full FE model is employed. Then the equation of motion of the structure expressed in Eq. (8.1) can be formatted into a discrete-time modal state-space representation as:

$$\mathbf{x}_{k+1} = \mathbf{A}_d \mathbf{x}_k + \mathbf{B}_d \mathbf{u}_k + \mathbf{w}_k \tag{8.28}$$

$$\mathbf{y}_k^m = \mathbf{C}_d^m \mathbf{x}_k + \mathbf{D}_d^m \mathbf{u}_k + \mathbf{v}_k \tag{8.29}$$

where $\mathbf{x}_k = \left\{ \mathbf{q}_k^r \;\; \dot{\mathbf{q}}_k^r \right\}^T \in \Re^{2r}$ is the discrete-time state vector; $\mathbf{w}_k \in \Re^{2r}$ and $\mathbf{v}_k \in \Re^{N_m}$ denote the white Gaussian system modeling error and measurement noise vectors with covariance matrices $\mathbf{Q}$ and $\mathbf{R}^m$, respectively. In this representation, the vibration of the structure is supposed to be expressed as the superposition of the first several modal responses as $\mathbf{d}(t) = \mathbf{\Phi}^r \mathbf{q}^r(t)$, where $\mathbf{\Phi}^r \in \Re^{n \times r}$ is the collection of first r columns of the mass-normalized mode shape $\mathbf{\Phi}$, which is obtained by eigenvalue analysis $\left(\mathbf{K} - \mathbf{\Omega}^2 \mathbf{M}\right)\mathbf{\Phi} = \mathbf{0}$. Kalman filter, as a well-known unbiased and minimal variance estimator, is adopted here to give an optimal estimate of state vector $\mathbf{x}_k$ (Kalman, 1960; Zhang *et al*., 2012) as:

$$\hat{\mathbf{x}}_{k+1} = \left(\mathbf{I} - \mathbf{K}_k \mathbf{C}_d^m\right)\left(\mathbf{A}_d \hat{\mathbf{x}}_k + \mathbf{B}_d \mathbf{u}_k\right) + \mathbf{K}_k \left(\mathbf{y}_{k+1}^m - \mathbf{D}_d^m \mathbf{u}_{k+1}\right)$$

in which the Kalman gain $\mathbf{K}_k = \mathbf{P}_k \mathbf{C}_d^{mT} \left(\mathbf{C}_d^m \mathbf{P}_k \mathbf{C}_d^{mT} + \mathbf{R}^m\right)^{-1}$. In the element level damage identification, the responses of the suspicious substructure are intended to be reconstructed from the measured responses due to their high correlation with the damages in the suspicious substructure. The reconstructed responses at the desired locations are obtained as:

$$\mathbf{y}_k^e = \mathbf{C}_d^s \hat{\mathbf{x}}_k + \mathbf{D}_d^s \mathbf{u}_k \tag{8.30}$$

in which $\mathbf{C}_d^s \in \Re^{N_r \times 2r}$ and $\mathbf{D}_d^s \in \Re^{N_r \times p}$ consist of modal shapes corresponding to DOFs of the suspicious substructures, where N_r denotes the number of locations whose

responses are reconstructed.

From Eq.(8.28) and Eq.(8.29), it is noted that the frequencies, damping ratios and mode shapes of measurement points in the damaged state are needed in deriving the estimator $\hat{\mathbf{x}}_k$ through Kalman filter. The former two could be extracted by the experimental modal analysis (EMA) and the later can be replaced by mode shapes of measurement points in the intact state since these mode shapes usually alter slightly when the installed sensors away from damage. When reconstructing the responses of the suspicious substructure as Eq.(8.30), the availability of the mode shapes of the suspicious substructure in the damaged state is of main concern. As introduced in Chapter 5 and Chapter 6, they are possibly obtained by using Radial-basis-function (RBF), which is a kind of the multi-hidden-layer feedforward network artificial neural network (ANN) with sigmoid functions as transfer functions for the neurons in the hidden layers and linear functions for the output layer. The basic idea of RBF network applications in mode shape prediction is to build a model to establish the relationships between modal parameters and mode shapes through a training process using the input and output data of the appropriate training sets.

We set the connection between the parameters extracted from the measurement on the limited sensors and the mode shapes of the suspicious substructure through the RBF network. Thus, the input to the network could be the frequency-domain parameters, such as frequencies, displacement (strain) coordinate modal assurance criterion (CoMAC) values or the combination of them, or the frequency response function (FRF) related properties; and the output of the network is the collection of mass-normalized mode shape of the suspicious substructure. In Chapters 5 and 6, the

frequencies, displacement, and strain CoMAC are used as the inputs to RBF network. However, simulation studies show that modal identification using the responses on 35 sensors through the subspace state space system identification is too time-consuming to afford. Therefore, in the element-level damage identification of TMB, the integration of frequency response function (FRF) is alternatively used as the input to RBF network for mode shape prediction. Then the procedure of model properties extraction could be avoided to save the computation efforts. The basic formula of FRF expresses as:

$$\mathbf{H}_{ji}(\omega)=\frac{\mathbf{X}_j(\omega)}{\mathbf{F}_i(\omega)}=\sum_{r=1}^{m}\frac{\varphi_{jr}\varphi_{ir}}{\omega_r^2-\omega^2+j2\xi_r\omega_r\omega} \tag{8.31}$$

where $\mathbf{H}_{ji}(\omega)=\frac{\mathbf{X}_j(\omega)}{\mathbf{F}_i(\omega)}=\sum_{r=1}^{m}\frac{\varphi_{jr}\varphi_{ir}}{\omega_r^2-\omega^2+j2\xi_r\omega_r\omega}$ is the displacement of the structure on the *j*-th measurement location in the frequency domain and $\mathbf{F}_i(\omega)$ is the input to the structure at the *i*-th location in the frequency domain; φ_{jr} and φ_{ir} are the *r*-th mode shapes on the site *j* and *i*, respectively; ω_r and ξ_r is the circular frequency and modal damping ratio of the *r*-th mode and *m* denotes the number of modes. FRF can be viewed as a function of frequency which describes the relationship between the excitation force and the response. Clearly, it characterizes the essential features of structures. The integration of its amplitude, expressed as $I_j=\int_{\omega_l}^{\omega_u}\left|\mathbf{H}_{ji}(\omega)\right|d\omega$, which represents the overall information on frequency, mode shape and damping ratio of the structure, is used as the inputs to RBF network.

The appropriate training sets (damage scenarios) generated by numerical analysis

using the FE model of the damage free structure are used in network training. In each damage scenarios, the elements of the suspicious substructure are impaired to the certain value of the training damage sets. Then the dynamic responses on the measurement points are achieved by transient analysis using the predefined damage. To make the designed RBF network more robust to measurement noise in mode shapes prediction, the simulated responses are added by certain simulated measurement noise. The network training input data can be obtained through the noise-corrupted dynamic responses. The output data $\mathbf{\Phi}_k^s$ can be obtained by eigenvalue analysis using the full FE model of the structure with certain preset damages. Finally, the RBF network is trained using the input and output data by tuning the weight and center vector of neurons.

8.2.4.3 Element-level damage identification via response reconstruction

After damage occurrence, the integration of FRF derived using the measurement data can be imported into the trained RBF network to predict the mass-normalized displacement mode shapes $\mathbf{\Phi}_d^s$ and the strain mode shapes $\mathbf{\Psi}_d^s$ of the suspicious substructure. Finally, the response of the damaged suspicious substructure can be reconstructed using the Kalman filter-based method introduced in above section. And local damages exist inside the substructure can be further located and quantified through FE model updating as

$$\mathbf{S}_{\boldsymbol{\theta}^s}^k \Delta\boldsymbol{\theta}^{s,k+1} = \Delta\mathbf{y}_d^{e,k} \tag{8.32}$$

in which $\Delta\mathbf{y}_d^{e,k} = \mathbf{y}_d^e - \mathbf{y}_a^{e,k}$ denotes the discrepancy of the reconstructed response $\mathbf{y}_d^e$ of

the suspicious substructure and the analytical response $\mathbf{y}_a^{e,k} = \mathbf{y}_a^e\left(\boldsymbol{\theta}^{s,k}\right)$ on the *s*-th substructure; $\mathbf{S}_{\boldsymbol{\theta}^s}^k = \left[\mathbf{S}_{\theta_1^s}^k, \cdots, \mathbf{S}_{\theta_i^s}^k, \cdots, \mathbf{S}_{\theta_{Ns}^s}^k\right] \in \Re^{N_r \cdot N_t \times N_s}$ is the sensitivity matrix of the analytival response $\mathbf{y}_a^{e,k}$ with respect the damage vector $\boldsymbol{\theta}^{s,k}$. Besides, the dimension of updating vector is also dramatically decreased since $N_s << N_e$. Similarly, sparse regularization is employed to solve Eq.(8.32) as:

$$\Delta\boldsymbol{\theta}^{s,k+1} = \underset{\Delta\boldsymbol{\theta}^{k+1} \in \Re^{Ne}}{\operatorname{argmin}}\left(\left\|\mathbf{S}_{\boldsymbol{\theta}^s}^k \Delta\boldsymbol{\theta}^{s,k+1} - \Delta\mathbf{y}_d^{e,k}\right\|_2^2 + \mu\left\|\Delta\boldsymbol{\theta}^{s,k+1}\right\|_1^1\right) \tag{8.33}$$

Then the final damage vector as Eq. (8.3) is obtained as:

$$\boldsymbol{\theta} = \left[\mathbf{0}_{N_1}; \cdots; \mathbf{0}_{N_{s-1}}; \boldsymbol{\theta}^s; \mathbf{0}_{N_{s+1}}; \cdots, \mathbf{0}_{N_{Nn}}\right] \tag{8.34}$$

8.2.5. Some Considerations of the Proposed Method

For the proposed multi-level damage identification via response reconstruction method, the following aspects are worth highlighting:

1. In the proposed method, response reconstruction is only performed in the element-level damage identification. The main reason is that to predict the mode shape of on the boundary DOFs of the entire structure using the RBF network, which is needed in reconstructing the response of damaged state, is an intractable task. Thus the substructure level damage detection is firstly performed to decrease the computation demand of the mode shape prediction as well as response reconstruction while increasing the mode shape prediction accuracy.

2. In the substructure level damage detection, the damage dimension is remarkably reduced, making the damage detection over the condensed substructures by directly using the limited measured responses feasible. An equivalent damage vector is sought to account and signify the existence of damages on the suspicious substructure, while the extent of the identified damage vector, which only shows the relative severity of the damage, is not of such importance.

3. In the element-level damage identification, theoretically, the local damage can be identified by performing model updating using limited measured response over the suspicious substructure, of which the damage dimension is significantly reduced. However, considering that the installed sensors probably are not in the vicinity of the suspicious substructure, the multi-type responses of the substructure are thus reconstructed using the Kalman filter based method. The full FE model of the structure is employed in response reconstruction to avoid the tedious transformation from boundary DOFs to internal DOFs.

8.3 Testbed of TMB

Up to now, there are still no successful applications of vibration-based damage identification applied to large civil structures (Xu and Xia, 2012). The main reason is that large civil structures, such as long-span suspension bridges, are usually large in dimension and complex in structural components. Besides, the operational environments also have significant effects on the energetic vibrations of the structure. In consideration of all the above, it is necessary and meaningful to examine the feasibility and performance of the proposed multi-level damage identification method

in the well-controlled laboratory environment before applying it to real civil structures.

A laboratory-based testbed of the Tsing Ma suspension bridge, shown as in Figure 8.2, was established in the Structural Dynamic Laboratory of The Hong Kong Polytechnic University. The testbed was modeled and constructed based on the prototype of Tsing Ma suspension bridge in a geometric scale of 1:150. Tsing Ma Bridge (TMB) is the longest suspension bridge in the world carrying both highway and railway, connecting the Tsing Yi Island and Ma Wan Island in Hong Kong. The main span across the Tsing Yi Island and Ma Wan Island is 1,377 m long. All of the major structural components of the Tsing Ma Bridge have been included in the testbed so that the model can represent the real vibration of the major structural components of long suspension bridges and structural condition related studies can be conducted on this testbed. Two kinds of materials were chosen in the bridge model design and fabrication: (1) steel is used for the bridge towers, piers, cables, suspenders, and anchorages; and (2) aluminum is utilized for the bridge deck. More details on the design principles and setup of the physical bridge model can be found in references in by Zhang (2012) and Xu (2012).

The bridge model is settled on a rectangular hollow section steel foundation beam in length of 14.64 m. The foundation beam, sitting on five sets of roller bearings with a uniform spacing of 3.16 m, can be moved perpendicular to or along the bridge liking a shaking table or kept fixed (see Figure 8.3). For a better control of the testing condition, the foundation beam is fixed, and the superstructure of the TMB testbed is excited by an exciter laterally acting on the deck.

The bridge deck, as the main component focused on in this study, is a composite steel structure consisting of a series of cross frames supported on longitudinal trusses acting compositely with stiffened steel plates. There is a total of 242 cross frames in the bridge deck model. These cross frames are linked up by two outer longitudinal trusses and two inner longitudinal trusses by welding. The diagonal bracings are arranged between two neighboring cross frames throughout the entire two outer longitudinal trusses. In the two inner longitudinal trusses, the diagonal bracings are arranged between two neighboring cross frames only in the side spans and the areas near the bridge towers. To simulate the stiffened steel plates of the prototype bridge deck, aluminum plates of 0.5 mm thick are laid on the lower level of the bridge deck in the middle by a special adhesive. Geometric measurements and modal tests are subsequently conducted on the physical bridge model to identify its geometric configuration and dynamic characteristics. Finally, the FE model of the physical bridge model is established using a commercial software ANSYS, and then FE model updating is performed using the measured modal properties.

8.4 Numerical Investigation on the TMB Testbed

To evaluate the feasibility and performance of the proposed multi-level damage identification via response reconstruction method, numerical investigations on the considerably large TMB testbed are to be conducted in this section.

8.4.1 FE Model of TMB Testbed

For the model dependent damage identification, a delicate FE model of the physical

model which correctly captures the actual structural dynamic behavior in some pre-determined range is indispensable. A member-based detailed three-dimensional FE model of the TMB testbed is needed in the structural condition evaluation related studies. The FE model was firstly established by Zhang (2012) in the commercial software ANSYS. The tower legs with varying cross-section were modeled by the three-dimensional tapered spatial Beam44 elements; the portal beams connecting the two adjacent tower legs were modeled with prismatic spatial Beam4 elements; Piers M1, M2, T1, T2, and T3 were all similarly modeled using the Beam4 elements with fixed constraints. The main cable and suspender as the load-bearing member were modeled using the uniaxial tension-only Link10 elements. The geometric nonlinearity in the main cables due to cable and suspenders tension under the weight of the deck was considered in the elements by activating the stress stiffness effect. Mass21 elements were added in the connection of suspenders with main cable and deck respectively to account for the masses of the clampers. The deck truss was constituted by 242 frame grids of 2 typical configurations modeled using the Beam4 elements along the bridge deck. Besides, the element Shell63 was used to model the plate laying on the bottom chords of the cross frames. More detailed introduction on the FE model can be found in the references by Zhang (2012).

The original FE model is too complex for the inverse problem of damage identification. Thus it is refined to a more tight one while without losing its representing capacity. The refined FE model of TMB testbed (as shown in Figure 8.4) is composed of 7658 elements and 3262 nodes and forms 18752 active DOFs after imposing boundary conditions. A pre-stressed non-linear static analysis is conducted

in ANSYS to form the effective stiffness and mass matrices of the TMB in working condition. Then all the model details, including the effective stiffness and mass matrices, node, element, and DOFs are imported to MatLab for the subsequent processing for CMS condensation and multi-level damage identification.

The TMB testbed is horizontally excited by a narrow-banded force sequence with a bandwidth of 2-8.25 Hz on the windward edge (Node 12024) of the 102-th frame grid from Man Wan (MW) side to Tsing Yi (TY) side. Its dynamic responses are calculated using first-order hold (FOH) state space formulation in modal coordinate system expressed by Eqs. (8.28) and (8.29), in which first 28 truncated modes are used and the time integration interval $\Delta t = 1/500\,s$. The numerical time duration is 16s. To include the noise effect, the simulated responses are added by the normally distributed noise sequences as Eq.3.35. The standard deviations of noise sequences are set as 0.14×10^{-6} m/m, 0.58×10^{-5} m and 0.56×10^{-2} m/s^2 for strain, displacement, and acceleration, respectively, which are similar to those measured in the laboratory test. The standard deviation of noise and real response varies from 0.84%~11.4% since the noise amplitude of each type response stays the same while the simulated real (noise-free) response varies along the locations.

8.4.2 Optimal Sensor Placement Design

As the main stress-bearing components, the responses of the 8 longitudinal beams are mainly monitored in the study, including horizontal displacement and acceleration of the nodes and strain on the midpoint of the elements. These locations are selected as the target sensor locations set. For response reconstruction, the active 1928 horizontal

DOFs out of 1936 nodes on the 8 longitudinal beams and 1928 elements of the 8 longitudinal beams are chosen as the candidate sensor location set. The optimal sensor placement should be optimized individually for known excitation scenario and unknown excitation scenario and the final sensor placement configuration should incorporate the two scenarios.

8.4.2.1 Mode selection in response reconstruction

As we known, the contribution of each analytical mode to the overall dynamic vibration differs from one to another. Besides, some analytical modes may not be excited under certain excitation. As the vibration of the deck is of main concern in this study, the local mode of side span cable can be abandoned in response reconstruction. Therefore, a proper subset of modes that contribute mostly to the reconstruction accuracy should be chosen when conducting the response reconstruction on such a large structure.

The first 28 vibration modes from the FE model, as listed in Table 8.1, are considered as candidates for the estimation of the state vector. The target modes for sensor location optimization and response reconstruction are selected from these modes. Zhang (2012) proposed a method to check the contribution of *j*-th mode by deleting the *j*-th row and column of the measurement system matrices corresponding to the *j*-th mode in response reconstruction, and the induced reconstruction accuracy is regarded as the contribution of the *j*-th mode. And the modes that contribute mostly are selected as the proper mode subset. Using this method, the contribution coefficient of the first 28 analytical modes is shown in Figure 8.5. It is noted that the first mode contributes mostly as expected. Thus 11 modes, including 1st, 3rd, 5th, 6th, 7th, 11th, 12th, 18th,

19th, 25th and 26th mode are chosen for response reconstruction.

8.4.2.2 Response reconstruction results

Figure 8.6 shows the steady reconstruction error covariance trace variation along the increasing optimal sensor number. It is observed that with the increase of the optimal sensors number, the reconstruction error decreases dramatically in the first 20 selected sensors but it converges to a stable value when the sensor number exceeds 30. Besides, when using the same number of sensors, the reconstruction error when the excitations are unknown is a bit bigger than that when the excitations are known. It is because the estimated excitations introduce additional errors in response reconstruction when the excitation is unknown. If 35 optimal sensors are selected, the optimal sensors include 8 accelerometers, 4 displacement meters and 23 FBG sensors for the scenario of known excitation and 8 accelerometers, 5 displacement meters and 22 FBG sensors for the scenario of unknown excitation. Due to the restriction of the laser displacement meters in the laboratory and for easy measurement, some modifications are conducted in the sensor configuration.

Table 8.2 shows the overall information of the final sensor placement configuration with the sensor numbers before modification listed in brackets. The sensor locations finally selected for measurement can be found in Table 8.3 and Table 8.4 for known excitation and unknown excitation respectively, in which the index of the grid frame is shown in Figure 8.7. Figure 8.8 depicts the spatial configuration of the finally selected sensor locations in the test.

The accuracy of the reconstructed response with the designed optimal sensor

placement configuration is measured by the relative percentage accuracy (RPA) expressed as Eq.(8.35).

$$RPA = \left(1 - \frac{\left\| \mathbf{y}^e - \mathbf{y}^r \right\|_2}{\left\| \mathbf{y}^r \right\|_2} \right) \times 100 \tag{8.35}$$

When the value approaches 100, the response reconstruction accuracy is higher. The minimal, maximal and average RAP of each type response under both known and unknown excitation are listed in Table 8.5. It is observed that all the 3 types of reconstructed responses are of high accuracies with the mean RAP above 98 %. Some typical responses of 3 types are shown in Figure 8.9 when the full knowledge of acting excitations is available. When the external excitations are unknown, the RAP of reconstructed excitation is 98.78%. However, it is also noted that the accuracy of the reconstructed responses is a bit degraded compared with that of known excitation scenario. Some typical reconstructed responses and excitation are presented in Figure 8.10.

8.4.3 Multi-level Damage Identification via Response Reconstruction

8.4.3.1 FE model condensation and damage simulation

The vibration and structural condition of TMB testbed deck is of special concern in this study. It is composed of 8 longitudinal beams and 242 frame grids of 2 typical configurations (shown in Figure 8.7) longitudinally along the bridge deck. Each frame grid has 8 intersection points with the 8 longitudinal beams and they are ranked as index number 1-8 as shown in Figure 8.7. The frame grids from Ma Wan side to Tsing Yi side are numbered as grid 1~ grid 242. CMS condensation is performed on the

entire bridge deck whilst the other components, including suspension cables, suspenders, towers and piers are fully modeled without any condensation processing. Every 2 grids and the associated beams constitute a substructure in CMS condensation except the last 3 frame grids constituting the 120-th substructure, forming totally 120 substructures in the entire deck. The intersection points of longitudinal beams and frame grids on the boundary of substructures, suspender connection points and external loading acting points are selected as the boundary DOFs; the others are internal DOFs. Some typical substructures are depicted in Figure 8.11. Each substructure is reduced using CMS condensation, and the first 8 fixed-interface normal modes are kept when forming the transformation matrix as Eq.(8.6). Then the reduced substructures are assembled into a whole condensed structure with 9248 DOFs using the primal assembly method.

Modal analysis is firstly conducted using the full FE model in ANSYS, and the first 10 modal frequencies are tabulated in Table 8.6. To check the accuracy of the CMS condensation, modal analysis is firstly conducted using the reduced FE model in MatLab and listed in Table 8.6. Comparing the two, it is found that the model condensation using CMS method is of high accuracy. The maximal discrepancy along the first 10 frequencies is -0.020%, indicating that the condensed FE model is of high representing capacity although the number of DOFs is dramatically decreased from 19875 to 9248.

Structural damages are generated by cutting 2 longitudinal beams (E4930 and E4942) which belong to the 67-th substructure. Consequently, the stiffness contribution of the 2 elements to the global structure is set zero while the mass contribution is reserved as

Eq.(8.2). This is deliberately designed to simulate the stiffness reduction due to structural damage. Model analysis is then conducted after introducing damage by performing eigenvalue analysis using the stiffness and mass matrices of the damaged structure. It is observed that the preset damage introduces noticeable discrepancy with a maximum of 3.42 percentages on the first mode, much larger than that caused by CMS condensation processing. Please be reminded that the stress redistribution due to omitting the stiffness contribution of the two damaged elements under gravity is ignored in this damage simulation. This is an important assumption in the following damage simulation. To check the stress redistribution (consequently affect the effective stiffness of cable system) due to damage in the non-linear static analysis, the damage is also simulated by setting the elastic modulus of the damaged beams as an infinitely small value, i.e. 1e-16, then the pre-stressed large-deformation static analysis is performed. The relative percentages errors of strain, defined as $\left[\left(s_u - s_d\right)/s_u\right]\times 100$, on the 95 suspenders on the south and north side of TMB are depicted in Figure 8.12. Here s_u and s_d are the elastic strains before and after damage, respectively. The horizontal axis is the frame grid number, and the red dash line indicates the section where generated damages exist. It is evident that the largest strain variation in the suspenders occurs in the vicinity of damage location, with the largest value of 0.3%. The strain variation in suspenders shows that stress redistribution due to damage is slight. Besides, the pre-stressed modal analysis is performed after a non-linear static analysis in ANSYS, in which the stress redistribution in static analysis is included. The first 10 frequencies are tabulated in Table 8.6. For comparison, Table 8.6 also lists the first 10 modal frequencies of damaged structure simulated in MatLab ignoring stress redistribution effect, where the stiffness

contributions of element E4930 and E4942 are subtracted from the global effective stiffness matrix. It can be seen that stress redistribution due to damage is negligible since these two damage simulation schemes introduce almost the same frequency discrepancies. Thus in the following section, the stress redistribution of cable system under gravity is ignored for computation ease.

8.4.3.2 Substructure level damage detection

The simulated responses at the locations of the selected sensors are firstly used for damage detection over the 120 condensed super elements, in which the equivalent damage parameter $\tilde{\boldsymbol{\theta}} \in \Re^{120}$ is updated using Eq.(8.23). The identification results on the substructure level are shown in Figure 8.13. It is observed that noticeable negative variation of -0.86 occurs on the 67-th super element, signifying that certain damages arise in the corresponding substructure. This is understandable since inside the 67-th substructure, the element 4930 and 4942 are damaged. They introduce the overall equivalently damage on the substructure with a value that is supposed to fall within the range of -1~0.

As pointed out before, although damage may occur on certain elements in a substructure with different severities, a uniform damage extend is assumed and represented by an entry in the equivalent damage vector to narrow the damage dimension. The narrowed damage vector amounts to the real damage vector in terms of making the dynamic properties of the supposed substructure-level damaged structure are as close as possible to that of the actual damaged structure.

Table 8.7 lists the first 10 modal frequencies of the structure with equivalent damage

vector and the damage-free structure, compared with that of the real damaged structure. It is observed that the frequencies of the structure with equivalent damage vector are very close to those of the preset damaged structure. The discrepancies between them are much less than the ones between the damage-free structure and the really damaged structure. On the first mode, which contributes mostly to overall vibration of the deck, the relative error, express as $(f_d - f_e)/f_d \times 100$, is -0.015%, much less than the relative error (-3.59%) between real damage and damage-free structure.

Figure 8.14 also shows the RPEs (Eq.3.36) of the dynamic response of the equivalently damaged structure with respect to that of really damaged structure on the 35 virtually measurement locations. Most of the RPEs are less than 15% except some strain measurement locations (S3, S6, S9, S13, S18, and S19), indicating that the substructure level identified structure is capable of representing the dynamic response of the damaged structure. For comparison, the RPEs of the dynamic response of the damage-free structure on that of the damaged structure are also plotted. Clearly, the RPEs of the equivalently damaged structure are dramatically less than that the damage-free structure. Thus, the substructure level identified structure is equivalent to the damaged structure regarding modal properties and dynamic responses on the measurement locations.

To further check the ability to identify the damage over the segmented substructures, 4 damage scenarios (as listed in Table 8.8) are designed and the substructure level damage detection is performed. The identification results are presented in Figure 8.15 and the summarized in Table 8.8. It is noted that when structural defects occur in the

two elements 4930 and 4942 or the elements 4942 is totally disabled; the damaged substructure can be correctly detected. However, when the element 4942 is partially disabled with an extent of -0.90, besides the actual damage exists in the 67-th substructure detected, the 103-th substructure is mistakenly detected as damaged. When the damage severity is decreased to -0.75 (damage scenario 5), the substructure level damage is falsely identified in the wrong substructure. We can see that when the damage extents are slight (less than -1.0 in the single element), the proposed method has the limited capability to detect the damage in substructure level.

8.4.3.3 Element level damage identification

The integration of the FRF amplitude on the 35 virtually measured locations calculated and imported to the trained RBF network to predict the strain mode shape and horizontal displacement mode shape of the identified 67-th substructure. The lower- and upper-frequency boundary is 2 Hz and 8.25 Hz, respectively. Welch's averaged periodogram method is used to estimate the transfer FRF. The output of the RBF network is the 34 horizontal displacement mode shapes and 39 strain mode shapes on the 8 longitudinal beams inside the detected 67-th substructure. The mode shape prediction effectiveness using RBF network is examined by the diagonal value of the coordinate mode assurance criteria (CoMAC) between the predicted coordinate mode shapes and the analytical ones obtained by eigenvalue analysis using the FE model of the damaged structure. Table 8.9 lists the CoMAC values of the 11 modes used in response reconstruction. It is observed that the mode shape prediction using RBF network is quite satisfying. Most displacement mode shapes are predicted with a quite high accuracy with the 5-th mode bearing the lowest CoMAC of 0.9650. A further

check reveals the amplitude of the 5-th mode is quite small compared with others, which is probably the main reason. In general, the shape prediction accuracy of strain mode is a bit degraded compared with that of the displacement mode. The diagonal CoMAC between the predicted and the real strain mode shapes values are 0.9996 ~ 0.9999.

After the strain and displacement mode shape are predicted, the strain, displacement, and acceleration on the 67-th substructure can be reconstructed using Eq.(8.30). The reconstructed responses on the identified substructures, together with the response on the measurement points, are finally further used for model updating at the element level over the detected substructure, of which the damage vector dimension is 52.

The identification results on the element level are shown in Figure 8.16. Physically, the damage vector should be constrained as $-1 \le \boldsymbol{\theta}^s \le 0$. Figure 8.16-a shows the damage identification result without constraints $\boldsymbol{\theta} \ge -1$, which indicates that there are approximately two damages of -0.8 and -1.4 on the 34-th and 46-th elements, respectively.

From Table 8.10 which lists the elements inside the 67-th substructure, we can find the 34-th and 46-th elements are exactly the elements E4930 and E4942. The damages are correctly localized, and the extents are approximately quantified. If the constraint $-1 \le \boldsymbol{\theta}^s \le 0$ is set in updating, the identification result is given in Figure 8.16-b, which demonstrates that the damage extents are exactly quantified on the elements E4930 and E4942. Figure 8.17 shows the result of element level damage identification on the 67-th substructure without response reconstruction. From the figure, it is noted that

although the result indicates certain damage on the 46-th element of the 67-th substructure, the preset damage on the 34-th element is not recognized and the damage severity on the 46-th element is notably larger than the preset one. Comparison between Figure 8.16 and Figure 8.17 clearly demonstrates the superiority and the necessity of response reconstruction in the element level damage identification.

8.5 Concluding Remarks

To alleviate the difficulty in identifying local damage over a damage space of large dimension, a multi-level damage identification via response reconstruction method is proposed in this chapter. Following a divide-and-conquer strategy, the entire massive structure is divided into several manageable substructures, and each substructure is condensed using the CMS technique. Consequently, the dimension of the damage vector is dramatically reduced, and the identifiability of damage is increased. After the damage region is detected, accurate damage localization and further damage quantification are performed over the elements of the suspicious damage region. Since local responses inside the damaged substructure are mostly beneficial for regional damage localization and quantification, Kalman filter based response reconstruction is performed to reconstruct the responses on the substructure. Basing on the simulation studies of the TMB testbed, some concluding remarks that should be noted are given as follows:

(1) A prerequisite of model condensation to reduce the damage dimension is that the condensed FE model should be of enough accuracy. The model discrepancy involved in model condensation procedure should be remarkably less than that

caused by structural damage. Thus the CMS technique, as one kind of dynamic substructuring technique, is employed in the proposed multi-level damage identification method over the traditional static substructuring technique. Simulation studies on the TMB show that the CMS technique is adequately accurate for model condensation. Besides, the number of substructure portioning, the master DOFs selection and the number of fixed-interface normal modes all have influences on the accuracy of the CMS technique. They should be properly handled when using the CMS technique.

(2) Regarding the mode shape prediction in damaged state, RBF network is employed in this study. The output of the RBF network is the strain and displacement mode shapes of the key locations. Basing on the identification result of the substructure level detection, only the strain and displacement mode shapes of the key locations inside the suspicious substructure are predicted in the element level damage identification. Thus the efforts in mode prediction using RBF network are dramatically reduced and the prediction accuracy is increased.

(3) Considering the remarkable complexity in the model building of the TMB testbed and computational demand in damage identification, the FE model of the TMB testbed is established using the commercial software ANSYS and the damage identification is performed in MatLab. The non-linear effect is included in forming the effective stiffness matrix and the mass matrix of TMB testbed by conducting the pre-stressed large-deformation static analysis. However, after the effective stiffness matrix is formed, it is assumed that the TMB behaves linearly under normal working condition. The stress redistribution due to damages on the deck is

ignored. Simulation results show that this assumption is acceptable.

The results of the TMB testbed demonstrate that the proposed multi-level damage identification via response reconstruction does improve the identification accuracy of damage localization and quantization considerably. However, its effectiveness should be further checked in laboratory test before practical application, which will be investigated in Chapter 9.

Table 8.1 Mode selection for sensor placement optimization

Mode	Analyzed	Measured	Direction	Span	Parts
1	3.858	3.907	Lateral	Main	cables, deck
2	5.126		Lateral	Main	cables
3	5.257	4.981	Lateral	Main	cables
4	5.281		Lateral	Main	cables
5	5.404	5.371	Lateral	Main	cables, deck
6	5.915	5.273	Vertical	Main	cables, deck
7	6.346	5.664	Vertical	Main	cables, deck
8	8.401	7.875	Lateral	Ma Wan	cables
9	8.415		Lateral	Ma Wan	cables
10	8.635		Lateral	Main	cables
11	8.693	7.911	Lateral	Main	cables, deck
12	9.139	8.643	Lateral	Main	cables
13	9.188		Lateral	Main	cables
14	9.194	8.789	Torsion	Main	cables, deck
15	9.415	9.081	Lateral	Tsing Yi	cables
16	9.427		Lateral	Tsing Yi	cables
17	9.490	9.191	Vertical	Tsing Yi	cables
18	9.620		Torsion	Main	cables, deck
19	9.718	9.766	Torsion	Main	cables, deck
20	10.843	9.961	Vertical	Main, Tsing Yi	cables, deck
21	12.173		Lateral	Main	cables, deck
22	12.189	10.890	Lateral	Main	cables, deck
23	13.256	12.452	Lateral	Main	cables, deck
24	13.267		Lateral	Main	cables, deck
25	13.925	14.064	Lateral, Torsion	Main	cables, deck
26	15.034		Lateral, Torsion	Main	cables, deck
27	15.841		Lateral	Main	cables
28	15.875	14.259	Lateral	Main	cables

Table 8.2 Optimal sensor placement results

Excitation	Accelerometer	Disp. transducer	FBG sensors	subtotal
Known	9 (8)	3 (4)	23 (23)	35
Unknown	7 (8)	4 (5)	24 (22)	35
Final	14	4	35	53

Table 8.3 Final sensor placement for known excitation scenario

Accelerometer				
Sensor NO.	Grid NO.	Node	Index	SE NO.
1	94	1869	4	47
2	96	1909	4	48
3	108	12147	7	54
4	116	12303	6	58
5	134	2667	3	67
6	144	12861	5	72
7	158	13149	8	79
8	166	13309	8	83
9	182	13629	8	91

Table 8.3 (continued)

Displacement meter			
Grid NO.	Node	Index	SE NO.
118	12347	7	59
128	2549	4	64
152	3029	4	76

Table 8.3 (continued)

FBG Strain				
Sensor NO.	Grid NO.	Node	Index	SE NO.
1	16	3999	7	8
2	42	4202	2	21
3	42	4206	6	21
4	55	4306	2	27
5	57	4326	6	28
6	93	4610	2	46
7	98	4654	6	49
8	102	4683	3	51
9	102	4687	7	51
10	113	4771	3	56
11	127	4882	2	63
12	129	4899	3	64
13	129	4903	7	64
14	130	4911	7	65
15	132	4923	3	66
16	137	4966	6	68
17	142	5002	2	71
18	208	5531	3	104
19	208	5534	6	104
20	209	5538	2	104
21	209	5543	7	104
22	211	5557	5	105
23	214	5578	2	107

Table 8.4 Final sensor placement for unknown excitation scenario

Accelerometer (Final Unknown)				
Sensor NO.	Grid NO.	Node	Index	SE NO.
1	94	1869	4	47
2	128	2547	3	64
3	128	2549	4	64
4	134	2667	3	67
5	136	12707	7	68
6	138	12741	5	69
7	138	12747	7	69

Table 8.4 (continued)

Displacement meter				
Sensor NO.	Grid NO.	Node	Index	SE NO.
1	118	12347	7	59
2	128	2549	4	64
3	140	2789	4	70
4	152	3029	4	76

Table 8.4 (continued)

FBG Strain				
Sensor NO.	Grid NO.	Node	Index	SE NO.
1	1	3873	1	1
2	17	4003	3	8
3	55	4305	1	27
4	93	4610	2	46
5	94	4622	6	47
6	95	4630	6	47
7	107	4722	2	53
8	117	4806	6	58
9	127	4882	2	63
10	128	4890	2	64
11	128	4894	6	64
12	129	4899	3	64
13	129	4903	7	64
14	130	4911	7	65
15	132	4923	3	66
16	142	5002	2	71
17	156	5118	6	78
18	208	5531	3	104
19	208	5534	6	104
20	209	5538	2	104
21	209	5543	7	104
22	210	5551	7	105
23	211	5558	6	105
24	214	5578	2	107

Table 8.5 RPA of the reconstructed responses

Response Type	Known Excitation			Unknown Excitation		
	Min	Max	Mean	Min	Max	Mean
Strain	69.03	99.87	99.18	67.08	99.34	98.66
Displacement	97.17	99.89	99.80	96.59	99.31	99.12
Acceleration	82.62	99.79	98.95	77.81	99.49	98.17

Table 8.6 Frequencies of the FE model of TMB testbed

Mode	ANSYS_Full	MatLab_Reduced		ANSYS_Damage		MatLab_Damage	
	f (Hz)	F (Hz)	Error (%)	f (Hz)	Error (%)	f (Hz)	Error (%)
1	3.858	3.857	0.018	3.725	3.424	3.722	3.512
2	5.126	5.127	-0.002	5.128	-0.023	5.127	-0.002
3	5.257	5.258	-0.005	5.258	-0.016	5.257	0.000
4	5.281	5.283	-0.024	5.283	-0.022	5.283	-0.024
5	5.404	5.405	-0.018	5.383	0.376	5.382	0.401
6	5.915	5.915	-0.001	5.915	0.009	5.896	0.333
7	6.346	6.346	-0.007	6.262	1.317	6.236	1.730
8	8.401	8.402	-0.020	8.403	-0.022	8.402	-0.019
9	8.415	8.416	-0.020	8.417	-0.022	8.416	-0.020
10	8.635	8.635	-0.001	8.637	-0.025	8.635	-0.001

Table 8.7 Frequencies of the structure with the equivalent damage and real damage

Mode	Real damage	Equivalent damage		Damage-free	
	f_d (Hz)	f_e (Hz)	Error (%)	f_u (Hz)	Error (%)
1	3.722	3.723	-0.015	3.856	-3.592
2	5.127	5.127	0.000	5.127	0.000
3	5.257	5.256	0.023	5.258	-0.007
4	5.283	5.283	0.000	5.283	0.000
5	5.382	5.383	-0.017	5.404	-0.401
6	5.896	5.905	-0.158	5.896	-0.012
7	6.236	6.198	0.608	6.326	-1.444
8	8.402	8.402	0.000	8.402	0.000
9	8.416	8.416	0.000	8.416	0.000
10	8.635	8.635	0.000	8.635	0.000

Table 8.8 Summary of substructure level damage identification results

Scenario	Designed Damage		Identification Result
	E4930	E4942	
1	-0.50	-1.00	Correct
2	0	-1.00	Correct
3	0	-0.90	Partially correct
4	0	-0.75	Wrong

Table 8.9 CoMAC value of the RBF network predicted displacement and strain mode shape with the analytical mode shape of damaged structure

Mode Serial Number	Mode Num in FE model	Strain	Displacement
1	1	0.9998	1.0000
2	3	0.9998	1.0000
3	5	0.9998	1.0000
4	6	0.9999	1.0000
5	7	0.9998	0.9650
6	11	0.9996	1.0000
7	12	0.9998	1.0000
8	18	0.9999	1.0000
9	19	0.9996	1.0000
10	25	0.9998	1.0000
11	26	0.9998	1.0000

Table 8.10 List of beam elements in the 67-th substructure

Index	Elem number	Elem material	Elem type	Real constant	Node Left	Node Right
1	2129	1000	4	1001	2661	2663
2	2130	1000	4	1001	12661	12663
3	2131	1000	4	1001	2661	12661
4	2132	1000	4	1002	2663	2664
…	…	…	…	…	…	…
33	4929	1100	4	1011	2641	2661
34	4930	1100	4	1011	2643	2663
35	4931	1100	4	1011	2647	2667
…	…	…	…	…	…	…
45	4941	1100	4	1011	12661	12681
46	4942	1100	4	1011	12663	12683
47	4943	1100	4	1011	12667	12687
48	4944	1100	4	1011	12669	12689
49	5933	1200	4	1012	2647	2663
50	5934	1200	4	1012	12647	12663
51	6175	1200	4	1012	2663	2687
52	6176	1200	4	1012	12663	12687

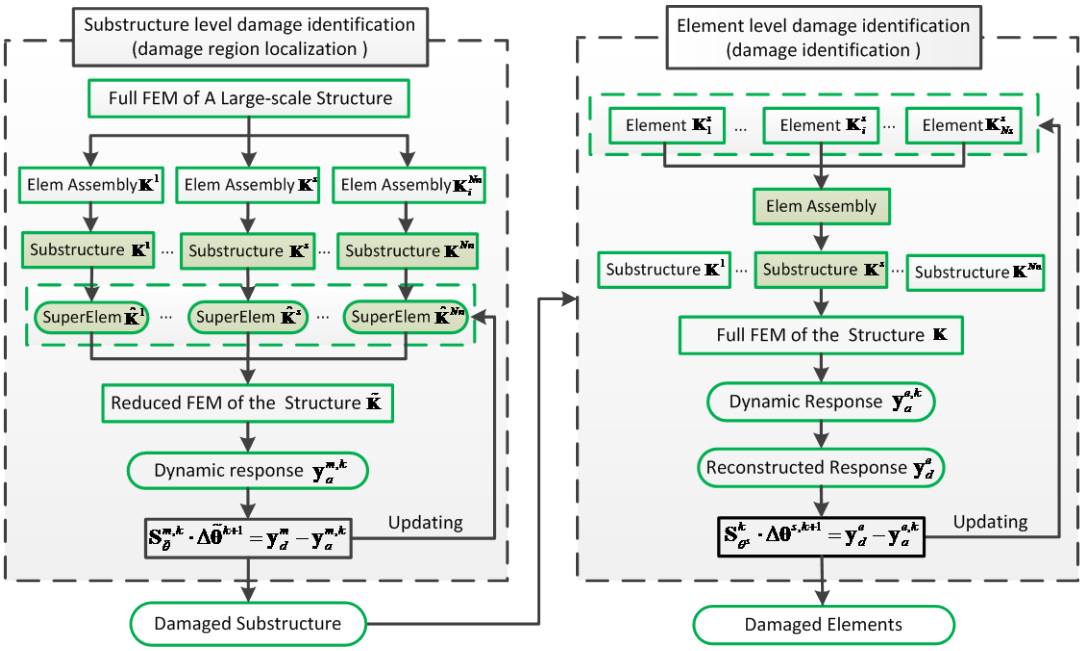

Figure 8.1 Schematic diagram of multi-level damage identification via response reconstruction

Figure 8.2 Tsing Ma Bridge testbed in the laboratory

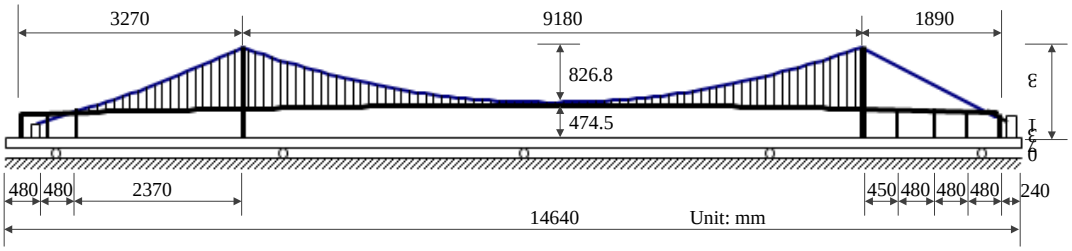

Figure 8.3 Configuration of Tsing Ma Bridge testbed

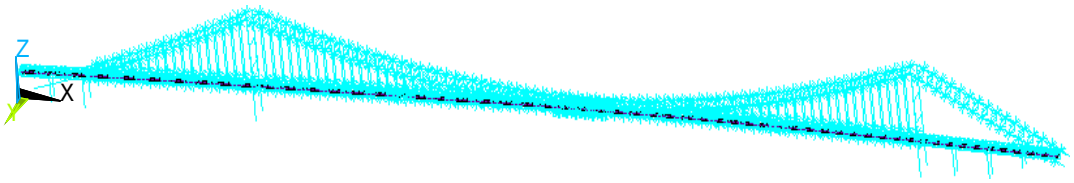

Figure 8.4 The FE model of TMB testbed established in ANSYS

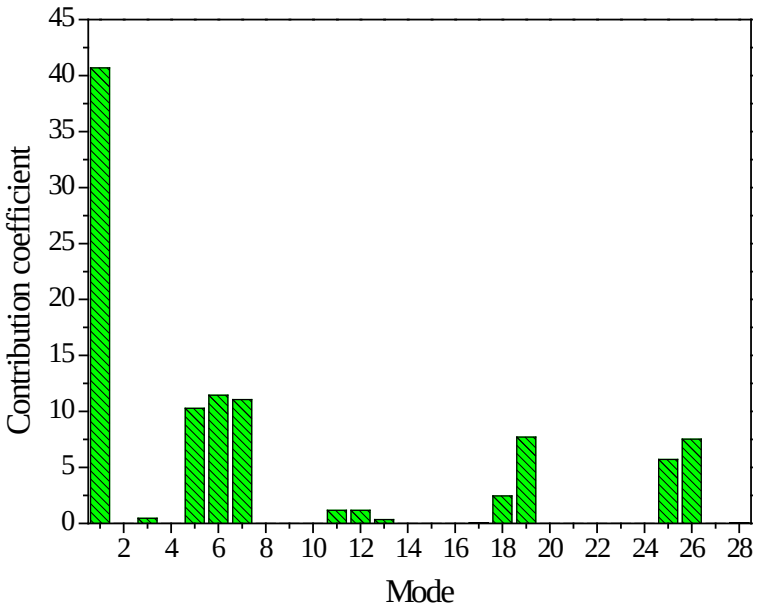

Figure 8.5 Mode contribution in response reconstruction

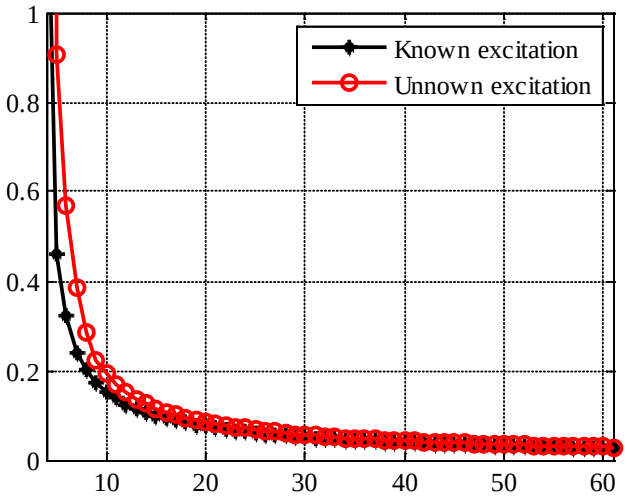

Figure 8.6 Response reconstruction error covariance trace along the increasing optimal sensor number

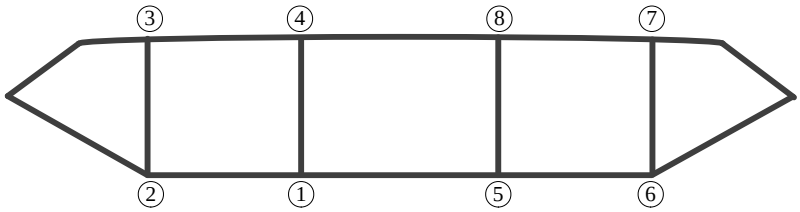

(a)

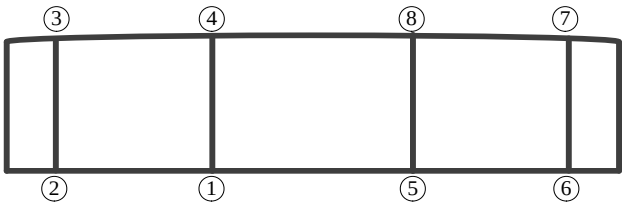

(b)

Figure 8.7 Two typical frame grid in the deck

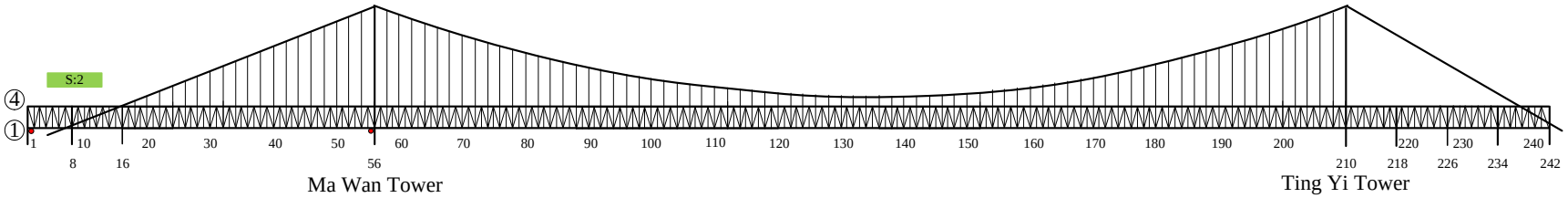
S:2
④
①
1 10 20 30 40 50 60 70 80 90 100 110 120 130 140 150 160 170 180 190 200 220 230 240
8 16 56 210 218 226 234 242
Ma Wan Tower
Ting Yi Tower

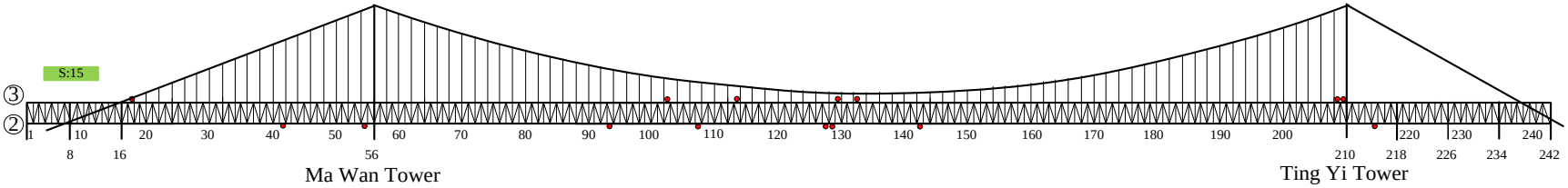
S:15
③
②
1 10 20 30 40 50 60 70 80 90 100 110 120 130 140 150 160 170 180 190 200 220 230 240
8 16 56 210 218 226 234 242
Ma Wan Tower
Ting Yi Tower

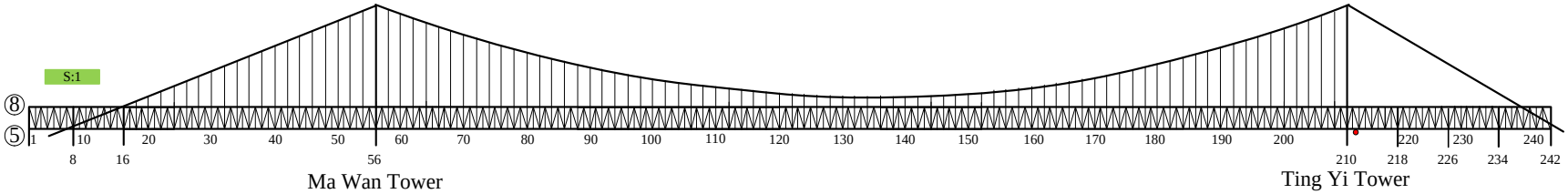
S:1
⑧
⑤
1 10 20 30 40 50 60 70 80 90 100 110 120 130 140 150 160 170 180 190 200 220 230 240
8 16 56 210 218 226 234 242
Ma Wan Tower
Ting Yi Tower

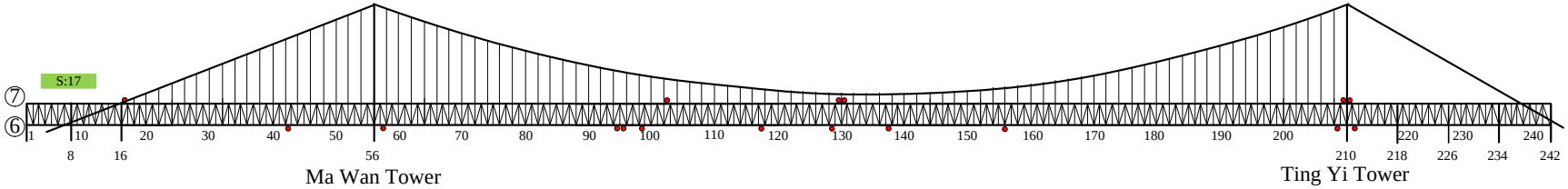
S:17
⑦
⑥
1 10 20 30 40 50 60 70 80 90 100 110 120 130 140 150 160 170 180 190 200 220 230 240
8 16 56 210 218 226 234 242
Ma Wan Tower
Ting Yi Tower

(a)

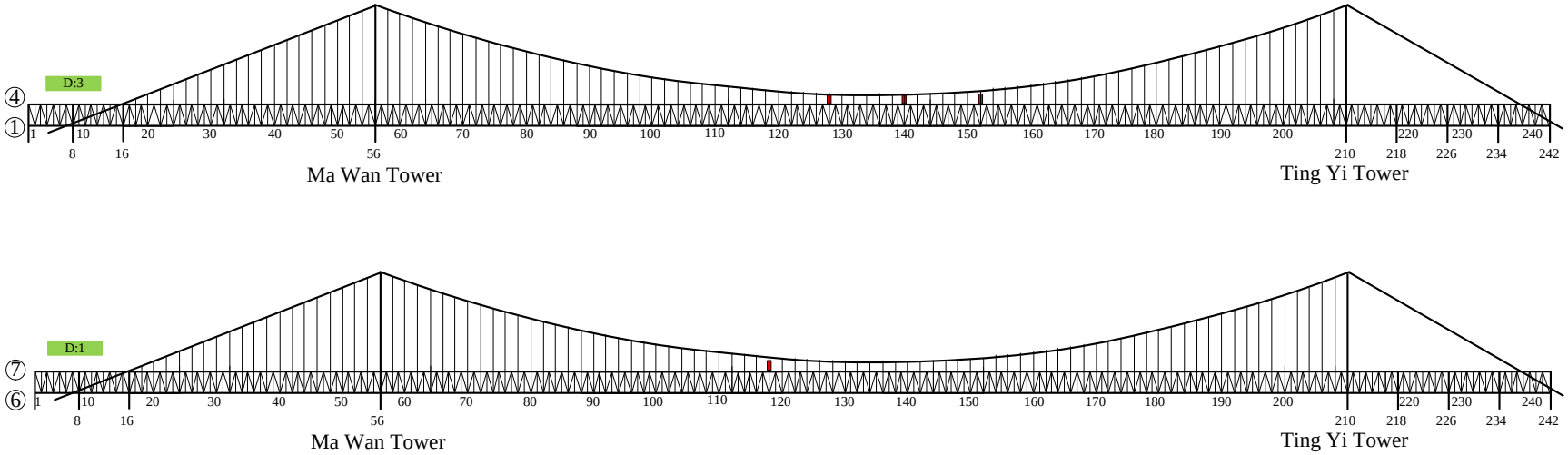
D:3
④
①
1 10 20 30 40 50 60 70 80 90 100 110 120 130 140 150 160 170 180 190 200 220 230 240
8 16 56 210 218 226 234 242
Ma Wan Tower
Ting Yi Tower
D:1
⑦
⑥
1 10 20 30 40 50 60 70 80 90 100 110 120 130 140 150 160 170 180 190 200 220 230 240
8 16 56 210 218 226 234 242
Ma Wan Tower
Ting Yi Tower

(b)

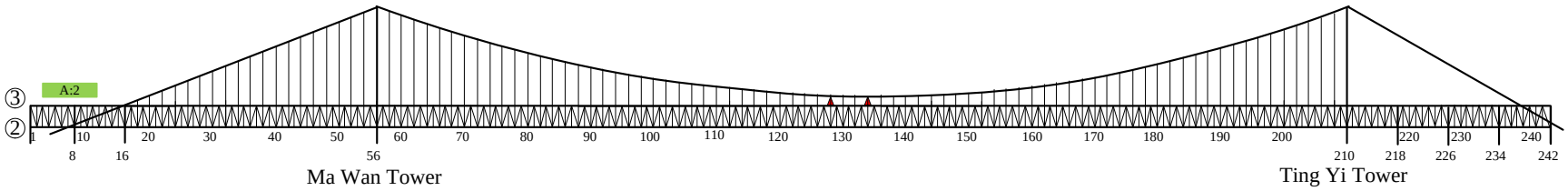
A:2
③
②
1 10 20 30 40 50 60 70 80 90 100 110 120 130 140 150 160 170 180 190 200 220 230 240
8 16 56 210 218 226 234 242
Ma Wan Tower
Ting Yi Tower

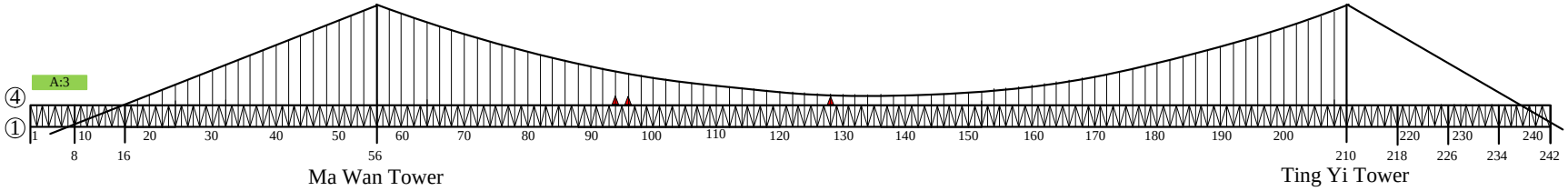
A:3
④
①
1 10 20 30 40 50 60 70 80 90 100 110 120 130 140 150 160 170 180 190 200 220 230 240
8 16 56 210 218 226 234 242
Ma Wan Tower
Ting Yi Tower

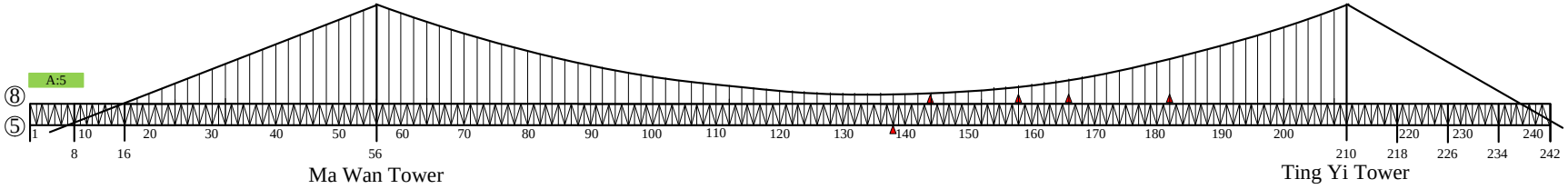
A:5
⑧
⑤
1 10 20 30 40 50 60 70 80 90 100 110 120 130 140 150 160 170 180 190 200 220 230 240
8 16 56 210 218 226 234 242
Ma Wan Tower
Ting Yi Tower

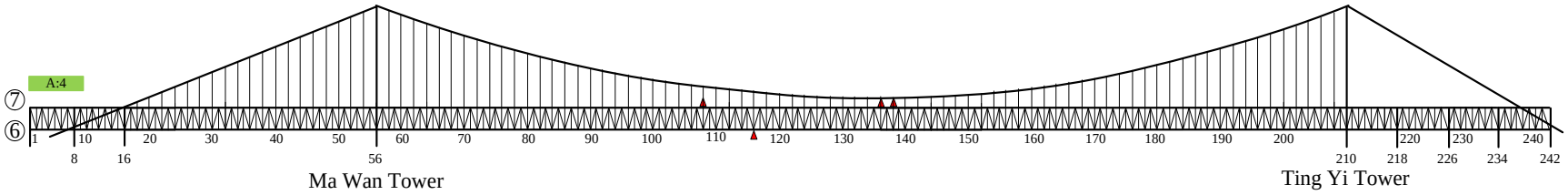

(c)

Figure 8.8 Total sensor placement layout in test: (a) FBG sensors, (b) Displacement meters and (c) Accelerometers meters

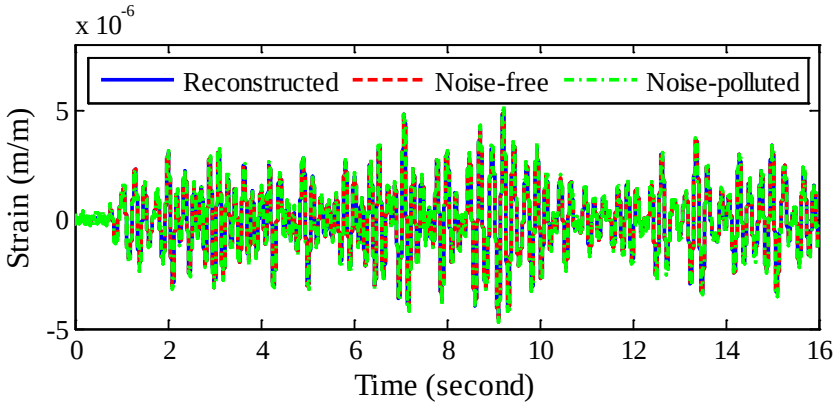
x 10^-6
Reconstructed
Noise-free
Noise-polluted
Strain (m/m)
5
0
-5
0
2
4
6
8
10
12
14
16
Time (second)

(a)

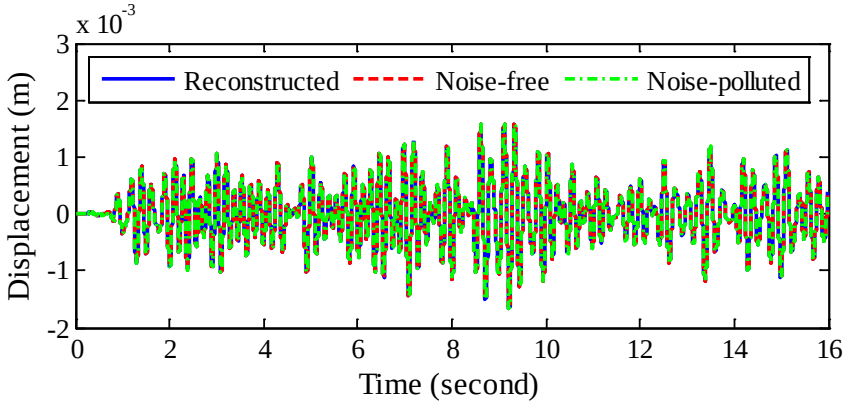
x 10^-3
Reconstructed
Noise-free
Noise-polluted
Displacement (m)
3
2
1
0
-1
-2
0
2
4
6
8
10
12
14
16
Time (second)

(b)

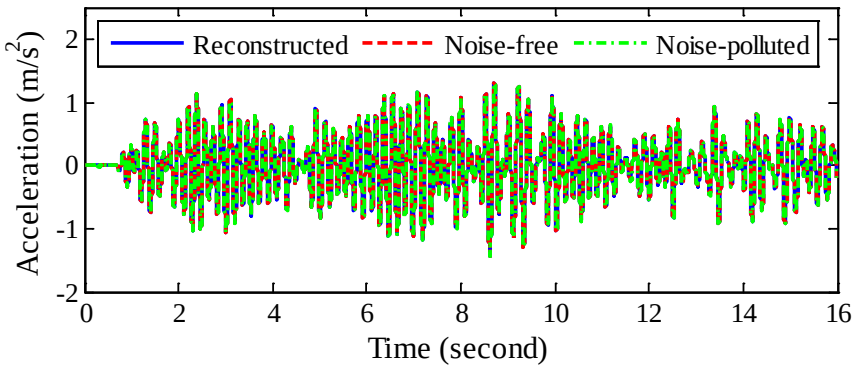
Reconstructed
Noise-free
Noise-polluted
Acceleration (m/s^2)
2
1
0
-1
-2
0
2
4
6
8
10
12
14
16
Time (second)

(c)

Figure 8.9 Comparison of reconstructed response with the noise-free and noise-polluted response under known excitation: (a) strain on element 3885; (b) displacement of node 2489 (c) acceleration on node 4958;

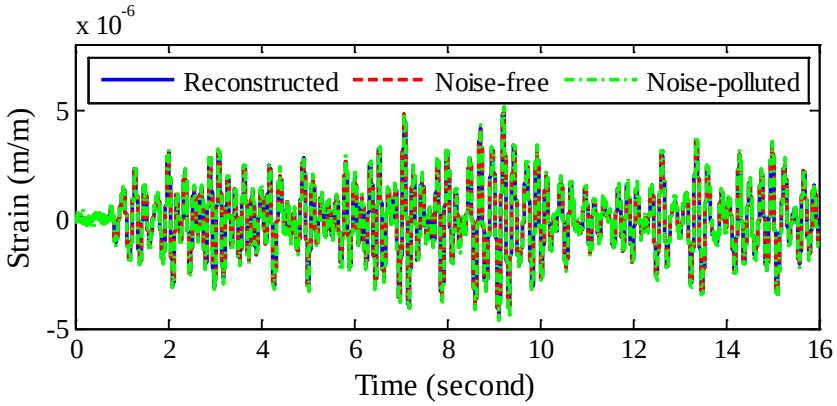

(a)

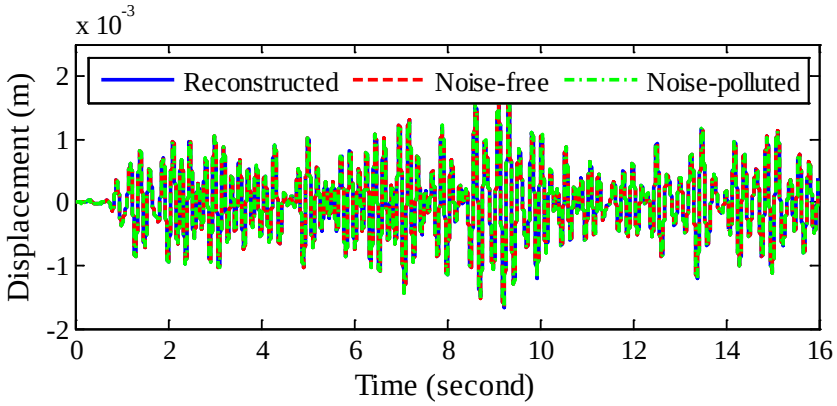

(b)

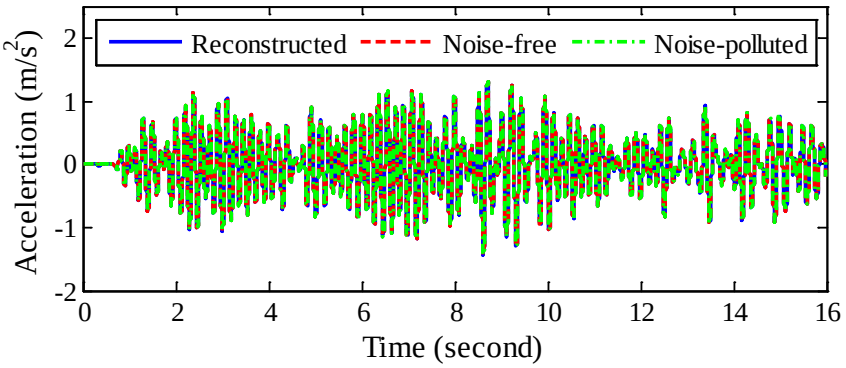

(c)

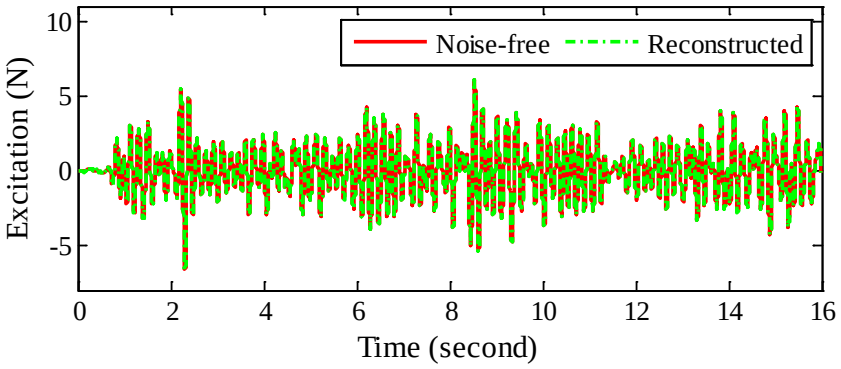

(d)

Figure 8.10 Comparison of reconstructed response with the noise-free and noise-polluted response: (a) strain on Element 3885; (b) displacement of Node 2489 (c) acceleration on Node 4958 and (d) excitations.

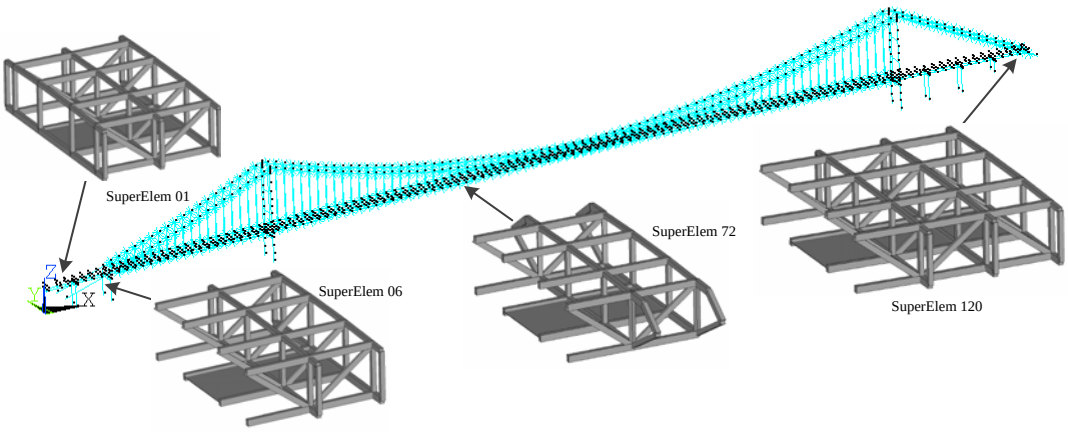

Figure 8.11 CMS condensed FE model

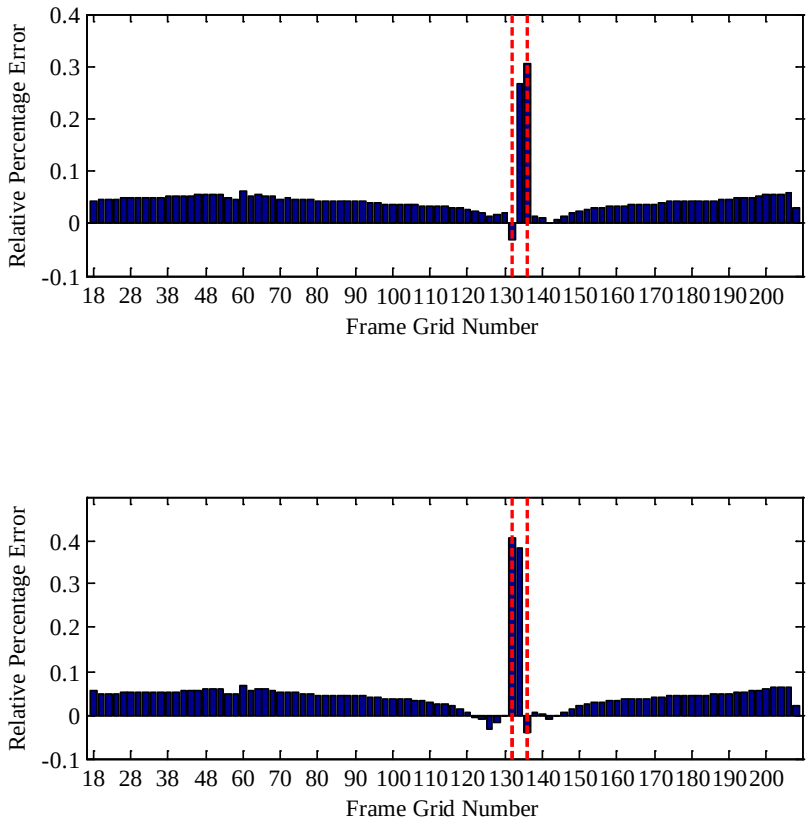

Figure 8.12 Strain variation in the suspenders along the frame grids: south side (top)

and north side (bottom)

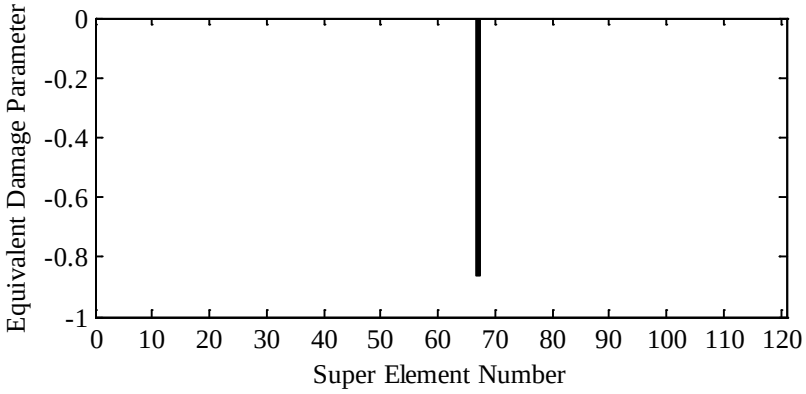

Figure 8.13 Damage identification of TMB testbed at substructure level

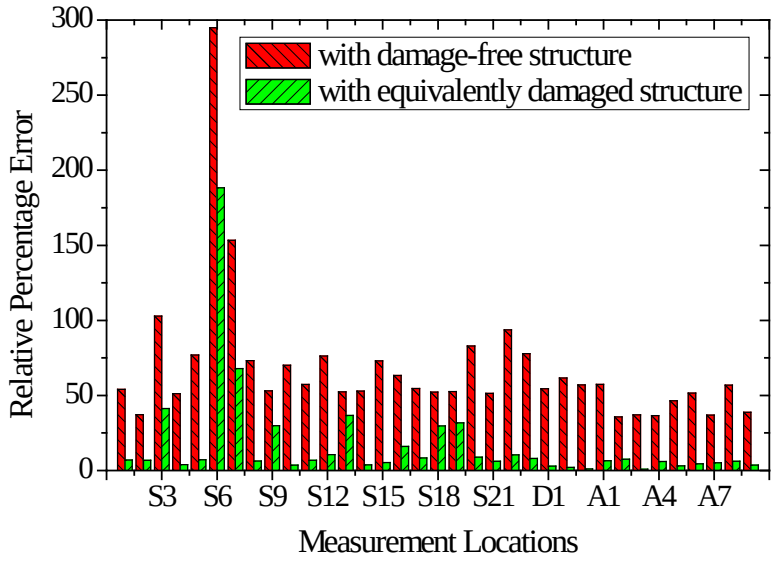

Figure 8.14 Response RPEs of damaged structure with damage-free structure and the equivalently damaged structure

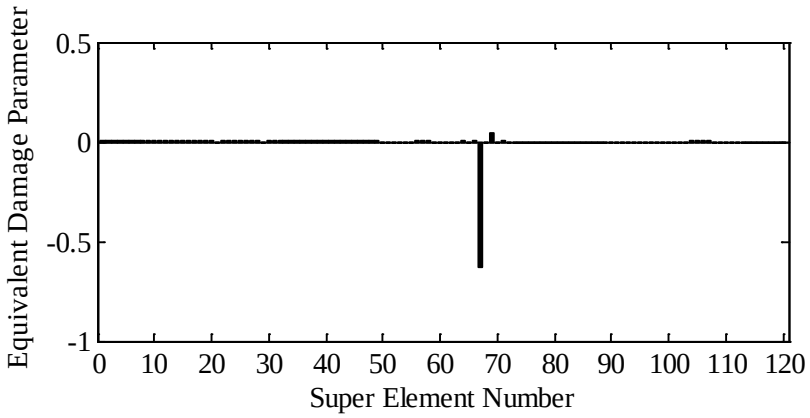
Equivalent Damage Parameter
0.5
0
-0.5
-1
0 10 20 30 40 50 60 70 80 90 100 110 120
Super Element Number

(a)

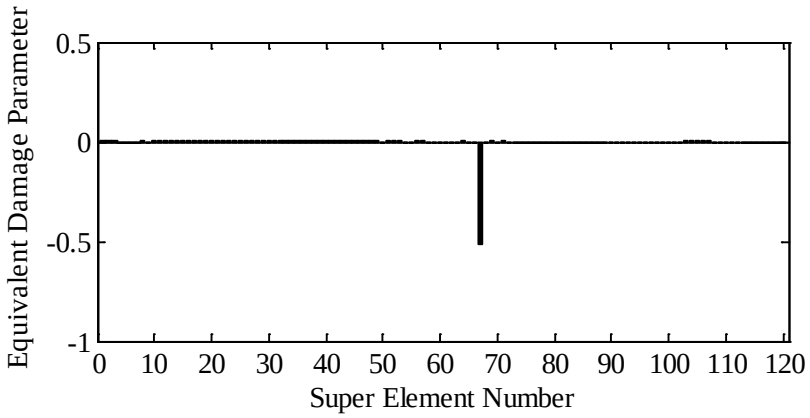
Equivalent Damage Parameter
0.5
0
-0.5
-1
0 10 20 30 40 50 60 70 80 90 100 110 120
Super Element Number

(b)

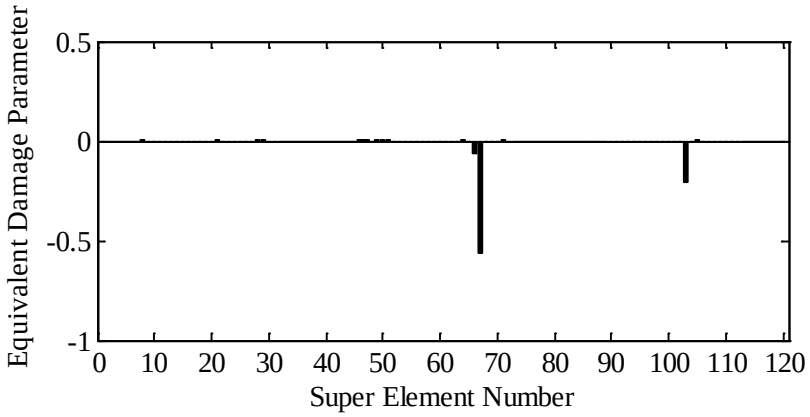
Equivalent Damage Parameter
0.5
0
-0.5
-1
0 10 20 30 40 50 60 70 80 90 100 110 120
Super Element Number

(c)

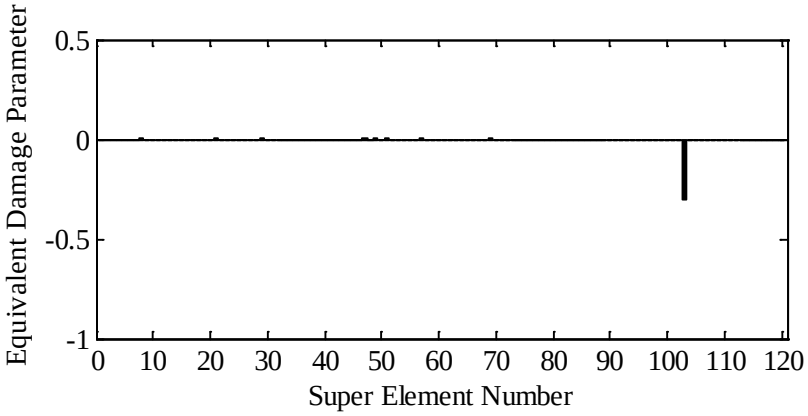

(d)

Figure 8.15 Substructure-level damage identification results of 4 damage scenarios: (a) case 1, (b) case 2, (c) case 3 and (d) case 4

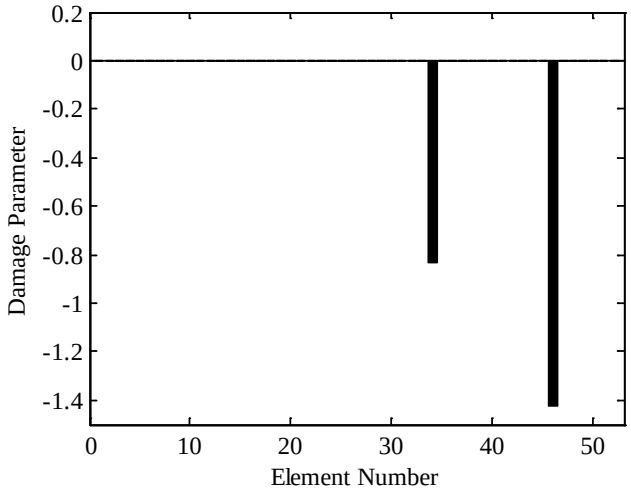

(a)

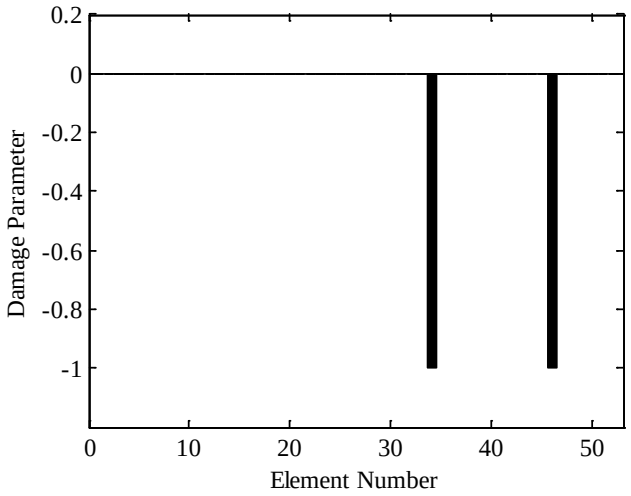

(b)

Figure 8.16 Damage identification of TMB testbed at element level with response reconstruction: (a) with constraint $\boldsymbol{\theta}^s \leq 0$ and (b) with constraint $-1.0 \leq \boldsymbol{\theta}^s \leq 0$

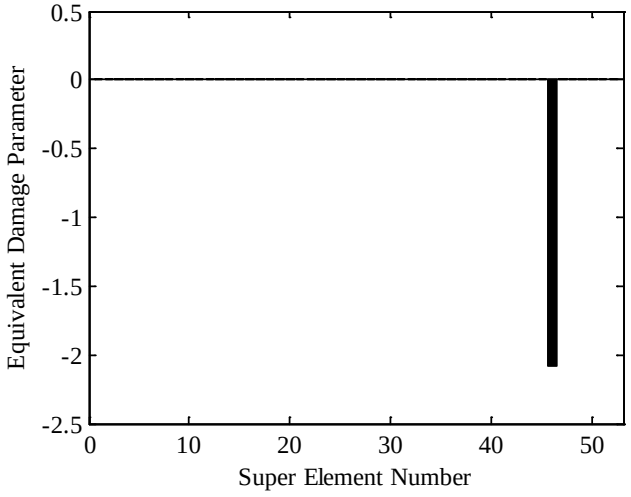

Figure 8.17 Damage identification of TMB testbed at element level without response reconstruction

CHAPTER 9

EXPERIMENTAL INVESTIGATION OF MULTI-LEVEL DAMAGE IDENTIFICATION ON THE TMB TESTBED

9.1 Introduction

Equation Section 9In Chapter 3, the optimal multi-type sensor placement under unknown excitation has been introduced; the relevant experimental studies have been conducted on an overhanging beam, and the results were presented in Chapter 7. Nevertheless, even remarkable satisfying response reconstruction results were obtained on the simple overhanging beam, it is necessary to further check the effectiveness of the proposed method on a relatively large structure before applying it to real large structures. In Chapter 8, the multi-level damage identification via response reconstruction was introduced, and simulation studies on a relatively large structure Tsing Ma Bridge (TMB) testbed concerning the Tsing Ma suspension bridge in Hong Kong were conducted. With the multi-level damage identification framework established in Chapter 8, it is possible to solve the intractable damage identification of a large structure in a multi-level way: firstly in the manageable substructure level and then inside the suspicious substructure on the detailed element level. This chapter aims to apply the multi-type sensor optimal placement for response and excitation

reconstruction and multi-level damage identification via response reconstruction to the well-controlled TMB testbed in the laboratory. The main objectives of laboratory tests on the TMB testbed include the following: (1) verify the effectiveness of optimal multi-type sensor placement for response reconstruction when the external excitations are unknown, and (2) verify the effectiveness and practicability of multi-level damage identification via response reconstruction when the external excitations are known. The experience obtained from this exercise can shed light on the application of the proposed method to real long-span suspension bridges.

9.2 Experimental Setup

9.2.1 Sensors Installation

There are three types of sensors, including Fiber Bragg grating (FBG) strain sensors, displacement meters, and accelerometers, were installed at the optimally selected locations of the physical bridge model, as determined in Chapter 8, to measure the structural responses. The total sensor deployment incorporates the designed sensor placements for the two scenarios: known excitation and unknown excitation. These two scenarios share some sensors in common. When a subset of sensors for one scenario is used for response reconstruction, the other sensors could be used for validation. Besides, 5 extra FBG sensors were also installed for validating the performance of response reconstruction under both known and unknown excitations.

To avoid the additional mass and damping induced by strain gauges and wires, FBG

sensors were utilized in the experiment instead of strain gauges to measure the strain responses. The FBG sensors were attached on the side face of the beam at the middle of the elements to measure the combined axial and flexural deformation of the beam. Stuck on the structural components, the FBG underwent certain deformation and introduced some shift in Bragg wavelength. The relative shift in the Bragg wavelength $\Delta\lambda/\lambda$ due to an applied strain (ε) and a change in temperature ΔT is approximately given by

$$\frac{\lambda}{\Delta\lambda} = K_\varepsilon \varepsilon + K_t \Delta T \tag{9.1}$$

The measured strain can be expressed as:

$$\varepsilon_m = \frac{\lambda}{\Delta\lambda} \Big/ K_\varepsilon = \varepsilon + c\Delta T \tag{9.2}$$

in which $K_\varepsilon \approx 0.79$ is the coefficient of strain; both K_t and c are coefficients, which are $17.79\times10^{-6}/\,^oC$ and $22.52\times10^{-6}/\,^oC$ respectively for the FBG stuck on steel host structures. In the test, 3 temperature compensation FBG sensors were installed in the MW span, TY span and main span, respectively; then the strain introduced by the structural deformation can be calculated as $\varepsilon = \varepsilon_m - \varepsilon_t$, where ε_t is the recorded strain in the temperature compensation sensors. There are 3 extra FBG sensors installed in the TY span, main span and MW span respectively for temperature compensation. LK-503 laser displacement transducers and KD1008 accelerometers were also equipped to capture the lateral vibration of the selected nodes on the deck. The weight

of each accelerometer is 1.2 g so that the additional weight of the accelerometers has little influence on the dynamic properties of the bridge model. All the sensor installations are shown in Figure 9.1.

9.2.2 Excitation Generation

The superstructure of the TMB testbed was driven by a random force series with frequencies ranging from 2 Hz to 8.25 Hz produced by a JZK-5 excitor at the forward edge of the 102-th frame grid. The excitation series were generated by a B&K 3160-B-022 signal generator and amplifiered by an SINOCREA YE5871 power amplifier to make the maximal excitation amplitude is about 9 N. For easier calculating the dynamic response, the amplitude of the excitation series varied from zero to a stable value by tuning the power amplifier, making the testbed vibrate from static state. The overview of the excitation generation setup is shown in Figure 9.2. Figure 9.3 shows the excitation time-history in 3 tests before damages were introduced. The sampling frequency for all tests was 1,000 Hz. It is observed that the repeatability of the excitation is quite satisfying and the excitation generation system is quite robust.

9.2.3 Data Acquisition

In this experiment, KD 5006 charge amplifiers were used as the signal conditioner to amplify the acceleration signals from the accelerometers. The displacement signals from the laser displacement transducers were conditioned by the LK 2503

conditioners. All the conditioned displacement and acceleration signals were collected and then processed by a 32-channel data acquisition system KYOWA EDX-100A, as shown in Figure 9.4. The optical sensing interrogator SM130 was employed to output light source for the FBG sensors and measure the wavelength of the light reflected from the FBG sensors. The dynamic strain responses from FBG sensors were recorded by using the V1.1 ENLIGHT system. The data acquisition systems are also illustrated in Figure 9.4.

The displacement and acceleration responses are captured using the different data acquisition unit from that used for capturing strain responses. The synchronization of the three types of responses to the same time is required for the reconstruction of the multi-metric responses. Therefore, a synchronous strain hammer was designed to fulfill the synchronization of the strain, displacement, and acceleration responses. One FBG sensor and one resistance strain gauge were embedded in this hammer, as shown in Figure 9.5. This hammer was used to generate an impact signal by hitting on a simple structure, which is totally separated from the bridge model. The impact signal was generated just before the recording of the measurement data from the bridge during the tests. On the one hand, the impact response of the FBG sensor of the hammer was collected by the SM130 optical sensing interrogator system, which also collected the responses from all the FBG sensors on the bridge. On the other hand, the impact response from the resistance strain gauge of the hammer was recorded by the DCS-100A data collection system, which also recorded the responses from all the displacement transducers and accelerometers on the bridge. The two sets of response

time histories were then utilized to determine the synchronous time for the strain, displacement, and acceleration responses by locating the impact peaks.

9.2.4 Experimental Procedure

Before damage occurs, the exciting sequence recorded by the load cell and the responses of 3 type captured by the 58 installed sensors were collected at a sampling frequency of 1,000 Hz and a sampling duration of the 80s. In each testing, the synchronous hammer was used to generate the impulsive signal for time synchronization. A typical strain data on the synchronous hammer was shown in Figure 9.6. The collected data were synchronized to the same time and resampled to 500 Hz before utilization. This portion of the data served to update the FE model built with nominal values to establish a baseline model for undamaged structure. Besides, they were also used to verify the effectiveness of multi-type response reconstruction under both known and unknown excitation. For the second portion of the experiment, the beam members in the locations corresponding to the preset damage were cut in order to simulate damage imposed to the structure. The excitations were repeated, and the responses of the TMB testbed in the damaged state were also collected. The resulting data were then used for multi-level damage identification.

9.3 FE Model Updating

Finite element model discrepancy between the real structures under investigation is inevitable due to the simplifications made during the modelling process and

unavoidable uncertainties in geometrical dimension, physical properties and boundary conditions. FE model updating is to be performed in this section to provide to refined reference model for the following response reconstruction and damage identification studies.

9.3.1 FE Model Updating Flow Chart

A parameterized FE model updating is performed to refine the established FE model in the time domain. Although the FE model of TMB testbed has been updated by Zhang (2012) using an objective function defined in terms of frequencies and mode shapes, it is further updated with an objective defined using the dynamic response in this section. The main reason is that a more delicate FE model that can represent the structure's dynamic behavior is needed for model-dependent damage identification. Besides, some parameters, for example, the damping effect, which was not included in the frequency domain updating, should be tuned for better dynamic response representation. Considering the remarkable model building and non-linear static analysis capacity of ANSYS and outstanding dynamic response simulation and optimisation algorithms solving capacity of MatLab, the time domain updating is performed by synergistically executing ANSYS and MatLab: the parameterized FE model is built and the pre-stressed large deformation static analysis is conducted by programming in ANSYS Parametric Design Language (APDL); the dynamic response is calculated and the optimisation is solved in MatLab; the interface linking between the two is fulfilled by executing the APDL file in MatLab programming. The optimization flow diagram is shown in Figure 9.7. In the proposed updating strategy,

the following advantages should be pointed out:

(1) The parametric FE model is defined in terms of variables by means of APDL, and thus the values of the different variables will be changed according to the updating loop until a minimum is reached.

(2) The geometric stiffness of the cables and suspenders, mainly caused by the weight of the bridge, are included in the exported active stiffness matrix by performing the pre-stressed large deformation static analysis in ANSYS using the APDL file.

(3) The ANSYS and MatLab are jointly linked by the script like: '!C:\Program Files\ANSYS Inc\...\ANSYS140.exe -b -p ane3fl -i E:\Temp\...\mainupdating.inp -o E:\Temp\...\out.txt', in which the 'mainupdating.inp' is an executable APDL file that establishes and analyzes the FE model as well as export the effective stiffness and mass matrices in ANSYS.

Using the above updating strategy, the optimization parameters can be easily modified due to the advantages of creating and solving a parametric FE model by means of APDL. Thus the overall proposed updating loop can be created without user intervention so that the proposed updating methodology is done completely automatically until the solution is found or stopping criteria is achieved.

9.3.2 Updating Parameters and Objective Functions

The parameters to be updated should be properly selected to achieve a satisfying and

physical meaningful updating result. To this end, physical and mathematical insights, as well as engineering experience, are always demanded. On the one hand, the selected parameters should represent some uncertainties of the model and the updated results should preserve the physical meaning of the model. On the other hand, the defined objective function should be sensitive to the selected parameters. Sources of the discrepancies between the experimental and analytical results may lie in the imprecision of the geometrical and material parameters, the boundary conditions, and the connections of the member components.

For this reduced-scale bridge model, the geometrical parameters can be comparatively accurately measured, and the boundary conditions can be simulated under control. Thus, the geometrical parameters and the boundary conditions in the initial FE model will not be updated. However, the rigid connections among beam elements and between beam elements and shell (plate) elements in particular may not represent the real connections very well; neither do the spring connections between the deck and towers. It is thus reasonable to consider adjusting the stiffness of the cross frame, plate, longitudinal beams, and diagonal bracings as well as springs. Besides, the axial forces in the cables and suspenders in the physical model, to some extent, are likely to be different from those in the FE analysis. In this connection, the sectional stiffness of the suspenders and the cables are also chosen as the candidates for adjustment. Furthermore, the member masses are not weighted or measured against those of the analytical ones, and accordingly, the densities of the main cross frame, longitudinal beams, and the plate may also be selected as updated parameters.

A sensitivity analysis computes the sensitivity coefficient defined as the rate of change in a particular response quantity with respect to a change in a structural parameter. The parameters with high sensitivity can be further examined and selected for model updating, while those with low sensitivity can be eliminated from the updating parameters. A well-conditioned updated problem necessitates the selection of those parameters which will be most effective in reducing the discrepancies between the analytical results and their identified counterparts. In this study, the sensitivity analysis is performed by calculating the sum of the dynamic response variation norm on the measurement points when each parameter increases by 10% with respect to the nominal value.

It is observed from Figure 9.8 that among the 20 candidate parameters to be potentially updated; the Young's modulus of bearing between MW tower, M2 pier and deck *Ectd*, the spring stiffness of lateral connection between TY, MW tower and deck *Kconl* and added stiffness due to the installed exciter *ak* show almost negligible influences on the dynamic responses. As a result, a total of 17 parameters (see Table 9.1) were chosen for updating.

The objective functions are formulated in terms of the discrepancy between analytical and experimental dynamic response as shown below

$$J(p)=\sum_{i=1}^{m}\frac{\left\|\mathbf{y}_i^s(p)-\mathbf{y}_i^m\right\|}{\left\|\mathbf{y}_i^m\right\|} \tag{9.3}$$

where p denote the selected parameters for updating, and m is the number of sensors used in updating. Among the totally deployed 58 sensors of 3 types, the responses of 16s on the 24 sensors including 9 accelerators, 3 displacement meters and 12 FBG strain sensors (as listed in Table 9.1) are used for updating. All the responses on other sensors are used for validating the updating results.

To make the updating result physically meaningful, the parameters of Young's modulus and density are constrained as $0.8p_0 \le p < 1.2p_0$, where p_0 is the nominal value of the parameter. Considering large uncertainties exist on the constraints between the deck and piers, towers, the stiffness' of connection are constrained as $1.0\times10^{-6}p_0 \le p < 1.0\times10^{6}p_0$. Moreover, the Rayleigh damping ratios are also constrained similarly. Finally, The FE model updating forms a constrained minimization problem. Among the different optimization algorithms available in MatLab, the primal-dual interior point method has been selected to optimize the problem.

9.3.3 FE Model Updating Results

Table 9.2 lists the variations in the updating parameters. The initial values of the parameters of Young's modulus and density in the table are the design values, and the initial values of constraint stiffness are provided by Zhang (2012). It can be seen that there are slight to moderate reductions in the elastic modulus and density of the components, indicating that the initial guess of the modules is relatively accurate. It can also be found that the connection stiffness and Rayleigh damping ratio have

significant changes.

The updating results are checked in term of dynamic response. Simulated results were regenerated with the updated model and are compared with the experimental results. Figure 9.9, Figure 9.10 and Figure 9.11 depict the comparison of tested and simulated response on accelerometer A10, displacement meters D3 and FBG strain sensor S24, respectively. It is evident that after FE model updating the tested responses match better with simulated responses than that before model updating. These results show a significant improvement in the FE model's ability to reflect the actual behavior of the tested TMB.

Figure 9.12 shows the relative norm of discrepancy between the tested and simulated responses on the updating sensors. It is observed that after updating the discrepancies are dramatically decreased among the 24 updating sensors, and the mean relative norm of the discrepancy is reduced from 0.6 to 0.3 approximately. Figure 9.13 shows the differences on the other 34 sensors for validation. We can see that almost all the differences of 39 validating sensors are decreased remarkably except that 2 FBG sensors (S10 and S 39) are a bit increased. It is also noticed that relative percentage errors on S2, S3 and S39 are a bit higher. This is mainly because these FBG sensors are installed near the fixing ends of the deck, and the vibration amplitudes of them are quite small.

9.4 Response and Excitation Reconstruction and Validation

The joint response and excitation reconstruction is performed through Kalman filter under unknown input (KF-UI) by using the measured responses from the 35 optimized sensors (as shown in Table 8.4) and the updated FE model of TMB testbed. The typical comparison of reconstructed and recorded responses from accelerometer A10, displacement meters D3 and FBG strain sensor S24 are respectively shown in Figure 9.14, Figure 9.15 and Figure 9.16. It is observed that the reconstructed responses match the tested ones very well. Compared with the simulated responses shown in Figure 9.9 to Figure 9.11, the reconstructed response matches even better than the simulated response with reference to the actual response. This is mainly because Kalman filter based response reconstruction could take advantages of the model information as well as the measurement information, thus inducing more accurate response estimation. Figure 9.17 also depicts the reconstructed excitation series and the tested excitation series. We can see that the reconstructed excitation coincides with the tested one to a certain satisfaction. The relative norm of the discrepancy is also employed to measure the discrepancy between the tested and reconstructed responses on the validation sensors (those sensors that are not used in response reconstruction) and the results are shown in Figure 9.18. It is observed that on almost all the validation sensors, the reconstructed responses match better than simulated responses produced by the FE model, except for S20, S39, and A14. It should be pointed out that the tested response is noise-corrupted. Thus it does not represent the real response of the structure and just used here as a reference for validation.

9.5 Multi-level Damage Identification and Validation

9.5.1 Substructure Level Damage Identification

In consideration of the actual sensors deployment (especially the FBG sensors) and easy operation circumstances, the damage on the bridge deck is generated by cutting 2 longitudinal beams as shown in Figure 9.19. Consequently, the stiffness contributed by the components to the overall stiffness is prejudiced while the contributions of mass are reserved. This is purposely designed to simulate the component degradation due to crack or connection looseness and others. Both of the pre-set damages belong to the 67-th substructure.

Firstly, the measured responses of the 35 sensors are used for detecting the preset damage over the 120 substructures. For computation ease, only the recorded data of 4s (12s~16s) after the testbed are excited steadily are used in the multi-level damage identification. The substructure element level damage detection result is shown in Figure 9.20. It is noted that about certain damage is detected on the 67-th substructure with a value of -0.797, a bit less than that in the simulation study in Chapter 8. Additionally, a small minus value of -0.045 is also noticed in the adjacent 66-th substructure. However, this tiny error is negligible compared with the value on the 67-th substructure. The result indicates that certain damages exist inside the 67-th substructure, which is consistent with the fact that the generated damages on E4930 and E4942 locate inside the 67-th substructure.

9.5.2 Element Level Damage Identification

The strain, displacement, and acceleration of 67-th substructure are firstly reconstructed prior to the element level damage identification. The FRFs of the responses on the 35 sensors are calculated using the Welch's averaged periodogram method with a frequency resolution of $f_s/nfft = 500/4096 = 0.12$ Hz. The FRF amplitudes are integrated in the range of 2~8.25 Hz, and they are then used as the inputs to RBF network to predict the horizontal displacement mode shapes and strain mode shapes on the 8 longitudinal beams inside the detected 67-th substructure. The predicted strain and horizontal displacement mode shapes are depicted Appendix C, compared with the analytical ones calculated by eigenvalue analysis using the FE model of the damaged structure. The coordinate modal assurance criteria (CoMAC) values between the predicted mode shape and the analytical model shapes are tabulated in Table 9.3. We note that the accuracy of the predicted mode shapes using the tested data is slightly decreased compared with that of the predicted mode shapes using the simulated responses. The multi-type response of the identified 67-th substructure can be reconstructed using the Kalman filter based theory. Finally, the reconstructed responses of the identified substructures, together with the response on the measurement points, are used for the element level damage identification over the detected 67-th substructure.

The identification results on the element level are shown in Figure 9.21. Figure 9.21-a shows the damage identification result without constraining $\boldsymbol{\theta} \geq -1$, which indicates that there are approximately two damages of -3.8 and -2.7 on the 34-th and 46-th

elements (corresponding to the 34-th and 46-th elements), respectively. We can see that the damages are correctly localized but the damage extents are not quantified. If the constraint $-1 \le \boldsymbol{\theta}^s \le 0$ is set in updating, the identification result is given in Figure 9.21-b, which demonstrates that the damage extents are exactly quantified on the elements E4930 and E4942. There are no false-positive errors on the other elements, mainly because the sparsity promoting property of sparse regularization. To demonstrate the benefits of response reconstruction for local damage identification, Figure 9.22 shows the result of element level damage identification on the 67-th substructure without response reconstruction. It is obvious that although the preset damage on the 34-th element is identified with a rough severity of -1.2, the preset damage on the 46-th element is not detected. What's more, a notable false-positive error is found on the 38-th element. The results in Figure 9.21 and Figure 9.22 clearly indicate the superiority and the necessity of response reconstruction in identifying local damages.

9.6 Concluding Remarks

This chapter presents the experimental studies on the TMB testbed. Two issues are investigated, including the optimal multi-type sensor placement for response reconstruction when the external excitations are unknown and multi-level damage identification via response reconstruction when the external excitations are known. Before that, time domain FE model updating in terms of dynamic response is performed by interfacing ANSYS and MatLab. According to the experimental results,

some remarks are given as follows:

(1) The integration of ANSYS and MatLab for model updating can take advantages of the remarkable model building and non-linear static analysis capacity of ANSYS and outstanding dynamic response simulation and optimization algorithms solving capacity of MatLab. This strategy is especially suitable in the circumstances where the FE model is too complex to be established, or the nonlinear relationship between the FE model and the updating parameters are difficult to be expressed. The discrepancies between analytical response and tested response are dramatically decreased after the model updating.

(2) Response reconstruction results show that the designed sensor placement is capable of not only reconstructing the response of interested location but also estimate the deterministic excitation series exerted to the structure. The reconstructed responses are more accurate than the analytical responses compared to the tested response. This is mainly attributed to the fact that KF-UI based response reconstruction can take into consideration of the model building error and measurement noise.

(3) In the multi-level damage identification, the non-linear effect is included in forming the effective stiffness matrix of TMB testbed by conducting the pre-stressed large-deformation static analysis in ANSYS. However, the geometric stiffness variation due to stress redistribution induced by small damages on the deck is ignored. Test results show that this assumption is acceptable.

The response reconstruction under unknown excitations and the multi-level damage identification via response reconstruction have been numerically and experimentally verified on the relatively large structure, the testbed of Ting Ma suspension bridge. Some conclusions and recommendations regarding the whole thesis will be given in the next chapter.

Table 9.1 Sensor selection for model updating and validation

Sensor Type	Sensors for Updating		Sensors for Validation		Total Sensors
	Sensor Tag	Num.	Sensor Tag	Num.	
Accl.	A10, A9, A6, A11, A7, A8, A12, A13, A14	9	A4 A5, A3, A1, A2,	5	14
Disp.	D3, D2, D4	3	D1	1	4
Strn.	S38, S23, S40, S22, S25, S24, S35, S20, S21, S33, S27, S17	12	S19, S36, S18, S5, S37, S4, S34, S6, S7, S9, S31, S39, S8, S30, S26, S16, S32, S15, S29,S14, S11, S28, S12, S10, S13, S3, S2,	28	39

Table 9.2 Variations in updated parameters

Updating Parameters		Initial Values	Updated Values	Changes (%)
Description	Symbol			
E of steel tower	Est	2.05E+11	2.22E+11	8.2
E of main cables	Emc	9.40E+10	1.13E+11	20.0
E of box frames (aluminum alloy)	Ebf	6.89E+10	6.47E+10	-6.1
E of plates	Epl	2.00E+10	2.05E+10	2.5
E of suspenders	Esup	9.40E+10	1.12E+11	19.4
D of steel	Ds	7.80E+03	8.68E+03	11.3
D of aluminum alloy	Dt	2.72E+03	3.26E+03	20.0
D of steel strand	Dc	6.24E+03	4.99E+03	-20.0
D of plates where masses are added	Dp	4.47E+04	5.34E+04	19.5
D of truss beam density where masses are added	Db	8.25E+04	8.51E+04	3.2
Thickness of plates	Tk	5.00E-04	4.94E-04	-1.2
K of vertical connection between TY tower and deck	Kcont	3.00E+04	7.47E+04	149.1
K of vertical connection between M1,T1,T2,T3 pier and deck	Kconp	1.12E+05	2.48E+05	120.8
K of lateral connection between TY, MW tower and deck	Kconl	3.25E+08	1.02E+08	-68.6
K of vertical connection between MW tower, M2 pier and deck	Kconv	4.50E-06	9.19E-06	104.2
Mass Rayleigh damping ratio	Dampa	2.09E-01	3.66E-01	74.8
Stiffness Rayleigh damping ratio	Dampb	5.85E-04	5.89E-12	-100.0

Table 9.3 CoMAC value of the predicted displacement and strain mode shape with the analytical mode shape of damaged structure

Mode Serial Number	Mode Num in FE model	Strain		Displacement	
		Simu.	Test	Simu.	Test
1	1	0.9998	0.9092	1.0000	0.9999
2	3	0.9998	0.8760	1.0000	0.9996
3	5	0.9998	0.9109	1.0000	0.9999
4	6	0.9999	0.9726	1.0000	0.9708
5	7	0.9998	0.8681	0.9650	0.9510
6	11	0.9996	0.6798	1.0000	0.9996
7	12	0.9998	0.7079	1.0000	0.9981
8	18	0.9999	0.8052	1.0000	0.9991
9	19	0.9996	0.7910	1.0000	0.9995
10	25	0.9998	0.7465	1.0000	0.9401
11	26	0.9998	0.9161	1.0000	0.9955

Figure 9.1 Sensor installations in the test: FBG sensor (top left), installed FBG sensors for temperature compensation (bottom left), laser displacement transducers (top right), and accelerometers (bottom right).

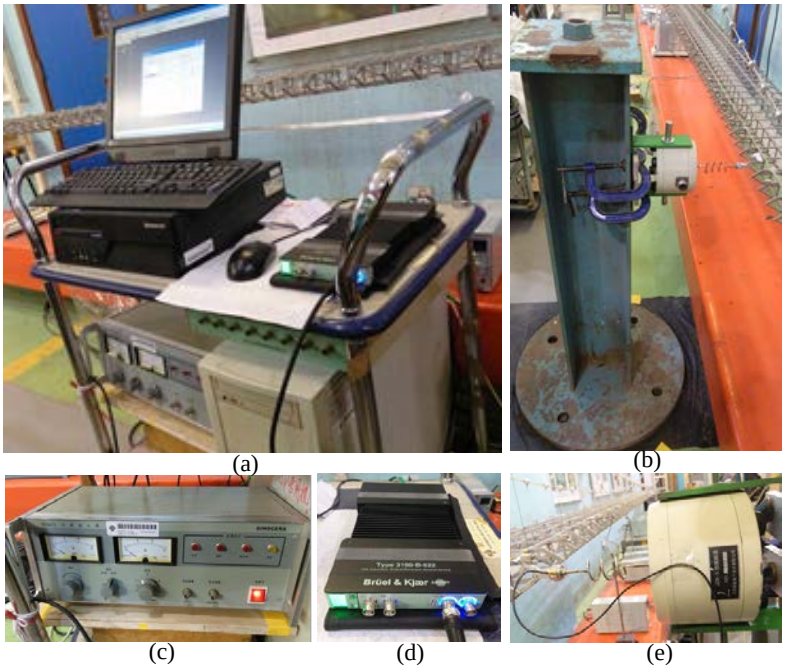

Figure 9.2 Excitation generation system in the test: (a) the overall view of the excitation system, (b) the steel column to host the excitator, (c) SINOCREA YE5871 power amplifier, (d) B&K 3160-B-022 signal generator and (e) JZK-5 exciter.

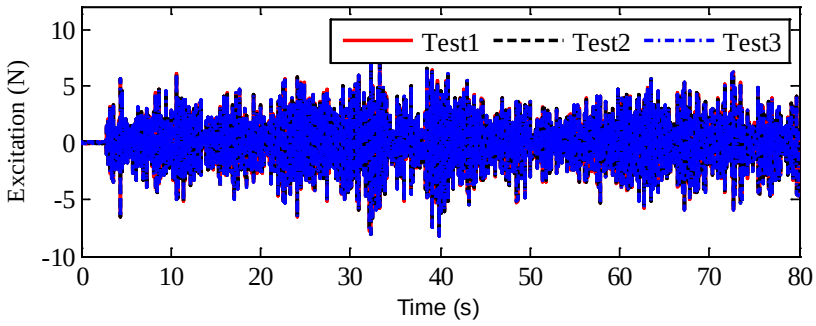

(a)

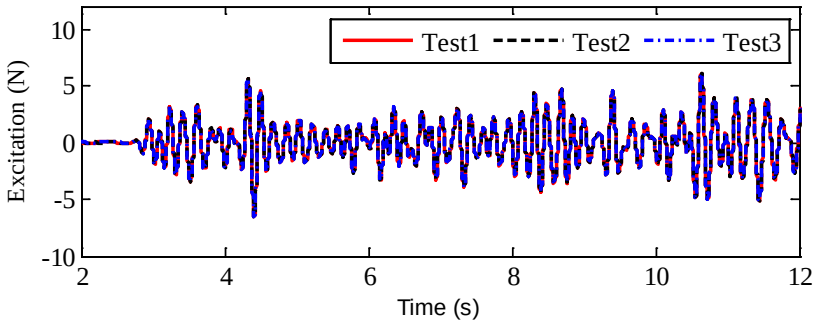

(b)

Figure 9.3 Excitation time-history in 3 tests: (a) overall view of the time-history and (b) a close-view in 7~12 s

(a)

(b)

(c)

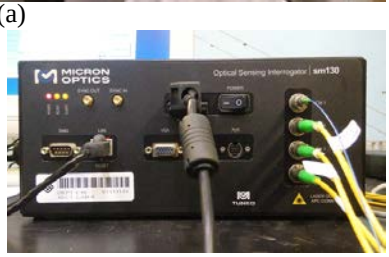

(d)

Figure 9.4 Data acquisition systems in the test: (a) the overall view of the system, (b) KD 5006 charge amplifiers, (c) KYOWA EDX-100A data acquisiter and (d) optical sensing interrogator sm130.

Figure 9.5 Synchronous strain hammer

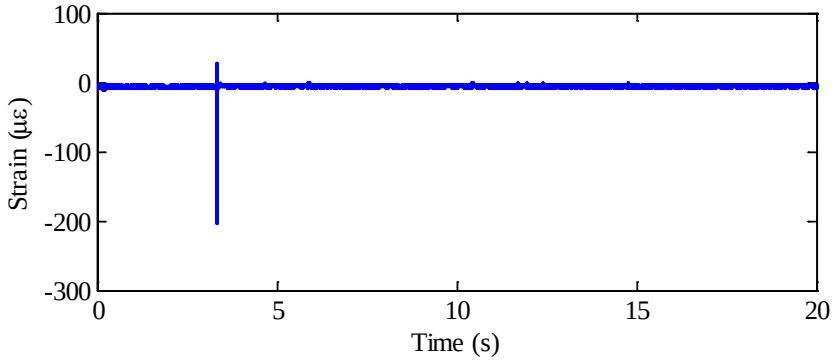

(a)

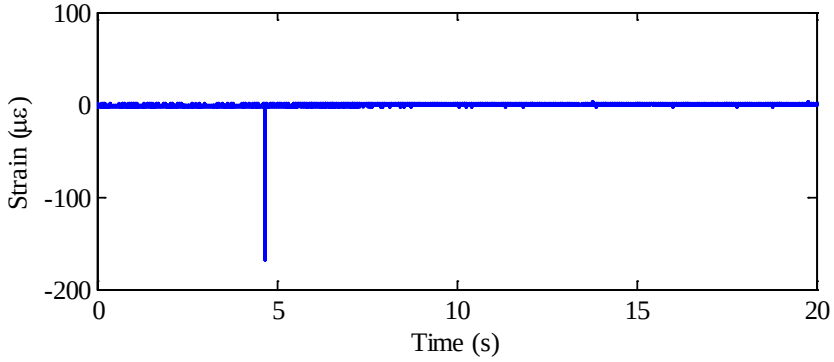

(b)

Figure 9.6 Impulsive signal generated by (a) strain gauge and (b) FBG sensor for time synchronization

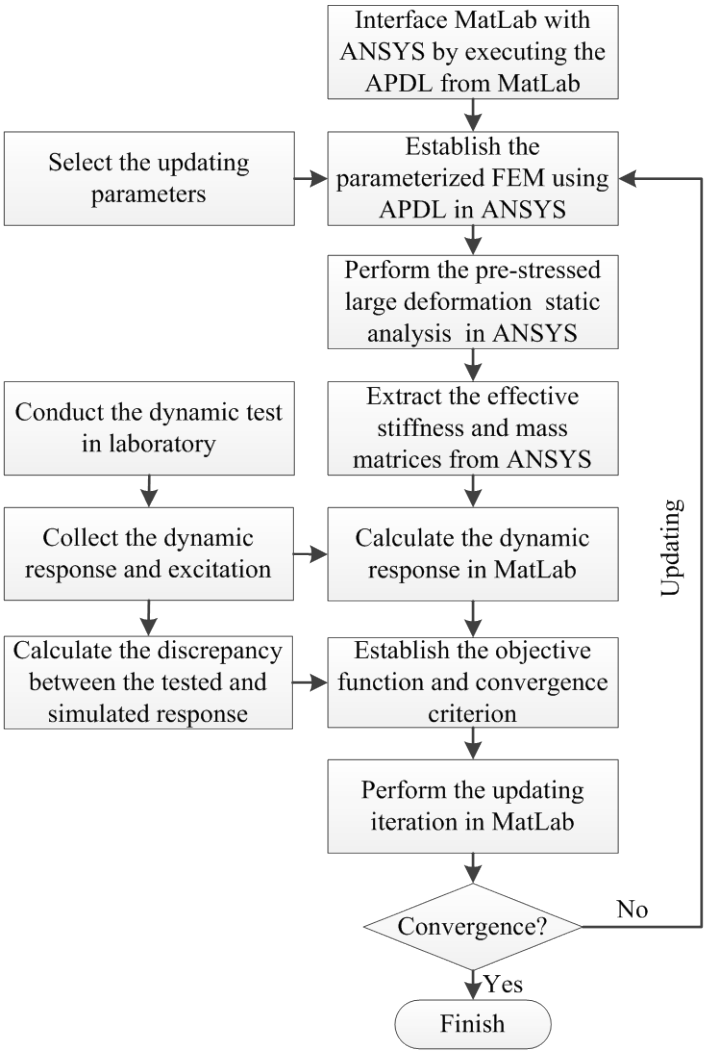

Figure 9.7 Flow diagram of FE model updating by interfacing MatLab and ANSYS

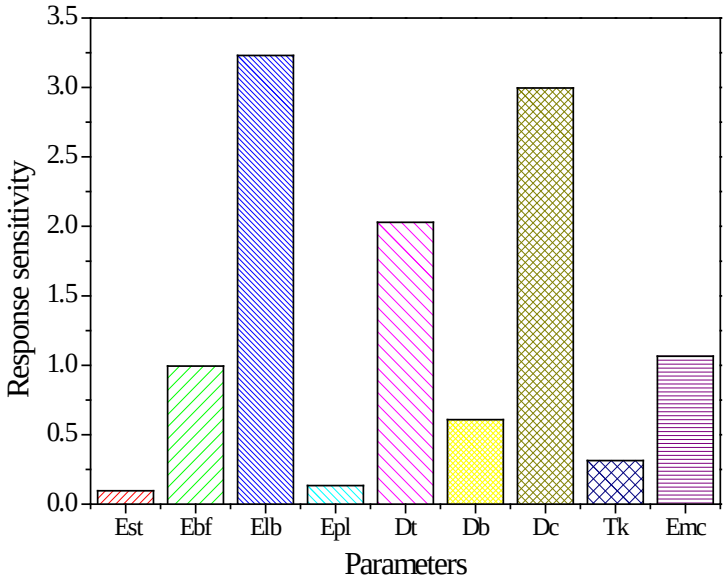

Figure 9.8 Response Sensitivity of TMB Model to Selected Parameters: *Est* (E of steel tower), *Ebf* (E of box frames), *Elb* (E of longtudinal beam), *Epl* (E of plates), *Emc* (E of main cables), *Esup* (E of suspenders), *Dt* (D of aluminium alloy), *Ds* (D of steel), *Dc* (D of steel strand), *Tk* (thickness of plates), *Kcont* (K of vertical connection between TY tower and deck), *Kconp* (K of vertical connection between M1,T1,T2,T3 pier and deck), *Kconl* (K of lateral connection between TY, MW tower and deck), Ectd: E of bearing between MW tower, M2 pier and deck), *Kconv* (K of vertical connection between MW tower, M2 pier and deck), *Dp* (D of plates where masses are added), *Db* (D of truss beam density where masses are added), *ak* (added stiffness due to the installed excitor), *Dama (*mass Rayleigh damping ratio) and *Damb* (stiffness Rayleigh damping ratio), in which E denotes Young's modulus, D denotes density and K denotes spring stiffness.

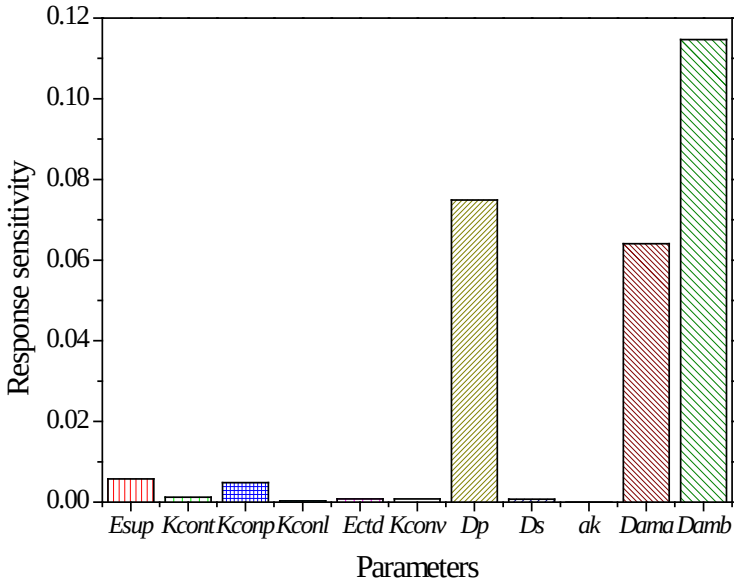

Figure 9.8 (*Continued)*

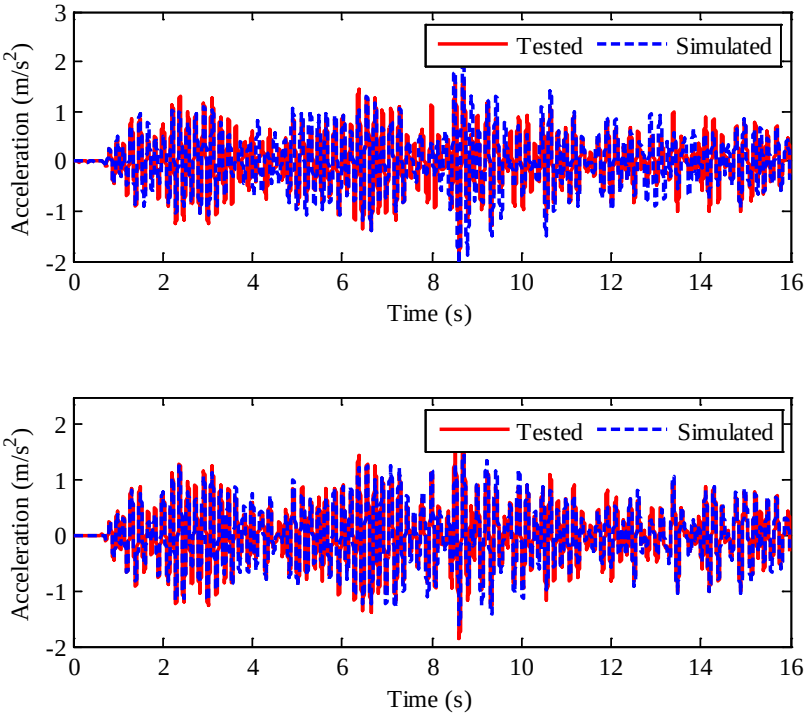

Figure 9.9 Comparison of tested and simulated acceleration response on A10: before model updating (top) and after model updating (bottom)

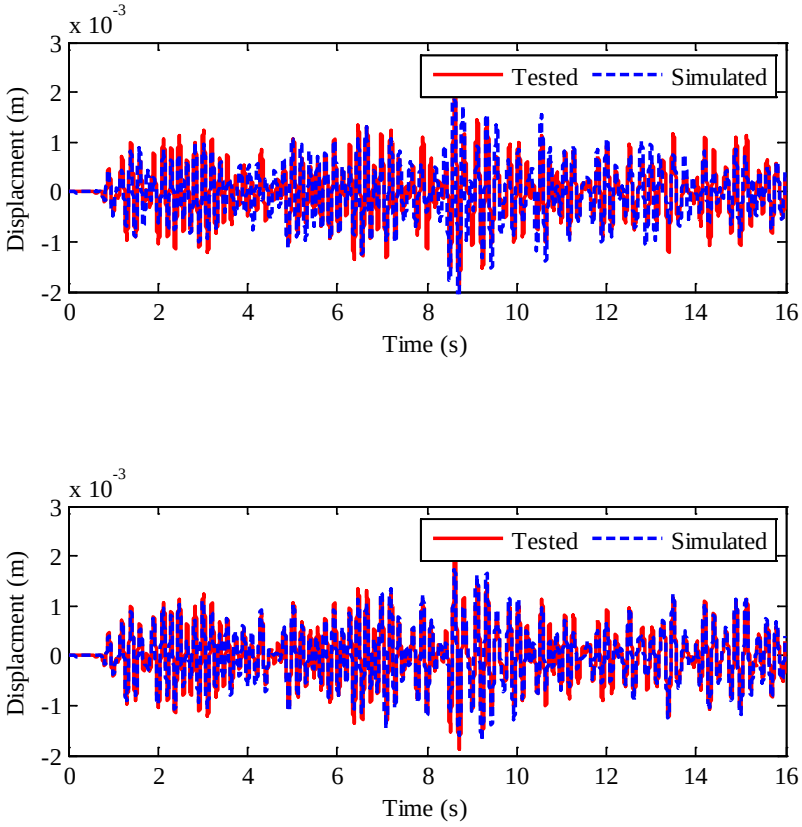

Figure 9.10 Comparison of tested and simulated displacement response on D3: before model updating (top) and after model updating (bottom)

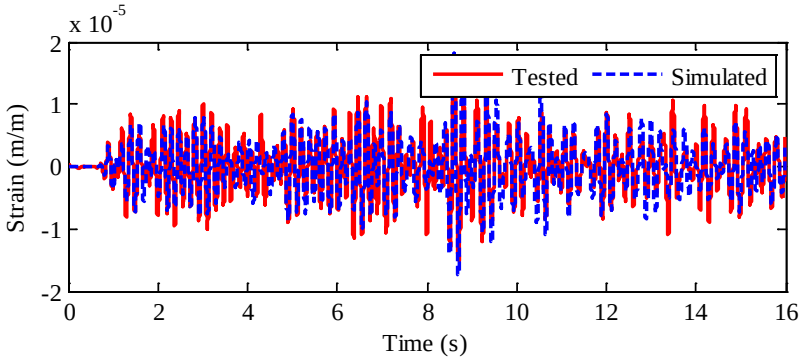

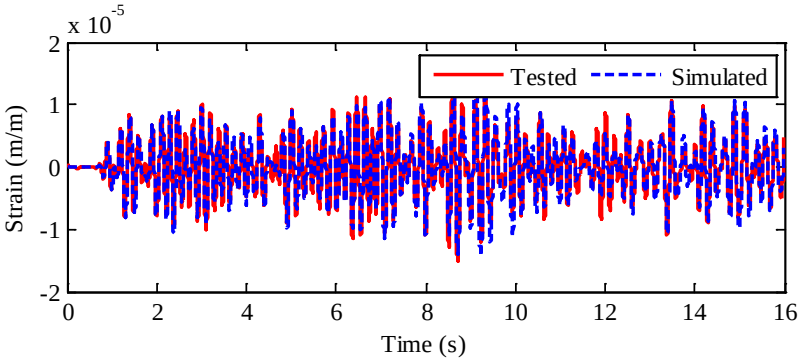

Figure 9.11 Comparison of tested and simulated strain response on S24: before model updating (top) and after model updating (bottom)

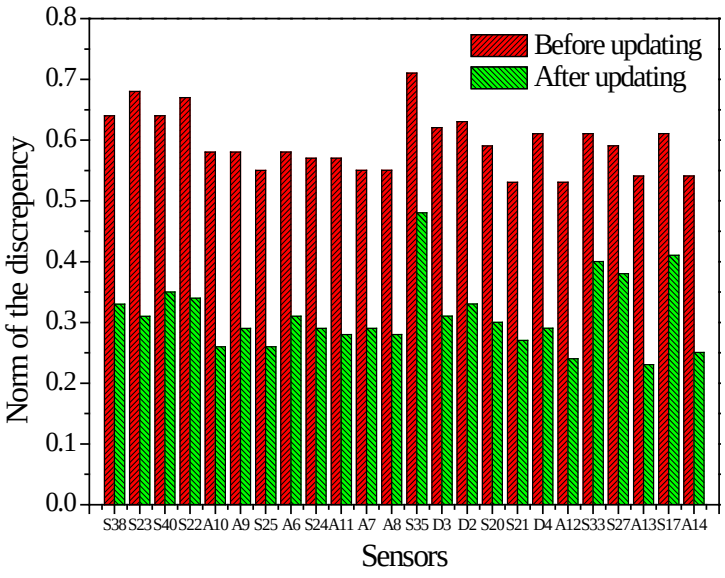

Figure 9.12 Relative norm of discrepancy between the tested and simulated responses on the updating sensors

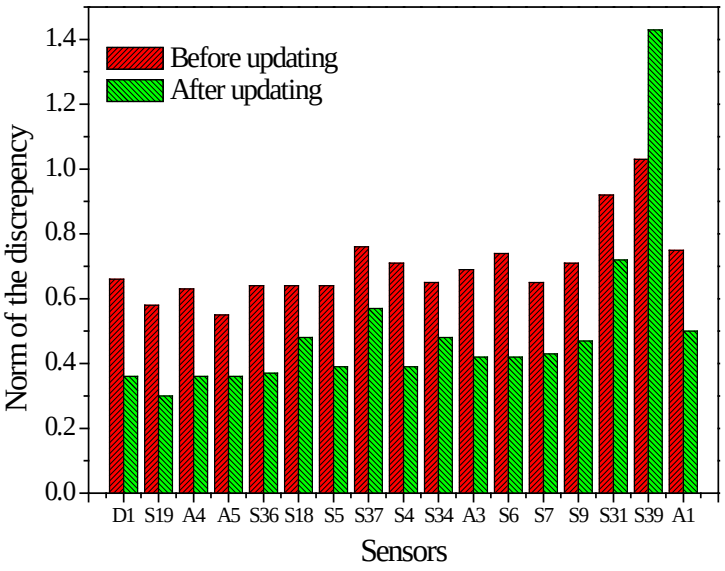

Figure 9.13 Relative norm of discrepancy between the tested and simulated responses on the validation sensors

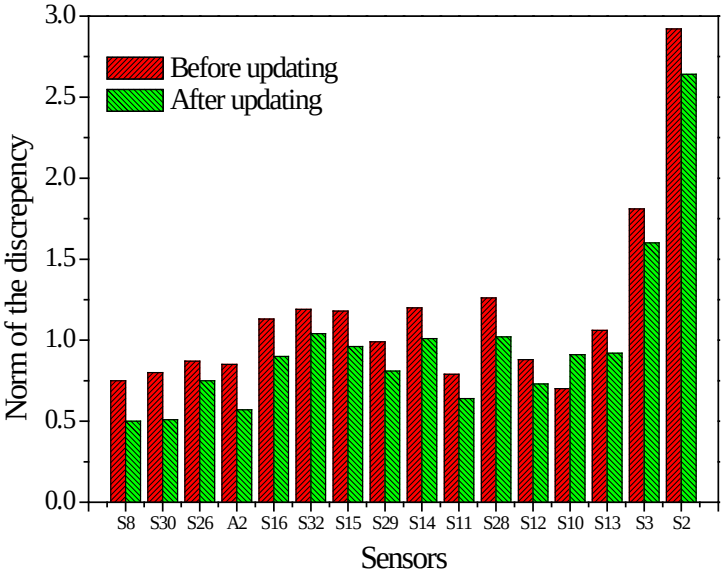

Figure 9.13 (continued)

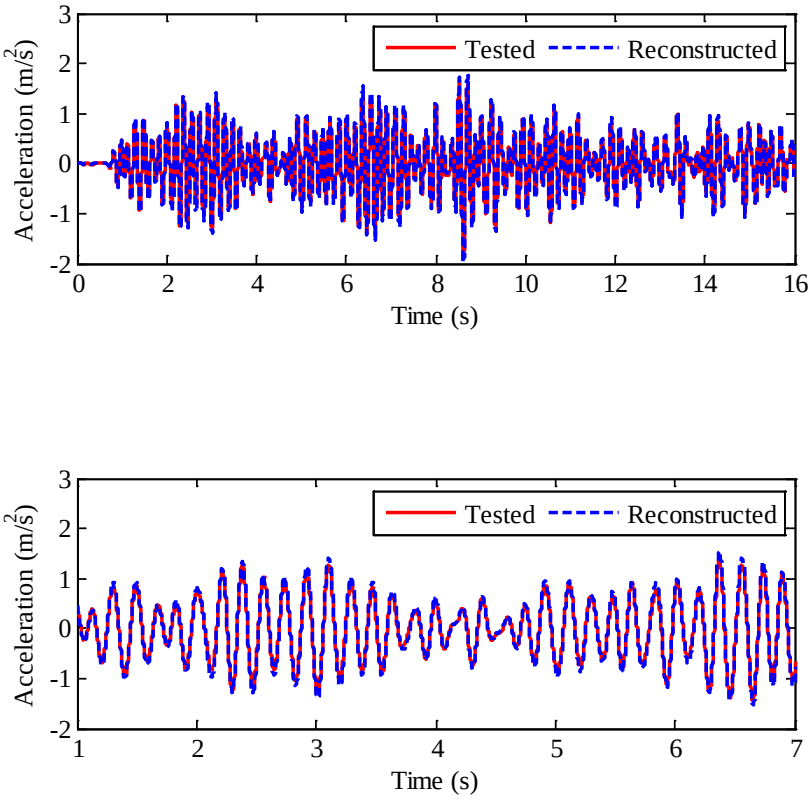

Figure 9.14 Comparison of tested and reconstructed acceleration response on A10: an overall view (top) and a close-up view between 1~7s (bottom)

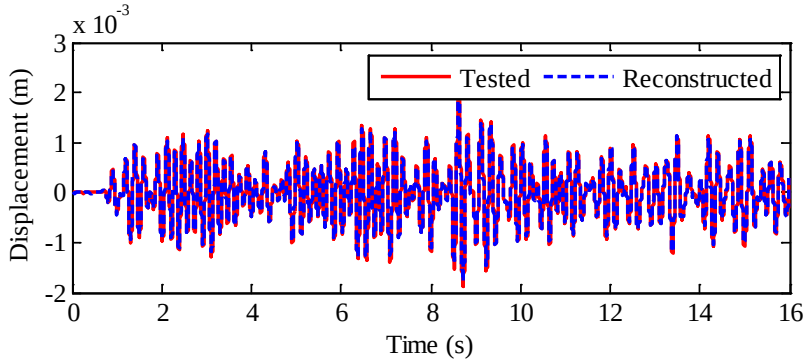

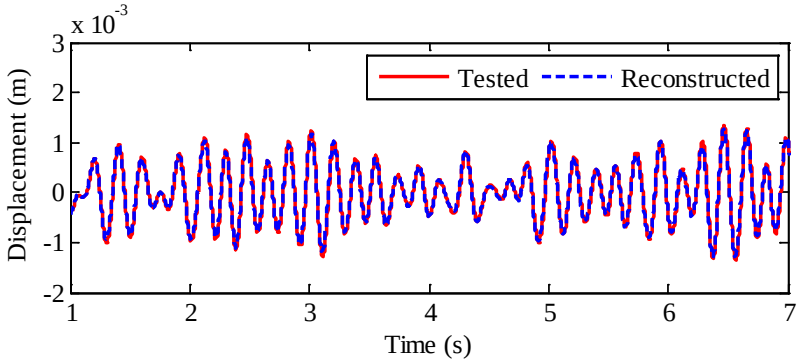

Figure 9.15 Comparison of tested and reconstructed acceleration response on D3: an overall view (top) and a close-up view between 1~7s (bottom)

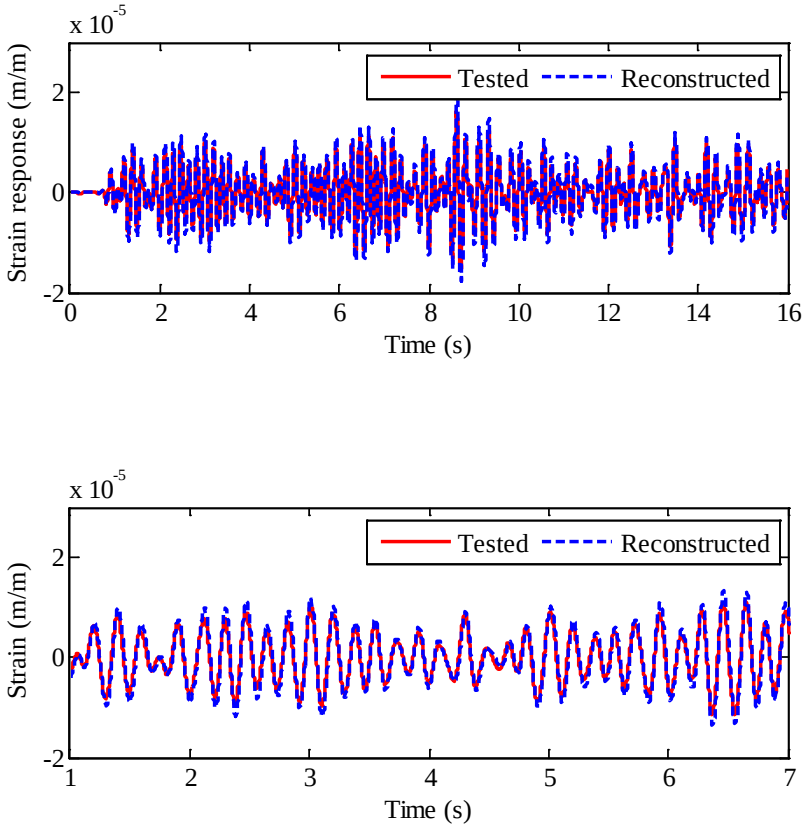

Figure 9.16 Comparison of tested and reconstructed acceleration response on S24: an overall view (top) and a close-up view between 1~7s (bottom)

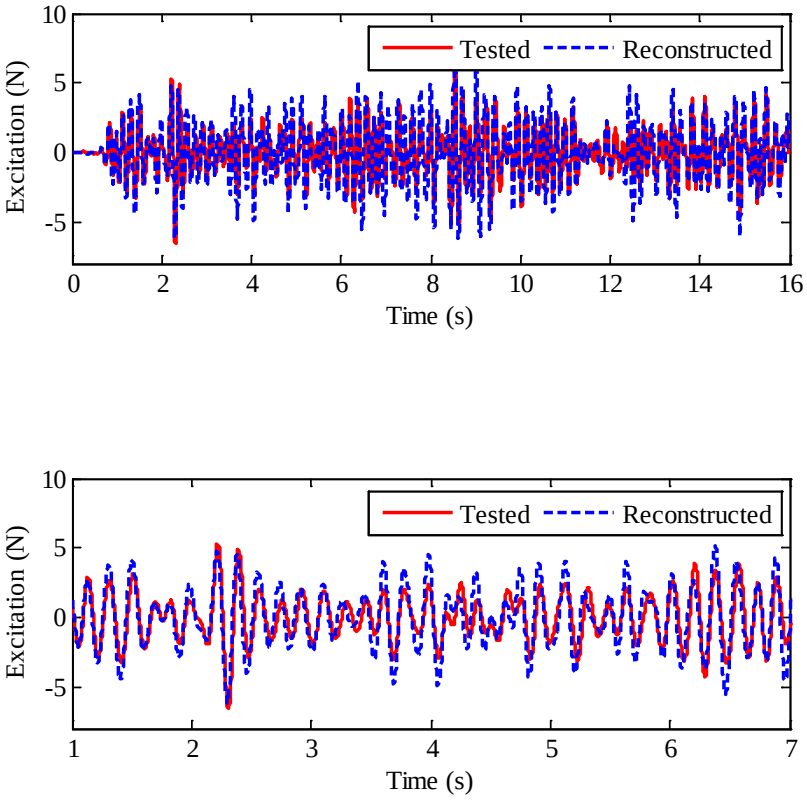

Figure 9.17 Comparison of tested and reconstructed excitation: an overall view (top) and a close-up view between 1~7s (bottom)

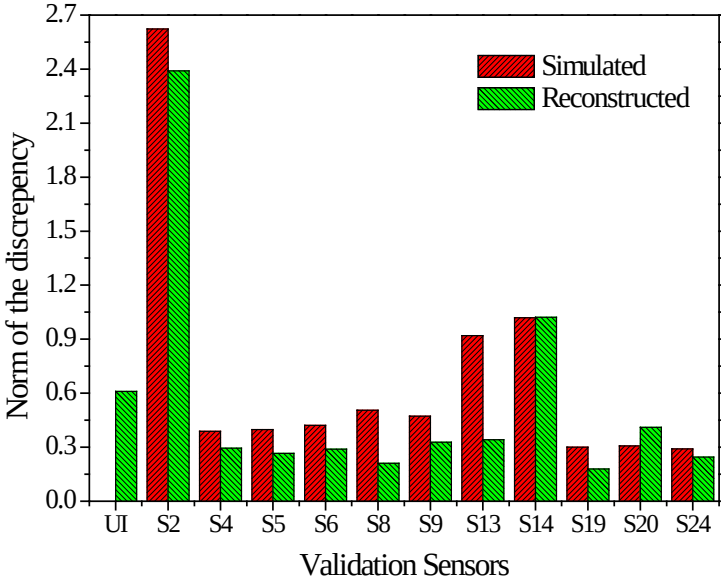

Figure 9.18 Norm of the discrepancy on the validation sensors

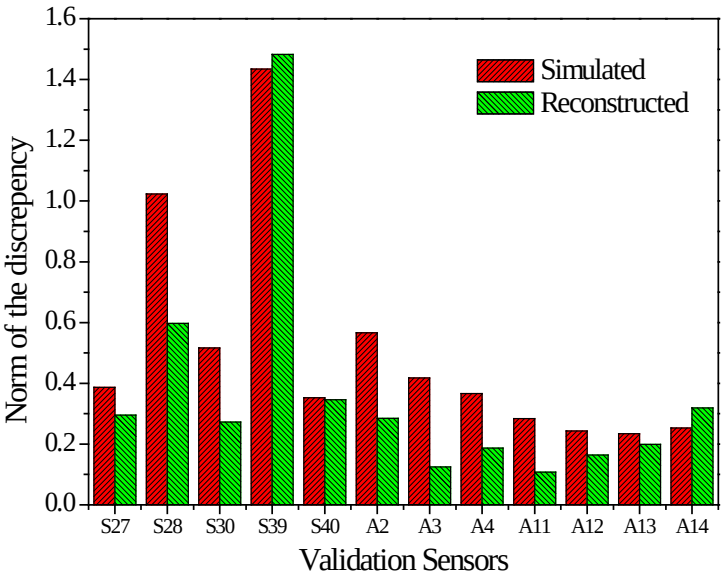

Figure 9.20 (continued)

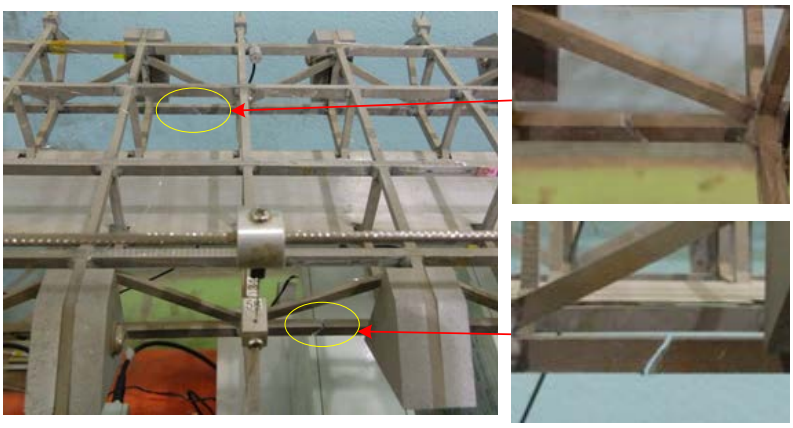

Figure 9.19 Beam cutting to simulate the structural damage in the test

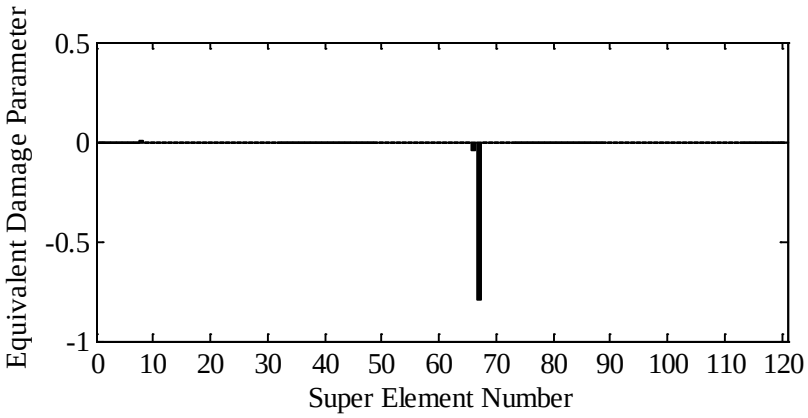

Figure 9.20 Substructure level damage in the test

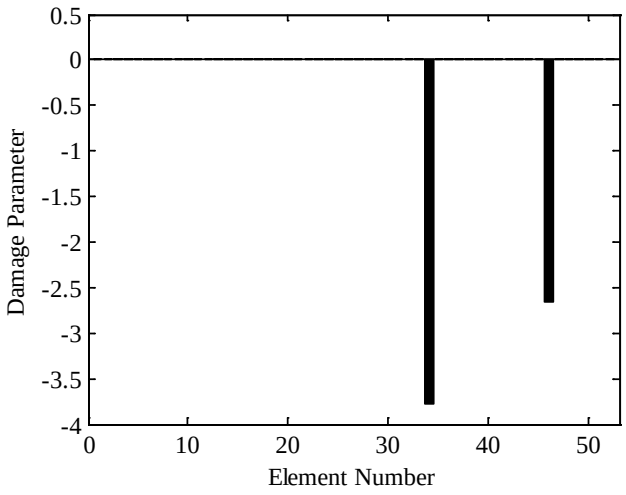

(a)

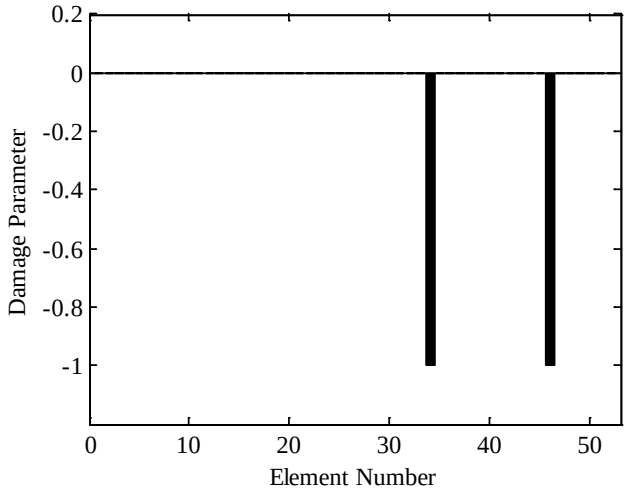

(b)

Figure 9.21 Substructure level damage with response reconstruction in the test: (a) with constraint $\boldsymbol{\theta}^s \leq 0$ and (b) with constraint $-1.0 \leq \boldsymbol{\theta}^s \leq 0$

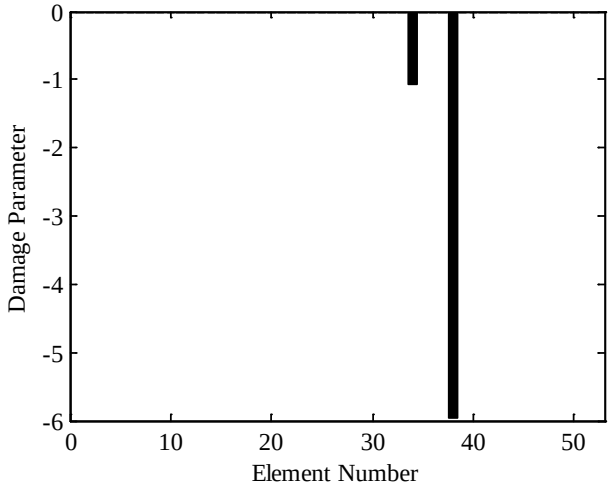

Figure 9.22 Substructure level damage without response reconstruction in the test

CHAPTER 10

CONCLUSIONS AND RECOMMENDATIONS

10.1 Conclusions

This thesis focuses on the development of novel finite element (FE) model updating-based damage identification methods for large civil structures in consideration of optimal multi-type sensor placement, joint response and excitation reconstruction, sparse regularization, and substructuring technique. In particular, this study is dedicated to: (1) proposing an optimal multi-type sensor placement method for best joint response and excitation reconstruction, using the Kalman filter under unknown input (KF-UI); (2) proposing a sparse regularization, specifically ℓ_1 norm regularization, to replace traditional Tikhonov regularization to constrain the norm of the solution as well as to promote the sparsity of the solution in FE model updating-based damage identification; (3) combining the Kalman filter-based response reconstruction with the sparse regularized FE model updating for damage identification of large structures with limited sensors; (4) extending the dynamic response reconstruction-oriented damage identification method to situations where the time histories of excitations are unknown; (5) proposing a multi-level damage identification method for large civil structures using the substructuring technique and response reconstruction; and (6) conducting experimental studies on a simple overhanging beam and a relatively large structure (i.e., the Ting Ma suspension bridge testbed) to validate the effectiveness of the proposed methods. The main contributions and conclusions of this study are summarized below.

1. The multi-type structural responses as well as pre-located excitations can be reconstructed simultaneously through the KF-UI by using the noise-corrupted measurement from the limited sensors, and the FE model of the structure, in which the measurement noise and model error can be dealt with, providing the well-reconstructed responses for the structure at key locations where no sensors are installed and the deterministic excitations acting upon the structure.

2. Proper multi-type sensor placement is optimized based on the asymptotic stability property of the state estimation error from the KF-UI, which allows the best joint response and excitation reconstruction. A heuristic forward sequential sensor placement algorithm, which produces near-optimal sensor deployment, is more computationally efficient for solving the optimization problem and, thus, more applicable to optimal sensor placement on larger civil structures. The designed sensor placement works independently of external excitation, provided that the locations of excitations on the structure, the subset of modes adopted in response reconstruction and environmental noise characteristics remain the same.

3. Compared to traditional Tikhonov regularization, sparse regularization not only constrains the norm of the solution but also promotes the sparsity of the solution (i.e., it maintains the smallest number of non-zero entries in the solution as possible). This motivation is consistent with incipient structural damage, which typically occurs in certain elements or substructures, so that only some entries in the solution are non-zero while the others are zero. Thus, the sparse regularization bears some superiority in terms of less iteration to achieve convergence and less false–positive errors in the solution when performing the FE model updating-based damage identification.

4. To obtain a meaningful solution in the sparse regularized model updating for damage identification, the regularizing parameter, which balances the trade-off between the residual norm and the solution sparsity, should be selected properly. Different from the Tikhonov regularization in the aspect that several well-known methods, such as the L-curve method or general cross-validation, are available, there are no reliable or generally applicable methods for determining optimal regularizing parameters for sparse regularization. This difficulty could be alleviated by using a re-weighted strategy, which iteratively increases the weights of small entries to encourage zero entries in the solution.

5. Kalman filter-based response reconstruction is beneficial to damage identification of large structures because it supplements the limitations of sensor measurement, under the circumstances of both known excitation and unknown excitation. A fusion of the multi-type responses is advantageous not only to increase the accuracy of responses and excitation reconstructions but also to enhance the accuracy of damage identification. This is primarily due to different types of sensors being able to capture structural responses in different frequency regions, and the fusion of multi-type responses manifests a broad bandwidth that incorporates both global and local information regarding the structural conditions.

6. When performing FE model updating based damage identification on large structures that usually consist of massive elements or substructures, a multi-level damage identification strategy may be a wise choice when searching for local damage over a large dimensional damage space. Substructure-level damage detection is first performed over condensed substructures through component mode synthesis (CMS)

technique to identify possible damaged regions; an equivalent damage vector is sought to account for the overall consequence of damages inside the substructure. Further damage localization and quantification are conducted over the elements belonging to suspicious substructures using the reconstructed multi-type responses of the substructure, which are effective for identifying local damages inside a substructure. The proposed multi-level damage identification not only narrows the damage space in substructure- and element-level damage identification but also dramatically decreases the computation efforts of iterative updating, thus increasing the identifiability of damage in the entire procedure.

7. Experimental validations were conducted on a simple overhanging beam, 4 m in length, and the relatively complex Tsing Ma Suspension Bridge (TMB) testbed. Test results from the overhanging beam demonstrate the superiority of sparse regularization over traditional Tikhonov regularization in FE model updating based damage identification. It is also shown that under both known and unknown excitations, multi-type response reconstruction and fusion benefit to damage identification in obtaining more accurate results when the sensor number is limited. Both test results from the overhanging beam and the TMB testbed verify the feasibility of joint response and excitation reconstruction with the optimized sensor placement configuration. Using the proposed multi-level damage identification with response reconstruction method, the preset damages on two longitudinal beams in the deck of the TMB testbed are correctly localized and quantified.

10.2 Recommendations for Future Studies

Although progress has been made in these studies in the development and promotion of a model updating based damage identification that is more applicable to large civil structures, several important issues require further investigations.

1. Although in theory, both single and multiple deterministic excitations of any type (random, harmonic, impulsive, or other) can be reconstructed using KF-UI-based response reconstruction when the number of excitations is not larger than the sensor number or the mode number, only the case of single excitation acting upon the structure is numerically and experimentally investigated in this thesis. The effectiveness of the proposed optimal sensor placement method for joint response and excitation under the circumstances of multiple excitations should be examined in further studies. Joint response and excitation reconstruction under moving loads, which is also a significant loading condition for long-span bridges, is also worth being paid attention to in the future studies.

2. Only three frequently-used sensors, including strain gauges (or Fiber Bragg grating strain sensors), displacement meters, and accelerometers, are used in this thesis for the best response reconstruction. Different types of sensor are equally weighted in this study by setting the weighting matrix as the inversion of noise covariance. With the development of sensor technologies, other types of sensors, such as inclinometers and velocity instruments, could also be employed within the proposed optimal sensor placement framework for specific objectives. Other weighting strategies, such as taking the cost of each type of sensor into consideration, could also be used in practical

applications.

3. Among the several *p*-norm ($0 \le p \le 1$) sparsity promoting regularizations, ℓ_1 norm regularization ($p = 1$) is adopted in this thesis to enhance the accuracy of damage identification because ℓ_1 norm-regularized optimization is a convex problem admitting efficient solution through the use of linear programming techniques. However, when $0 \le p < 1$, *p*-norm regularization promotes increased sparsity. Its advantage in model updating based damage identification is worth investigating. Moreover, a reliable and generally applicable method to determine the regularizing parameters to balance the trade-off between the residual norm and the solution norm is also needed.

4. Because Kalman filter-based response reconstruction is a kind of model based or modal properties based method, the mode shapes of desired locations are required and obtained from the radial basic function network after certain damage occurs. Other mode shape prediction methods could be also incorporated in the proposed response reconstruction-oriented damage identification method. Variations of Kalman filters, such as the extended Kalman filter or robust Kalman filter that are used for state estimation, can also be used to increase response reconstruction accuracy.

5. Although the proposed multi-level damage identification with response reconstruction has been demonstrated in simulation studies and validated in laboratory tests over the Tsing Ma suspension bridge testbed, the robustness of the method should be further examined before practical application. The uncertainty involved in the proposed method is also worth analyzing and quantifying.

6. In this thesis, structural damage is modeled as stiffness degradation to simulate common defects, such as crack growth, corrosion, or bolts loosening in structures. However, a more elaborate damage model is needed to capture the detailed characteristics of specific structural damage. The structural nonlinearity because of damage, which has been ignored in this study, should be included in future research for more accurate structural condition evaluations.

7. Damage prognosis, which predicts structural safety and operational lifetime, has not been touched in this thesis. For that, the established damage evolution and loading prediction models are indispensable. To exploit the advantages of response reconstruction for damage prognosis is also a meaningful research topic.

APPENDIX A

CONVERSION OF STATE SPACE MODEL IN CONTINUOUS TIME TO DISCRETE TIME

Equation Section 1The continuous-time state-space description of a linear time invariant system

$$\begin{aligned}\dot{\mathbf{x}}(t) &= \mathbf{A}_c\mathbf{x}(t) + \mathbf{B}_c\mathbf{u}(t)\\ \mathbf{y}(t) &= \mathbf{C}_c\mathbf{x}(t) + \mathbf{D}_c\mathbf{u}(t)\end{aligned} \tag{A.1}$$

First equation of Eq. (A.1) can be formatted into Eq.(A.2):

$$\dot{\mathbf{x}}(t) - \mathbf{A}_c\mathbf{x}(t) = \mathbf{B}_c\mathbf{u}(t) \tag{A.2}$$

Multiplying $e^{-\mathbf{A}_c t}$ to the both sides of Eq.(A.2)yields:

$$e^{-\mathbf{A}_c t}\left[\dot{\mathbf{x}}(t) - \mathbf{A}_c\mathbf{x}(t)\right] = e^{-\mathbf{A}_c t}\mathbf{B}_c\mathbf{u}(t) \tag{A.3}$$

Eq.(A.3) is equivalently expressed as the following

$$\frac{d\left[e^{-\mathbf{A}_c t}\mathbf{x}(t)\right]}{dt} = e^{-\mathbf{A}_c t}\mathbf{B}_c\mathbf{u}(t) \tag{A.4}$$

Defining a time step Δt, and assuming that the state $\mathbf{x}_k = \mathbf{x}(k\Delta t)$ at the time $t_k = k\Delta t$ ($k = 1, 2, \cdots$) is known, convolution integral on the both sides of Eq.(A.4) at the interval $\left[t_k, t_{k+1}\right]$ is expressed as:

$$\int_{t_k}^{t_{k+1}} d\left[e^{-\mathbf{A}_c t}\mathbf{x}(t)\right] = \int_{t_k}^{t_{k+1}} e^{-\mathbf{A}_c \tau}\mathbf{B}_c\mathbf{u}(\tau)d\tau \tag{A.5}$$

The integral of left side of Eq.(A.5) is:

$$\int_{t_k}^{t_{k+1}} d\left[e^{-\mathbf{A}_c t}\mathbf{x}(t)\right] = e^{-\mathbf{A}_c t}\mathbf{x}(t)\Big|_{x_k, t_k}^{x_{k+1}, t_{k+1}} = e^{-\mathbf{A}_c t_{k+1}}\mathbf{x}_{k+1} - e^{-\mathbf{A}_c t_k}\mathbf{x}_k = e^{-\mathbf{A}_c t_k}\left(e^{-\mathbf{A}_c \Delta t}\mathbf{x}_{k+1} - \mathbf{x}_k\right) \tag{A.6}$$

Zero-order-hold assumption:

Tow assumptions are usually made for the inter-sample behavior of $\mathbf{u}(t)$. If the zero-order-hold assumption, that is $\mathbf{u}(t) = \mathbf{u}_k$ ($(t_k < t < t_{k+1})$), is adopted, the integral of the right side of Eq.(A.6) is expressed as:

$$\begin{aligned}\int_{t_k}^{t_{k+1}} e^{-\mathbf{A}_c \tau}\mathbf{B}_c\mathbf{u}(\tau)d\tau &= \int_{t_k}^{t_{k+1}} e^{-\mathbf{A}_c \tau}\mathbf{B}_c\mathbf{u}_k d\tau = \int_{t_k}^{t_{k+1}} e^{-\mathbf{A}_c \tau}d\tau\mathbf{B}_c\mathbf{u}_k = \left[-\mathbf{A}_c^{-1}\left(e^{-\mathbf{A}_c \tau}\Big|_{t_k}^{t_{k+1}}\right)\right]\mathbf{B}_c\mathbf{u}_k \\ &= \left[-\mathbf{A}_c^{-1}\left(e^{-\mathbf{A}_c (t_k + \Delta t)} - e^{-\mathbf{A}_c t_k}\right)\right]\mathbf{B}_c\mathbf{u}_k = -\mathbf{A}_c^{-1}e^{-\mathbf{A}_c t_k}\left(e^{-\mathbf{A}_c \Delta t} - \mathbf{I}\right)\mathbf{B}_c\mathbf{u}_k\end{aligned} \tag{A.7}$$

Combing Eq.(A.6) with Eq.(A.7), it is finally derived that

$$\mathbf{x}_{k+1} = e^{\mathbf{A}_c \Delta t}\mathbf{x}_k + \left(e^{\mathbf{A}_c t} - \mathbf{I}\right)\mathbf{A}_c^{-1}\mathbf{B}_c\mathbf{u}_k \tag{A.8}$$

Thus continuous-time state-space as Eq.(A.1) can be written in the discrete-time formulation as:

$$\begin{aligned}\mathbf{x}_{k+1} &= \mathbf{A}_d\mathbf{x}_k + \mathbf{B}_d\mathbf{u}_k \\ \mathbf{y}_{k+1} &= \mathbf{C}_d\mathbf{x}_k + \mathbf{D}_d\mathbf{u}_k\end{aligned} \tag{A.9}$$

in which the discrete-time system matrices are expressed as:

$$\mathbf{A}_d = e^{\mathbf{A}_c \Delta t}; \mathbf{B}_d = \left(e^{\mathbf{A}_c \Delta t} - \mathbf{I}\right)\mathbf{A}_c^{-1}\mathbf{B}_c; \mathbf{C}_d = \mathbf{C}_d; \mathbf{D}_d = \mathbf{D}_d \tag{A.10}$$

First-order-hold assumption:

If the zero-order-hold assumption, that is $\mathbf{u}(t) = \left[\mathbf{u}_k + \frac{t - t_k}{\Delta t}\left(\mathbf{u}_{k+1} - \mathbf{u}_k\right)\right]$ $\left(\left(t_k < t < t_{k+1}\right)\right)$, is adopted, the integral of the right side of Eq.(A.6) is expressed as:

$$\begin{aligned}\int_{t_k}^{t_{k+1}} e^{-\mathbf{A}_c \tau}\mathbf{B}_c\mathbf{u}(\tau)d\tau &= \int_{t_k}^{t_{k+1}} e^{-\mathbf{A}_c \tau}\mathbf{B}_c\left[\mathbf{u}_k + \frac{\tau - t_k}{\Delta t}\left(\mathbf{u}_{k+1} - \mathbf{u}_k\right)\right]d\tau \\ &= \int_{t_k}^{t_{k+1}} e^{-\mathbf{A}_c \tau}d\tau\mathbf{B}_c\mathbf{u}_k + \int_{t_k}^{t_{k+1}} e^{-\mathbf{A}_c \tau}\frac{\tau - t_k}{\Delta t}d\tau\mathbf{B}_c\left(\mathbf{u}_{k+1} - \mathbf{u}_k\right) \\ &= \left[-\mathbf{A}_c^{-1}\left(e^{-\mathbf{A}_c\left(t_k + \Delta t\right)} - e^{-\mathbf{A}_c t_k}\right)\right]\mathbf{B}_c\mathbf{u}_k = -\mathbf{A}_c^{-1}e^{-\mathbf{A}_c t_k}\left(e^{-\mathbf{A}_c \Delta t} - \mathbf{I}\right)\mathbf{B}_c\mathbf{u}_k\end{aligned} \tag{A.11}$$

The first part of the right side of Eq.(A.11) is easily obtained as Eq.(A.7). Moreover, the second part of the right side of Eq.(A.11) is

$$\begin{aligned}\int_{t_k}^{t_{k+1}} e^{-\mathbf{A}_c \tau}\frac{\tau - t_k}{\Delta t}d\tau &= \frac{1}{\Delta t}\left[-\int_{t_k}^{t_{k+1}} e^{-\mathbf{A}_c \tau}\mathbf{A}_c^{-1}d\tau - \left[e^{-\mathbf{A}_c \tau}\left(\tau - t_k\right)\mathbf{A}_c^{-1}\right]\Big|_{t_k}^{t_{k+1}}\right] \\ &= -\frac{1}{\Delta t}\left[e^{-\mathbf{A}_c \tau}\left(\tau - t_k\right)\mathbf{A}_c^{-1} + e^{-\mathbf{A}_c \tau}\mathbf{A}_c^{-1}\mathbf{A}_c^{-1}\right]\Big|_{t_k}^{t_{k+1}} \\ &= -\frac{1}{\Delta t}e^{-\mathbf{A}_c t_k}\left[e^{-\mathbf{A}_c \Delta t}\left(\Delta t\mathbf{A}_c^{-1} + \mathbf{A}_c^{-1}\mathbf{A}_c^{-1}t_k\right) - \mathbf{A}_c^{-1}\mathbf{A}_c^{-1}\right] \\ &= -\frac{1}{\Delta t}e^{-\mathbf{A}_c t_k}\left[\Delta t e^{-\mathbf{A}_c \Delta t}\mathbf{A}_c^{-1} + \left(e^{-\mathbf{A}_c \Delta t} - \mathbf{I}\right)\mathbf{A}_c^{-1}\mathbf{A}_c^{-1}\right]\end{aligned} \tag{A.12}$$

All integrals in (A.5) are assembled, forming the following equation:

$$\begin{aligned}e^{-\mathbf{A}_c t_k}\left(e^{-\mathbf{A}_c \Delta t}\mathbf{x}_{k+1} - \mathbf{x}_k\right) &= e^{-\mathbf{A}_c t_k}\mathbf{A}_c^{-1}\left(\mathbf{I} - e^{-\mathbf{A}_c \Delta t}\right)\mathbf{B}_c\mathbf{u}_k \\ &+ \frac{-1}{\Delta t}e^{-\mathbf{A}_c t_k}\left[\Delta t e^{-\mathbf{A}_c \Delta t}\mathbf{A}_c^{-1} + \left(e^{-\mathbf{A}_c \Delta t} - \mathbf{I}\right)\mathbf{A}_c^{-1}\mathbf{A}_c^{-1}\right]\mathbf{B}_c\left(\mathbf{u}_{k+1} - \mathbf{u}_k\right)\end{aligned} \tag{A.13}$$

The above Eq.(A.13) is finally derived as:

$$\begin{aligned}
\mathbf{x}_{k+1} &= e^{\mathbf{A}_c\Delta t}\mathbf{x}_k - \mathbf{A}_c^{-1}e^{\mathbf{A}_c\Delta t}\left(e^{-\mathbf{A}_c\Delta t}-\mathbf{I}\right)\mathbf{B}_c\mathbf{u}_k + \frac{e^{\mathbf{A}_c\Delta t}}{\Delta t}\left[\Delta t e^{-\mathbf{A}_c\Delta t}\mathbf{A}_c^{-1} + \left(e^{-\mathbf{A}_c\Delta t}-\mathbf{I}\right)\mathbf{A}_c^{-1}\mathbf{A}_c^{-1}\right]\mathbf{B}_c\left(\mathbf{u}_{k+1}-\mathbf{u}_k\right) \\
&= e^{\mathbf{A}_c\Delta t}\mathbf{x}_k - \mathbf{A}_c^{-1}\left(\mathbf{I}-e^{\mathbf{A}_c\Delta t}\right)\mathbf{B}_c\mathbf{u}_k + \frac{-1}{\Delta t}\left[\Delta t\mathbf{A}_c^{-1} + \left(\mathbf{I}-e^{\mathbf{A}_c\Delta t}\right)\mathbf{A}_c^{-1}\mathbf{A}_c^{-1}\right]\mathbf{B}_c\left(\mathbf{u}_{k+1}-\mathbf{u}_k\right) \\
&= e^{\mathbf{A}_c\Delta t}\mathbf{x}_k + \left(e^{\mathbf{A}_c\Delta t}-\mathbf{I}\right)\mathbf{A}_c^{-1}\mathbf{B}_c\mathbf{u}_k + \left[\Delta t\mathbf{A}_c^{-1} + \left(\mathbf{I}-e^{\mathbf{A}_c\Delta t}\right)\mathbf{A}_c^{-1}\mathbf{A}_c^{-1}\right]\mathbf{B}_c\frac{\left(\mathbf{u}_k-\mathbf{u}_{k+1}\right)}{\Delta t} \\
&= e^{\mathbf{A}_c\Delta t}\mathbf{x}_k + \left(e^{\mathbf{A}_c\Delta t}-\mathbf{I}\right)\mathbf{A}_c^{-1}\mathbf{B}_c\mathbf{u}_k + \left[\mathbf{A}_c\Delta t + \left(\mathbf{I}-e^{\mathbf{A}_c\Delta t}\right)\right]\mathbf{A}_c^{-1}\mathbf{A}_c^{-1}\mathbf{B}_c/\Delta t\,\mathbf{u}_k \\
&\quad - \left[\mathbf{A}_c\Delta t + \left(\mathbf{I}-e^{\mathbf{A}_c\Delta t}\right)\right]\mathbf{A}_c^{-1}\mathbf{A}_c^{-1}\mathbf{B}_c/\Delta t\,\mathbf{u}_{k+1} \\
&= e^{\mathbf{A}_c\Delta t}\mathbf{x}_k + \left(e^{\mathbf{A}_c\Delta t}-\mathbf{I}\right)\mathbf{A}_c^{-1}\mathbf{B}_c\mathbf{u}_k - \left[e^{\mathbf{A}_c\Delta t}-\mathbf{A}_c\Delta t-\mathbf{I}\right]\mathbf{A}_c^{-2}\mathbf{B}_c/\Delta t\,\mathbf{u}_k \\
&\quad + \left[e^{\mathbf{A}_c\Delta t}-\mathbf{A}_c\Delta t-\mathbf{I}\right]\mathbf{A}_c^{-2}\mathbf{B}_c/\Delta t\,\mathbf{u}_{k+1}
\end{aligned} \tag{A.14}$$

Submitting Eq.(A.14) into the second equation of Eq.(A.9), it can be derived that

$$\begin{cases} \mathbf{A}_d = e^{\mathbf{A}_c\Delta t};\mathbf{B}_d = \mathbf{B}_0 + \mathbf{A}_d\mathbf{B}_1 \\ \mathbf{C}_d = \mathbf{C}_c;\mathbf{D}_d = \mathbf{C}_c\mathbf{B}_1 + \mathbf{D}_c \end{cases} \tag{A.15}$$

in which

$$\mathbf{B}_0 = \left(\mathbf{A}_d-\mathbf{I}\right)\mathbf{A}_c^{-1}\mathbf{B}_c - \mathbf{B}_1;\mathbf{B}_1 = \left(\mathbf{A}_d-\mathbf{A}_c\Delta t-\mathbf{I}\right)\mathbf{A}_c^{-2}\mathbf{B}_c/\Delta t \tag{A.16}$$

APPENDIX B

DERIVATION OF KALMAN FILTER UNDER UNKNOWN INPUT

Equation Section 2The dynamics of a structure can be represented in a discrete-time state space representation as:

$$\begin{aligned}\mathbf{x}_{k+1} &= \mathbf{A}_d \mathbf{x}_k + \mathbf{B}_d \mathbf{u}_k + \mathbf{w}_k \\ \mathbf{y}_k^m &= \mathbf{C}_d^m x_k + \mathbf{D}_d^m u_k + \mathbf{v}_k\end{aligned} \tag{B.1}$$

where $\mathbf{x}_k \in \Re^n$ is the state vector, $\mathbf{u}_k \in \Re^p$ is an unknown input vector, and $\mathbf{y}_k^m \in \Re^m$ is the measurement. The process noise $\mathbf{w}_k \in \Re^n$ and the measurement noise $\mathbf{v}_k \in \Re^m$ are assumed to be mutually uncorrelated, zero mean, white random signals with known covariance matrices $\mathrm{cov}\left(\mathbf{w}_k, \mathbf{w}_j\right) = \mathbf{Q}\delta_{kj}$ and $\mathrm{cov}\left(\mathbf{v}_k, \mathbf{v}_j\right) = \mathbf{R}\delta_{kj}$ .We suppose that $\left(\mathbf{A}_d, \mathbf{C}_d^m\right)$ is observable and that $\mathbf{x}_0$ is independent of and for all *k*. Also, we assume that an unbiased estimate $\hat{\mathbf{x}}_0$ of the initial state $\mathbf{x}_0$ is available with the covariance matrix $\mathrm{cov}\left(\mathbf{x}_0, \mathbf{x}_0\right) = \mathbf{P}_0^x$. We consider a recursive three-step filter of the form:

$$\hat{\mathbf{x}}_k^- = \mathbf{A}_d \hat{\mathbf{x}}_{k-1}^+ + \mathbf{B}_d \hat{\mathbf{u}}_{k-1} \tag{B.2}$$

$$\hat{\mathbf{u}}_k = \mathbf{M}_k \left(\mathbf{y}_k^m - \mathbf{C}_d^m \hat{\mathbf{x}}_k^-\right) \tag{B.3}$$

$$\hat{\mathbf{x}}_k^+ = \hat{\mathbf{x}}_k^- + \mathbf{K}_k \left(\mathbf{y}_k^m - \mathbf{C}_d^m \hat{\mathbf{x}}_k^-\right) \tag{B.4}$$

where $\hat{\mathbf{x}}_k^-$ and $\hat{\mathbf{x}}_k^+$ denotes the a *priori* the a *posteriori* estimate and of the state vector $\mathbf{x}_k$ and $\hat{\mathbf{u}}_k$ is the estimate of external excitation $\mathbf{u}_k$ .The matrices $\mathbf{M}_k \in \Re^{m\times p}$ and $\mathbf{K}_k \in \Re^{n\times p}$ should be determined when designing the three-step filter.

Firstly we will estimate $\mathbf{x}_k$ using the measurements up to time $k-1$. The error in the estimate $\hat{\mathbf{x}}_k^-$ given by Eq. (B.2) is expressed by

$$\tilde{\mathbf{x}}_k^- = \mathbf{x}_k - \hat{\mathbf{x}}_k^- = \left(\mathbf{A}_d\mathbf{x}_{k-1} + \mathbf{B}_d\mathbf{u}_{k-1} + \mathbf{w}_{k-1}\right) - \left(\mathbf{A}_d\hat{\mathbf{x}}_{k-1}^+ + \mathbf{B}_d\mathbf{u}_{k-1}\right) = \mathbf{A}_d\tilde{\mathbf{x}}_{k-1}^+ + \mathbf{B}_d\tilde{\mathbf{u}}_{k-1} + \mathbf{w}_{k-1} \quad \text{(B.5)}$$

in which $\tilde{\mathbf{x}}_k^+ = \mathbf{x}_k - \hat{\mathbf{x}}_k^+$ and $\tilde{\mathbf{u}}_k = \mathbf{u}_k - \hat{\mathbf{u}}_k$. Consequently, the covariance matrix of $\hat{\mathbf{x}}_k^-$ is given by

$$\mathbf{P}_k^{x-} = E\left[\tilde{\mathbf{x}}_k^-\left(\tilde{\mathbf{x}}_k^-\right)^T\right] = \begin{bmatrix}\mathbf{A}_d & \mathbf{B}_d\end{bmatrix}\begin{bmatrix}\mathbf{P}_{k-1}^{x+} & \mathbf{P}_{k-1}^{xu}\\ \mathbf{P}_{k-1}^{ux} & \mathbf{P}_{k-1}^{u}\end{bmatrix}\begin{bmatrix}\mathbf{A}_d^T\\ \mathbf{B}_d^T\end{bmatrix} + \mathbf{Q}_{k-1} \quad \text{(B.6)}$$

with $\mathbf{P}_k^{x+} = E\left[\tilde{\mathbf{x}}_k^+\left(\tilde{\mathbf{x}}_k^+\right)^T\right]$, $\mathbf{P}_k^u = E\left[\tilde{\mathbf{u}}_k\left(\tilde{\mathbf{u}}_k\right)^T\right]$ and $\left(\mathbf{P}_k^{xu}\right)^T = \mathbf{P}_k^{ux} = E\left[\tilde{\mathbf{x}}_k^+\left(\tilde{\mathbf{u}}_k^T\right)\right]$.

Then we will estimate the unknown input. The innovation is defined as $\tilde{\mathbf{y}}_k^m = \mathbf{y}_k^m - \mathbf{C}_k^m\hat{\mathbf{x}}_k^-$

$$\tilde{\mathbf{y}}_k = \mathbf{y}_k^m - \mathbf{C}_d^m\hat{\mathbf{x}}_k^- = \mathbf{C}_d^m\mathbf{x}_k + \mathbf{D}_d^m\mathbf{u}_k + \mathbf{v}_k - \mathbf{C}_d^m\hat{\mathbf{x}}_k^- = \mathbf{C}_d^m\left(\mathbf{x}_k - \hat{\mathbf{x}}_k^-\right) + \mathbf{D}_d^m\mathbf{u}_k + \mathbf{v}_k = \mathbf{D}_d^m\mathbf{u}_k + \mathbf{e}_k \quad \text{(B.7)}$$

$$\mathbf{e}_k = \mathbf{C}_d^m\left(\mathbf{x}_k - \hat{\mathbf{x}}_k^-\right) + \mathbf{v}_k = \mathbf{C}_d^m\tilde{\mathbf{x}}_k^- + \mathbf{v}_k \quad \text{(B.8)}$$

Since $\hat{\mathbf{x}}_k^-$ is unbiased, it follows from (B.8) that $E\left[e_k\right] = 0$ and consequently,

$$E\left[\hat{\mathbf{u}}_k\right] = E\left[\mathbf{M}_k\tilde{\mathbf{y}}_k\right] = E\left[\mathbf{M}_k\left(\mathbf{D}_d^m\mathbf{u}_k + \mathbf{e}_k\right)\right] = E\left[\mathbf{M}_d^m\mathbf{D}_d^m\mathbf{u}_k\right] = \mathbf{M}_k\mathbf{D}_d^m E\left[\mathbf{u}_k\right] \qquad \text{(B.9)}$$

Thus an unbiased estimator for all possible $\mathbf{u}_k$ can be obtained if and only if $\mathbf{M}_k$ satisfies $\mathbf{M}_k\mathbf{D}_d^m = \mathbf{I}$. The matrix $\mathbf{M}_k = (\mathbf{D}_d^{mT}\mathbf{D}_d^m)^{-1}\mathbf{D}_d^{mT}$ corresponding to the least square (LS) solution satisfies the condition. However, from the Gauss–Markov theorem, it is not necessarily minimum-variance because in general

$$\tilde{\mathbf{R}}_k = E\left[\mathbf{e}_k\mathbf{e}_k^T\right] = \mathbf{C}_k\mathbf{P}_k^{x-}\mathbf{C}_k^T + \mathbf{R} \neq c\mathbf{I} \qquad \text{(B.10)}$$

Under the assumption that $\tilde{\mathbf{R}}_k$ is positive definite, an invertible matrix $\tilde{\mathbf{S}}_k$ satisfying $\tilde{\mathbf{S}}_k\tilde{\mathbf{S}}_k^T = \tilde{\mathbf{R}}_k$ ($\tilde{R}_k$ is symmetric) can always be found, for example, by a Cholesky factorization.

$$\tilde{\mathbf{S}}_k^{-1}\tilde{\mathbf{y}}_k = \tilde{\mathbf{S}}_k^{-1}\mathbf{D}_d^m\mathbf{u}_{k-1} + \tilde{\mathbf{S}}_k^{-1}\mathbf{e}_k \qquad \text{(B.11)}$$

Under the assumption that $\tilde{\mathbf{S}}_k^{-1}\mathbf{D}_d^m$ has full column rank, the LS solution $\hat{\mathbf{u}}_{k-1}$ of Eq. (B.11) equals

$$\hat{\mathbf{u}}_{k-1} = \left(\mathbf{D}_d^m\tilde{\mathbf{R}}_k^{-1}\mathbf{D}_d^{mT}\right)^{-1}\mathbf{D}_d^{mT}\tilde{\mathbf{R}}_k^{-1}\tilde{\mathbf{y}}_k \qquad \text{(B.12)}$$

Note that solving Eq. (B.11) by LS estimation is equivalent to solving (B.7) by weighted LS estimation with weighting matrix $\tilde{\mathbf{R}}_k^{-1}$. Then for the $\mathbf{M}_k$ given by

$$\mathbf{M}_k = \left(\mathbf{D}_d^m\tilde{\mathbf{R}}_k^{-1}\mathbf{D}_d^{mT}\right)^{-1}\mathbf{D}_d^{mT}\tilde{\mathbf{R}}_k^{-1} \qquad \text{(B.13)}$$

$\hat{\mathbf{u}}_k$ is the minimum-variance unbiased estimator of $\mathbf{u}_k$ given $\tilde{\mathbf{y}}_k$.

APPENDIX C

PREDICTED MODE SHAPES OF THE SUBSTRUCTURE USING RBF NETWORK

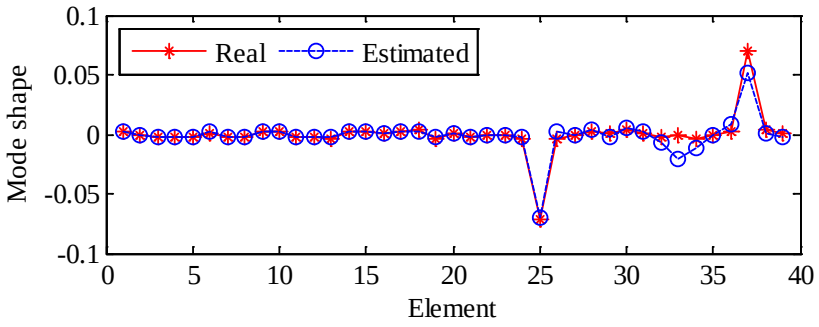

(a)

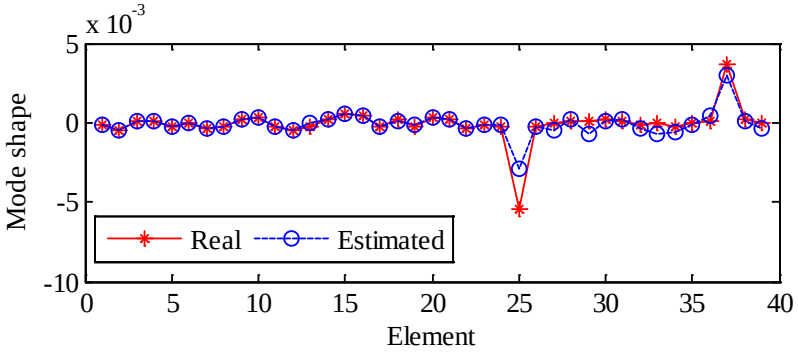

(b)

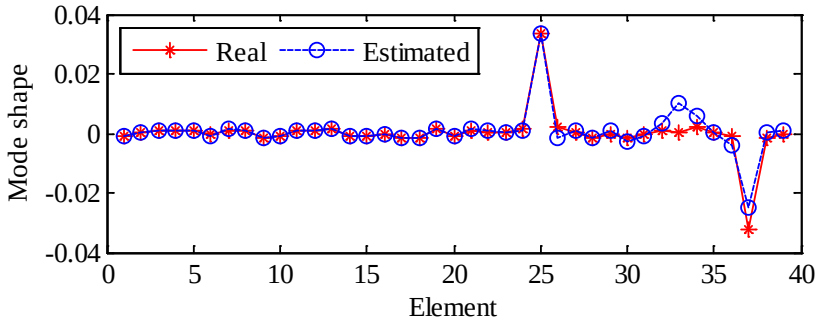
Real
Estimated
Mode shape
Element
0.04
0.02
0
-0.02
-0.04
0
5
10
15
20
25
30
35
40

(c)

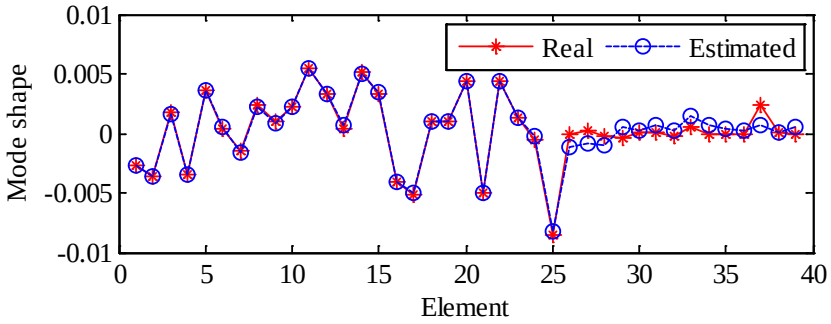
Real
Estimated
Mode shape
Element
0.01
0.005
0
-0.005
-0.01
0
5
10
15
20
25
30
35
40

(d)

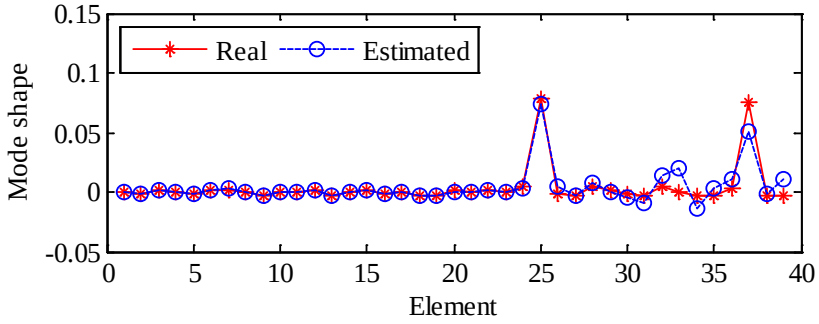
Real
Estimated
Mode shape
Element
0.15
0.1
0.05
0
-0.05
0
5
10
15
20
25
30
35
40

(e)

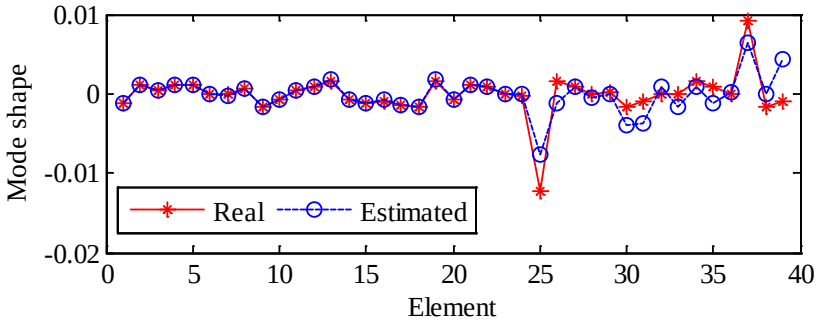
0.01
0
-0.01
-0.02
Mode shape
Real
Estimated
0
5
10
15
20
25
30
35
40
Element

(f)

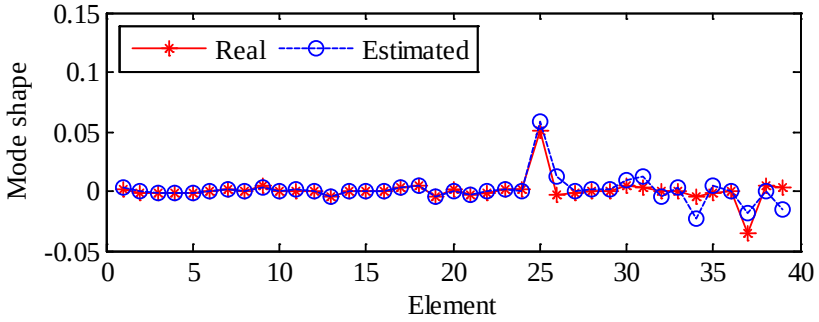
0.15
0.1
0.05
0
-0.05
Mode shape
Real
Estimated
0
5
10
15
20
25
30
35
40
Element

(g)

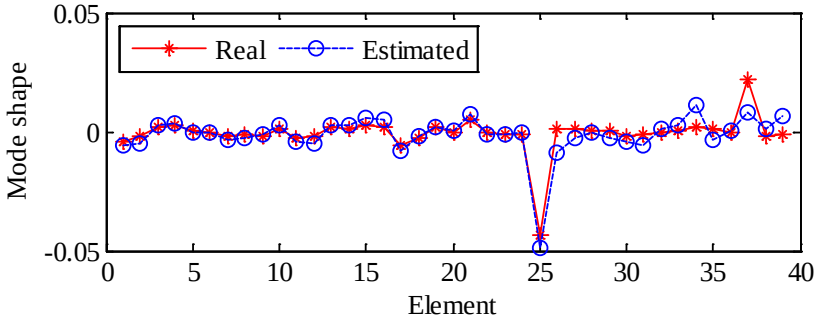
0.05
0
-0.05
Mode shape
Real
Estimated
0
5
10
15
20
25
30
35
40
Element

(h)

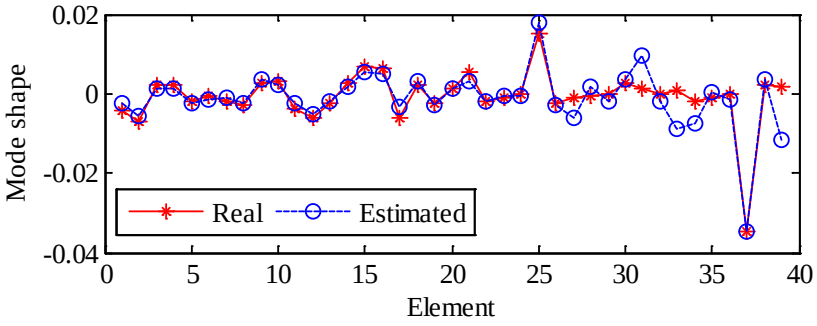

(i)

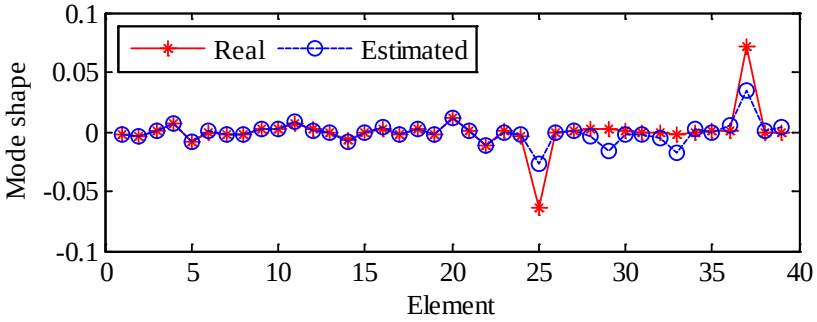

(j)

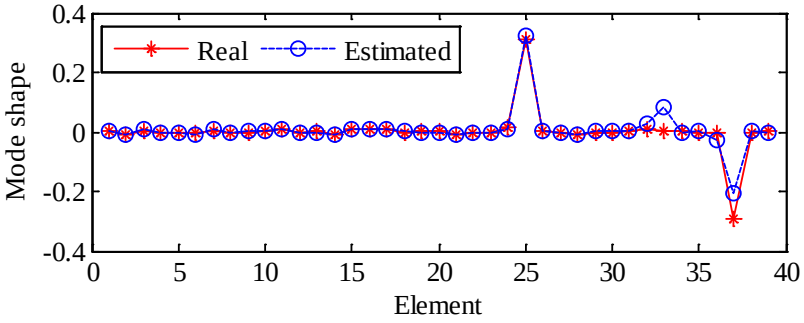

(k)

Figure C.1 Predicted strain mode shape of the 67-th substructure: (a) ~ (k) for the 1-st~11-th mode shape

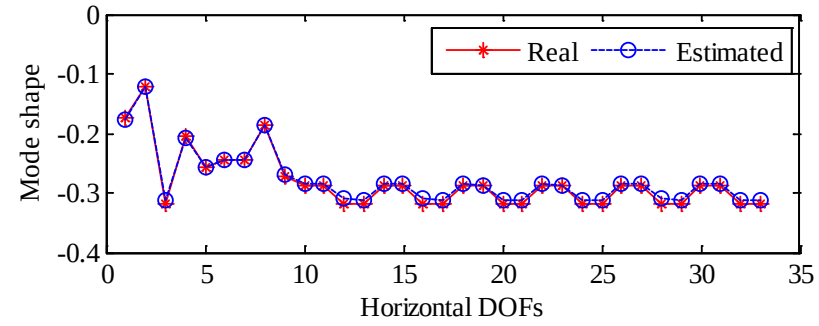
Real
Estimated
Mode shape
Horizontal DOFs
0
-0.1
-0.2
-0.3
-0.4
0
5
10
15
20
25
30
35

(a)

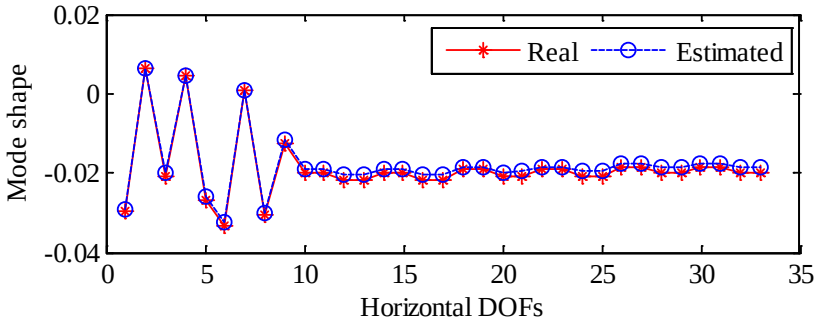
Real
Estimated
Mode shape
Horizontal DOFs
0.02
0
-0.02
-0.04
0
5
10
15
20
25
30
35

(b)

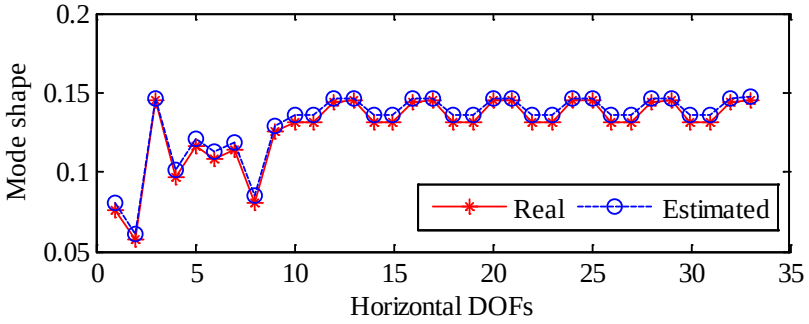
Real
Estimated
Mode shape
Horizontal DOFs
0.2
0.15
0.1
0.05
0
5
10
15
20
25
30
35

(c)

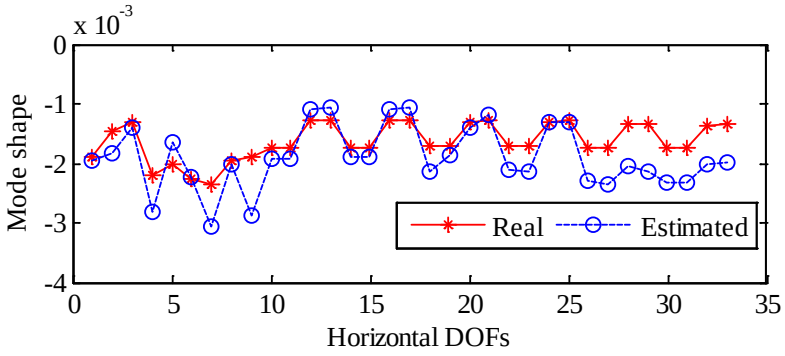
x 10^-3
0
-1
-2
-3
-4
Mode shape
Real
Estimated
0
5
10
15
20
25
30
35
Horizontal DOFs

(d)

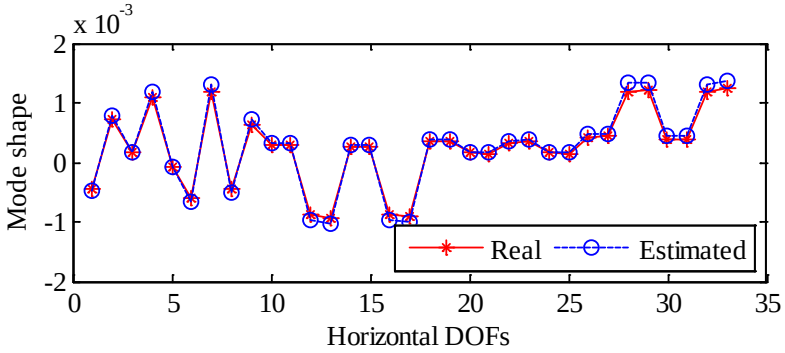
x 10^-3
2
1
0
-1
-2
Mode shape
Real
Estimated
0
5
10
15
20
25
30
35
Horizontal DOFs

(e)

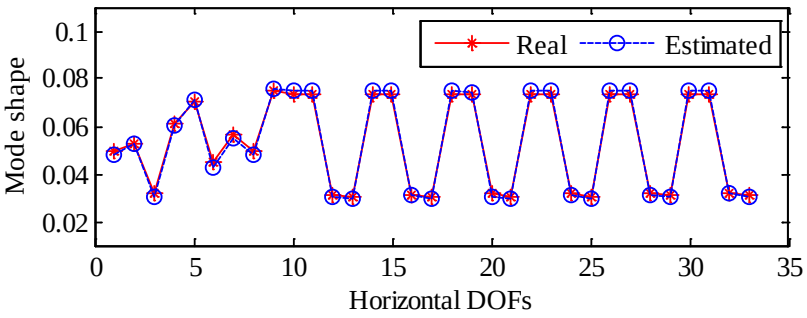
0.1
0.08
0.06
0.04
0.02
Mode shape
Real
Estimated
0
5
10
15
20
25
30
35
Horizontal DOFs

(f)

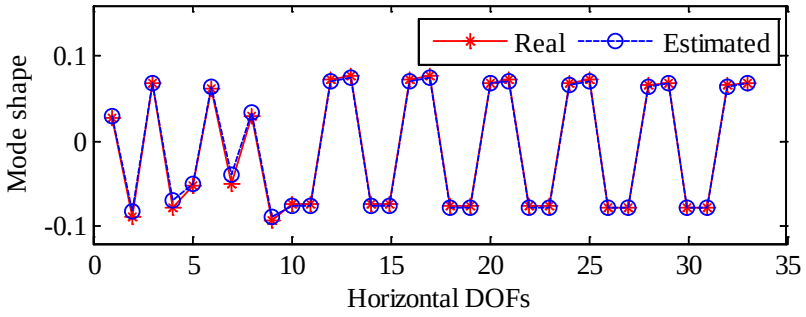
Real
Estimated
Mode shape
0.1
0
-0.1
0
5
10
15
20
25
30
35
Horizontal DOFs

(g)

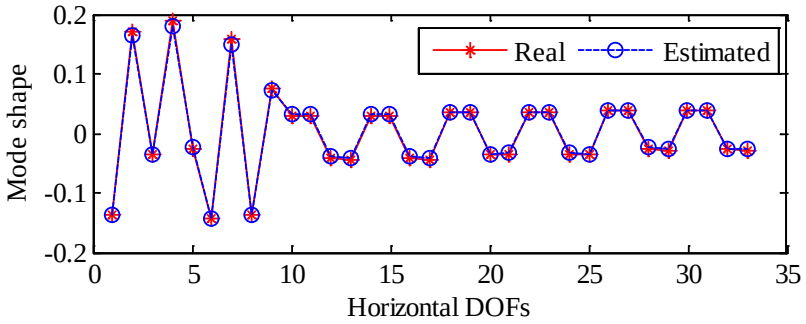
Real
Estimated
Mode shape
0.2
0.1
0
-0.1
-0.2
0
5
10
15
20
25
30
35
Horizontal DOFs

(h)

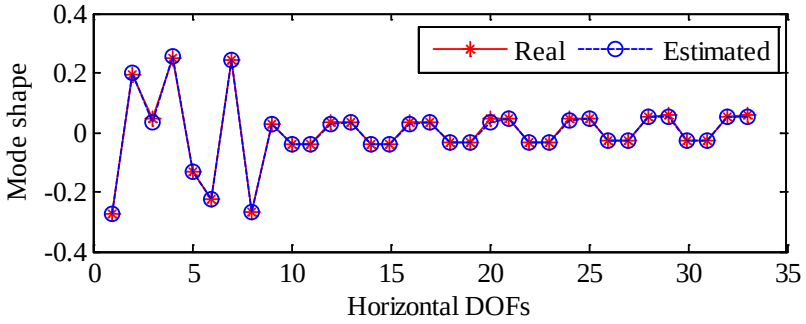
Real
Estimated
Mode shape
0.4
0.2
0
-0.2
-0.4
0
5
10
15
20
25
30
35
Horizontal DOFs

(i)

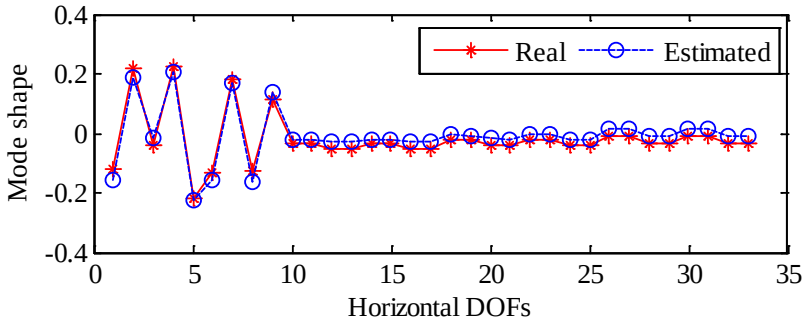

(j)

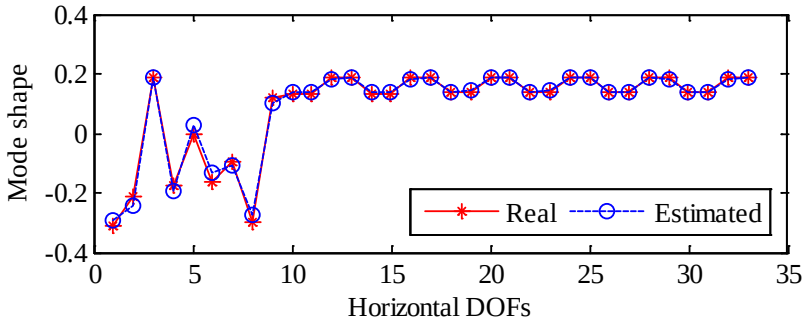

(k)

Figure C.2 Predicted horizontal displacement mode shape of the 67-th substructure: (a) ~ (k) for the 1-st~11-th mode shape

REFERENCES

Abdullah M.M., Richardson A., & Hanif J. (2001). Placement of sensors/actuators on civil structures using genetic algorithms. *Earthquake Engineering and Structural Dynamics,* 30: 1167-1184.

Ahmadian H., Mottershead J.E., & Friswell M.I. (1998). Regularization methods for finite element model updating, *Mechanical Systems and Signal Processing*, 12 (1): 47–64.

Aktan A.E., Lee K.L., Chuntavan, C., & Aksel, T. (1994). Modal testing for structural identification and condition assessment of constructed facilities. *The Proceeding of the 12th International Modal Analysis Conference*, Honolulu, Hawaii.

Arash Nasseri. (2010). Seismic response reconstruction and evaluation of nonlinear static analysis procedures using data from instrumented buildings. Northeastern University, January.

Anderson B.D.O., & Moore J.B. (1979). *Optimal Filtering. Courier Corporation.*

ASCE (2013). Report Card for American Infrastructure issued by the American Society of Civil Engineers, The American Society of Civil Engineers

Asma F., & Bouazzouni A. (2005). Finite element model updating using FRF measurements. *Shock and Vibration*, 12(5): 377-388.

Azam S.E., Chatzi E., & Papadimitriou C. (2015). A dual Kalman filter approach for state estimation via output-only acceleration measurements, *Mechanical Systems and Signal Processing* 60-61: 866-886.

Azarbayejani M., Eli-Osery A.I., Choi K.K., & Reda Taha M.M. (2008). A probabilistic approach for optimal sensor allocation in structural health monitoring, *Smart Materials and Structures*, 17: 055019.

Balageas D., Fritzen C.P., & Güemes A. (Eds.) (2006). *Structural Health Monitoring*, UK: ISTE, London.

Baruch M. (1978). Optimisation procedure to correct stiffness and flexibility matrices using vibration data, *AIAA Journal*, 16(11): 1208--1210.

Berman A., & Nagy E.J. (1983). Improvement of large analytical model using test data, *AIAA Journal*, 21(8): 1169-2273.

Beck A., & Teboulle M. (2009). A fast iterative shrinkage-thresholding algorithm for linear inverse problems, *SIAM Journal on Imaging Sciences*, 2 (1):183-202.

Bernal D. (2006). Flexibility-based damage localization from stochastic realization results, *Journal of Engineering Mechanics*, 132(6):651-658.

Bisby, L.A., & Briglio, M.B. (2004). ISIS Canada Educational Module No. 5: An Introduction to Structural Health Monitoring, Prepared by ISIS Canada, Page 3.

Bao Y., Yu Y., & Li H. (2014). Compressive sensing-based lost data recovery of fast-moving wireless sensing for structural health monitoring, *Structure Control and Health Monitoring*, 22(3): 443-448.

Boyd S., & Vandanberghe L. (2004). *Convex Optimization*, Cambridge University Press, New York, NY.

Brown R.G., & Hwang P.Y.C. (2012). *Introduction to Random Signals and Applied*

Kalman Filtering with Matlab Exercises, 4th ed, John Wiley and Sons.

Brownjohn M.W. James, De Stefano, A., Xu, Y.L., Wenzel, H., & Aktan, A.E. (2011). Vibration-based monitoring of civil infrastructure: challenges and successes, Journal of Civil Structural health Monitoring, 1: 79-95.

Bruckstein A., Donoho D., & Elad M. (2009). From sparse solutions of systems of equations to sparse modeling of signals and images, *SIAM Review*, 51(1): 34–81.

Bui H.D. (1994). Inverse *Problems in the Mechanics of Materials: An Introduction*, CRC Press, Boca Raton

Cacciolaa P., Maugerib N., & Muscolinob G. (2011). Structural identification through the measure of deterministic and stochastic time-domain dynamic response, *Computers and Structures*, 89 (19–20): 1812–1819.

Caesar B. (1987). Updating system matrices using modal test data. *Proceeding of the 5th IMAC*, 453-459, London, England.

Candes E., Wakin M., & Boyd S. (2008). Enhancing sparsity by reweighted ℓ1 minimization, *Journal of Fourier Analysis and Applications*, 14: 877-905.

Candes E.J., & Tao T. (2006). Near optimal signal recovery from random projections: universal encoding strategies. *IEEE Transactions on Information Theory*, 52(12):5406–5425.

Cawley P., & Adams R.D. (1979). The location of defects in structures from measurements of natural frequencies, *Journal of Strain Analysis*, 14(2), 49-57.

Chan W.S., Xu Y.L., Ding X.L., & Dai W.J. (2006), Integrated GPS-accelerometer

data processing techniques for structural deformation monitoring, *Journal of Geodesy*, 80(12): 705-719.

Chan T.H.T., Li Z.X., Yu Y., & Sun Z.H. (2009), Concurrent multi-scale modeling of civil infrastructures for analyses on structural deteriorating-Part II: model updating and verification, *Finite Element in Analysis and Design*, 45(11): 795-805.

Chen S., Lin W., Yu J., & Qi A. (2014). Free-Interface Modal Synthesis Based Substructural Damage Detection Method, *Shock and Vibration* 2014: 741697.

Cho S., Sim S.H., Park J.W., & Lee J., (2014). Extension of indirect displacement estimation method using acceleration and strain to various types of beam structures, *Smart Structures & System*, 14(4): 699-718.

Cobb R.G., & Liebst B.S. (1997). Sensor placement and structural damage identification from minimal sensor information, *AIAA Journal*, 35, 369-374.

Cornwell P., Doebling S.W., & Farrar C.R. (1999). Application of the strain energy damage detection method to plate-like structures, *Journal of Sound and Vibration*, 224 (2):359–374.

Cottin N., Felgenhauer H.P., & Natke H.G. (1984). On the parameter identification of elastomechanical systems using input and output residuals. *Ingenieure Archiv*, 54(5):378-387.

Craig R.R., &. Bampton M.C.C. (1968). Coupling of Substructures for Dynamic Analysis, *AIAA Journal*, 6(7):1313–1319.

Craig R.R., & Chang C.J., (1976). A review of substructure coupling methods for dynamic analysis. In: NASA. Langley Research Center

Crowley J., Klosterman A., Rocklin G., & Vold H. (1984). Direct Structural Modification using Frequency Response Functions. *In Proceedings of the Second International Modal Analysis Conference*, Orlando, FL, Bethel, CT, February, Society for Experimental Mechanics.

Darouach M., & Zasadzinski M. (1997). Unbiased minimum variance estimation for systems with unknown exogenous inputs, *Automatica* 33 717–719.

D'Ambrogio W., & Fregolent A. (1998). On the use of consistent and significant information to reduce ill-conditioning in dynamic model updating, *Mechanical Systems and Signal Processing* 12 (1): 203–222.

Danai K, Civjan S. A., & Styckiewicz M. M. (2013). Sensor location selection for structures via identifiability analysis in the time-scale domain, *Journal of Sound and Vibration*, 332(24): 6296-6311.

Ding, Y.L., Li, A.Q., Du, D.S., & Liu, T. (2010). Multi-scale damage analysis for a steel box girder of a long-span cable-stayed bridge, *Structure and Infrastructure Engineering*, 6(6): 725-739.

Doebling, S.W., Farrar, C.R., Prime, M.B., & Shevitz D.W. (1996). Damage Identification and Health Monitoring of Structures and Mechanical Systems from Changes in Their Vibration Characteristics: A Literature Review. Los Alamos National Laboratory Report LA-13070-MS, Los Alamos.

Doebling S.W., Farrar C.R., & Prime M.B. (1998). A summary review of vibration-based damage identification methods, *Shock and Vibration Digest*, 30 91–105.

Donoho D.L. (2006). Compressed sensing. *IEEE Transactions on Information Theory*, 52(4): 1289–1306.

Erazo K., & Hernandez E.M. (2014). A model-based observer for state and stress estimation in structural and mechanical systems: experimental validation, *Mechanical Systems and Signal Processing*, 43: 141–152.

Esfandiari A., Sanayei M., Baskhtiari Nejad F., & Rahai A. (2010a). Finite Element Model Updating Using Frequency Response Function of Incomplete Strain Data, *AIAA Journal*, 48(7):1420-1433.

Esfandiari A., Bakhtiari Nejad F., Sanayei M., & Rahai A. (2010b). Structural finite element model updating using transfer function data, *Computers and Structures*, 88(1-2):54-64.

Ewins D.J. (1984). *Modal Testing: Theory and Practice*. England: Research Studies Press Ltd.

Ewins D.J., & Liu W. (1998). Transmissibility properties of MDOF systems, *Proceedings of the 16th International Modal Analysis Conference (IMACXVI)*, Santa Barbara, California, USA, pp. 847–854.

Fang H., & Callafon R.A. (2012). On the asymptotic stability of minimum-variance unbiased input and state estimation, *Automatica* 48: 3183–3186.

Farhat C., & Hemez F.M. (1993). Updating finite element dynamic models using an element-by-element sensitivity methodology, *AIAA Journal*, 31: 1702-1711.

Farrar C.R., Baker W.E., Bell T.M., Cone K.M., Darling T.W., Duffey T.A., Eklund A. & Miglori A. (1994). Dynamic characterization and damage detection in the I-40

bridge over the Rio Grande. Los Alamos National Laboratory Report LA–12767–MS, Los Alamos National Laboratory, P.O. Box 1193, Los Alamos, NM, 87544, USA.

Farrar, C. R., & Worden, K. (2012). *Structural Health Monitoring: a Machine Learning Perspective*. John Wiley & Sons.

Fox R.L., & Kapoor M.P. (1968). Rate of change of eigenvectors and eigenvalues, *AIAA Journal*, 12(6): 2426-2429.

Friswell M.I., & Mottershead J.E. (1995). *Finite Element Model Updating in Structural Dynamics*. Kluwer Academic Publishers: Boston.

Friswell M.I., Inman D.J., & Pilkey D.F. (1998). Direct updating of damping and stiffness matrices, *AIAA journal*, 36(3): 491-493.

Fritzen C.P., Jennewein D., & Kiefer T. (1998). Damage detection based on model updating methods. *Mechanical Systems and Signal Processing*. 12: 163-186.

Fujino, Y., & Siringoringo, D. M. (2011). Bridge monitoring in Japan: the needs and strategies. *Structure and Infrastructure Engineering*, 7(7-8), 597-611.

Gang X., Chai S, Allemang RJ, & Li L. (2014). A new iterative model updating method using incomplete frequency response function data. *Journal of Sound and Vibration*, 333(9): 2443-2453.

Garcia Palencia A.J., & Bell E.S. (2013). A Two-Step model updating algorithm for parameter identification of linear elastic damped structures. *Computer Aided in Civil and Infrastructures*, 28(7):509-521.

Gawronski W.K. (2004). *Dynamics Identification and Control of Structures*. Springer-Verlag, New York.

Gillijns S., & Moor B.D., (2007). Unbiased minimum-variance input and state estimation for linear discrete-time systems with direct feedthrough, *Automatica*, 43 (5): 934–937.

Gladwell G.M.L. (1964). Branch Mode Analysis of Vibrating Systems, *Journal of Sound and Vibration*, 1: 41–59.

Goh L.D., Bakhary N., Rahman A.A., & Ahmad B.H. (2013). Application of Neural Network for Prediction of Unmeasured Mode Shape in Damage Detection, *Advances in Structural Engineering*, 16 (1): 99-113.

Golub G., Heath M., & Wahba G. (1979). Generalized cross-validation as a method for choosing a good ridge parameter, *Technometrics*, 21: 215–223.

Greene W.H., & Haftka R.T. (1991). Computational aspects of sensitivity calculations in linear transient structural analysis, *Structure Multidiscipline Optimization*, 3: 176–201.

Groetsch, C.W. (1984). *The theory of Tikhonov Regularization for Fredholm Equations of the First Kind*, Pitman Advanced Publishing, Boston

Guyan R. (1965). Reduction of stiffness and mass matrices. *AIAA Journal*, 3(2): 380.

Hansen, P.C., (1992). Analysis of discrete ill-posed problems by means of the L-curve, *SIAM review*, 34(4), 561-580

Hansen, P.C. (1998). *Rank-deficient and Discrete Ill-Posed Problems: Numerical*

Aspects of Linear Inversion, SIAM, Philadelphia

He J. & Ewins D.J. (1986). Analytical stiffness matrix correction using measured vibration modes, *International Journal of Analytical and Experimental Modal Analysis*, 1: 9-14.

He J., Xu Y.L., Zhang C.D., & Zhang X.H. (2015). Optimum control system for earthquake-excited building structures with minimal number of actuators and sensors. *Smart Structures and Systems*, 16 (6): 981-1002.

He, W.Y., & Zhu, S. (2013). Progressive damage detection based on multi-scale wavelet finite element model: numerical study, *Computers and Structures*, 125: 177-186

He, W.Y., Zhu, S., & Ren, W.X. (2014). A wavelet finite element-based adaptive scale damage detection strategy, *Smart Structures and Systems*, 14(3): 285- 305

Heo G., Wang M.L., & Satpathi D. (1997). Optimal transducer placement for health monitoring of long span bridge, *Soil Dynamics and Earthquake Engineering*, 16: 495–502.

Heredia-Zavoni E., & Esteva L. (1998). Optimal instrumentation of uncertain structural systems subject to earthquake motions, *Earthquake Engineering and Structural Dynamics*, 27 (4): 343–362.

Heredia-Zavoni E., Montes-Iturrizaga R., & Esteva L. (1999). Optimal instrumentation of structures on flexible base for system identification, *Earthquake Engineering and Structural Dynamics*, 28 (12): 1471–1482.

Hernandez E.M., Bernal D., & Caracoglia L. (2013). On-line monitoring of wind

induced stresses and fatigue damage in instrumented structures. *Structure Control and Health Monitor*, 20: 1291–1302.

Ho D.D., Nguyen K.D., Yoon H.S., & Kim J.T. (2012). Multiscale Acceleration-Dynamic Strain-Impedance Sensor System for Structural Health Monitoring, *International Journal of Distributed Sensor Networks*, 2012: 709208.

Hong Y.H., Kim H.K., & Lee H.S. (2010). Reconstruction of dynamic displacement and velocity from measured accelerations using the variational statement of an inverse problem, *Journal of Sound Vibration*, 329 (23): 4980–5003.

Hou J., Jankowski L., & Ou J. (2011). A Substructure Isolation Method for Local Structural Health Monitoring, *Structural Control and Health Monitoring*, 18(6): 601–618.

Hsieh C.S., (2010). On the global optimality of unbiased minimum-variance state estimation for systems with unknown inputs, *Automatica*, 46(4): 708–715.

Hua X.G. (2006). Structural health monitoring and condition assessment of bridge structures, Ph.D. Thesis, Department of Civil and Structural Engineering, The Hong Kong Polytechnic University, Hong Kong.

Hua X.G., Ni Y.Q., & Ko J.M. (2009). Adaptive regularization parameter optimization in output-error-based finite element model updating, *Mechanical Systems and Signal Processing*, 23: 563-579.

Huang, H.W. & Yang, & J.N., (2008). Damage identification of substructure for local health monitoring, *Smart Structures and Systems*, 4(6): 795-807.

Huang, Q., Xu, Y.L., Li, J.C., Su, Z.Q., & Liu, H.J. (2012). Structural damage

detection of controlled building structures using frequency response functions, *Journal of Sound and Vibration*, 331(15): 3476-3492.

Hurty W.C. (1965). Dynamic Analysis of Structural Systems using Component Modes, *AIAA Journal*, 3(4): 678–685.

Imamovic N., (1998). Model validation of large finite element model using test data. Ph.D. dissertation. Imperial College London.

Jaishi B., & Ren W.X. (2006). Damage detection by finite element model updating using modal flexibility residual, *Journal of Sound and Vibration*, 290(1):369-87.

Jensen H.A., Millas E., Kusanovic D. & Papadimitriou C. (2014). Model reduction techniques for Bayesian finite element model updating using dynamic response data, *Computer Methods in Applied Mechanics and Engineering*, 279: 301-324

Jetmundsen B., Bielawa R.L., & Flannelly W.G. (1988). Generalized frequency domain substructure synthesis, *Journal of the American Helicopter Society*, 33: 55-65.

Jo H., & Spencer B.F. (2014). Multi-metric Displacement Monitoring using Model-based Kalman Filter, *Proceeding Of 6th World Conference on Structural Control and Monitoring*, Barcelona, Spain.

Kammer D.C. (1991). Sensor placement for on-orbit modal identification and correlation of large space structures, *Journal of Guidance, Control, and Dynamics*: 14(2): 251-9.

Kammer D.C., & Triller M. J. (1992). Effective sensor placement for on-orbit modal identification of sequentially assembled large space structures, *In The Proceedings*

of IMAC 10: 954-964. The university of Wisconsin.

Kammer D.C., & Yao L. (1994). Enhancement of on-orbit modal identification of large space structures through sensor placement, *Journal of Sound and Vibration*, 171(1): 119-139.

Kammer D.C. (1997). Estimation of Structural Response Using Remote Sensor Locations, *Journal of Guidance, Control, and Dynamics*, 20 (3): 501-508.

Kammer D.C. & Tinker M.L. (2004). Optimal placement of triaxial accelerometers for modal vibration tests, *Mechanical Systems and Signal Processing*, 18: 29-41.

Kirkegaard P.H., & Brincker R. (1994). On the optimal locations of sensors for parametric identification of linear structural systems, *Mechanical Systems and Signal Processing*, 8: 639-647.

Klerk D., Rixen D.J., & Jong J. (2006). The Frequency Based Substructuring Method Reformulated According to the Dual Domain Decomposition Method. *In Proceedings of the Twenty Fourth International Modal Analysis Conference*, St. Louis, MO, Bethel, CT, February. Society for Experimental Mechanics.

Klerk D., Rixen D.J., & Voormeeren S.N. (2008). General Framework for Dynamic Substructuring: History, Review and Classification of Techniques, *AIAA Journal*, 46(5): 1169-1181.

Koh C.G., See L.M., & Balendra T. (1991). Estimation of structural parameters in time domain: a substructure approach, *Earthquake Engineering and Structural Dynamics*, 20(8): 787-801.

Koh C.G., & Shankar K. (2003). Substructural Identification Method without Interface

Measurement, *Journal of Engineering Mechanics*, 129(7): 769-776.

Kubrusly C.S., & Malebranche H. (1985) Sensors and Controllers Location in Distributed Systems – a Survey, *Automatica*, 21: 117-128.

Kim H.M., & Bartkowicz T.J. (1993). Damage detection and health monitoring of large space structures, *Sound and Vibration*, 27: 12-12.

Law S.S., Ward H.S., Shi G.B., Chen R.Z., Waldron P., & Taylor C. (1995a). Dynamic assessment of bridge load-carrying capacities. I, *Journal of Structural Engineering*, 121(3): 478-487.

Law S.S., Ward H.S., Shi G.B., Chen R.Z., Waldron P., & Taylor C. (1995b). Dynamic assessment of bridge load-carrying capacities. II, *Journal of Structural Engineering*, 121(3): 488-495.

Law, S.S., & Ding, Y. (2010a). Substructure Methods for Structural Condition Assessment, *Journal of Sound and Vibration*, 330(15): 3606-3619.

Law S.S., Li J., & Ding Y. (2010b). Structural response reconstruction with transmissibility concept in frequency domain, *Mechanical Systems and Signal Processing*, 25: 952-968.

Lee, H.S., Kim, Y.H., Park, C.J., & Park. H.W. (1999). A new spatial regularization scheme for the identification of geometric shapes of inclusions in finite bodies, *International Journal for Numerical Methods in Engineering*, 46(7), 973-992

Lei Y., Jiang Y., & Xu Z. (2012). Structural damage detection with limited input and output measurement signals, Mechanical Systems and Signal Processing 28: 229-243.

Li D.S., Li H.N., & Fritzen CP. (2007). The connection between effective independence and modal kinetic energy methods for sensor placement, *Journal of Sound and Vibration*, 305(4): 945-955.

Li H.N., Li D.S., & Song G.B. (2004). Recent applications of fiber optic sensors to health monitoring in civil engineering, *Engineering Structures*, 26: 1647-1657.

Li J., & Law S.S. (2011). Substructural response reconstruction in wavelet domain, *Journal of Applied Mechanics* 78:041010.

Li J., & Law S.S. (2012). Substructural damage detection with incomplete information of the structure, *Journal of Applied Mechanics*, 79(4): 041003.

Li X.Y., & Law S.S. (2010). Adaptive Tikhonov regularization for damage detection based on nonlinear model updating, *Mechanical Systems and Signal Processing*, 24: 1646-1664.

Lim K.B. (1990). A Method for optimal actuator and sensor placement for large flexible structures, *Journal of Guidance, Control, and Dynamics*, 19 (1): 1352-1360.

Limongelli M.P. (2003). Optimal location of sensors for reconstruction of seismic responses through spline function interpolation, *Earthquake Engineering and Structural Dynamics*, 32(7): 1055-1074.

Link M., & Zhang L. (1992). Experience with different procedures for updating structural parameters of analytical models using test data, *In The Proceedings of IMAC 10*, San Diego CA.

Liu F. Q., & Zhang L. M. (2000), Successive method for optimal placement of

actuators and sensors, *Journal of Astronautics*, 21 (3): 64-69.

Liu L., Su Y., Zhu J., & Lei Y. (2016), Data fusion based EKF-UI for real-time simultaneous identification of structural systems and unknown external inputs, *Measurement*, 88: 456-467.

Liu Y., Li Y., Wang D., & Zhang S. (2014). Model Updating of Complex Structures Using the Combination of Component Mode Synthesis and Kriging Predictor, *The Scientific World Journal*

Li Z.X., Zhou T.Q., Chan T.H.T., & Yu Y. (2007). Multi-scale numerical analysis on dynamic response and local damage in long-span bridges, *Engineering Structures*, 29: 1507-1524

Li, Z.X., Chan, T.H.T., Yu, Y., & Sun, Z.H. (2009). Concurrent multi-scale modeling of civil infrastructures for analyses on structural deterioration, Part I: modeling methodology and strategy, *Finite Elements in Analysis and Design*, 45: 782-794.

Lourens E., Papadimitrioua C., Gillijnsc S., Reyndersa E., De Roeck G., & Lombaer G. (2012). Joint input-response estimation for structural systems based on reduced-order models and vibration data from a limited number of sensors, *Mechanical Systems and Signal Processing*, 29: 310-327.

Lu Z.R., & Law S.S. (2007). Features of dynamic response sensitivity and its application in damage detection, *Journal of Sound and Vibration*, 303(1): 305–29.

Ma X., Vakakis A.F., & Bergman L.A. (2001). Karhunen-Loeve modes of a truss: transient response reconstruction and experimental verification, *AIAA journal*, 39(4): 687-696.

MacNeal R.H. (1971). A Hybrid Method of Component Mode Synthesis, *Computers and Structures*, 1(4): 581-601.

Maes K., Iliopoulos A., Weijtjensc W., Devriendtc C., & Lombaerta G. (2016). Dynamic strain estimation for fatigue assessment of an offshore monopile wind turbine using filtering and modal expansion algorithms, *Mechanical Systems and Signal Processing*. 76-77: 592-611

Majumder L., & Manohar C.S. (2003). A time-domain approach for damage detection in beam structures using vibration data with a moving oscillator as an excitation source, *Journal of Sound and Vibration*, 268 (4): 699-716.

Mares C., Friswell M.I., & Mottershead J.E. (2002). Model updating using robust estimation, *Mechanical* Systems *and Signal Processing*, 16 (1):169-183.

Maes K., Lourens E., Van Nimmen K., Reynders E., De Roeck G., & Lombaert G. (2015). Design of sensor networks for instantaneous inversion of modally reduced order models in structural dynamics, *Mechanical Systems and Signal Processing*, 52-53: 628-644.

Malioutov D.M. (2003). A sparse signal reconstruction perspective for source localization with sensor arrays. M.S. thesis, Massachusetts Institute of Technology, Cambridge, MA.

Meng X., Dodson A.H., & Roberts G.W. (2007). Detecting bridge dynamics with GPS and tri-axial accelerometers, *Engineering Structures*, 29(11): 3178-3184.

Meo M., & Zumpano G. (2005). On the optimal sensor placement techniques for a bridge structure, *Engineering Structures*, 27, 1488-1497.

Morozov V.A. (1984). *Methods for Solving Incorrectly Posed Problems* (translation ed.: Nashed M. Z.). Wien, New York: Springer 1984.

Mottershead J.E., & Friswell M.I. (1993). Model updating in structural dynamics: a survey, *Journal of Sound and Vibration*, 167: 347-375.

Naets F., Cuadrado J., & Desmet W., (2015). Stable force identification in structural dynamics using Kalman filtering and dummy-measurements, *Mechanical Systems and Signal Processing*, 50: 235-248.

Natke H.G., Cottin N., Prells U. (1994). Problems and related countermeasures in mathematical model improvement: a survey, *in Proceedings of the ICOSSAR 93, Sixth International Conference on Structural Safety and Reliability*, Innsbruck, Austria, 9–13 August 1993, A.A. Balkema, Rotterdam, Brookfield, 1994.

Nelson R.B. (1976). Simplified calculation of eigenvector derivatives, *AIAA Journal*, 14 (9): 1201-1205.

Norden E., Huang Z., Shen S.R., Long M.C., Wu H.H., Shih Q., & Zheng C. (1998). The empirical mode decomposition and the Hilbert spectrum for nonlinear and non-stationary time series analysis, *Proceedings of the Royal Society*, 454: 903-993.

Odelson B.J., Rajamani M.R., & Rawlings J.B. (2006). A new auto-covariance least-squares method for estimating noise covariances, *Automatica*, 42(2): 303-308.

Ojalvo I.U. (1987). Efficient computation of mode shape derivatives for large dynamic systems, *AIAA Journal*, 25(10): 1386-1390.

Overschee P.V., & Moor B.D. (1994). N4SID: Subspace algorithms for the identification of combined deterministic-stochastic systems, *Automatica*, 30: 75-93.

Overschee P., & Moor B.D. (2012). *Subspace Identification of Linear Systems: Theory, Implementation, Applications.* Springer Science & Business Media.

Padula, L.S., & Kincaid R.K. (1999). Optimization Strategies for Sensor and Actuator Placement. NASA/TM-1999-209126, April.

Pan S., Su H., Wang H., & Chu J. (2011). The study of joint input and state estimation with Kalman filtering, *Transactions of the Institute of Measurement and Control*, 33(8): 901-918.

Palanisamy R.P., Cho S., Kim H., & Sim S.H. (2015). Experimental validation of Kalman filter-based strain estimation in structures subjected to non-zero mean input, *Smart Structures* and *Systems*, 15(2): 489-503.

Papadopoulos M., & Garcia E. (1998). Sensor placement methodologies for dynamic testing, *AIAA Journal*, 36(2): 256-263.

Papadimitriou C., Beck J.L., & Au S.K. (2000). Entropy-based optimal sensor location for structural model updating, *Journal of Vibration and Control*, 6(5): 781–800.

Papadimitriou C. (2004). Optimal sensor placement methodology for parametric identification of structural systems, *Journal of Sound and Vibration*, 278(4-5): 923-47.

Papadimitriou C. (2005). Pareto optimal sensor locations for structural identification, *Computer Methods in Applied Mechanics and Engineering*, 194 (12–16): 1655–

1673.

Papadimitriou C., Fritzen C.P., Kraemer P., & Ntotsios E. (2010). Fatigue predictions in entire body of metallic structures from a limited number of vibration sensors using Kalman filtering, *Structural Control Health Monitoring*, 18(5): 554-573.

Papadimitriou C., & Papadioti D.C. (2013). Component mode synthesis techniques for finite element model updating, *Computers and Structures*, 126:15-28.

Park, H.W. (2002). Regularization techniques in system Identification for Damage Assessment of Structures, Ph.D. Thesis, Department of Civil Engineering, Seoul National University.

Park J., Sandberg I.W. (1991). Universal approximation using radial-basis-function networks, *Neural Computation*, 3(2): 246-257.

Park J.W., Sim S.H., & Jung H.J. (2013). Displacement Estimation using Multimetric Data Fusion, *IEEE/ASME Transactions on Mechatronics*, 18(6): 1675-1682.

Park J.W., Sim S.H., & Jung H.J. (2014). Wireless Displacement Sensing System for Bridges using Multi-sensor Fusion. *Smart Materials and Structures*, 23(4): 045022.

Park N.G., & Park Y.S. (2003). Damage detection using spatially incomplete frequency response function, *Mechanical System and Signal Processing*, 17(3): 519-532.

Park U.S., Choi J. W., Yoo W. S., *et al*. (2003). Optimal placement of sensors and actuators using measures of modal controllability and observability in a balanced coordinate. *KSME International Journal*, 17(1): 11-22.

Penny J.E.T., Friswell M.I., & Garvey S.D. (1994). Automatic Choice of Measurement Locations for Dynamic Testing, *AIAA Journal*, 32, 407-414.

Rao A.R.M., & Anandakumar G., (2007). Optimal placement of sensors for structural system identification and health monitoring using a hybrid swarm intelligence technique, *Smart Materials and Structures*, 16(6): 2658.

Ribeiro J.S., & Maia N. (2000). On the generalization of the transmissibility concept, *Mechanical Systems and Signal Processing*, 14: 29-36.

Richardson M., & Mannan M.A. (1990). Detection and location of structural cracks using FRF measurements, In *Proceeding of the 8th International Modal Analysis Conference*, 512-518.

Rixen D. (2004). A dual Craig–Bampton method for dynamic substructuring, *Journal of Computational and Applied Mathematics*, 168 (1):383-391.

Ross R.G. (1971). Synthesis of stiffness and mass matrices from experimental vibration modes. *In National Aeronautics and Space Engineering and Manufacturing Meeting*, Society of Automotive Engineers, pp 2627-2635.

Rubin S. (1975). Improved Component-Mode Representation for Structural Dynamic Analysis, *AIAA Journal*, 13: 995–1006.

Salawu O.S. (1997). Detection of structural damage through changes in frequency: a review, *Engineering Structures*, 19(9): 718-723.

Sanayei M., Esfandiari A., Baskhtiari Nejad F., & Rahai A. (2012). Quasi-linear sensitivity-based structural model updating using experimental transfer functions, *Structural Health Monitoring*, 11(6): 656-670

Santosa F., & Symes W. (1986). Linear inversion of band-limited reflection seismograms, *SIAM Journal on Scientific and Statistical Computing*, 7(4):1307-1330.

Sassano M, & Astolfi A. (2014). Dynamic generalized controllability and observability functions with applications to model reduction and sensor deployment, *Automatica*, 50 (5): 1349-1359.

Setola R. (1998). A spline-based state reconstruction for active vibration control of a flexible beam, *Journal of Sound and Vibration*, 213 (5): 777-790.

Shah PC, & Udwadia F.E. (1978). A methodology for optimal sensor locations foridentification of dynamic systems. *Journal of Applied Mechanics, Transactions ASME*, 45(1):188-96.

Shan D., Li Q., Khan I., & Zhou X. (2015). A novel finite element model updating method based on substructure and response surface model, *Engineering Structures*, 103 147-156.

Shi, Z.Y., Law, S.S., & Zhang, L.M. (1998). Structural damage localization from modal strain energy change, *Journal of Sound and Vibration*, 218(5): 825-844.

Shi, Z.Y., Law, S.S., & Zhang, L.M. (2000a). Structural damage detection from modal strain energy change, *Journal of Engineering Mechanics*, 126(12): 1216-1223.

Shi Z.Y., Law S.S., & Zhang L.M. (2000b). Optimum sensor placement for structural damage detection, *Journal of Engineering Mechanics*, 126(11):1173-9.

Shih C.Y., Tsuei Y.G., Allemang R.J., & Brown D.L. (1988). Complex mode indication function and its applications to spatial domain parameter estimation,

Mechanical Systems and Signal Processing, 2 (4), July.

Shulz M.J., & Inman D.J. (1994). Model updating using constrained eigenstructure assignment, *Journal of Sound and Vibration*, 178(1): 113-130.

Sidhu J., & Ewins D. J. (1984). Correlation of finite element and modal test studies of a practical structure, In *The Proceedings of IMAC 2*, pp: 756-762.

Sim S.H., Spencer B.F., & Nagayama T. (2011). Multimetric Sensing for Structural Damage Detection, *Journal of Engineering Mechanics*, 137(1): 22-31.

Skelton R.E. (1988). *Dynamic Systems Control: Linear Systems Analysis and Synthesis*. Wiley, New York.

Smyth A., & Wu M.L., (2007). Multi-rate Kalman filtering for the data fusion of displacement and acceleration response measurements in dynamic system monitoring, *Mechanical Systems and Signal Processing*, 21(2): 706–723.

Staszewski WJ, & Worden K. (2001). Overview of optimal sensor location methods for damage detection. *SPIE's 8th Annual International Symposium on Smart Structures and Materials*. International Society for Optics and Photonics, pp 179-187.

Steenackers G., Devriendt C., & Guillaume P. (2007). On the use of transmissibility measurements for finite element model updating, *Journal of Sound and Vibration*, 303: 707-722.

Studer, M., & Peters, K. (2004). Multi-scale sensing for damage identification, *Smart Materials and Structures*, 13: 283-294.

Sun, B. Xu, Y.L., & Li, Z.X. (2016). Multi-scale model for linking collective behavior of short and long cracks to continuous average fatigue damage, *Engineering Fracture Mechanics*, 157(3): 141-153.

Sun, B. Xu, Y.L., & Li, Z.X. (2016). Multi-scale fatigue model and image-based simulation of collective short cracks evolution process, *Computational Materials Science*, 117: 24-32,

Sung S.H., Park J.W., Nagayama T., & Jung H. J. (2013). A multi-scale sensing and diagnosis system combining accelerometers and gyroscopes for bridge health monitoring, *Smart Material and Structures*, 23: 015005.

Tan R.C.E., & Andrew A.L. (1989). Computing derivatives of eigenvalues and eigenvectors by simultaneous iteration. Institute of Mathematics and its Application, *Journal of Numerical Analysis*, 9(1): 111-122.

Tee K.F., Koh C.G., & Quek S.T. (2005). Substructural First- and Second-order Model Identification for Structural Damage Assessment, *Earthquake Engineering and Structural Dynamics*, 34(15): 1755-1775.

Thoren A. R. (1972). Derivation of mass and stiffness matrices from dynamic test data, *AIAA Conference Paper*, 1(72), 346.

Tibshirani R. (1996). Regression shrinkage and selection via the LASSO, *Journal of the Royal Statistical Society (Series B)*, 58: 267-288.

Tikhonov A.N., & Arsenine V.Y. (1977). *Solutions to Ill-Posed Problems*, Winston-Wiley, New York

Titurus B., & Friswell M.I. (2008). Regularization in model updating, *International*

Journal for Numerical Methods in Engineering, 75(4): 440-478.

Trendafilova I., Heylen W. (1998). Fault localization in structures from remote FRF measurements: influence of the measurement points. *Proceedings of the 23rd International Conference on Noise and Vibration*, Leuven, Belgium, pp.149–156.

Trinh T.N., & Koh C.G. (2011). An Improved Substructural Identification Strategy for Large Structural Systems, *Structural Control and Health Monitoring*, 19(8): 686-700.

Udwadia F.E. (1994). Methodology for optimal sensor locations for parameter identification in dynamic systems, *Journal of Engineering Mechanics*, 120(2): 368-390.

Urgueira A.P.V., Almeida R.A.B., & Maia N.M.M. (2011). On the use of the transmissibility concept for the evaluation of frequency response functions, M*echanical Systems and Signal Processing*, 25 (3): 940-951.

Varoto P., & McConnell K. (1998). Single point vs. multipoint acceleration transmissibility concepts in vibration testing, In *Proceedings of the 16th International Modal Analysis Conference (IMACXVI)*, Santa Barbara, California, USA, pp. 83–90.

Wan Z., & Li S. (2014). Structural response reconstruction based on the modal superposition method in the presence of closely spaced modes, *Mechanical Systems and Signal Processing*, 42: 14-30.

Wang F.Y., Xu Y.L., & Qu W.L. (2014), Mixed-dimensional finite element coupling for structural multi-scale simulation, *International Journal of Finite Elements in*

Analysis and Design, 92: 12-25.

Wang J., Law S.S., & Yang Q.S. (2013). Sensor placement methods for an improved force identification in state space, *Mechanical Systems and Signal Processing*, 41(1): 254-267.

Wang J., Law S.S., & Yang Q.S. (2014). Sensor placement method for dynamic response reconstruction, *Journal of* Sound *and Vibration*, 333(9): 2469-2482.

Wang M., Wang D., & Zheng G. (2012). Joint dynamic properties identification with partially measured frequency response function, *Mechanical System and Signal Processing*, 27:499-512.

Worden K., & Burrows A.P. (2001). Optimal sensor placement for fault detection, *Engineering Structures*, 23: 885-901.

Wang S. (2013). Iterative modal strain energy method for damage severity estimation using frequency measurements, *Structural Control and Health Monitoring*, 20(2): 230-240.

Weber B., Paultre P., & Proulx J. (2009). Consistent regularization of nonlinear model updating for damage identification, *Mechanical Systems and Signal Processing*, 23 (6): 1965-1985.

Weng S. (2010). A new substrucural method for model updating of large-scale structures. The Hong Kong Polytechnic University, Hong Kong, June

Weng S., Xia Y., Xu Y.L., & Zhu H.P. (2011a). Substructure based approach to finite element model updating, *Computers and Structures*, 89: 772-782.

Weng S., Xia Y., Xu Y.L., & Zhu H.P. (2011b). Substructuring approach to finite element model updating, *Computers and Structures*, 89 (9-10): 772-782.

Weng S., Xia Y., Zhou X.Q., Xu Y.L., & Zhu H.P. (2012). Inverse Substructure Method for Model Updating of Structures, *Journal of Sound and Vibration*, 331 (25): 5449-5468.

Wu D., & Law S.S. (2004a). Model error correction from truncated modal flexibility sensitivity and generic parameters. I: simulation. *Mechanical Systems and Signal Processing* 18: 1381-1399.

Wu D., & Law S.S. (2004b). Model error correction from truncated modal flexibility sensitivity and generic parameters. II: experimental verification, *Mechanical Systems and Signal Processing*, 18: 1401-1419.

Yan W.J., & Ren W.X. (2014). Closed-form modal flexibility sensitivity and its application to structural damage detection without modal truncation error, *Journal of Vibration and Control*, 20 (12): 1816-1830

Yong S., Zhu M., & Frazzoli E. (2013). A unified filter for simultaneous input and state estimation for linear discrete-time stochastic systems, *Automatica*, 63: 321-329.

Xiao, X., Xu, Y.L., & Zhu, Q. (2014), Multiscale modeling and model updating of a cable-stayed bridge II: model updating using modal frequencies and influence lines, *Journal of Bridge Engineering*, 20(10): 04014113.

Xing Z., & Mita A. (2012). A Substructure Approach to Local Damage Detection of Shear Structure, *Structural Control and Health Monitoring*, 19(2): 309-318.

Xu Y.L., & Chen J. (2004). Structural damage detection using empirical mode

decomposition: experimental investigation, *Journal of Engineering Mechanics*. 130(11): 1279-1288.

Xu Y.L., Zhang J., Li J.C. & Xia Y. (2009). Experimental investigation on statistical moment-based structural damage detection method, *Structural Health Monitoring*, 8 (6): 555-571.

Xu Y.L., & Xia Y. (2011). *Structural Health Monitoring of Long-Span Suspension Bridges*, CRC Press.

Xu Y.L., Zhang J., Li J., & Wang X.M. (2011). Stochastic damage detection method for building structures with parametric uncertainties, *Journal of Sound and Vibration*, 330: 4725-4737.

Xu Y.L., Zhang X.H., Zhan S., Hong X.J., Zhu L.D., Xia Y., & Zhu S. (2012). A test-bed for structural health monitoring of long-span suspension bridges, *Journal of Bridge Engineering*, ASCE, 17(6): 896-906.

Xu Y.L., Huang Q., Zhan, S., Su Z.Q., & Liu H.J. (2014). FRF-based damage detection of controlled buildings with podium structures: experimental investigation, *Journal of Sound and Vibration*, 333: 2762-2775.

Xu Y.L., Zhang X.H., Zhu S., & Zhan S. (2016). Multi-type sensor placement and response reconstruction for structural health monitoring of long-span suspension bridges, *Science Bulletin*, 61(4):313-329.

Yang J.N., & Huang H.W. (2007). Substructure damage identification using a damage tracking technique, Proceedings *of SPIE -The International Society for Optical Engineering*, San Diego, California, USA.

Yao L., Sethares W.A., & Kammer D.C. (1993). Sensor placement for on-orbit modal identification via a genetic algorithm, *AIAA Journal*, 31(10): 1167-9.

Yang J., & Zhang Y. (2011). Alternating direction algorithms for ℓ_1 -problems in compressive sensing, *SIAM Journal on Scientific Computing*, 33(1-2): 250-278.

Yang Y., & Nagarajaiah S. (2013). Output-only modal identification with limited sensors using sparse component analysis, *Journal of Sound and Vibration*, 332(19): 4741–4765.

Yang Y., & Nagarajaiah S. (2013). Output-only modal identification with limited sensors using sparse component analysis, *Journal of Sound and Vibration*, 332(19): 4741–4765.

Yang Y., & Nagarajaiah S. (2014). Blind denoising of structural vibration responses with outliers via principal component pursuit, *Structure Control and Health Monitoring*, 21(6): 962-978.

Yang Y., & Nagarajaiah S. (2015). Output-only modal identification by compressed sensing: Non-uniform low-rate random sampling. *Mechanical Systems and Signal Processing*, 56-57: 15-34.

Yu J.X., Xia Y., Lin W., & Zhou X.Q. (2016), Element-by-element model updating of large-scale structures based on component mode synthesis method, *Journal of Sound and Vibration*, 362:72-84.

Yuan Z.X., Yu K.P. (2015). Finite element model updating of damped structures using vibration test data under base excitation, *Journal of Sound and Vibration*, 340(31): 303-316.

Yuen K.V., Katafygiotis L.S., Papadimitriou C., Mickleborough N.C. (2001). Optimal sensor placement methodology for identification with unmeasured excitation, *Journal of Dynamic Systems, Measurement and Control*, 123(4): 677-686.

Yuen K.V., & Katafygiotis L.S. (2006). Substructure identification and health monitoring using noisy response measurements only, *Computer-Aided Civil and Infrastructure Engineering*, 21(4): 280-291.

Yun, C.B., & Lee, H.J. (1997). Substructural Identification for Damage Estimation of Structures, *Structural Safety*, 19(1), 121-140.

Yun S., & Toh K.C.A. (2011). Coordinate gradient descent method for ℓ_1-regularized convex minimization, *Computational Optimization and Applications*, 48(2): 273-307.

Zhang D.Y., & Johnson E.A. (2012). Substructure Identification for Shear Structures: Cross Power Spectral Density Method, *Smart Materials and Structures*, 21(5): 055006.

Zhang J., Xu Y.L., Xia Y., & Li J. (2011). Generalization of the statistical moment-based damage detection method, *Structural Engineering and Mechanics*, 38(6): 715-732.

Zhang X.H. (2012) Multi-scale monitoring of long-span suspension bridges, PhD Thesis, The Hong Kong Polytechnic University, October.

Zhang X.H., Zhu S., Xu Y.L., & Hong X.J. (2011). Integrated optimal placement of displacement transducers and strain gauges for better estimation of structural response, *International Journal of Structural Stability and Dynamics*, 11(3):

581-602.

Zheng Z.D., Lu Z.R., Chen W.H., & Liu J.K. (2015). Structural damage identification based on power spectral density sensitivity analysis of dynamic responses, *Computers and Structures*, 146: 176-184.

Zhou X. Q., Xia Y., & Hao H. (2013). Sensor placement for structural damage detection considering measurement uncertainties, *Advances in Structural Engineering*, 16(5): 899-907.

Zhu H. P., & Xu Y.L. (2005) Damage detection of mono-coupled periodic structures based on sensitivity analysis of modal parameters, *Journal of Sound and Vibration*, 285 (1-2): 365-390.

Zhu,Q. Xu Y.L., & Xiao X. (2015). Multi-scale modelling and model updating of a cable-stayed bridge, Part I: modelling and influence line analysis, *Journal of Bridge Engineering*, ASCE, 20(10): 04014113.

Zhu S., Zhang X.H., Xu Y.L., & Zhan S. (2013). Multi-type sensor placement for structural health monitoring, *Advances in Structural Engineering*, 16 (10): 1779-1797.

Zhu S., He, W.Y., & RenW.X. (2014). Adaptive-scale damage detection for frame structures using beam-type wavelet finite element: experimental validation, *Journal of Earthquake and Tsunami*, 7(3): 1350024.

Ziaei-Rad S., & Imregun M. (1996). On the accuracy required of experimental data for finite element model updating, *Journal of Sound and Vibration*, 196 (3): 323-336.

Ziaei-Rad S., & Imregun M. (1999). On the use of regularization techniques for finite

element model updating, *Inverse Problem in Engineering*, 7(5): 471-503.